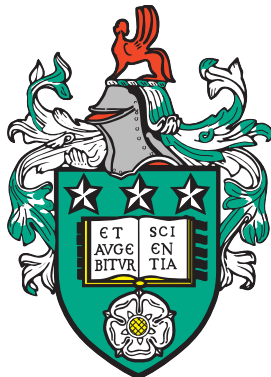




UNIVERSITY OF LEEDS

Numerical Simulations of Dusty Colliding Wind Binaries



Joseph Eatson
University of Leeds
School of Physics and Astronomy

Submitted in accordance with the requirements for the degree of

Doctor of Philosophy

April, 2022

To my Mum, without her help these past twenty-seven years there's no way I would
have gotten this far.

Thank you so much, for everything.

*“Space is **big**. Really big. You just won’t believe how vastly, hugely, mind-bogglingly big it is. I mean, you may think it’s a long way down the road to the chemist’s, but that’s just peanuts to space.”*

DOUGLAS ADAMS
The Hitchhiker’s Guide to the Galaxy

“I am aware that quoting Douglas Adams in an astrophysics thesis is an absolutely enormous cliché, but I want to do it anyway.”

ME

Discussing the inclusion of a quote in this thesis

Acknowledgements

I suppose a good place to start when thanking people in a thesis is to start with family. To my mum, when I asked you for help funding my doctoral degree, you said yes, instantly and without hesitation. Considering all you have done and sacrificed for me throughout my life, your agreement to help me was another act of kindness that I can barely repay (trust me, I've done the maths). You've been there for me every step of the way, I could not ask for a more wonderful mum, and I hope I can make you proud. Thank you to the rest of my family, in particular my dad, Cress, Olivia, Maddy, Oscar¹, my mum's partner (and soon to be my stepdad!) Neil, and my grandparents. You are the best family anyone could ask for and thank you for being so supportive.

I also owe a debt to my supervisor, Dr Julian Pittard, you've gone above and beyond when it came to my supervision. Your help and advice throughout this project have been astounding, from sending corrections to papers within a single day, to patiently explaining the finer points of the work when I was completely clueless in the first² year. I'm still amazed how you can rattle off a paper or three from memory when I've come into your office asking questions about a very specific part of my work. Honestly, how do you do that? It's very impressive!

No good thesis³ wouldn't be complete without a commitment to the authors' friends. I first met some of you on the literal first day of my undergraduate degree, it's quite incredible how you've all tolerated my nonsense for so long. From essentially forcing my way into Rob's house so I could cook some disastrous fried chicken, to playing *Super Smash Bros.* all night long on its release day, to watching trashy movies over the internet at the height of a global pandemic, these are moments I'll treasure for the rest of my life. In particular, those who are still in Leeds, Rob⁴, Matt, Kelsie, Alex and Sam; as well as those who aren't: Martin, Elliot, Caz, Andy, John and Devon. Congratulations are also in order for Kelsie and Alex on their wedding, you did it you two! Thank you, all of you, for filling my life with joy this past decade⁵.

To my partner Pruthvi, I cannot even begin to describe how unlikely it is that the two of us even met. Two people finding and falling for each other on the more

¹And Alf!

²And arguably second, third and fourth.

³Though the quality of this one is debatable.

⁴"People can put whatever they want in footnotes, nobody reads them." - Dr Rob Welch

⁵And for helping to proof-read my thesis, it's a tremendous help.

esoteric circles of the internet is like two particles colliding in the tenuous interstellar medium... If you'll excuse the extremely trite metaphor. You've been loving, kind, helpful, and the most wonderful partner anyone could ask for. I am truly blessed to know you and love you.

I would also like to thank the fantastic team at Leeds' ARC High-Performance Computing department, considering the bulk of this thesis involves many 3D numerical simulations, my use of ARC 4's compute nodes can be described as somewhere from "excessive" to "taking the piss"¹. I also apologise for that one time I ran my simulations on the login nodes for multiple days, I swear it was an accident.

I would also like to thank two figures from my formative years for inspiring me. The first is my 9th year Physics teacher, Isobel Why, who kindled my interest in the field, she was the finest teacher I ever had, turning me from an underachieving student to a keen and committed aspiring physicist. She truly had faith in all of her students and pushed them far beyond what they thought themselves capable of. Whilst she left teaching shortly after that year, I will never forget her impact on my life and my work. Another is quite indirect, but still important, I would be amiss to thank Winchell "Nyrath" Chung, curator of the website [Atomic Rockets](#)². Winchell's work is perhaps one of the most complete and exhaustive archives of real-life and fictional rocketry and space exploration resources - whilst I haven't called on his work much during my career in astrophysics, I pored over this website when I was younger (perhaps reading it more thoroughly than any of my course textbooks). It was fascinating, insightful and inspiring not only to me but to thousands of readers; the number of projects, from hard SFF novellas to honest-to-goodness research proposals hinge on his tireless efforts to catalogue humankind's exploration of space in both reality and fiction. I learned of his cancer diagnosis whilst writing this thesis, and it cut me to my core. Without his work, I don't think I would have turned a fascination with space into a lifelong passion. Thank you so much, both of you, you may not realise it, you may not ever read this, but you changed my life.

Finally, I would like to thank Leandro Panizzon and his wife, Margarita. Though Methylphenidate was originally synthesised by him to treat her low blood pressure, it also works quite well for dragging my attention-deficit disorder riddled brain through this PhD.

¹I have quantified the amount of CPU time I have used up, it is in the region of 250 core-years!

²http://projectrho.com/public_html/rocket/

Abstract

Colliding wind binary (CWB) systems are exceptionally easy to understand at the most fundamental level. These systems consist of two stars in a binary system that produce winds that collide. Unlike many pieces of terminology in astrophysics, this one is fairly simple and self-explanatory.

This is where the simplicity ends, however.

These systems produce titanic quantities of x-rays, making them some of the brightest continuous x-ray sources in the galaxy. The innermost wind collision region is an enormous shocked region with temperatures typically on the order of 10^8 Kelvin, driving these x-ray emissions. Whilst being very bright, they are distant, rare, and their innermost depths are shrouded by dense stellar winds produced by the dominant Wolf-Rayet star driving their titanic shocks. As such, these systems are fundamentally very complex to observe *and* simulate.

What is most interesting is that despite violent shocks, intense x-ray emissions and hot stellar winds, small interstellar dust grains of amorphous carbon can form. The quantity of these grains varies from system to system but can be produced in quantities on the order of $10^{-6} M_{\odot} \text{ yr}^{-1}$ in the most extreme dust-producing systems. The mechanisms of this dust creation and production are extremely poorly understood, as such we aim to shed some light on these systems through *in silico* work.

Through this project, we have developed a model to simulate CWB systems using the open-source `Athena++` hydrodynamical code. We have also incorporated a passive scalar model to simulate dust growth, destruction and radiative cooling. Using this model we have performed a parameter space search in order to understand which wind and stellar parameters affect dust growth and production in a CWB system. We have also performed a simulation of the episodic dust-producing CWB system, WR140. Our results have determined which parameters are the most influential on dust growth within these systems. We have also managed to replicate the periodic nature of dust production in WR140 without artificial constraints, lending credence to the accuracy of our model.

Whilst there is much to be done in the future, and many more systems to be simulated (in particular the recently discovered WR+WR CWB systems WR48a and WR70-16) we find that this model is a good first step towards shedding light on these elusive and dust shrouded systems...

CONTENTS

1	Introduction & Motivation	1
1.1	Motivation & Goals	4
1.2	Thesis Structure	5
2	Background	7
2.1	Early-Type Stars	8
2.1.1	Formation	9
2.1.2	The p-p & CNO fusion cycles	11
2.1.3	Stellar winds	13
2.1.3.1	Driving mechanisms	14
2.1.3.2	Line-driven wind theory	15
2.1.4	Evolved early-type stars	18
2.1.4.1	Wolf-Rayet stars	20
2.1.4.2	The death of a star	24
2.2	Interstellar Dust	25
2.2.1	Dust composition	29
2.2.2	The importance of interstellar dust	29
2.3	Colliding Wind Binary Systems	31
2.3.1	History of CWB observation	31
2.3.2	The wind collision region	32
2.3.3	Cooling in the WCR	35
2.3.3.1	“Cool” medium	37
2.3.3.2	“Warm” medium	38
2.3.3.3	“Hot” medium	39
2.3.3.4	Radiative effects in WCRs	40

CONTENTS

2.3.3.5	Dust cooling	42
2.3.4	Dust formation in CWB systems	45
2.3.5	Important WCd systems	48
2.3.5.1	WR98a	49
2.3.5.2	WR140	50
2.3.5.3	WR104	51
2.3.6	WR+WR systems	53
2.3.6.1	WR70-16 (“Apep”) – a recently discovered WR+WR system . .	53
2.3.6.2	WR48a – revisiting a WR+WR candidate	55
2.4	Summary	55
3	Methodology & Numerical Simulation	57
3.1	The History & Mathematics of Numerical Simulations	58
3.2	The Purpose of Numerical Simulations	62
3.3	The MG Hydrodynamical Code	64
3.4	The Athena++ hydrodynamical code	66
3.5	Mesh Refinement	67
3.6	Simulating CWB systems	71
3.6.1	Assumptions	72
3.6.2	Stars, wind propagation & refinement	73
3.6.3	Cooling in numerical simulations	74
3.6.4	Plasma cooling	76
3.6.4.1	Other calculation methods	77
3.6.5	Dust cooling	78
3.6.5.1	Integration Method	81
3.6.5.2	Lookup table	82
3.6.5.3	The Dwek and Werner (1981) approximation	84
3.6.5.4	Calculating n_e	85
3.6.6	Model implementation	86
3.7	The BIDMAS Adverted Scalar Dust Model	90
3.7.1	BIDMAS features	90
3.7.2	Implementation	91
3.7.2.1	Dust injection	92
3.7.2.2	Assumptions & limitations	95
3.7.2.3	Dust cooling	95

CONTENTS

3.7.2.4	Dust evolution	96
3.7.3	Contemporary dust models	99
3.7.3.1	The Hendrix dust model	99
3.7.4	Future dust models	100
3.8	Summary	102
4	An Exploration of Dust Growth Within WCd Systems	105
4.1	Introduction	106
4.2	Methodology	109
4.2.1	Gas and dust cooling	111
4.2.2	Numerical modelling of dust through advected scalars	115
4.3	Model Parameters	118
4.3.1	Cooling mechanisms	118
4.3.2	Wind momentum ratio	119
4.3.3	Separation distance	119
4.3.4	Data collection	120
4.4	Results	121
4.4.1	Mass loss rate variation	126
4.4.2	Terminal velocity variation	128
4.4.3	Separation variation	132
4.5	Summary & Conclusion	134
4.5.1	Wind mixing within the WCR	135
4.5.2	Summary	135
5	Exploring Dust Growth in WR140	137
5.1	Introduction	138
5.2	Methodology	141
5.2.1	Radiative cooling	142
5.2.2	Dust model	143
5.3	System parameters	146
5.3.1	WR140 parameters	148
5.3.2	Simulation parameters	148
5.3.3	Data collection	149
5.4	Results	150
5.4.1	Instabilities	155

CONTENTS

5.4.2	Influence of varying wind velocity on dust production	157
5.5	Summary	158
6	Final Notes and Conclusions	161
6.1	Conclusions	162
6.1.1	Causes of dust growth in WCd systems	163
6.1.2	The role of eccentricity in dust formation	164
6.1.2.1	Radiative driving	165
6.2	Future Study	165
6.2.1	More complex models	165
6.2.2	Further simulations of observed systems	166
6.2.3	Radiative transfer	166
6.2.4	WR+WR systems	166
6.2.5	<i>Telescopes: The Next Generation</i>	167
6.3	Other Observations	168
6.3.1	<i>How I Learned to Stop Worrying and Love Numerics</i>	168
6.3.2	Become a researcher, see the world!	169
6.3.3	Paul Erdős was probably onto something	169
6.3.4	Carinae Strain: PhD research in a time of pandemic	169
6.4	The Last Word	170
A	Breakdown of Computational Models	171
A.1	Initialisation	172
A.2	Cooling Model	172
A.3	Dust Model	173
B	Software Carpentry	175
B.1	Software & Resource Acknowledgements	176
B.2	Parallelism & Amdahl's Law	178
B.3	Datatypes & Visualisation	181
B.4	Version Control	183
References		184

LIST OF FIGURES

1.1	<i>NASA APOD images of Wolf-Rayet and CWB systems</i>	2
1.2	<i>Chandra & NuSTAR imagery of η Carinae (Hamaguchi et al., 2018)</i>	3
2.1	Reaction rates at the center of the sun	12
2.2	ρ_w comparison of main sequence winds	14
2.3	Planck's law radiance comparison with resonance lines	16
2.4	Radiative line driving velocity and density profile	17
2.5	Luminosity and lifetime as a function of stellar mass	19
2.6	<i>M1-67 nebula around WR124 (Marchenko et al., 2010)</i>	21
2.7	Examples of mass loss over the lifetime of a high-mass star	22
2.8	Stellar evolution tracks of massive stars	24
2.9	Grain lifetime comparison	28
2.10	<i>A diagram of the Wind Collision Region (Eichler & Usov, 1993)</i>	32
2.11	Comparison of wind momentum ratio, η , on WCR structure	33
2.12	Wind shock fraction, as a function of η	35
2.13	WC & solar abundance plasma cooling curves	36
2.14	The 21 cm spectral line	38
2.15	O ⁺ and O ⁺⁺ spectral line transitions	39
2.16	A comparison of the influence of radiative cooling on a CWB system	42
2.17	Dust cooling vs. plasma cooling	43
2.18	H_{el} and H_{coll} comparison	45
2.19	Map of WR stars on the galactic plane	47
2.20	L' photometry of episodic dust making stars	49
2.21	<i>Multiwavelength image of WR98a (Monnier et al., 2007)</i>	50
2.22	<i>Spiral structure of WR104 (Soulain et al., 2018)</i>	51

LIST OF FIGURES

2.23 <i>VLT image of Apep (Callingham et al., 2019)</i>	54
3.1 A Riemann problem	60
3.2 Adaptive mesh refinement comparison	68
3.3 Athena++ adaptive mesh refinement example	69
3.4 AMR breakdown in Athena++	70
3.5 Static mesh refinement in Athena++	71
3.6 Comparison of dust and plasma cooling rates in post-shock environment	79
3.7 3D plot of $\mathcal{K}(x^*, z)$	81
3.8 Plot of $\mathcal{K}(x^*, z)$ for discrete values of z	82
3.9 h_e integration accuracy comparison	83
3.10 Dust lookup table methods comparison	85
3.11 Electron transparency method accuracy – Λ_d	86
3.12 OB and WR electron-ion ratios	87
3.13 Cooling sub-step method evolution comparison	89
3.14 z_i testing	92
3.15 WCR dust fraction testing comparison	92
3.16 z_i and a_i parameter tweaking	93
3.17 An x-ray radiative transfer example	101
3.18 <i>Radiative transfer images of WR98a (Hendrix et al., 2016)</i>	102
4.1 Static mesh refinement example	111
4.2 WR and OB $\Lambda(T)$ cooling curves	113
4.3 OB and WR electron-ion ratios	114
4.4 Comparison of dust formation rates with cooling methods	122
4.5 Comparison of dust and plasma cooling rates in post-shock environment	122
4.6 Instabilities due to cooling	123
4.7 Density comparison of simulations with differing radiative processes	124
4.8 Temperature comparison of simulations with differing radiative processes	125
4.9 Wind mixing due to radiative methods	125
4.10 Baseline simulation z , full extent	126
4.11 Dust production rate for simulations varying mass loss rate	127
4.12 Comparison of the dust production rate for simulations varying v^∞	128
4.13 Dust density comparison of terminal velocity varying systems	129
4.14 OB terminal velocity wind dust comparison	130
4.15 Wind colour comparison of $\eta = 0.04$ winds	131

LIST OF FIGURES

4.16 Comparison of dust density in simulations with strong secondary wind	131
4.17 Dust formation rate versus binary separation distance	132
4.18 A comparison of the structures of simulations varying d_{sep}	133
5.1 Numerical grid of the WR140 system simulation at $z = 0$	150
5.2 A graph of the dust production rate in the WCR of WR140	151
5.3 A graph of the overall dust mass in the simulation of WR140	151
5.4 Comparison of simulation dust production rate and L' photometry	152
5.5 Comparison of simulation dust mass and L' photometry	153
5.6 Gas density in a simulation of the WR140 system	155
5.7 Dust density in a simulation of the WR140 system	156
5.8 Wind “colour” in a simulation of the WR140 system	156
5.9 Radial velocity as a function of the orbital phase for the stars in WR140	159
6.1 <i>First telescope alignment evaluation image from the JWST</i>	167
B.1 Cumulative CPU time on ARC4	176
B.2 Demonstration of Amhdal’s law	180
B.3 Strong scaling test of <code>Athena++</code>	181

LIST OF FIGURES

LIST OF TABLES

2.1	Comparison of fusion process reaction rates	11
2.2	Stellar wind comparison	14
2.3	Cooling processes at various temperature ranges	36
2.4	Number of confirmed WCd systems	46
2.5	Wind properties of systems considered for simulation	48
2.6	Orbital properties of systems considered for simulation	49
3.1	Benchmarking of the <code>rk3</code> and <code>ssprk5_4</code> integrators	67
3.2	Time taken to simulate 10^4 timesteps of a double mach reflection test	69
3.3	Parameter space of Λ_d 3-parameter lookup table.	83
3.4	Dust cooling calculation comparison	85
3.5	Cooling method accuracy comparison	89
4.1	Abundances by mass used for OB and WR stars	112
4.2	Wind properties of the baseline system.	118
4.3	Baseline system orbital properties.	118
4.4	Cooling series simulation parameters.	119
4.5	Terminal velocity series wind parameters	120
4.6	Parameters of simulations varying the separation distance	120
4.7	Average rate of dust production for the set of different radiative simulations	124
4.8	Average rate of dust production for the mass loss rate simulation set.	127
4.9	Average rates of dust production for the terminal velocity simulation set.	130
4.10	Average rates of dust production for the separation distance simulation set	133
5.1	Confirmed WCd systems	140
5.2	Grain critical energy	146

LIST OF TABLES

5.3	WR140 system parameters	148
5.4	Abundances by mass used for OB and WR stars	149
5.5	Advected scalar yields from WR140 simulation	150

Abbreviations

List of common abbreviations, a section is referenced when applicable. Entries are separated by field.

Physics		
BIDMAS	Binary Interaction Dust Model with Accretion and Sputtering	Section 3.7
3α	Triple- α	Section 2.1.4
AGB	Asymptotic Giant Branch	Section 2.1.4
CAK	Castor, Abbott & Klein (1975)	Section 2.1.3.2
CNO	Carbon Nitrogen Oxygen	Section 2.1.2
CWB	Colliding Wind Binary	Section 2.1
GCR	Galactic Cosmic Ray	Section 2.3.3
GMC	Giant Molecular Cloud	Section 2.1
ISM	InterStellar Medium	Section 2.1
KH	Kelvin-Helmholtz	Section 2.1
LBV	Luminous Blue Variable	Section 2.1
MESA	Modules for Experiments in Stellar Astrophysics	Section 2.1.4
MIST	MESA Isochrones and Stellar Tracks	Section 2.1.4
OB	O or B type star	Section 2.1
p-p	Proton-Proton	Section 2.1.2
PAH	Polycyclic Aromatic Hydrocarbon	Section 2.2
RSG	Red Supergiant	Section 2.1
WC	Wolf-Rayet Carbon phase	Section 2.1.4.1
WCd	Dust forming WC star	Section 2.3.4
WCR	Wind Collision Region	Section 2.3.2
WN	Wolf-Rayet Nitrogen phase	Section 2.1.4.1
WO	Wolf-Rayet Oxygen phase	Section 2.1.4.1
WR	Wolf-Rayet	Section 2.1.4.1
Computer Science		
AVX	Advanced Vector Extensions	
GCC	GNU Compiler Collection	
GNU	GNU's Not Unix! ¹	
GPU	Graphics Processing Unit	
ICC	Intel Compiler Collection	
JIT	Just In Time	Appendix B.3
MP	Multi Processing	Appendix B.2
MPI	Message Passing Interface	Appendix B.2
SIMD	Single Instruction, Multiple Data	

¹Frustrating, I know.

SMT	Simultaneous Multi-Threading	
Mathematics		
CFL	Courant-Friedrichs-Lowy	Section 3.1
HLLC	Harten-Lax-van Leer-Contact	Section 3.1
RK	Runge-Kutta	3.1
TEF	Temporal Evolution Function	Section 3.6.4.1

Common Symbols

List of common symbols, if symbol requires a derivation, the appropriate equation within this thesis will be referenced. If the symbol is a constant, the value in CGS units will be provided.

Variables		
a	Grain radius	Section 2.2
C	Courant-Friedrichs-Lowy condition	Eq. 3.4
f	Wind shock fraction	Eq. 2.23
h_e	Electron transparency	Section 2.3.3
H	Grain heating rate	Eq. 3.14
H_{coll}	Grain heating rate due to atoms and ions	Eq. 3.14
H_{el}	Grain heating rate due to electrons	Eq. 3.14
i	Inclination	Section 2.3.5
\mathcal{L}	Cooling rate per unit volume	Eq. 2.25
L_\star	Stellar luminosity	Section 2.1.4
M_\star	Stellar mass	Section 2.1.4
\dot{M}	Mass loss rate	Section 2.1.3
t_{cool}	Cooling timescale	Eq. 2.27
t_{esc}	Escape timescale	Eq. 2.28
v_∞	Wind terminal velocity	Section 2.1.3
z	Dust-to-gas mass ratio	Section 3.7.2
β	Electron ion ratio	Eq. 4.12
η	Wind momentum ratio	Eq. 2.19
$\Lambda(T)$	Plasma Cooling function	Section 4.2.1
ξ	Grain sticking efficiency	Eq. 4.17
θ_c	WCR conic opening angle	Eq. 2.21
τ_{KH}	Kelvin-Helmholtz timescale	Eq. 2.1
τ_{ff}	Free-fall timescale	Eq. 2.2
μ	Mean molecular mass	Eq. 2.24
κ	Sub-timestep fraction	Section 3.6.6
Φ	Orbital phase	Section 3.6.2
χ	Cooling parameter	Eq. 2.29
γ	Ratio of specific heats	Eq. 3.7

Subscripts & Superscripts		
x_{WR}	Wolf-Rayet, synonymous with primary star	
x_{OB}	OB type, synonymous with secondary star	
x_w	Either wind	
x_g	Gas, typically refers to stellar wind	

x_d	Aggregate dust fluid	
x_{gr}	Single dust grain	
x_H	Hydrogen	
x_e	Electron	
x_u	Upper, typically the closest bin $>$ value in a lookup table	
x_l	Lower, typically the closest bin $<$ value in a lookup table	
x^∞	Terminal, such as terminal velocity, v^∞	
Constants		
u	Atomic Mass Unit	$1.661 \times 10^{-24} \text{ g}$
m_H	Hydrogen mass	1.00784 u
m_e	Electron mass	0.00055 u
k_B	Boltzmann Constant	$1.381 \times 10^{-16} \text{ erg K}^{-1}$
σ	Stefan-Boltzmann constant	$5.670 \times 10^{-5} \text{ erg cm}^{-2} \text{ s}^{-1} \text{ K}^{-4}$
c	Speed of light in a vacuum	$2.998 \times 10^{10} \text{ cm s}^{-1}$
M_\odot	Solar mass	$1.988 \times 10^{33} \text{ g}$
$M_\odot \text{ yr}^{-1}$	Solar mass per year	$6.301 \times 10^{25} \text{ g s}^{-1}$
L_\odot	Solar luminosity	$3.828 \times 10^{33} \text{ erg s}^{-1}$
R_\odot	Solar radius	$6.957 \times 10^{10} \text{ cm}$
AU	Astronomical Unit	$1.496 \times 10^{13} \text{ cm}$
pc	Parsec	$3.086 \times 10^{18} \text{ cm}$
“Warm”	Warm temperature regime	$10^4 - 10^5 \text{ K}$ ¹

¹Varies from researcher to researcher.

CHAPTER 1

Introduction & Motivation

1. INTRODUCTION & MOTIVATION

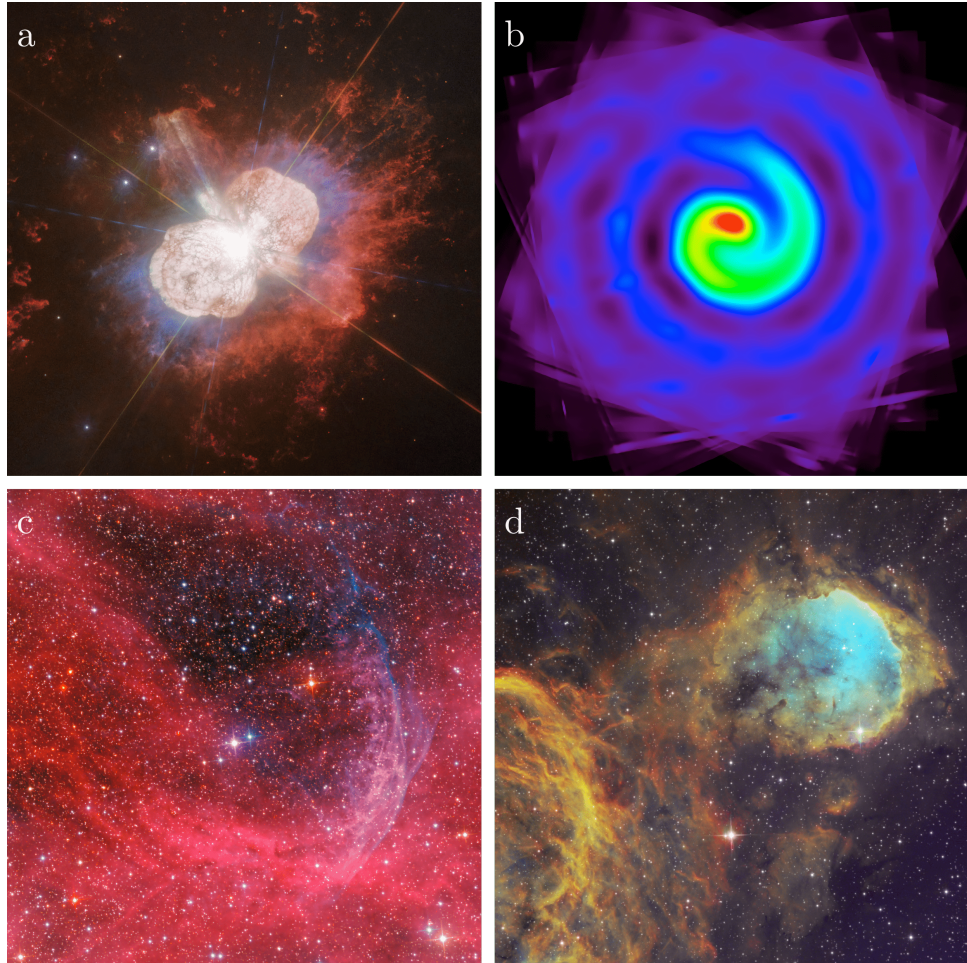


Figure 1.1: NASA Astronomy Picture of the Day (APOD) images of Wolf-Rayet and CWB systems. (a) The LBV+O system η Carinae (<https://apod.nasa.gov/apod/ap190220.html>). (b) The persistent dust forming colliding wind binary (WCd) system WR 104 (<https://apod.nasa.gov/apod/ap140603.html>). (c) The WR134 ring nebula (<https://apod.nasa.gov/apod/ap120621.html>). (d) The Wolf-Rayet nebula surrounding WR23 (<https://apod.nasa.gov/apod/ap210208.html>). Wolf-Rayet and CWB systems are, without a doubt, some of the most striking systems in the galaxy.

Colliding Wind Binary (CWB) systems are perhaps one of the most striking types of stellar system. Beauty, as they say, is in the eye of the beholder – and nearly every astrophysicist believes that parts of their specialist subjects hold tremendous aesthetic qualities. Figure 1.1, however, really does show off the intrinsic beauty of both Wolf-Rayet (WR) stars and CWB systems.

These systems can produce a variety of beautiful outbursts, from Wolf-Rayet nebulae to delicate interstellar dust clouds forming around them in the infrared. The latter form either fine

filaments, or pinwheels extending out for parsecs, with an enormous amount of structural variety. On top of the visible and infrared, these systems are also visible from the radio to gamma rays, emitting copious amounts of radiation though both thermal and non-thermal mechanisms.

Massive stars have an incredibly outsized influence on their local interstellar medium (ISM). Even in a single system, these stars produce winds capable of perturbing their local medium, forming pockets of high density material that can drive star formation, as well as ionising this medium, producing HII regions. WR stars turn the metaphorical dial of this influence up to eleven, driving enormous quantities of hot, ionised wind into the ISM. Massive stars literally tear themselves apart over a period of around 500,000 years, flinging many solar masses worth of material into space at an appreciable fraction of the speed of light. These stars too, are destined to die in violent, chaotic, and beautiful¹ ways, such as supernovae and gamma-ray bursts (GRBs).

If these stars form a close binary with colliding winds we observe incredibly powerful shocks, as the mechanical energy equivalent to the luminance of a thousand suns acts on a region only a few solar radii in size. This heats this wind collision region (WCR) to temperatures in excess of 10^8 K as these winds crash headlong into each other. These systems are among the brightest continuous x-ray sources in the night sky (Fig. 1.2), and provoked much scientific debate before the discovery of their true nature.

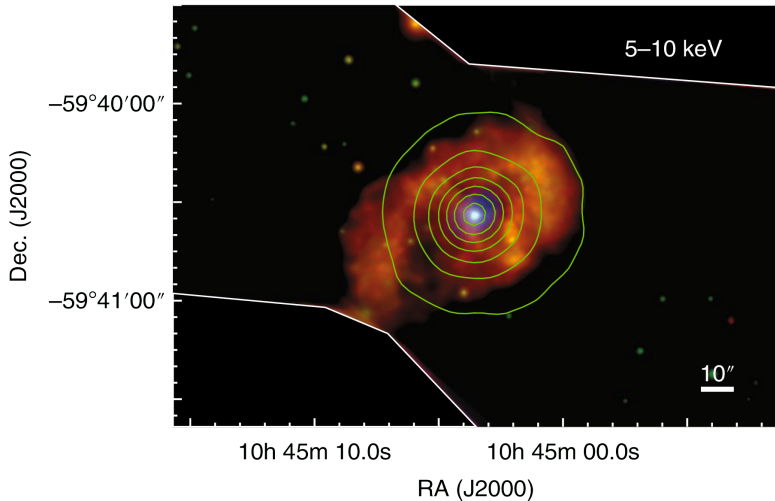


Figure 1.2: Chandra x-ray imagery of η Carinae at the soft x-ray minimum of 2009, with contours from the NuSTAR 5 – 10 keV x-ray band. CWB systems are incredibly bright in x-ray bands due to the powerful shock heating driving thermal x-ray processes. Image sourced from Hamaguchi et al. (2018).

¹Provided you are not in the blast radius.

1. INTRODUCTION & MOTIVATION

However, a most puzzling question is how dust forms in certain CWB systems (which we refer to as WCd systems throughout this thesis). These systems have violent shocks, incredibly high temperatures, and produce copious amounts of ionising radiation. So how can it be that something as tenuous as interstellar dust can form? The mechanisms behind formation and growth are extremely poorly understood, and as such we intend to glean some information on the mechanisms and yields of dust production processes in these systems.

1.1 Motivation & Goals

Dust formation in early-type star systems is a relatively poorly understood phenomenon. As the grains should be readily destroyed by shocks and ionising radiation, nascent grain cores must require some form of shielding or rapid dust growth mechanisms in order to form larger grains. We find that these binary systems can produce volumes of dust equivalent to asymptotic giant branch stars, the most prolific late-type dust forming systems. Dust formation is also vital for the formation of planets and complex organic molecules throughout the galaxy, so understanding the mechanisms behind its formation is of significant scientific interest. CWB systems are – for a variety of reasons – very difficult to both observe *and* simulate. WR CWB systems are quite distant, with the nearest systems being typically more than 2 kpc from Earth, making the wind collision region (WCR) very difficult to observe. The WCR is also shrouded by dense stellar winds, occluding the shock region. These systems are also comparatively rare, making it more difficult to typify these systems. If we simulate these systems, we find other difficulties such as a requirement of 3D simulation in order to model orbital effects. CWB systems also have a large variation in length scales that render the simulations very computationally challenging.

The main goal of the project was to develop a dust model that was computationally inexpensive to implement, such that it could be included in large-scale numerical models. This dust formation model¹ was designed to be as modular as possible, and to be relatively straightforward to implement additional dust evolution mechanisms. By the end of the project, dust evolution and destruction mechanisms were implemented, as was dust cooling through gas-grain collisional excitation.

The second goal of the project was to simulate a variety of WCd systems using this dust model running within a hydrodynamical simulation. WCd systems can be sub-categorised by the time dependence of their dust formation:

¹Christened **BIDMAS**, or binary interaction dust model with accretion and sputtering.

- “Episodic” systems that produce dust over a small section of their orbit.
- “Variable” systems whose dust production varies significantly over their orbital period.
- “Persistent” systems whose dust did not vary significantly over the orbital period.

The first type of WCd system modelled was the variable dust forming system WR98a. We found that this system was the easiest to simulate, due to its comparatively sedate winds and larger orbital spacing. In addition to simulating a system with parameters similar to WR98a, a parameter space search was conducted using WR98a as a baseline: wind properties predicted to be influencing the dust production rate were varied, in order to understand their effects. The episodic dust forming system WR140 was also simulated, whose dust formation is theorised to be due to its high orbital eccentricity. This was a more complex affair, as the system was far more complex to simulate than WR98a. This section of the project had to be partially truncated due to time constraints, and a partial orbit of the system near periastron was opted for in lieu of a full orbit of the system.

Whilst the main goals of the project were completed, there is still much that is not understood about dust formation in these systems. Development of a more complex model, as well as synthetic astronomical imaging through radiative transfer models were topics considered for later stages of this project but could not be accomplished due to time. However, these projects present interesting avenues of future research. Other wind features, such as radiative line driving, would also be included in future models, in order to understand their role in dust formation, and how they influence grain growth and dust yields. Furthermore, simulation of other systems, such as the WR+WR systems WR70-16 “Apep” and WR48a would be interesting follow-up simulation targets.

1.2 Thesis Structure

The structure of this thesis could be described as somewhat unconventional, this is because of two primary reasons:

- Difficulties in the early and middle sections of the project.
- The field itself requiring a significant degree of explanation.

Throughout the 2nd and 3rd years of this PhD, there were many issues with getting this project to even progress at all. This was mostly due to being unable to get the original hydrodynamical

1. INTRODUCTION & MOTIVATION

code used in this experiment to work with our dust model (Section 3.3). This code was ultimately abandoned by the 3rd year and replaced with a more modern and easier to develop code, **Athena++** (Section 3.4). Additionally the outbreak of a global pandemic resulted in a stalling of some aspects of the work in the thesis. This meant that there was a lot of time to develop the codebase and theorise on the nature of these systems, but much of the actual data collection was performed in the last few months of the project. As such, there is a great deal of discussion of the background and methodology, and an enormous amount of discussion on the future of this particular field. While the primary objectives of this PhD were achieved, many aspects of this thesis that were planned out at the start of the project were unfortunately truncated or removed. This was extremely disappointing, of course, but I hope to continue work on this field outside of this PhD, and develop a more advanced dust model for numerical simulation.

Astrophysical fluid dynamics straddles two particularly complex fields: physics and computer science. Because of this, the first two chapters of this thesis are both background chapters¹. In Chapter 2 we discuss the physics of massive stars and dust, before synthesising these two sections in order to discuss dust producing CWB systems. In Chapter 3 we discuss the underlying principles of numerical simulation, and discuss our model, from the choice of numerical code to the underlying mechanisms and methodology. Afterwards, we will move on to Chapters 4 & 5. These chapters have been adapted from two papers written concurrently with this thesis:

1. *An Exploration of Dust Growth Within WCd Systems Using An Advedted Scalar Dust Model* (Eatson et al., 2022a).
2. *Exploring Dust Growth in the Episodic WCd System WR140* (Eatson et al., 2022b).

These chapters serve to provide more concise explanations of our work, while also providing the results of this research, particularly dust formation rates of both persistent and episodic WCd systems. Finally, we will conclude with some remarks on future work that could be performed in this field, as well as with some observations made over the course of this project.

¹A friend of mine wrote their thesis on computational biophysics that had not one, not two, but *three* background chapters, so it could be worse.

CHAPTER 2

Background

2. BACKGROUND

Colliding wind binary (CWB) systems sit at the intersection of many fascinating fields. Unfortunately this means that a broad swathe of stellar astrophysics must be discussed in order to investigate them in any detail. In this chapter we will discuss the many underlying subjects of CWB systems. First, we shall start with massive, early-type stars – how they form, what drives their titanic energy outputs, as well as their inevitable and violent deaths. Afterwards, we will discuss interstellar dust, the fragile, microscopic grains that act as chemical refineries across the cosmos. In particular, we will discuss their formation, growth and destruction mechanisms, in order to understand how such an object can arise in such a violent system as a CWB. We will then move on to discussing colliding wind binary systems, wind parameters and cooling mechanisms. Finally, we will synthesise what we have discussed by detailing the crux of this project: the dust producing colliding wind binary (WCd) system. This chapter largely covers the underlying physics of these systems, while the next chapter (Ch. 3) concerns the simulation of these physical phenomena and effects.

2.1 Early-Type Stars

The term Early-type stars is quite possibly the epitome of bad naming conventions in astrophysics. It's a very old term, coming from the dawn of astrophysics itself, it is quite opaque as to what it means, and is also by definition *completely wrong*. In fact it is one of the most wrong pieces of terminology I can think of¹. The first generation of astrophysicists² found themselves asking very big, very fundamental questions such as “what even *are* stars?” and “what possible mechanism can allow a star to shine for so long?” Each of these questions was rather pressing for the burgeoning field, and the scientific community was aching for an answer.

Of course, like all pressing questions of the late 19th century, it fell to Lord Kelvin to provide a convincing – albeit incorrect – answer. Kelvin assumed that gravitational collapse was the mechanism for a stars long-term heating, with younger, “early” stars shining the brightest. Not only was the mechanism incorrect, but typically older main sequence stars are more luminous than their younger counterparts of a similar mass! However, as is the case with astrophysical terminology, the term stuck, to the confusion of many young astrophysicists. Instead, we now know that stars produce their energy through fusion. These reactions vary from sub-stellar

¹Aside from astrophysicists calling something “warm”, of course. That can quite literally mean anything from 10 to 1,000,000 Kelvin, depending on who you ask, what they’re writing about, or how they’re feeling at that particular moment. In fact, I’ll probably end up falling into this same trap somewhere in this thesis as well!

²As opposed to astronomers or natural philosophers.

deuterium and lithium burning, to main sequence p-p & CNO hydrogen burning processes, and finally to the triple- α and other exotic fusion processes for evolved high-mass stars.

The more massive the star, the greater the internal temperature and pressure, allowing for more exotic fusion processes. As all fusion reactions are highly dependent on temperature, stars with only a few dozen solar masses are thousands of times more luminous than our sun – but only last a fraction of the time (Carroll & Ostlie, 2014). These stars have luminosities in the range of $10^4 L_\odot$ and lifespans on the order of 10 Myr, less than 0.1% of the lifespan of our sun. The adage of a candle burning twice as bright and lasting half as long doesn't quite express the differences between high-mass stars and low-mass stars, it would instead be better to compare a candle and a stick of dynamite.

We define high-mass stars as stars that are sufficiently massive to undergo carbon fusion near the end of their lives. Defining high-mass as stars that are predominantly driven by the CNO cycle or late-life helium burning can include intermediate mass stars, which form degenerate cores and evolve into white dwarfs. Many works – including this one – define a high-mass, early-type star as having a mass of $> 8 M_\odot$. This includes stars in the O-type and some B-subtype (B0 and B1) classes in the Harvard classification system (Ward-Thompson & Whitworth, 2011, p. 143).

2.1.1 Formation

All stars form from the collapse of giant molecular clouds (GMCs), enormous, cold clouds containing truly staggering amounts of gas. The largest of these clouds are on the order of a few parsecs across, and contain $10^6 M_\odot$ of potential star-stuff. These clouds are somewhat stable, and must be perturbed in order to collapse. This is easier said than done, but can be induced by stellar winds from nearby stars and shock-waves from supernovae (Bodenheimer, 2011, Ch. 3). As the cloud collapses, energy is radiated through emission line processes, which lowers the radius of thermostatic equilibrium. As the GMC collapses further it begins to fragment, forming the molecular clumps and cloud cores that will eventually condense into protostars. As one of these fragments condenses, it forms a proto-stellar core. This collapse can be described in the form of a series of timescales. Firstly, the Kelvin-Helmholtz (KH) timescale¹, τ_{KH} , which is the time required for the proto-stellar core to radiate away its kinetic energy:

¹The idea of gravitational contraction as expounded by Lord Kelvin does in fact apply to stars, just not with regards to how their energy is produced.

2. BACKGROUND

$$\tau_{\text{KH}} \approx \frac{GM_\star^2}{R_\star L_\star}, \quad (2.1)$$

where G is the gravitational constant, M_\star is the proto-stellar core mass, R_\star is the radius of the core and L_\star is the core luminosity. The other timescale is the free-fall timescale, τ_{ff} , which is the time taken for a molecular cloud fragment to fully collapse onto the core, given by the equation

$$\tau_{\text{ff}} \approx \sqrt{\frac{3\pi}{32G\rho_\star}}, \quad (2.2)$$

where ρ_\star is the mean density of the collapsing cloud. The equation of motion for this system is

$$\frac{d^2r}{dt^2} = -\frac{GM_\star}{r^2}, \quad (2.3)$$

for any point with radius r from the centre in the cloud, assuming spherical symmetry (Ward-Thompson & Whitworth, 2011, p. 96).

In the case of a massive star, the KH timescale is significantly shorter than the free-fall timescale ($\tau_{\text{KH}} \ll \tau_{\text{ff}}$), meaning that the material at the center of the collapsing cloud begins to fuse *prior* to the cessation of collapse. This burgeoning star begins to drive the collapsing material away through radiation pressure, blowing this material outwards, causing it to accrete and shock material within the GMC (Bodenheimer, 2011, Ch. 5).

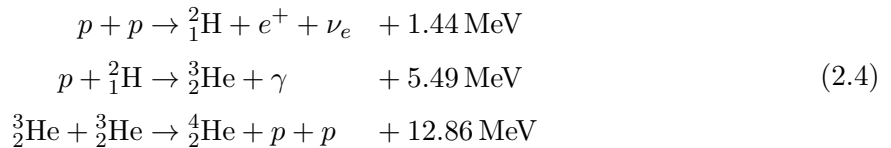
As more massive cores collapse, they are more prone to fragmentation, the angular velocity of the fragments can cause them to begin orbiting one another, eventually forming a binary or multiple star system. Close binary systems can also form by way of fragmentation in the proto-stellar disk. Due to this fragmentation it has been observed that roughly 2/3rds of all main sequence stars are found to be in a multiple system (Ward-Thompson & Whitworth, 2011, p. 113), with approximately 20% of stars in close binary orbits. However, in the case of massive stars, this value is significantly higher, with > 82% of stars with masses > 16 M_⊙ being found to be in a close binary system (Chini et al., 2012). As such, the environment within an OB association is one of many tight knit groups of young stars, which completely disrupt the local area¹.

Process	Reaction rate	Energy released per nucleon	Significant in
p-p	$\epsilon \propto T^{3.5}$ at 5×10^6 K	6.54 MeV	Low-mass stars
CNO	$\epsilon \propto T^{18}$ at 10^6 K	6.18 MeV	High-mass stars
3α	$\epsilon \propto T^{40}$ at 10^8 K	0.61 MeV	Post-main-sequence high-mass stars

Table 2.1: A comparison of reaction rates and released energy for the p-p chain reaction, CNO reaction and triple-alpha reaction. Whilst the 3α reaction has a much higher temperature dependence for the reaction, it requires much higher pressures, and produces considerably less energy per nucleon. These factors contribute to the high luminosities and short lifespans of high-mass stars.

2.1.2 The p-p & CNO fusion cycles

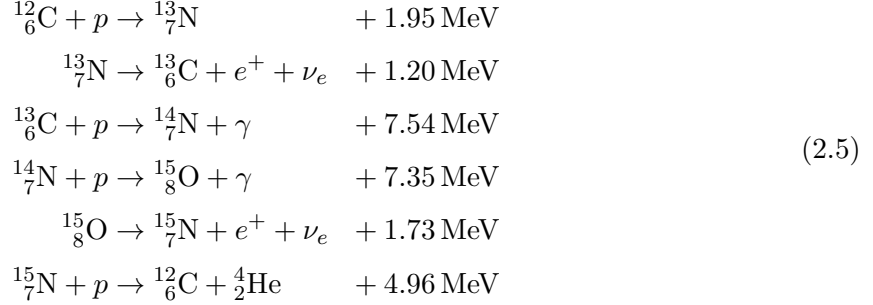
As we have previously discussed, the KH mechanism is not the driving force behind the generation of energy in a star, instead, this energy is derived through nuclear fusion processes. We shall briefly discuss the various nuclear fusion processes in order to understand why massive stars are so luminous, as well as how their lives end. Nuclear fusion in stars was first proposed by Eddington (1920), though the exact processes continued to be a mystery for nearly 2 decades – until Bethe (1939) discovered the p-p fusion reaction chain that drives approximately 90% of the energy generation of the sun. The p-p fusion chain dominates energy generation for stars between $0.08 M_\odot \lesssim M_* \lesssim 1.3 M_\odot$, and releases energy by fusing protons into helium in the following manner:



Whilst the reaction is direct and efficient, due to its high energy production per nucleon (Table 2.1); the reaction rate has a poor temperature dependence of $\epsilon \propto T^{3.5}$ due to the small reaction cross-section. In more massive stars with core temperatures on the order of 10^8 K, the extreme luminosities we observe would simply not occur. The mechanisms underpinning fusion in intermediate and high-mass stars are much more energetic and temperature dependent. Above a certain core temperature, the catalytic CNO cycle produces significantly more energy:

¹This is similar to the environments around student areas, such as Hyde Park and Headingley.

2. BACKGROUND



The CNO I cycle – which was also discovered by Bethe – has a markedly higher temperature dependence on the reaction rate, $\epsilon \propto 10^{18}$ (Bethe, 1939; Wong, 1998, Ch. 10; see Fig. 2.1). The CNO cycle is dominant at internal temperatures $> 15.9 \text{ MK}$, corresponding to a stellar mass of $\gtrsim 1.3 M_\odot$ (Salaris & Cassisi, 2005, p. 121). The incredible temperatures at the cores of high-mass stars therefore result in a reaction rate orders of magnitude higher than the sun. This results in a convective core surrounded by a radiative envelope, and is the driving force behind the incredible observed luminosities of high-mass stars as they convert hydrogen to helium at a truly astounding rate (Salaris & Cassisi, 2005, Ch. 5).

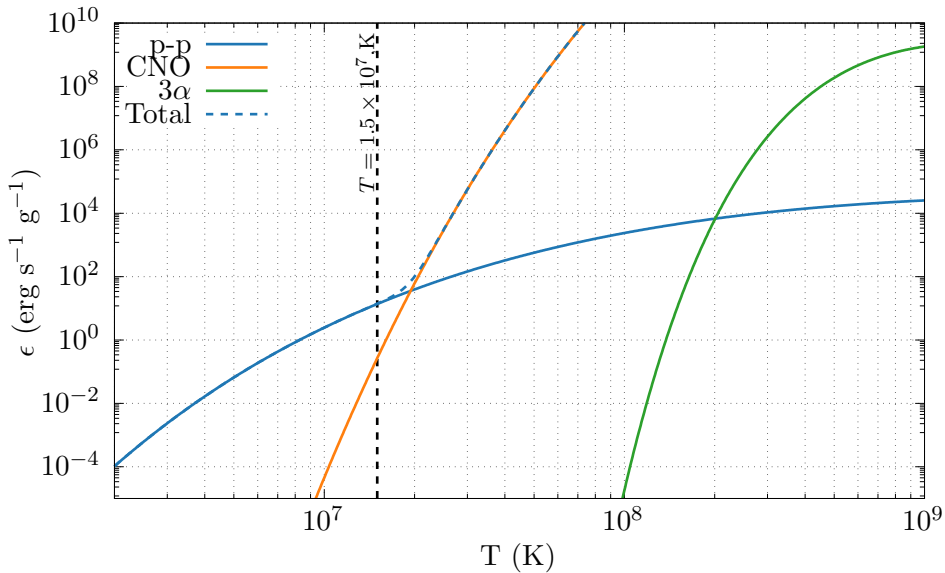


Figure 2.1: Reaction rates from p-p, CNO and triple- α fusion processes at the centre of the sun (Harris et al., 1983). At the solar core temperature of $1.5 \times 10^7 \text{ K}$ only 10% of the energy produced from fusion is through the CNO cycle. At higher internal temperatures the CNO cycle rapidly becomes dominant due to its stronger temperature dependence. The 3α process does not occur in the solar core, but becomes the dominant fusion process in high-mass stars leaving the main sequence. Solar abundances and a core density of 150 g cm^{-3} are assumed.

2.1.3 Stellar winds

The luminosities and temperatures of high-mass stars also drive extremely fast stellar winds through radiative line driving. These winds have on the order of 10^{10} times more momentum than winds from stellar-mass stars, and punch holes into the interstellar medium (ISM), forming wind-driven bubbles and champagne flows. These winds can also perturb GMCs, disrupting them and forming more stars nearby.

The study of stellar winds, of course, is quite hard from our vantage point on earth. Sampling the winds themselves is difficult due to the vast distances involved in sending a probe to collect the rarefied material from our stellar neighbourhood. We instead derive the properties of these extrasolar winds from spectrography, with the absorption and emission spectra of the winds betraying their composition. The velocity of these winds can be determined in much the same manner, through the Doppler shift of these emission lines. Early observations of stellar winds centred around the star P Cygni, the earliest known example of an evolved Luminous Blue Variable (LBV) star. The presence of peaks and troughs in the spectra of the star was the cause of some scientific curiosity. This effect could only be explained by the presence of a shell rapidly expanding away from the star. The troughs of this spectra corresponded to a blue-shifted adsorption lobe, from radiation passing through this shell, while the emission line itself corresponded to the expanding shell itself (Beals, 1929; Lamers & Cassinelli, 1999). Observations of other stars typified this event, it was found that every star had a stellar wind, though the speed and quantity of the ejected material could vary by many orders of magnitude.

In the simplest terms, we can describe a stellar wind as a spherical outflow from a star. We can describe this outflow in terms of its mass loss rate, \dot{M} as well as its terminal velocity, v^∞ , the maximum velocity a wind can obtain from its driving mechanism. We can use these to determine a profile of the density of a stellar wind as a function of its distance, r , from the star

$$\rho_w = \frac{\dot{M}}{4\pi v^\infty r^2}, \quad (2.6)$$

assuming the star is distant enough to behave as a point source. Whilst this barest description can give us some insight into how a wind behaves, we should discuss the driving mechanisms behind these winds, as well as the more complex models we use to describe them.

2. BACKGROUND

Classification	\dot{M} $M_\odot \text{ yr}^{-1}$	v_∞ km s^{-1}	Mechanism
Sun	10^{-14}	400	Thermal heating
PMS	$10^{-4} - 10^{-7}$	$200 - 500$	Rotation & magnetic fields
Red Giant	$10^{-7} - 10^{-9}$	30	Radiation pressure on dust grains
OB Star	$10^{-7} - 10^{-8}$	2,500	Radiation pressure & line driving
Wolf-Rayet	10^{-5}	1,500	Radiation pressure & line driving

Table 2.2: Comparison of stellar winds emitted from various classification of star.

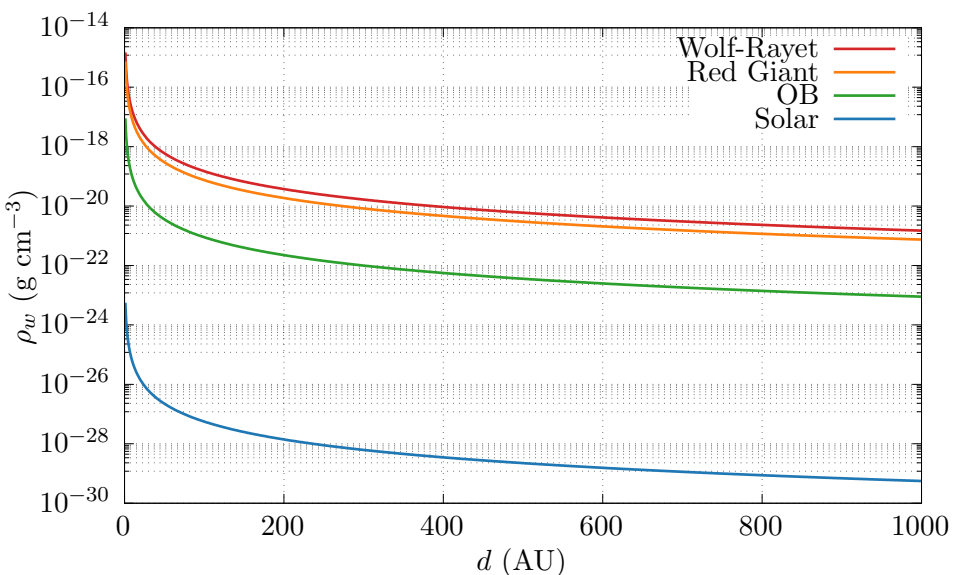


Figure 2.2: Comparison of the densities of various main sequence winds using the parameters specified in Table 2.2, wind densities are estimated using the smooth wind approximation described in Eq. 2.6.

2.1.3.1 Driving mechanisms

Low-mass main sequence stars, compared to other classes of star, have winds that are relatively thin, with a mass loss rate of $10^{-14} M_\odot \text{ yr}^{-1}$. Along with their middling velocity of 400 km s^{-1} this results in a wind density many orders of magnitude lower than other types of star (Fig. 2.2). The reason for this feeble outflow is the driving mechanism. The corona in stars with a convective envelope is approximately 3 orders of magnitude hotter than the stars photosphere, this hot corona exerts pressure on gas trapped within it, causing it to be expelled from the star. This mechanism is thermally driven and does not expel gas from the envelope, only gas dredged up to the corona, explaining this comparative weakness. In fact, winds from red dwarfs are found to be markedly denser, but the mechanisms behind their winds are less understood. As low-mass stars evolve and leave the main sequence, they swell into red giants, causing the surface

gravity of the star to decrease significantly. As the star expands and cools, dust condenses and forms in the photosphere. These dust grains adsorb photons more readily than ions and atoms do through Thompson scattering, and can adsorb a broad range of wavelengths due to their size. The dust grains are subsequently driven away by radiation pressure, the gas in the wind is coupled to the dust, driving it away in the form of a dense, optically thick, barely supersonic wind (Lamers & Cassinelli, 1999, Ch. 5). The mass loss rates of these stars are extremely high, no lower than $10^{-7} M_{\odot} \text{ yr}^{-1}$ and as high as $10^{-5} M_{\odot} \text{ yr}^{-1}$ with velocities on the order of $10 - 100 \text{ km s}^{-1}$, making the wind extremely dense.

By the 1970s the winds of early-type stars had been typified, finding mass loss rates between 10^{-8} to $10^{-5} M_{\odot} \text{ yr}^{-1}$ and wind velocities of 600 to $3,500 \text{ km s}^{-1}$. It was also found that the mass loss rate of these stars was almost proportional to the luminosity ($\dot{M}_{\star} \propto L_{\star}^{1.1}$; Cassinelli, 1979). This strongly suggested that the driving mechanism of these winds was based on radiation pressure, though thompson scattering would not be a sufficiently efficient process to drive winds of this magnitude. Furthermore, coronal heating and dust driving mechanisms were not possible, due to a lack of a convective envelope and lack of dust build up respectively.

2.1.3.2 Line-driven wind theory

Line-driven winds present an alternative driving mechanism for massive stars. A photon with an energy equal to the excitation energy of an emission line of an ion in the wind is adsorbed, exciting the ion. This ion then de-excites over a timescale of 10^{-8} s , emitting a photon at a random angle relative to the radial direction relative to the star, α . This emission of a photon produces a recoil force on the ion, resulting in a change in the radial velocity, Δv_r , such that:

$$\Delta v_r = v_r'' + v_r' - v_r = \frac{h\nu_0}{mc} (1 - \cos \alpha), \quad (2.7)$$

where v_r' is the ions radial velocity after the photon adsorption, v_r'' is the ions radial velocity after photon emission and ν_0 is the frequency of the resonating photon. Compared to conventional Thompson scattering, resonance lines are six orders of magnitude more opaque, making it a much more efficient process (Lamers & Cassinelli, 1999, Ch. 8). This driving force occurs in winds enriched with elements with a large number of resonant lines, where heavier ion species from C, N, O and Fe group elements adsorb the photons. Lighter elements such as H and He are carried along via Coulomb forces, coupled to the heavier elements so long as the medium is sufficiently dense.

2. BACKGROUND

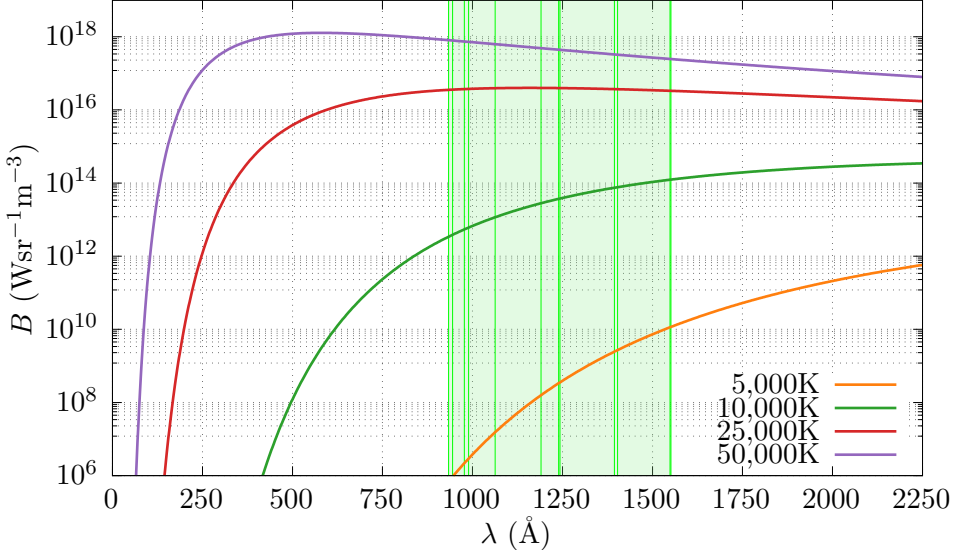


Figure 2.3: Spectral radiance against wavelength for black body objects at various effective temperatures, T_{eff} , a series of wavelengths corresponding with important resonance lines in Table 1 of Lucy and Solomon (1970) have been included. As temperature increases the spectral radiance at resonance line wavelengths dramatically increases, with a minimum of 6 orders of magnitude difference between the effective temperatures of a solar equivalent main sequence star and an O-type main sequence or Wolf-Rayet star.

But why is this effect not observed in lower mass stars? Resonance lines in heavier elements have comparatively high energy transitions, requiring ionising UV photons to excite them. For instance, the C III resonance line has an energy of 12.69 eV, so a photon requires a wavelength of 977 Å in order to be adsorbed (Fig. 2.3). Additionally, photons would only be adsorbed over a narrow range of frequencies. This inhibits efficient momentum transfer from UV photons without Doppler shift. As the outflow from the star has a distribution of radial velocities this results in a greater chance of resonance line adsorption if Doppler shift is considered. If we were to observe the outflow of a massive wind we observe a relatively low velocity component of the wind close to the star once the wind reaches a certain critical velocity. At a certain point we would observe a significant and rapid increase in the velocity of the wind, as the influence on adsorption due to Doppler shift results in the wind becoming much more opaque to UV photons. Eventually we would observe the wind reaching a terminal velocity, due to a decrease in photon flux from the inverse square law and the outflow becoming more diffuse as it spreads away from the star (Maciel, 2014, Ch. 10). This can be seen in Fig. 2.4, where the velocity increases sharply at a distance $(R/R_{\star}) - 1 > 10^{-3}$ as the wind begins to rapidly accelerate away from the star as opacity increases – with a corresponding decrease in wind density.

2.1 Early-Type Stars

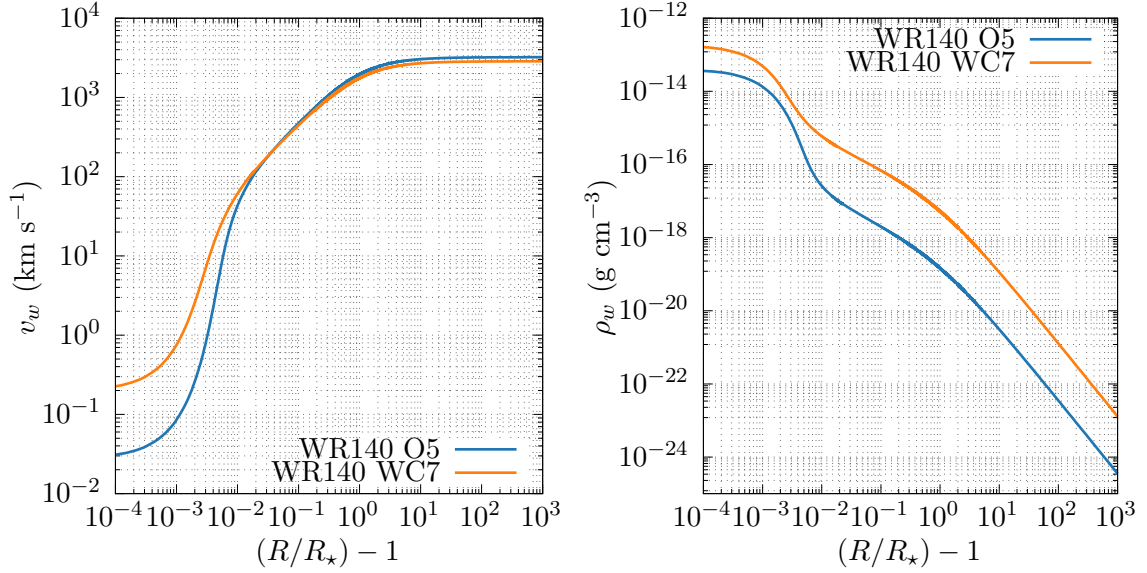


Figure 2.4: Velocity and density profiles of the WR and OB stars in the WR140 system. Acceleration is gradual until $(R/R_\star) - 1 > 10^{-3}$, where wind opacity drastically increases due to Doppler shift. The model uses the Castor, Abbott and Klein formalism, with the CAK parameters of the stars estimated to be $R_\star = 12 R_\odot$, $M_\star = 36 M_\odot$, $k = 0.37$, $\alpha = 0.60$ for the O4-5 star and $R_\star = 4 R_\odot$, $M_\star = 15 M_\odot$, $k = 0.48$, $\alpha = 0.57$ for the WC7 star.

Theories of radiation pressure being the main driving force for massive stars was first considered by astronomers in the early 20th century, and was first proposed by Saha (1919). Later, Milne (1926) predicted that after an initial acceleration phase from ion emission lines, Doppler shift would be sufficient for continuum photons frequencies to match the resonant lines – causing a much greater impulsive force. Early calculations of the force on stellar winds due to resonance lines by Lucy and Solomon (1970) found initial estimates for the mass loss rate based on a series of resonance lines in the C, N, Si and S species of ions. However these were found to underestimate the mass loss by approximately two orders of magnitude. This is in part due to the models simplicity, limitations in computing power and available data. The first major breakthrough was with more complex models demonstrated by Castor, Abbott and Klein (1975; abbreviated to CAK). The CAK model computed line forces from all emission lines in the C III ion, after estimating the line force from other ions by scaling the results of this calculation an estimate of mass loss rates for hot stars was calculated to within a factor of 3 of observational results. A much more complex emission line model developed by Abbott (1982) involved the calculation of the force from a startling 250,000 lines, however, this was found to be less accurate than the original CAK model! As researchers went back to the drawing board, improvements were made to the approximations and assumptions made by the CAK model, such as the finite

2. BACKGROUND

disk correction factor (Friend & Abbott, 1986; Pauldrach et al., 1986).

2.1.4 Evolved early-type stars

Unfortunately for the most massive stars, pesky limitations such as the conservation of energy severely curtail their lifespans. Despite being anywhere from 3 to 6 orders of magnitude brighter, the most massive stars typically only have between 1 and 2 orders of magnitude more mass to fuse. We can assume the main sequence lifespan of a star is determined by the amount of available hydrogen in the star as well as the fusion rate of the star. We can therefore estimate this lifespan, τ_* , through the equation

$$\tau_* \approx \frac{M_*}{L_*}, \quad (2.8)$$

where M_* is the mass of the star and L_* is the luminosity of the star. Through observation a mass-luminosity relation was derived (Salaris & Cassisi, 2005, p. 139), such that:

$$\frac{L_*}{L_\odot} \propto \begin{cases} M_*/M_\odot^{2.6}, & \text{if } 0.2 M_\odot \lesssim M_* \lesssim 0.5 M_\odot \\ M_*/M_\odot^{4.5}, & \text{if } 0.5 M_\odot \lesssim M_* \lesssim 2 M_\odot \\ M_*/M_\odot^{3.6}, & \text{if } 2 M_\odot \lesssim M_* \lesssim 20 M_\odot. \end{cases} \quad (2.9)$$

We can then make the following estimate for the main sequence lifespan of an early-type star:

$$\tau_* \approx \tau_\odot \left(\frac{M_*}{M_\odot} \right)^{-2.5}. \quad (2.10)$$

Whilst this is a fairly simplistic reduction of the stellar mass loss rate, more advanced models such as the Modules for Experiments in Stellar Astrophysics (MESA) project show that this estimate is somewhat accurate. As we can see in Fig. 2.5, this estimate is somewhat accurate over near-solar mass and some lower mass early-type stars. Assuming a solar lifespan of $\tau_\odot = 10$ Gyr we find through Eq. 2.10 that a typical O-type star with a mass of $10 M_\odot$ has a main-sequence lifetime of ~ 30 Myr. It takes the sun approximately 230 Myr to orbit the galaxy, making the sun’s “age” approximately 19 galactic “years” old. Continuing with this analogy, we find that even the least luminous early-type star does not make it to its first birthday!

Eventually, the hydrogen in a massive star’s core is completely exhausted, leaving an inert helium core with a hydrogen envelope surrounding it. Near the edge of the depleted core,

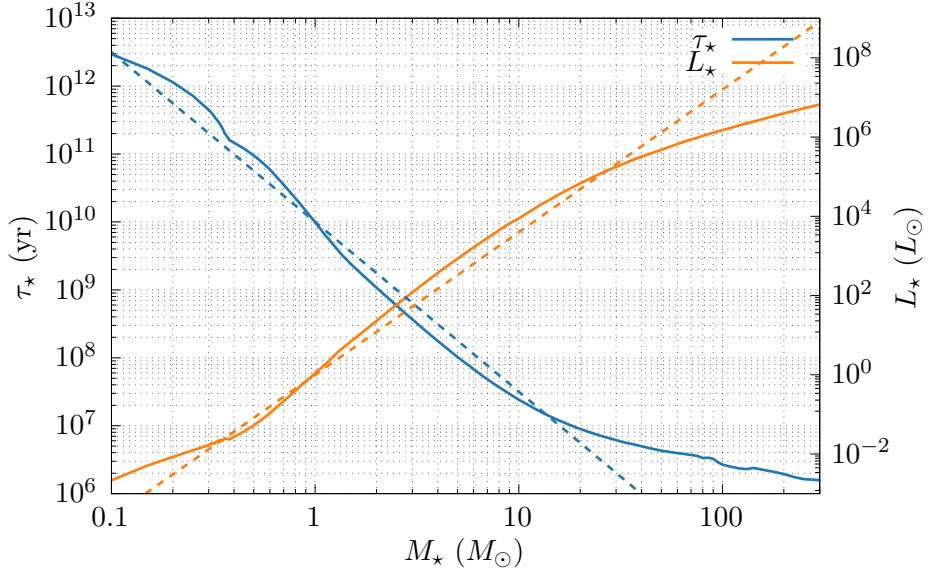


Figure 2.5: A comparison of luminosity and lifetime as a function of initial stellar mass. An estimate of the stellar lifetime of $\tau_* \approx \tau_\odot (M_*/M_\odot)^{-2.5}$ and an estimate for luminosity of $L_* \approx L_\odot (M_*/M_\odot)^{3.6}$ are overlaid with a dashed line. We can see that these estimates are suitable for stars $\lesssim 20 M_\odot$. Lifetime and luminosity data was derived from the MESA Isochrones and Stellar Tracks (MIST) project (Choi et al., 2016; Dotter, 2016; Paxton et al., 2011).

the temperature is still sufficient for hydrogen to burn, with energy production in the star transitioning to a shell-burning process. Schönberg and Chandrasekhar (1942) determined that as the star transitions from core to shell H-burning the temperature gradient in core and envelope is radiative, with an isothermal stratification. Due to this, there is a limiting factor on the stable core size of a star. Above this *Schönberg-Chandrasekhar* limit (q_{SC}) the core contracts on the KH timescale (Eq. 2.1), with the limit determined by the ratio of the mean molecular mass, μ , of the envelope and the core, such that:

$$q_{\text{SC}} \equiv \left(\frac{M_{\text{core}}}{M_{\text{tot}}} \right)_{\text{SC}} = 0.37 \left(\frac{\mu_{\text{env}}}{\mu_{\text{core}}} \right)^2. \quad (2.11)$$

For a star of solar composition we find $q_{\text{SC}} \sim 0.08$ (Salaris & Cassisi, 2005, Ch. 5). For low-mass stars, this collapse timescale is extremely slow. Instead the star expands into an asymptotic giant branch (AGB) star, continuing shell burning until the material is exhausted (Beech, 1988). This leaves behind a degenerate helium core in the form of a white dwarf, which continues to contract and emit radiation through KH processes¹.

¹Finally! Kelvin was right!

2. BACKGROUND

For massive stars the ratio of core mass to total mass is significantly higher, exceeding the Schönberg-Chandrasekhar limit. The outer envelope is driven away through radiation processes as the calculus of hydrostatic equilibrium shifts from contraction to expansion. The star then balloons into a red supergiant (RSG) star or an LBV star. Inside this giant star the core continues to collapse, compressing and heating further, eventually reaching temperatures sufficient for the commencement of helium burning through the Triple- α (3α) process:



The endothermic component of the 3α process, as well as the short reaction time prevents it from occurring in any reasonable quantity until core temperatures are in the order of hundreds of millions of Kelvin (Kippenhahn et al., 2012, Pt. 6). The reaction rate of the 3α process is proportional to T^{40} , which can result in staggering amounts of energy production. This process is far less energy efficient than hydrogen burning processes, and releases an order of magnitude less energy per nucleon (Table 2.1). Hence, the helium burning process can be as short as 500,000 yr. At this point the fate of the star is sealed, it hurtles off of the main sequence like a 1966 Ford Thunderbird from the edge of the Grand Canyon¹. Because of this helium burning, the most massive of early-type stars transition into a Wolf-Rayet (WR) star – one of the crucis of this thesis.

2.1.4.1 Wolf-Rayet stars

In the late 19th century, astronomers Charles Wolf and Georges Rayet noted a curious series of stars with exceptionally broad emission lines. Considering that stars previously had only been observed with narrow absorption lines, this was a particular scientific curiosity (Crowther, 2007). While the mechanism behind energy production in stars was not understood, the scientific community did understand that these winds were *staggeringly* hot. After the initial theories of stellar fusion reactions were developed by Bethe (1939), however, the picture came into sharper focus. Gamow (1943) proposed that these stars contained material produced in the central fusion reaction, which implied that the outer layers of the star had been completely stripped off. This was found to be the case, though categorical confirmation of this did not occur for several more decades. The thickness of these emission lines was easier to establish – these ions were moving *fast*. As such, it was safe to assume that the emission lines were not coming from the

¹See *Thelma and Louise* (1991) dir. Ridley Scott.



Figure 2.6: Reduced Hubble WFPC2 data of the WN star WR124, its extreme mass loss is currently producing the ejecta nebula M1-67 (Marchenko et al., 2010).

stars themselves, but from the winds!

Wolf-Rayet (WR) stars are produced when the largest early-type stars lose significant mass in the LBV stage (Fig. 2.6 & 2.7), while the internal core has the sufficient pressure and temperature required for helium burning. This drives the remnants of the outer envelope away, exposing more and more of the innards of the star, the inner envelope and core, which are still burning hydrogen and helium (Conti et al., 2012, Ch. 5). Whilst in the LBV phase mass loss rates can be higher, these are short but intense bursts of mass loss, rather than a continuous wind (Vink, 2015, Ch. 4). WR stars, in comparison, drive significant, continuous mass loss of the order of $10^{-5} M_{\odot} \text{ yr}^{-1}$, with wind velocities on the order of 10^3 km s^{-1} . The naked core has an extremely high surface temperature, between 30,000 K to 100,000 K, multiply ionising the outflowing hydrogen-deprived wind (Crowther, 2007). The temperature of this heat source also produces significant emissions in the far-UV, which drives the exceptional mass loss through radiative line driving. As the Wolf-Rayet evolves, layers of this burning region are stripped away from the surface of the star, contributing to the stellar wind. Because of this, the outflow becomes more hydrogen-depleted as the star ages, becoming more enriched with fusion by-

2. BACKGROUND

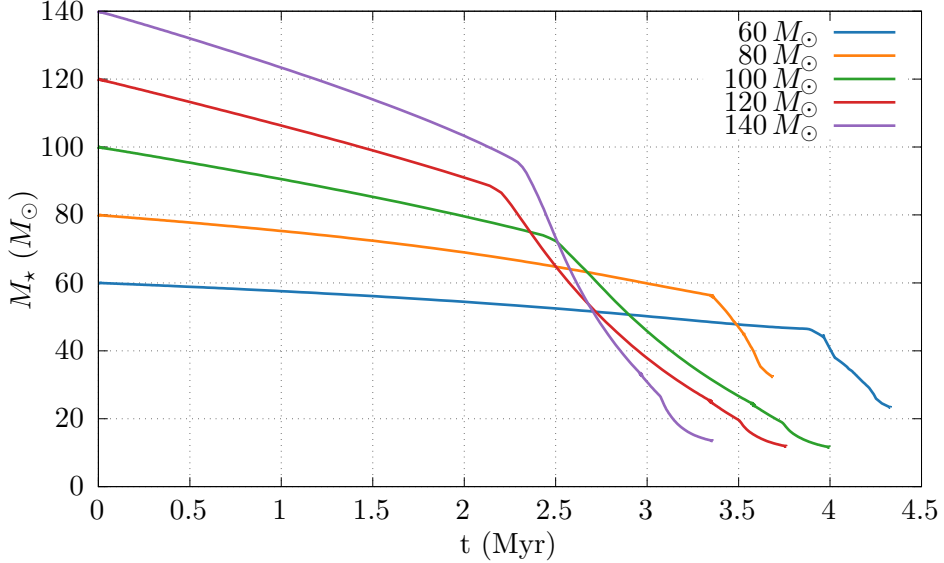


Figure 2.7: Examples of mass loss over the lifetime of a high-mass star. High mass stars clearly undergo significant mass loss as they transition into evolved LBV and WR stars. In all cases we see a reduction in mass loss rate during the terminal WR stage of their lives, and that the stars have shed well over half of their initial mass before entering their WR phase. Stellar evolution data was derived from the MIST project (Choi et al., 2016; Dotter, 2016; Paxton et al., 2011).

products, helium, carbon, nitrogen and oxygen.

Wolf-Rayets can also be subdivided into three distinct categories based on their prominent emission lines:

- WN: WR stars with a strong nitrogen emission line sequence, some helium lines.
- WC: WR stars with a strong carbon emission line sequence, some oxygen lines.
- WO: WR stars with a strong oxygen emission line sequence, some carbon lines.

Further subdivision can be done by measuring the brightness of these emission lines, for example, the WC4 subtype are the dimmest WC stars, with ascending values being brighter. Previously this measurement was more qualitative, and based on the relative ratio of line strengths, however more quantitative methodologies of categorising these stars have emerged (Crowther et al., 1998). Conti (1975) first proposed that massive stars would lose their outer envelopes while undergoing core helium burning. Initially the outermost hydrogen layer is ejected from the star, which is observed as a WN phase WR. As the star continues to evolve and the remaining envelope becomes helium depleted, we observe emission from the exposed core and innermost, carbon

and oxygen enriched shell (Neugent & Massey, 2019; Oswalt & Barstow, 2013). The “Conti scenario” that they described forms the basis for stellar evolution models from main sequence O-type stars to Wolf-Rayet stars. Further work has refined this evolutionary chain. Successive and intermediate stages occur depending on the initial mass of the O-type star, M_O . Crowther (2007) details this series of evolution modes for O-type stars evolving into WR stars:

$$O \rightarrow \begin{cases} LBV/RSG \rightarrow WN \rightarrow SN Ib & \text{for } 25 M_\odot < M_O < 40 M_\odot \\ LBV \rightarrow WN \rightarrow WC \rightarrow SN Ic & \text{for } 40 M_\odot < M_O < 75 M_\odot \\ WN(\text{H-rich}) \rightarrow LBV \rightarrow WN \rightarrow WC \rightarrow SN Ic & \text{for } M_O > 75 M_\odot. \end{cases} \quad (2.13)$$

This can also be seen in evolutionary tracks, such as those in Fig. 2.8. WC stars form from the most massive of O-type stars, and are the only observed dust-producing WR stars. The hydrogen in a WC stars envelope has been completely depleted, instead, the stellar wind is enriched with other elements such as helium, carbon and oxygen. The presence of large quantities of carbon in the outflow is of particular interest, as interstellar dust can condense and form. Whilst some WC stars are potentially capable of forming dust, this is predicted to be rare, and these stars only produce dust in small amounts (Medina et al., 2021). Certain binary systems can produce quantities of dust that can significantly impact their local environment, however. Within a binary system, it is typically paired with another massive star, such as an O-type or B-type. The RSG/LBV phase strips off the bulk of the stars outer envelope, resulting in a WR star that is significantly smaller and lighter than its partner. Despite this, the strong winds produced by the WR star completely dominate the winds of its larger compatriot. If these stars are sufficiently close these winds interact, driving extremely powerful shocks, extreme x-ray fluxes and the aforementioned dust formation. These binaries will be discussed in much more detail – of course – as they are the central objects of this thesis (Section 2.3).

The Wolf-Rayet phase only takes up a brief period of a typical massive stars lifespan, typically 5×10^5 yr, or $\lesssim 10\%$ of the main sequence lifespan of a representative O-type star. Despite this short-lived phase, the Wolf-Rayet leaves a marked impact on the surrounding stellar environment through stellar feedback and in some cases interstellar dust production.

2. BACKGROUND

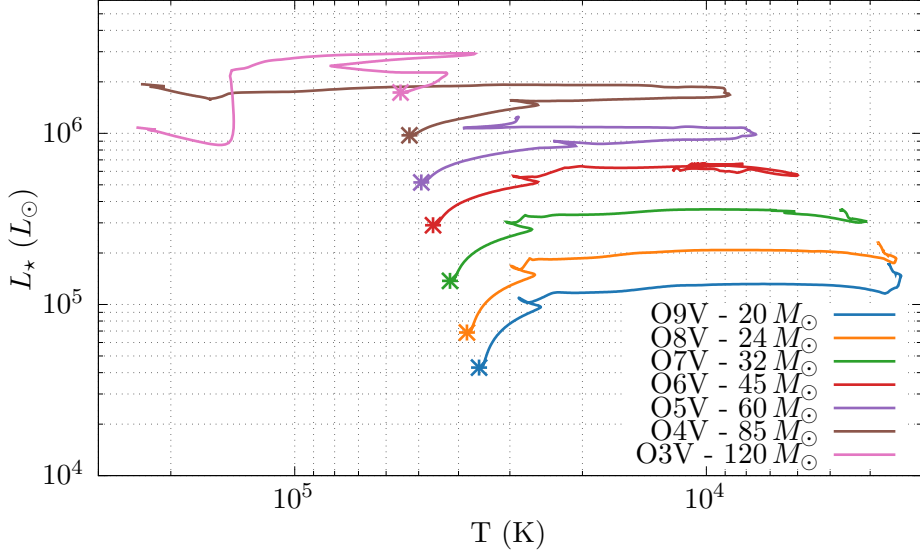
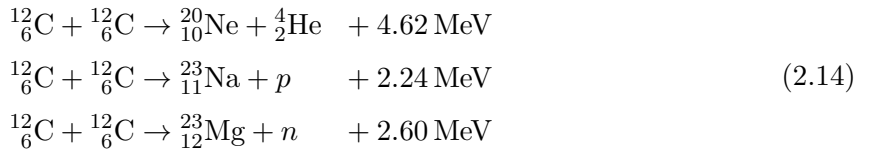


Figure 2.8: Stellar evolution tracks of rotating O-type stars from the zero-age main sequence (ZAMS; represented by a star) to their end of life. Higher mass O-type stars undergo a significant increase in brightness and temperature as they evolve into LBV and then WR stars. The O3V star in particular appears to undergo two separate phases, clearly indicative of the high-mass case of Eq. 2.13. The evolutionary tracks were derived from the MIST project (Choi et al., 2016; Dotter, 2016; Paxton et al., 2011).

2.1.4.2 The death of a star

The star, still shedding a significant portion of its mass, continues its death march¹. The core contracts further, heating to temperatures in the range of 10^9 K, carbon atoms are smashed together and burned, producing many heavier elements:



These reactions salvage minuscule amounts of energy per nucleon, burning through all carbon in the core in $\sim 10^3$ years. The core continues to contract, more vigorous and less efficient fusion processes begin to pile up on each other. The star burns neon, then oxygen, and then silicon – the latter of which has a flurry of reaction modes that produce many different elements, and burns through the entire reserves in approximately a day (Ryan & Norton, 2010, Ch. 6).

¹I understand that this section has taken a flair for the dramatic, but what *isn't* dramatic about the death of a star?

Finally, iron begins to deposit in the core of the star. All fusion processes at this point are endothermic. Suddenly without any exothermic fusion processes – and robbed of its only support mechanism against gravity – the star rapidly collapses. The core rushes in on itself, accelerating to a large fraction of the speed of light. This collapse produces truly unimaginable densities and temperatures in excess of 100 GK¹ within the core; protons capture electrons, forming neutrons and emitting copious amounts of neutrinos. Eventually neutron degeneracy suddenly halts the collapse, the near-relativistic core material suddenly rebounds and generates an enormous shock wave, causing the conditions inside the dying star to jump to more absurd temperatures and pressures. The rebounding material forms a core collapse supernova, ejecting heavy elements formed through neutron capture into an unsuspecting universe. What's left behind is a neutron star: the remnant of the electron capture mechanism from the original inward dive² (Longair, 2011, Ch. 13).

In the case of collapsing Wolf-Rayet stars and other supergiant evolved stars this can go even further. Neutron degeneracy is insufficient to halt the collapse and the core collapses into a black hole. The resultant jet of material from this hypernova³ makes up a gamma-ray burst (GRB), a phenomena that can threaten planets *thousands* of light years from their point of origin. We should stop here, this section was written to provide context as to what early-type stars fundamentally are: violent, destructive, and awe-inspiring. It seems absurd that these systems could produce anything as fragile as interstellar dust.

And yet they *do!*

2.2 Interstellar Dust

For much of the history of astronomy, interstellar dust was not its own field, nor was it studied in significant detail. Instead it was regarded as nothing but a *nuisance*. Early astronomy relied solely on visible light observations, and at these wavelengths dust obscures dim and distant stars, as well as the innermost depths of the galaxy. The first population counts of stars at the turn of the 20th century were hampered by this extinction, with Kapteyn (1909) noting:

“Undoubtedly one of the greatest difficulties, if not the greatest of all, in the way of

¹I can state a temperature of 100 GK but can you really *imagine* it? Can anyone really comprehend that kind of temperature?

²Randall Munroe of XKCD once stated a good description of supernovae that I like to tell people: “However big you think supernovae are, they’re *bigger* than that.”

³*Bigger than bigger than that!*

2. BACKGROUND

obtaining an understanding of the real distribution of the stars in space, lies in our uncertainty about the amount of loss suffered by the light on its way to the observer.”

The existence of dust grains was not considered until nearly a quarter of a century later, with research undertaken in 1930 by Robert J. Trumpler concluding that the observed interstellar reddening effect could only be accounted for by small grains of cosmic dust. As technology progressed and non-visible astronomy became possible, we were for the first time able to peer past these obscuring clouds, bypassing them entirely. The scientific community also found that the interstellar dust itself was interesting on its own, leading to further categorisation and parametrisation of these dust grains in the 1960’s and 1970’s (Whittet, 2002, pp. 4–13).

Small grains of interstellar dust are a loose collective of atoms and molecules held together by weak molecular bonds, and are typically on the order of 10 Å to 100 Å in size. These grains are formed from small, refractory dust cores around 5 Å across, in high density regions such as stellar atmospheres and dark interstellar clouds (Spitzer, 2008). This initial accretion process can be quite rapid due to implantation of impinging carbon ions from the accompanying stellar wind (Zubko, 1998). While the largest dust grains can be on the order of centimetres (in the case of protoplanetary disks), the initial grain size that we use in this project is 50 Å, which we determined through experimentation (Section 3.7.2.1). There are a multitude of ways that these dust grains can grow and shrink in size, though only a few are simulated in this work. This is due to either difficulty of implementation into our model or time constraints. The first such mechanism for growth and destruction that will be discussed is grain-grain collision. This interaction occurs in regions of high grain number densities and is dependent on the collision velocity between the grains, as well as the grain number density. Low velocity collisions result in grain mergers, where these grains will stick together. An initial attractive force through van der Waals interaction will occur, bringing the grains into contact. Upon collision the contact area will deform and flatten, allowing for the grains to coagulate and merge. Grain-grain coagulation occurs at very low velocities, typically $< 100 \text{ m s}^{-1}$, but this threshold velocity is typically lower for smaller, more tightly bound grains (Chokshi et al., 1993). At higher collision velocities small grains can simply bounce off of each other, doing very little damage outside of mutual ablation of the grains. At higher velocities still, grains can shatter and fragment each other. In the case of high velocity shocks with large grains, this can result in the grains being completely pulverised, turning from an accretion process to the principle cause of dust destruction (Jones, 2004; Jones et al., 1996).

The most important method of destruction of dust for this project is grain-gas sputtering,

this thermal interaction dominates dust destruction at all temperatures in shocks. As an ion collides with a dust grain in a shock, the surface near the impact site is vaporised, this impact also drives a shock wave into the grain, which cause it to melt and shatter. Over time material is ablated off of the dust grain, causing it to shrink in radius and eventually disintegrate. In the case of a spherical grain, as the gas collides with the grain, small amounts of it are vaporised and ejected from the surface, causing a reduction in grain radius, a , with a corresponding rate of radius change, \dot{a} . This rate of radius change varies depending on the composition of the grain. For instance, grains composed of ice would be more readily vaporised by impacts than sturdier grains composed of carbon or iron. In this spherical case the dust destruction rate is also proportional to the number density of the gas, as the grain will be destroyed faster if there are more gas-grain interactions.

Calculating the exact dust sputtering yield incurred on a grain is a very complex process, requiring a summation of sputtering yields across all projectile ion species. Instead, we use an approximation described by Draine (2011, Ch. 25) which significantly simplifies the process and does not require simulation of the dynamics of ions. Between 10^5 and 10^9 Kelvin the following approximation is valid:

$$\dot{a} \approx -\frac{1 \times 10^{-6}}{1 + T_6^{-3}} \left(\frac{n_{\text{H}}}{\text{cm}^{-3}} \right) \mu\text{m yr}^{-1}, \quad (2.15)$$

where T_6 is the gas temperature in units of 10^6 K. The dust destruction rate is dependent on the gas temperature, rapidly reducing below 10^6 K, and is found to be roughly flat from 10^6 K to 3×10^8 K (Tielens et al., 1994). We can therefore adopt a normalised grain lifespan τ_{gr} , which we can use to calculate the dust destruction rate in our simulations:

$$\tau_{\text{gr}} \equiv \frac{a}{\dot{a}} \approx 3 \times 10^6 \frac{a}{n_g} \text{yr}, \quad (2.16)$$

where n_g is the gas number density (Draine & Salpeter, 1979b; Dwek et al., 1996). The value of 3×10^6 yr was chosen for this project as it is more typical of temperatures in the post-shock region of a WCR, between 10^6 K and 10^7 K (Fig. 2.9). How this destruction rate is implemented into the simulations for this project is discussed in more detail in Section 3.7.

At lower velocities gas can impact onto grains and stick to their surface. This steady accretion process can be described in the form of another fairly efficient model. By considering a spherical grain moving through a flow of atoms with a number density n_a , a certain number of these atoms would collide and stick to the dust grain, this sticking probability is defined as ξ . This sticking

2. BACKGROUND

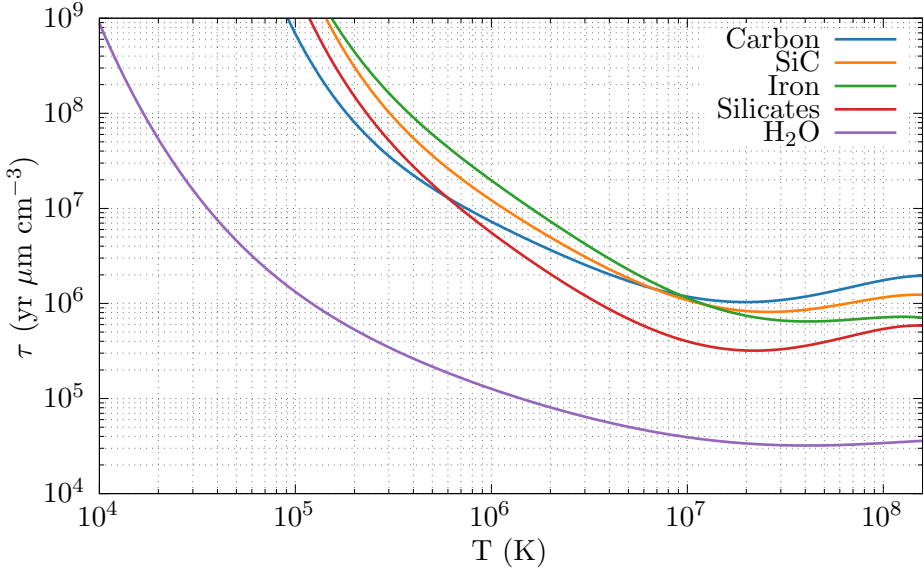


Figure 2.9: Comparison of grain lifetimes for various interstellar dust species undergoing thermal sputtering in a fast interstellar shock. Lifetime is normalised to a grain radius of $1\text{ }\mu\text{m}$ and a flow of 1 g cm^{-3} in a shock of solar abundance. Data is derived from 5th order polynomial fits calculated in Tielens et al. (1994, Table 4).

factor is found to be ≈ 1 for neutral atoms¹ (Watson & Salpeter, 1972). Above a threshold velocity, atoms fail to adhere to the grain surface in significant quantities, and at even higher velocities contribute to the sputtering process instead (Spitzer, 2008). For this research, this threshold temperature was defined as 14,000 K.

If we model a grain of radius a , the cross section, σ , of the grain moving through the gas would be $\sigma = \pi a^2$. In the case of a grain moving through a gas of composition x and density ρ_x where the grain is significantly larger than the atoms composing the gas, it is found that the rate of change in the grain mass, dm_{gr}/dt , is:

$$\frac{dm_{\text{gr}}}{dt} = \sigma w_x \rho_x = \pi a^2 \rho_x w_x \xi_x, \quad (2.17)$$

where w_x is the RMS velocity of the gas. The associated rate of change in grain radius, da/dt , is found to be:

$$\frac{da}{dt} = \frac{w_x \rho_x \xi_x}{4 \rho_{\text{gr}}}, \quad (2.18)$$

¹Though we adopt a more conservative value of 0.1 due to the turbulent nature of the environments that are studied in this project.

where ρ_{gr} is the bulk density of the dust grain.

A myriad of other dust destruction processes exist, such as electron-grain and cosmic ray-grain interaction. However, these are considered to be out of the scope of this project, and not influential in the case of a hot gas or dense post-shock environment (Jones, 2004). Outside of shocks, dominant destruction processes include thermal and photo-dissociation methods. UV light emitted from stars can ionise atoms on the surface of the grain, ejecting them from the surface, slowly “boiling” material from the grain. This of course makes the premise of our project all the more curious, with so many mechanisms underpinning dust destruction, particularly in hot, dense environments, how come we observe significant dust production in Wolf-Rayet binary systems?

2.2.1 Dust composition

The only species of interstellar dust studied in this thesis are composed of carbon. sp^2 (graphite) and sp^3 -bonded (diamond) dust grains have been detected from their characteristic emission lines, as well as hydrocarbon chains and Polycyclic Aromatic Hydrocarbons (PAHs). Complex organic molecules have also been detected in dusty environments, which are believed to have formed on the surface of dust grains, instead of forming within the ISM itself (Herbst & van Dishoeck, 2009). The primary dust detected in CWB systems is amorphous carbon grains, which are defined as grains with a mixture of sp^2 - and sp^3 -bonded carbon with no structural order or polymerisation (Draine, 2003). Other species of interstellar dust are abundant throughout the ISM. These species include water ice, as well as silicate and iron grains. These grain species have not been detected in dust producing CWB systems. Amorphous carbon grains are also markedly more resistant to erosion and fragmentation due to shocks than other grain types. Amorphous grains are also more resistant to thermal sputtering, due to their higher sublimation temperature. This resilience is vital if they are to survive in the extreme conditions of a CWB system (Draine & Salpeter, 1979a).

2.2.2 The importance of interstellar dust

We should ask ourselves, why are dust grains important enough to merit so much time and effort from researchers? Over this short section we will attempt to explain in brief why dust grains are so important.

Over 150 molecular species have been observed in the interstellar medium, with a surprisingly

2. BACKGROUND

complex degree of organic chemistry; of the molecules with six or more atoms that have been detected, 100% of these have been organic in nature. Such complex organic molecules include benzene, acetone and ethanol, which are complex molecules that should not form in significant yields in interstellar gas-phase chemistry. Instead, these organic species form on the surface of interstellar dust grains, with gas-phase chemistry accounting for simple molecule production such as H₂ and CO (Herbst & van Dishoeck, 2009). The role of dust as the chemical refineries of the interstellar medium has a number of effects when it comes to star and planetary formation, as well as organic and pre-biotic chemistry throughout the universe. It is no understatement to say that the universe would be markedly different if interstellar dust was not so abundant.

Dust grains are also vitally important in the star formation cycle. As a giant molecular cloud (GMC) collapses, it heats up. In an adiabatic case the increased temperature would provide a counterbalancing pressure on the collapsing cloud, forming a hydrostatic equilibrium and preventing the cloud from collapsing any further. In the case of extremely massive clouds, this collapse can still occur as gravity will dominate, but this equilibrium dictates the minimum mass for a cloud to collapse into a protostar. As such, for all but the most massive stars to form, energy must be lost in the form of radiation (Ward-Thompson & Whitworth, 2011). As cooling from dust grains is extremely efficient in cold, dense environments, this mechanism is well-suited for the environment of a GMC. In addition to cooling through rotational mechanisms of simple molecules in the gas-phase of the medium, these processes sufficiently cool the GMC, allowing for further collapse. In addition, dust grains would also provide a replenishing source of cooling molecules such as CO and OH through non-thermal grain desorption processes. The presence of dust grains within a GMC therefore strongly influences the minimum mass of stars (Williams & Cecchi-Pestellini, 2015).

Interstellar dust is also important for planetary formation. Collision between refractory dust grains is the first stage of planetesimal formation. Within the protoplanetary disk, low velocity collisions between micron-sized grains can occur, causing these grains to stick and rapidly accrete. If the local region of the disk is gravitationally unstable, these small grains will form a gravitationally bound cluster, and contract over time into a planetesimal. Afterwards, rapid accretion of other planetesimals gives rise to the formation of both rocky planets and gas giants (Apai & Lauretta, 2010). Dust is also a regulator of opacity, which determines the temperature structure and composition of the protoplanetary disk. Finally, and perhaps most importantly to the reader, the complex organic molecules produced in the dust grain are pre-biotic precursors to life (Birnstiel et al., 2016).

As the role of interstellar dust in star and planet formation, as well as the long-term implic-

ations of the formation of life in the universe are *slightly* out of the scope of this project, we will stop here, and move on to the topic of colliding stellar winds.

2.3 Colliding Wind Binary Systems

Colliding wind binaries (CWBs), in opposition to all known laws of astrophysical nomenclature is an easy to understand term: it is a binary system wherein stellar winds undergo collision. Unfortunately, the simplicity of the systems ends here, CWB systems are very poorly understood phenomena due to a variety of factors.

2.3.1 History of CWB observation

Early observations beyond the visual spectrum led to the discovery of many new astrophysical phenomena. One such discovery were extremely bright and variable thermal x-ray sources. Many of these early galactic x-ray sources were found to be compact objects, and many more contained the characteristic spectral lines of a Wolf-Rayet star. While single Wolf-Rayet stars are capable of producing x-rays if there are sufficient instabilities in the winds (Gosset et al., 2005), this is typically much fainter (Nazé et al., 2021; typically $L_{\text{x-ray}}/L_{\text{bol}} < 10^{-7}$) than what was being observed from these systems (Oskinova, 2015; Rauw, 2022; Seward et al., 1979). The existence of CWB systems were independently proposed by Prilutskii and Usov (1976) and Cherepashchuk (1976). Both research groups proposed that significant and variable x-ray flux would result from the collision between two stellar winds. As these winds collide the gas becomes shocked and heated to temperatures on the order of 10^8 K – hot enough to emit an appreciable quantity of x-rays. The x-ray variability can also be explained as a result of the orbital properties of the systems. X-ray variability would result from the following effects:

- Eccentricity in the orbits of the systems, leading to differing shock intensity and changing of the shock geometry, changing the fraction of the winds being shocked.
- Edge-on orbits resulting occlusion of x-rays by the stellar wind from each star.
- Photospheric eclipses in the case of high inclination angles.

Such effects could not be produced within a single star system (Pittard, 1999, p. 34). WR+OB systems were also found to be the brightest of such objects, while OB+OB binaries with significant x-ray flux were observed, these were typically less luminous. Early work was more

2. BACKGROUND

concerned with x-ray observation, in particular the systems γ^2 Velorum and V444 Cygni, which were noted in particular as prototypical CWB systems by Prilutskii and Usov (1976). Later, infrared observations of these systems found another, more curious attribute: a significant infrared excess correlating to dust formation around these systems (Williams et al., 1987). This will be discussed in more detail later in this section.

2.3.2 The wind collision region

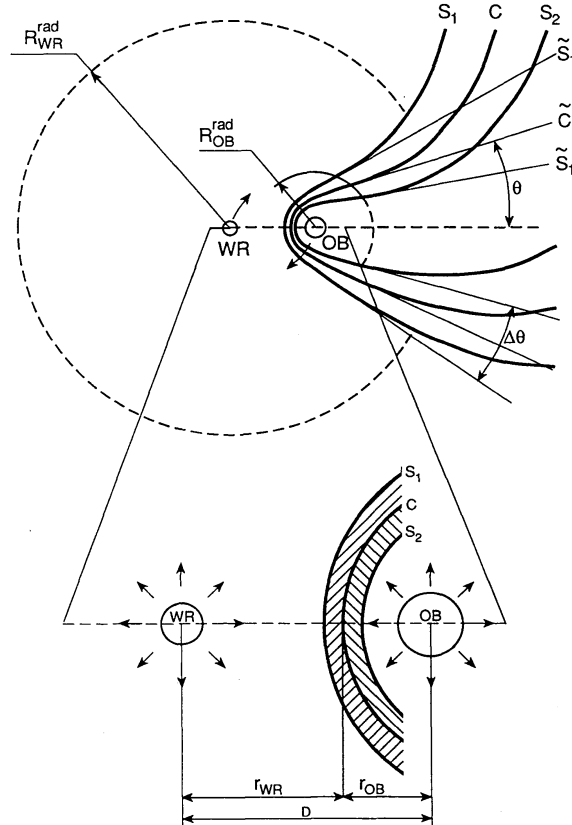


Figure 2.10: A diagram of a typical Wind Collision Region inside a WR+OB CWB system. The S_1 and S_2 surfaces denote the shock waves from the primary and secondary winds respectively, and C denotes the contact surface. The surfaces \tilde{S}_1 , \tilde{S}_2 and \tilde{C} represent conic approximations of their corresponding surfaces at intermediate distances from the OB star. The region of stellar wind collision is hatched in the bottom diagram (Eichler & Usov, 1993).

The wind collision region (WCR) is the most violent and turbulent region of a CWB system, a region of high gas density and even higher temperatures. If the interacting stellar winds are dense as they begin to interact, a shocked region of plasma in excess of 10^8 K is formed, the winds

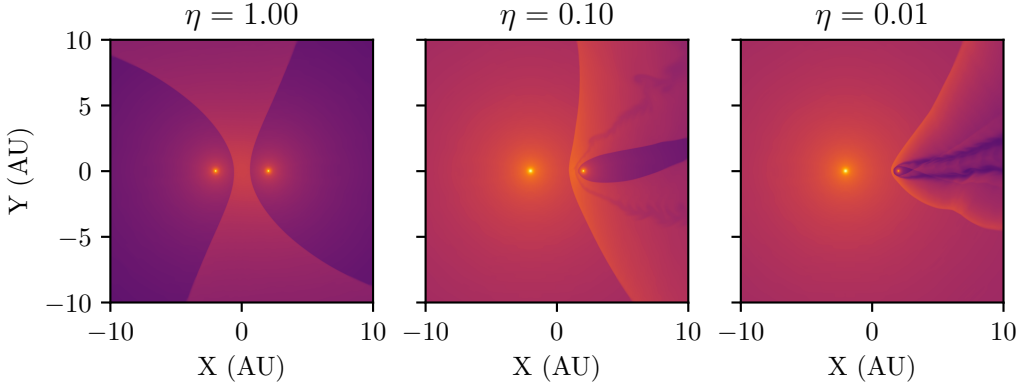


Figure 2.11: Comparison of the WCR structure of CWB systems with wind momentum ratios of 1, 0.1 and 0.01. Momentum ratio is varied by changing the mass loss rate of the second star, \dot{M}_2 . As η decreases, the WCR begins to wrap itself around the secondary star. Orbital effects are also shown in this example.

rapidly decelerate from hypersonic to subsonic, liberating an enormous amount of mechanical energy, on the order of $10^3 L_\odot$. This is the engine that drives the significant x-ray flux observed by astronomers in the 1970s, as well as other thermal and non-thermal emissions from radio waves to gamma rays (Eichler & Usov, 1993; Grimaldo et al., 2019). As a wind enters from either side of the wind collision region, it passes through a shock wave, and flows towards the centre of the wind collision region at the contact discontinuity, C (Fig. 2.10), and downstream of the system. The post-shock wind is driven by a combination of thermal pressure from the outflowing stellar wind, as well as the significant momentum the wind carried had pre-shock (Stevens et al., 1992).

The geometry of the WCR is influenced strongly by the wind parameters of both stars, the most important of which is the wind momentum ratio, or η , which we define as:

$$\eta = \frac{\dot{M}_{\text{OB}} v_{\text{OB}}^\infty}{\dot{M}_{\text{WR}} v_{\text{WR}}^\infty}, \quad (2.19)$$

where \dot{M}_{WR} and v_{WR}^∞ denotes the mass loss rate and wind terminal velocity of the primary (typically WR) star and \dot{M}_{OB} and v_{OB}^∞ denotes the mass loss rate and wind terminal velocity of the (typically OB) partner (Usov, 1991). A lower value of η indicates a more unbalanced wind, with a wind momentum ratio of 0.01 or lower being common for a typical WR+OB system. Additionally, if $\eta = 1$, we observe a sheet of interacting plasma flowing away from the system perpendicular to the orbital plane. In the case of a typical system where the WR stars momentum is significantly larger than OB's, we observe the WCR extend and envelop the OB

2. BACKGROUND

star, forming an approximately conical surface extending away from the Wolf-Rayet star (Fig. 2.11).

As the wind becomes more and more imbalanced, the contact discontinuity moves closer to the OB partner. The position of this discontinuity can be predicted with the equation

$$r_{\text{WR}} = \frac{1}{1 + \eta^{1/2}} d_{\text{sep}}, \quad r_{\text{OB}} = \frac{\eta^{1/2}}{1 + \eta^{1/2}} d_{\text{sep}}, \quad (2.20)$$

where r_{WR} is the distance from the WR star to the contact discontinuity, r_{OB} is the distance from the OB star to the contact discontinuity and d_{sep} is the orbital separation distance of the stars. We can also approximate the opening angle, θ_c , of the WCR using the equation provided by Eichler and Usov (1993)

$$\theta_c \simeq 2.1 \left(1 - \frac{\eta^{2/5}}{4} \right) \eta^{-1/3}, \quad \text{for } 10^{-4} \leq \eta \leq 1. \quad (2.21)$$

Work by Pittard and Dawson (2018) on determining the accuracy of opening angle estimations such as Eq. 2.21 found that this approximation is accurate under the condition $\eta > 0.01$, but begins to diverge significantly if this condition is exceeded. This was accomplished through a series of hydrodynamical simulations with different values for η , with the resultant opening angle calculated from the fully advected simulations. This work goes on to derive analytical solutions to the opening angles of the conic approximations of \tilde{S}_1 and \tilde{S}_2 . These solutions were found to be:

$$\theta_1 = 2 \tan^{-1} \left(\eta^{1/3} \right) + \delta\theta, \quad (2.22a)$$

$$\theta_2 = 0.658 \log_{10} (71.7\eta), \quad (2.22b)$$

where $\delta\theta$ is the opening angle of the WR shock in the limit that $\eta = 0$ (found to be $\delta\theta \approx \pi/9$). From these estimations the fraction of each wind that is shocked, f , can be calculated:

$$f_1 = \frac{1 - \cos(\theta_1)}{2}, \quad (2.23a)$$

$$f_2 = \frac{1 + \cos(\theta_2)}{2}. \quad (2.23b)$$

Pittard and Dawson (2018) observed that the entirety of the secondary wind was shocked if $\eta \lesssim 0.014$, while in the typical wind momentum ratio regime $0.001 \leq \eta \leq 0.01$, only $\sim 10\%$ of

the WR wind is shocked (Fig. 2.12). While useful for describing the geometry of WCR in broad strokes, these equations are based on adiabatic simulations with instantaneous acceleration, and thus have their limitations.

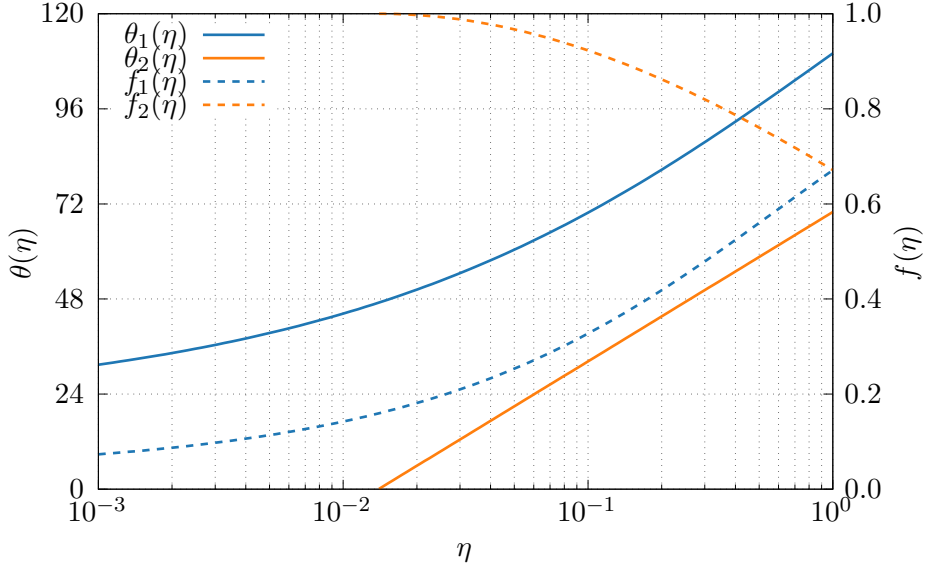


Figure 2.12: Comparison of the opening angle of \tilde{S}_1 and \tilde{S}_2 as a function of η . The wind shock fraction, f , is also plotted. $\approx 10\%$ of the primary wind is shocked under typical WR+OB conditions, while the entire secondary wind is typically shocked.

Orbital motion is a significant factor in the geometry of a WCR. As the stars orbit each other and the WCR curves and wraps around the system, the angle of the WCR relative to the outflow from the system is constantly changing. The conical approximation as described in Eichler and Usov (1993) was found to be valid to a distance of $r_{\text{OB}} \ll r \ll (P v_{\text{WR}}^\infty)/2$, where P is the orbital period. In systems with a short orbital period, this can result in the production of a pinwheel-like structure as the WCR extends away from the stars. For example, the systems WR104 and WR98a produce easily observable pinwheel structures, especially in the infrared.

2.3.3 Cooling in the WCR

Such violent regions of space are *exceedingly* hot. In a fixed frame of reference, the immediate post-shock temperature, T_s , is calculated via the formula:

$$T_s = \frac{3\mu m_H}{16k_B} V_s^2, \quad (2.24)$$

2. BACKGROUND

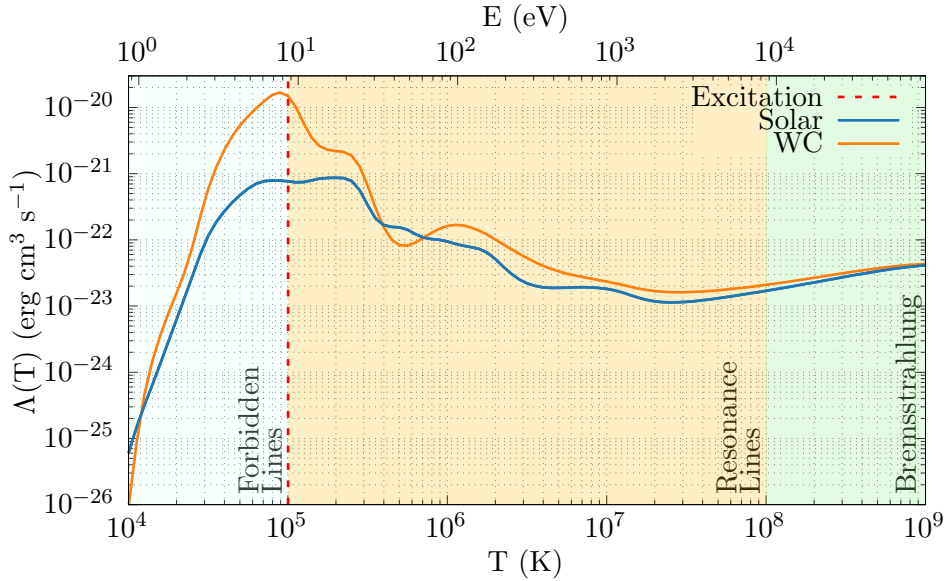


Figure 2.13: Normalised plasma cooling rates as a function of temperature and thermal energy for solar abundance and WC abundance winds. The regions where forbidden line, resonance line and bremsstrahlung emission are dominant are highlighted, with H ionisation and recombination occurring between the forbidden and resonance line sections at 10^5 K.

Temperature range	Dominant process	Spectral region
$T < 10^3$ K	Molecular cooling	IR
$5 \times 10^3 \text{ K} \lesssim T \lesssim 10^5$ K	Forbidden lines	21 cm, IR, Optical
$T \approx 10^5$ K	H excitation/ionisation	Optical, UV
$5 \times 10^5 \text{ K} \lesssim T \lesssim 10^8$ K	Resonance lines	Far UV, soft x-ray
$T \gtrsim 10^8$ K	Bremsstrahlung	Radio

Table 2.3: Breakdown of dominant cooling processes at various temperature ranges from Dyson (2021, Ch. 6). Whilst H excitation/ionisation occurs over a very short temperature range, it is extremely influential, causing a global peak in the cooling rate at $\approx 10^5$ K. These temperature ranges are depicted in Fig. 2.13.

where μ is the mean molecular mass, k_B is the Boltzmann constant¹, and V_s is the shock velocity (Maciel, 2014, Ch. 9). For stellar winds colliding with a relative velocity of $2,000 \text{ km s}^{-1}$ we find that the immediate post-shock temperature is of the order 10^8 K.

But how does the WCR cool to temperatures suitable for dust formation? Dust destruction occurs readily at temperatures $> 10^6$ K, with temperatures $< 10^4$ K being conducive to dust formation. Furthermore, this cooling has to be very rapid, as observations have shown that the bulk of dust formation occurs $\lesssim 100$ AU from the point of initial shock. In fact, winds moving at velocities in excess of $1,000 \text{ km s}^{-1}$ would clear this distance in less than half a year! In an

¹ $1.381 \times 10^{-16} \text{ erg K}^{-1}$

adiabatic shock, we would find that the gas cools purely through expansion in accordance with the ideal gas law; as the flow from the WCR begins to spread away, it cools on an extremely slow timescale. Gas and plasma within the gas are subject to a variety of cooling mechanisms, which contribute to removing energy from the medium. As atoms and ions are excited by collisions or photons, the particles are excited to higher energy levels, releasing photons and de-exciting to their ground state. These photons can leave the medium, and in dense mediums this can occur over multiple adsorption/re-emission events. This causes the photon to leave the gas through a “random walk” which is dependent on the wavelength of the photon and the density of the gas. Inversely, if the post-shock WCR is sufficiently dense, ionising radiation from the parent stars cannot penetrate deep into the WCR, protecting dust grains and preventing heating aside from a small contribution from galactic cosmic rays (GCRs).

Strong radiative cooling results in much higher compression levels of the post-shock gas than the adiabatic limit of $\rho_{\text{post-shock}} = 4\rho_{\text{pre-shock}}$. This is crucial to the formation of dust in the post-shock region, which relies on high densities as well as cool temperatures (this is explored further in Section 2.3.4).

The influence of each cooling mechanism varies over a particular temperature range, due to the collision energy of the atoms and ions. While there is some overlap, certain mechanisms are clearly dominant over specific temperature ranges (Table 2.3 and Fig. 2.13). In the “warm”¹ phase we find that forbidden line emission through atomic hydrogen or metallic ions is dominant, while at higher temperatures higher energy processes such as H recombination and resonance line emission dominate. At extremely high temperatures in the immediate post-shock WCR, free-free processes such as bremsstrahlung dominate (Dyson, 2021, Ch. 6). In this section we will discuss these primary mechanisms of cooling.

2.3.3.1 “Cool” medium

At temperatures from 10 to 10^3 K atomic excitation is extremely unlikely, other than heating events from adsorption of cosmic rays. Instead, spontaneous rotational and vibrational transitions in molecules shed what little thermal energy remains in these clouds. The most influential molecules on the temperature of these gas clouds are H₂O, H₂ and CO (Neufeld & Kaufman, 1993; Neufeld et al., 1995). Through molecular transitions for cooling and heating through cosmic rays, a stable temperature in the order of 10 K is maintained in these cold, dense clouds. While this mechanism is essential for understanding how molecular clouds remain so cool, heat-

¹See what I mean about the phrase “warm”?

2. BACKGROUND

ing from the parent stars will prevent the WCR from getting this cold.

2.3.3.2 “Warm” medium

Between 10^4 and 10^5 K, radiative cooling is dominated by forbidden line transitions¹. This mechanism releases energy through a hyperfine splitting of the $1s$ ground state of hydrogen, where the hydrogen atom spontaneously emits photons de-excite to a more stable spin state. Transition between a proton/electron parallel ($\uparrow\uparrow$) to antiparallel ($\uparrow\downarrow$) spin state emits a photon of energy $5.86 \mu\text{eV}$:

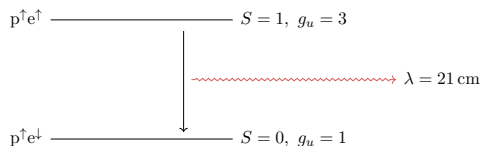


Figure 2.14: Energy level diagram of the 21 cm spectral line – an all-in-one galactic yard stick, stopwatch and cooling mechanism.

Despite the parallel spin state being metastable, with a very long lifetime of 11 Myr, it occurs extremely readily in a large volume of gas in the ISM. Gas at this temperature is relatively transparent to radio waves, and as such the 21 cm line can steadily remove energy through cooling². Due to the presence of enormous quantities of atomic hydrogen, the 21 cm line is one of the most prevalent type of radio emission in the galaxy³ (Draine, 2011, Ch. 8). In winds with a higher metallicity, forbidden line transitions from ions with more electron orbitals, can become dominant. Such ions include O^+ and O^{++} :

¹Like many other phenomena discussed in this thesis, this too is a misnomer. This transition was initially believed to be prohibited under contemporary models of atomic physics. This is in fact just astrophysicists jumping the gun again!

²In the fighting game community (FGC), this is referred to as “chip damage”.

³In fact, the wavelength and parallel spin state actually make up a set of fundamental units used in messages such as the *Voyager* and *Pioneer* messages due to its ubiquity.

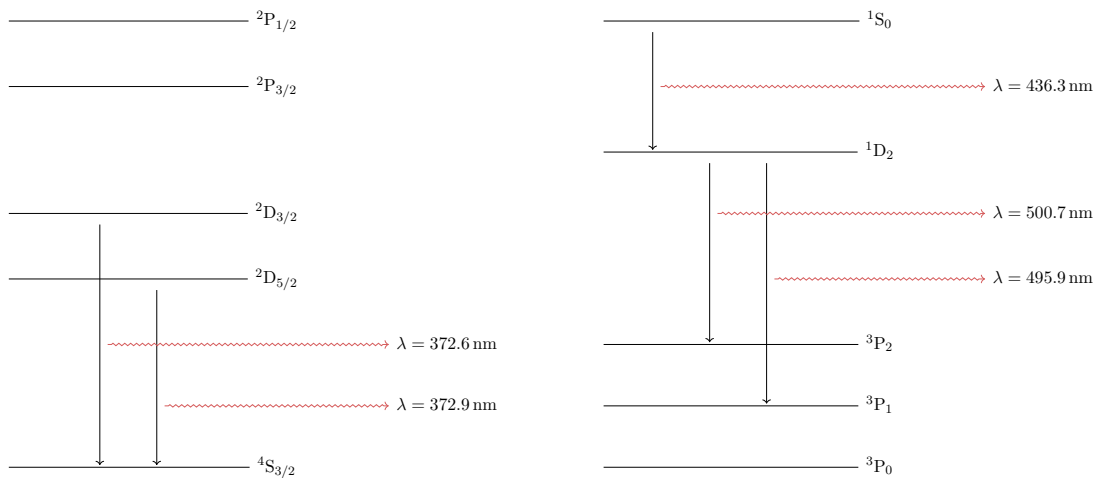


Figure 2.15: Forbidden line transitions in the O^+ (left) and O^{++} (right) ground states.

These transitions release significantly more energy, and as such are a more efficient way of removing energy from metal enriched winds, explaining the increase in cooling rate in the WC abundance wind in Fig. 2.13 (Dyson, 2021, Ch. 5). As the temperature increases, the rate of cooling peaks. In WCRs containing hydrogen this is consistent with recombination of electrons and hydrogen ions, releasing photons of energy 13.6 eV.

2.3.3.3 “Hot” medium

Beyond 10^6 K^1 forbidden line transitions are no longer dominant as metastable levels in the ground state of ions become increasingly rare as the species become more and more ionised (C^{3+} , O^{4+} etc.). Instead, resonance line transitions in metals, the driving force behind the stellar winds, begin to take over the role of cooling. These lines are not metastable like forbidden lines, and have much higher transition probabilities. As such, the emission rate is still quite high, but is constantly decreasing as temperature increases, as the probability for an ion being completely ionised increases. At temperatures in excess of 10^7 K , even these heavier ions are completely ionised. With their electrons stripped bare they simply do not have any resonance lines left! However, at these extreme temperatures, the WCR is cooled through radiation emitted via the bremsstrahlung² mechanism. This mechanism is comparatively simple: as the path of a high velocity charged particle is changed, it emits radiation equivalent to the change in velocity, in accordance with the conservation of energy. As this process is not determined by emission lines or

¹Which we have arbitrarily defined as “hot”.

²Or “braking radiation” if you have forgotten how to spell bremsstrahlung.

2. BACKGROUND

energy levels, it increases with temperature, as stronger deflections release higher energy photons. Therefore, this process acts as the dominant cooling process in the universe at temperatures beyond 10^9 K (Longair, 2011, Ch. 6).

2.3.3.4 Radiative effects in WCRs

CWB systems are interesting interstellar phenomena. Only a handful of phenomena in space that operate on such a large temperature range over such a short timespan like CWB systems do. These systems are highly dependent on the temperature, and therefore very dependent on the amount of cooling occurring in the system. This can present tremendous challenges trying to simulate them, due to the difficulty of calculating contributions to cooling. Simulating cooling can significantly impact the stability of the simulations, which are already hard enough to perform on their own. The first problem is solved by pre-calculating the emission rate of gas with a specific metallicity over a range of temperatures. This is accomplished using models such as the Mewe-Gronenschild-Kaastra (MEKAL) model, and incorporating the output of these models into the simulation in the form of a lookup table (Kaastra et al., 2013; Mewe et al., 1985).

In order to explore the contribution of cooling to the structure of the WCR, we must do what many¹ astrophysicists despise the most: describe something mathematically. First, in order to determine the amount of cooling occurring at a particular temperature, we summate the contributions of all energy loss mechanisms – from forbidden lines to bremsstrahlung – into a single value. We first define the energy loss rate of a volume of gas, $\mathcal{L}(T)$, which in the case of plasma cooling is calculated by the equation

$$\mathcal{L}(T) = \left(\frac{\rho}{m_H} \right)^2 \Lambda(T) = n_g^2 \Lambda(T), \quad (2.25)$$

where n_g is the number density of the gas and $\Lambda(T)$ is the emissivity of the gas (Stevens et al., 1992). This assumes that the photons produced will eventually leave the gas. As we can see, the rate of cooling in a gas is proportional to the square of the number density; as the density of the post-shock flow increases, it cools faster, despite having more internal energy. Other methods of cooling and heating are not as strongly dependent on the number density of the gas. For instance, dust cooling, which we will discuss later, has a dependence of $\mathcal{L}_d \propto n_g$, while cosmic ray heating has a dependence of $\mathcal{L}_{CR} \propto n_g^{-1/2}$ (Wiener et al., 2013).

¹But possibly not *all*.

2.3 Colliding Wind Binary Systems

Cooling becomes influential on the system if gas in the WCR is able to sufficiently cool before it can leave the WCR. To describe this Stevens et al. (1992) introduced the wind cooling parameter, χ , which is the ratio of the cooling time, t_{cool} , and the shock region escape time, t_{esc} :

$$\chi = \frac{t_{\text{cool}}}{t_{\text{esc}}}. \quad (2.26)$$

If we determine the cooling time as the amount of time required for the gas to radiate *all* of its energy, we find that

$$t_{\text{cool}} = \frac{e}{\mathcal{L}(T)} = \frac{3}{8} \frac{k_B T}{n_w \Lambda(T)}, \quad (2.27)$$

where e is the internal energy per unit volume of the gas and n_w is the pre-shock wind number density. This value is appropriate in the case of a strong shock with a ratio of specific heats of $\gamma = 5/3$. The escape timescale can be approximated with the equation

$$t_{\text{esc}} = \frac{d_{\text{sep}}}{c_s}, \quad (2.28)$$

where c_s is the sound speed. Stevens et al. (1992) describes an equation to approximate χ for each wind, which is used throughout this thesis:

$$\chi \approx \frac{v_8^4 d_{12}}{\dot{M}_{-7}}, \quad (2.29)$$

where v_8 is the wind terminal velocity in units of 10^8 cm s^{-1} , d_{12} is the orbital separation distance between the stars in units of 10^{12} cm and \dot{M}_{-7} is the mass loss rate of the star in units of $10^{-7} M_\odot \text{ yr}^{-1}$.

In the case of a star with a cooling parameter of $\chi \gg 1$, the resultant stellar wind behaves adiabatically in the post-shock environment, producing a smooth flow. As χ decreases and approaches 1, the post-shock wind is increasingly dominated by its radiative processes. The stars post-shock wind is assumed to be dominated by radiative processes if $\chi \leq 1$. In this case the gas cools rapidly after being shocked, leading to the formation of thermal instabilities. This is seen in Fig. 2.16, which compares a series of simulations with a wind momentum ratio of 0.02 and an increasing separation distance. As χ_{WR} decreases we see that the WCR shows clear signs of thermal instability, and an increasingly turbulent wind, in line with the predictions made in the equation. Instabilities can also be produced by other mechanisms, such as KH instabilities, through imbalanced wind velocities.

2. BACKGROUND

Based on this equation we can now infer that winds that are strongly radiative in the post-shock WCR environment are both slow¹ and dense. Therefore, we can infer that typically the WR stars wind behaves radiatively, while the OB star in a CWB system behaves adiabatically. Variability of χ can occur over a comparatively short timescale to the lifespan of the star due to the $\chi \propto d_{\text{sep}}^{-1}$ dependency. Whilst variation of v^∞ and \dot{M} for each wind will not vary significantly over the timescale of a single orbit, in the case of CWB systems with a highly eccentric orbit, the change in separation distance can cause χ to vary by up to two orders of magnitude.

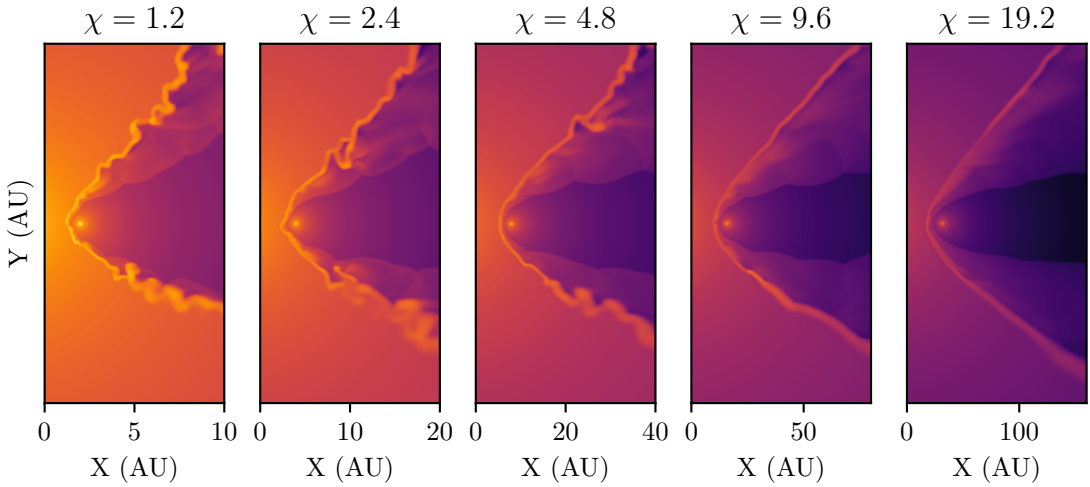


Figure 2.16: A comparison of the influence of radiative cooling on the structure of a CWB system. A system with a momentum ratio of $\eta = 0.02$ is simulated with an increasing orbital separation, such that χ increases. As can be seen the WCR becomes adiabatic and smooth the more χ_{WR} increases.

2.3.3.5 Dust cooling

Other radiative processes outside of gas/plasma cooling can influence the WCR. Interstellar dust can have a significant impact on cooling in dust producing CWB (WCd) systems. Collisional excitation and adsorption of photons can stochastically heat dust grains. This excess energy is then emitted in the form of infrared radiation (Dwek et al., 1996). The radiative emittance of a dust grain can be approximated as a black body, and hence radiates in accordance with the Stefan-Boltzmann law:

$$L = 4\pi r^2 \sigma T^4, \quad (2.30)$$

¹Comparatively, of course, we still observe winds travelling at almost 1% of c !

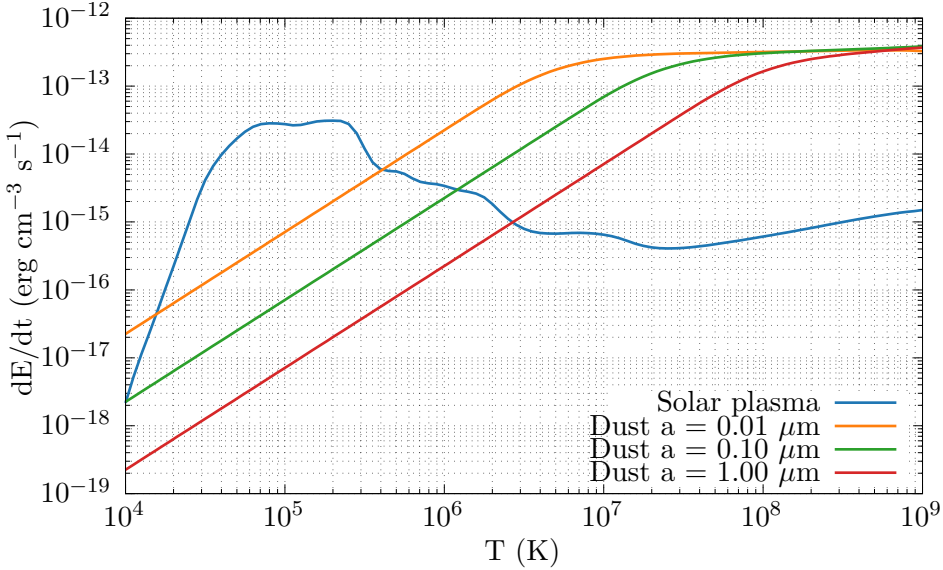


Figure 2.17: Comparison of plasma cooling to dust cooling with different grain sizes in a solar abundance gas, with a gas density of $10^{-20} \text{ g cm}^{-3}$ and a dust-to-gas mass ratio of 0.01.

where L is the grain luminance, r is the grain radius, σ is the Stefan-Boltzmann constant¹ and T is the grain temperature. At sufficiently high gas densities this radiative process can become the dominant cooling method in the ISM (Wolfire et al., 1995). In addition to this continuum emission, emission lines can also occur if characteristic vibrational modes in a grain lattice are excited, such as the silicate grain stretching and bending vibrational modes at $9.7 \mu\text{m}$ and $18.5 \mu\text{m}$ (Whittet, 2002, p. 212), as well as the $2,175 \text{ \AA}$ feature associated with PAHs (Draine, 2003). The presence of dust within the immediate post-shock environment significantly increases the cooling rate, but is dependent on more than just the number density of the gas and the temperature. In order to parametrise this, an energy loss rate, as formulated in Eq. 2.25 but for a volume of dust, \mathcal{L}_d is used:

$$\mathcal{L}_d(\rho_g, a, T) = n_d H_T(\rho_g, a, T), \quad (2.31)$$

where ρ_g is the gas density in the region, a is the grain radius, n_d is the number density of dust grains in the region and H_T is the average heating rate on a grain due to collisions with atoms, ions and free electrons. Fig. 2.17 compares \mathcal{L}_g for a solar abundance plasma and \mathcal{L}_d for dust within this plasma at varying grain sizes. At high temperatures we see that dust cooling is orders of magnitude more efficient.

¹ $5.670 \times 10^{-5} \text{ erg cm}^{-2} \text{ s}^{-1} \text{ K}^{-4}$.

2. BACKGROUND

Work by Dwek and Werner (1981) is used throughout this thesis to determine the rate of heating. Collisional heating of dust grains from either gas, plasma or free electrons is assumed to be the primary mechanism of heating, with dust grains radiating this collisional energy on timescales much shorter than the collisional timescale. It is found that the grain heating rate, H , can be calculated with the formulae:

$$H = \left(\frac{32}{\pi m} \right)^{1/2} n \pi a^2 (k_B T)^{3/2} h(a, T) \\ = 1.26 \times 10^{-19} \frac{n}{A^{1/2}} a^2 (\mu\text{m}) T^{3/2} h(a, T) \text{ erg s}^{-1} \quad (2.32)$$

where m is the grain mass, a is the grain radius, A is the mass of the incident gas particle in u, and n is the gas number density. $h(a, T)$ is the effective grain “heating factor”, or the fraction of the energy deposited into the grain through collision. The calculation of $h(a, T)$ was found to be difficult when simulating CWB systems. This is discussed in more detail in Section 3.6.5. Radiative heating is not calculated, as it is assumed that the dust grains are well shielded in the WCR from the UV emission of the parent stars. The contribution of heating due to each ion species and electron is individually calculated, and combined to find the total grain heating rate:

$$H_T = H_{\text{el}} + \sum_i H_i, \quad (2.33)$$

where H_i is the grain heating due to collisions from atoms and ions of an element, i . Whilst collision from atoms and ions is a somewhat important factor in grain heating, we find that the primary contribution of grain heating is due to electron-grain collisions. As can be seen in 2.18, heating due to electrons peaks between 10^5 and 10^6 K, with a ratio of contributions from electrons to ions of $\sim 100 : 1$. This is partially due to the increased electron number density, as the plasma can be multiply or completely ionised at higher temperatures. This is significant in the case of high-metallicity winds. However, above 10^6 K the electrons become less efficient at the heating of grains, resulting in a decreased influence in the overall grain cooling rate. The heating factor decreases as the electrons become too energetic, and can pass through the grain without significant energy transfer. This impact is especially important on small grains, as there is less material for the electrons to pass through.

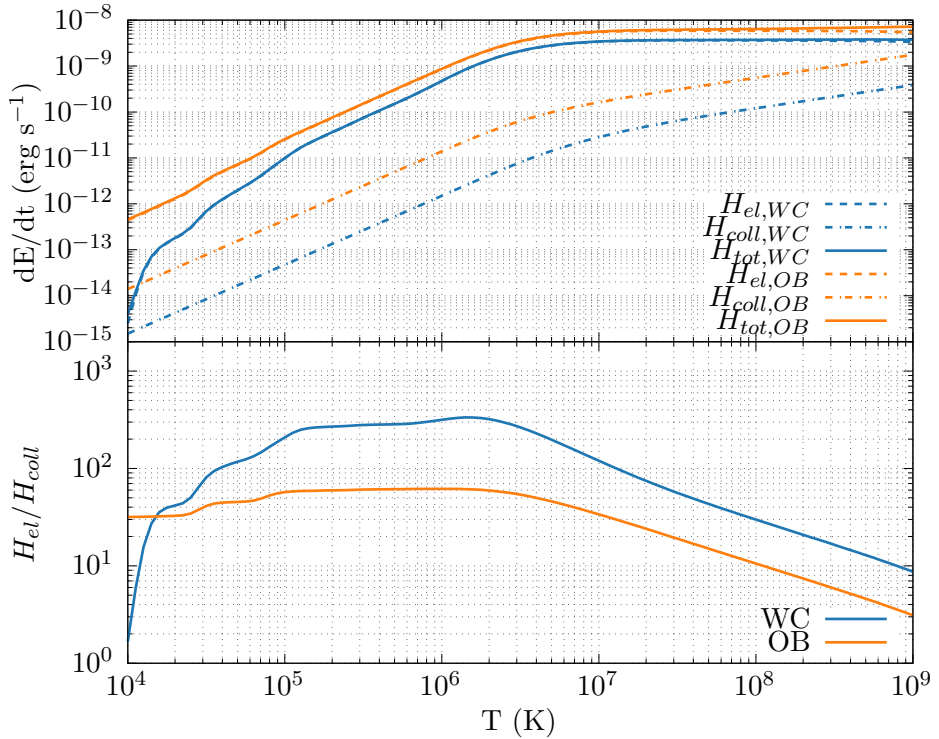


Figure 2.18: Comparison of grain heating rate due to ion collisional excitation, H_{coll} , and electron excitation, H_{el} . The dust grain has a grain radius of $5 \times 10^{-3} \mu\text{m}$ and is in a gas with a density of $10^{-20} \text{ g cm}^{-3}$ with solar and WC abundances.

2.3.4 Dust formation in CWB systems

Despite the extremely violent conditions thus far described in CWB systems, these systems appear to be extremely prolific producers of interstellar dust. Whilst single WC stars can produce small amounts of dust in the form of amorphous carbon grains (though this could be observed to be extremely rare, pending the results of Medina et al. (2021)), binary systems have been observed to convert more than 10% of their wind masses from ionised carbon into amorphous carbon dust grains¹. This can result in a dust production rate in excess of $10^{-6} M_{\odot} \text{ yr}^{-1}$, more than a typical AGB star. The dust production rate ranges from 10^{-10} to $10^{-6} M_{\odot} \text{ yr}^{-1}$ (Lau et al., 2020). Research by Zubko (1998) details dust growth around these regions. Grains were found to rapidly form from impinging carbon ions, up to grain sizes of approximately 100–200 Å. This dust forming behaviour has only been observed in cooler WC stars (predominantly WC9, with some WC7-8 examples). WN and WO systems have not been observed producing dust, this

¹In extreme cases.

2. BACKGROUND

is most likely due to amorphous grains being significantly more chemically stable and resilient to effects such as sublimation and photoevaporation than water ice or silicate grains (Draine & Salpeter, 1979a; Salpeter, 1977). Dust formation is also observed to form within the WCR, which can form quite beautiful pinwheel-shaped patterns, as dust streams away from the stars in the post-shock outflow.

	Persistent		Variable		Episodic	
	Total	Example	Total	Example	Total	Example
WC4	1	WR19	0	—	0	—
WC5	0	—	0	—	1	WR47C
WC6	1	WR124-10	0	—	0	—
WC7	3	WR102-22	0	—	4	WR140
WC8	6	WR13	1	WR48a	3	WR122-14
WC9	45	WR104	6	WR98a	1	WR75-11
Total	56		7		9	

Table 2.4: Number of confirmed WCd systems with known spectral type and dust formation type from the Galactic Wolf-Rayet Catalogue (Rosslowe & Crowther, 2015), systems with uncertain spectral types not included, while systems labelled “d” are included within the “persistent” category for their associated spectral type.

Whilst beautiful, Wolf-Rayet systems are elusively rare. The [Galactic Wolf-Rayet Catalogue](#)¹ (Rosslowe & Crowther, 2015) has a collection of 667² known galactic WR stars. 106 of such stars are contained within a binary system, with 41 such binaries containing WC stars. Rosslowe and Crowther (2015) notes that there are a total of 42 confirmed WCd systems, approximately 35% of all WC systems, though this value is somewhat out of date and includes single star systems. A more up-to-date estimate performed for this thesis using the updated dataset estimates a total of 80 WCd systems, of which 72 have well-determined spectral subtypes (Table 2.4 & Fig. 2.19). Rosslowe and Crowther (2015) goes on to estimate that out of an estimated total of 1,900 galactic WR stars, approximately 300 of these stars are predicted to be dusty WC stars. Whilst this is a far cry from the number of galactic AGB stars, which outnumber WCd stars by approximately 3 orders of magnitude (Ishihara et al., 2011), these systems can still significantly impact the surrounding interstellar medium – with strong stellar feedback propagating large quantities of dust into the surrounding medium.

Table 2.4 contains an excerpt of the observed WCd systems with clearly defined spectral subtypes. Most dust producing stars are either WC8 or WC9 subtypes, which are markedly cooler and less luminous than their WC4 counterparts. This reduced luminosity is potentially the driving factor for dust formation in the system. As WC8-9 systems have slower, cooler

¹<http://pacrowther.staff.shef.ac.uk/WRcat>

²At time of writing, with the last update being August 2020.

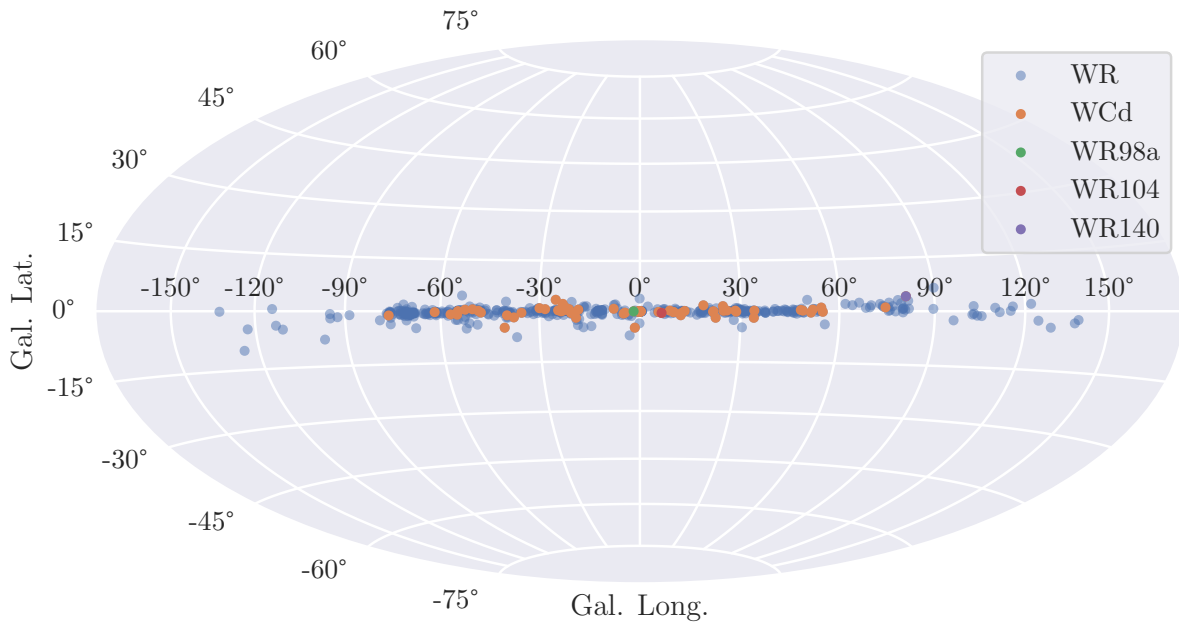


Figure 2.19: Map of WR stars on the galactic plane. WCd systems have been highlighted, as well as the simulated systems in this thesis, WR98a, WR104 and WR140.

winds (Niedzielski & Skorzynski, 2002), they are more strongly influenced by post-shock cooling, allowing for greater dust formation within the WCR. A small number of these systems have somewhat variable or episodic dust production cycles, such as WR98a and WR140, which are the two systems being simulated in this thesis. Furthermore, the bulk of WCd systems do appear to be in binary systems with a close periastron passage. In fact, the orbit appears to be a driving force behind how dust is produced in these systems, as we will later discuss.

A good starting point to understanding dust formation is to understand how the WCR can mitigate the mechanisms resulting in dust destruction, whilst aiding the processes involved in dust formation. As previously discussed, dust can be destroyed through high-velocity collisions with grains, as well as evaporation through heating or ionising radiation. These processes are mitigated through the cooling, as well as through the large amount of UV extinction due to the high density of the WCR. Meanwhile, the dust production rate increases within high density regions, as collisions between dust grains and gas occur at a much higher rate. The same can be said with dust grain cores, allowing for fast growth from gas and impinging ion accretion, and grain-grain collision as the number density of dust grains begins to increase. The accumulation of these effects results in a very fast initial growth rate, which tapers off as the post-shock region diffuses and expands.

2. BACKGROUND

The presence of instabilities driven by cooling and other factors leads to pockets of high density post-shock material. This can lead to “clumps” of highly dust-enriched post-shock stellar wind. These clumps would have additional protection from UV photons, and would also be cool enough for dust to form. Thus, the driving hypothesis for this theory is that these are regions where the bulk of dust formation would occur. Therefore, in order to achieve a high rate of dust formation, a dense, highly radiative post-shock WCR must be formed. As cooling in the post-shock region is dependent on separation distance, wind velocity and mass loss rate, these parameters should first be explored, with the knowledge gleaned used to direct an analysis of observed systems such as WR140.

Eccentricity is also theorised to play an important factor in the production of dust. We observe that highly eccentric systems can vary their dust production rates significantly. Fig. 2.20 shows the periodic change in mid-IR emission that can be explained as dust emission from small amorphous carbon grains, in the case of systems such as WR140 or WR125 dust production is periodically reduced to the point where associated emissions can drop by several magnitudes. This relation is clearly periodic, with a peak in dust production coinciding with the periastron passage of these systems. This implies that dust production is dependent on orbital separation, which will influence the degree of cooling occurring within the WCR, it could potentially also alter the wind velocity on collision, which will also influence dust production in the same manner. Further analysis of available dust producing CWB systems suggests that many WCd systems with circular orbits produce dust either persistently or with a degree of variability, while eccentric WCd systems solely produce dust episodically (Crowther, 2003; Williams, 2019).

2.3.5 Important WCd systems

The principle systems that are being simulated in this thesis are the variable dust forming system WR98a, and the episodic dust forming system WR140. The archetypal continuous dust forming system WR104 was also considered for simulation, but had to be cut due to time constraints. This system will also be discussed to provide a point of comparison between the two systems.

System	\dot{M}_{WR} ($M_{\odot} \text{ yr}^{-1}$)	\dot{M}_{OB} ($M_{\odot} \text{ yr}^{-1}$)	v_{WR}^{∞} (km s^{-1})	v_{OB}^{∞} (km s^{-1})	η	$\chi_{\text{WR,min}}$	\dot{M}_{D} ($M_{\odot} \text{ yr}^{-1}$)
WR98a	5.0×10^{-6}	5.0×10^{-8}	900	2000	0.0222	0.7970	$(6.10^{+1.77}_{-1.38}) \times 10^{-7}$
WR104	3.0×10^{-5}	6.0×10^{-8}	1220	2000	0.0033	0.2430	$(4.39^{+1.27}_{-0.97}) \times 10^{-6}$
WR140	5.6×10^{-5}	1.6×10^{-6}	2895	3200	0.0314	2.6866	$(8.11^{+4.83}_{-4.15}) \times 10^{-10}$

Table 2.5: Wind properties of systems considered for simulation in this thesis.

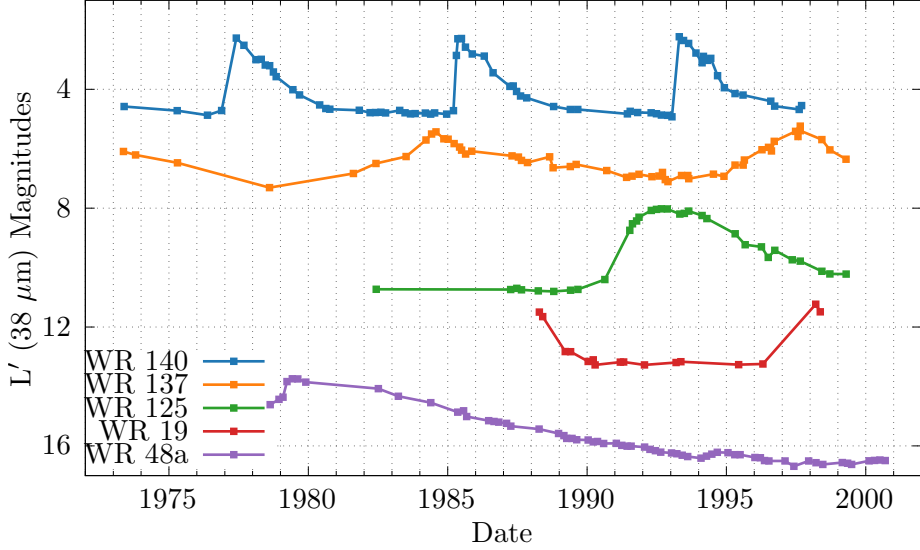


Figure 2.20: L' photometry for episodic dust making stars, data derived from Crowther (2003), and provided by PM Williams in private correspondence. WR140 and WR137 in particular have extremely predictable dust forming events which correspond to periastron passage in both systems.

System	Classification	Period (d)	Eccentricity (e)	Inclination (i)	M_{WR} (M_{\odot})	M_{OB} (M_{\odot})	Periastron (AU)	Apastron (AU)
WR98a	WC8-9+OB	556	~ 0	$35 \pm 6^\circ$	10.0	18.0	4.06	4.06
WR104	WC9d+B0.5V	245	0.0600	$\lesssim 16^\circ$	10.0	20.0	2.20	2.48
WR140	WC7+O5	2869	0.8993	$119.1 \pm 0.9^\circ$	10.31	29.27	1.53	26.9

Table 2.6: Orbital properties of systems considered for simulation in this thesis.

2.3.5.1 WR98a

WR98a (Fig. 2.21) was first found to be a WCd system by Monnier et al. (1999), and for a number of reasons was found to be an ideal candidate for simulation. WR98a was chosen for simulation primarily due to its moderate rate of dust formation, and comparatively docile winds. With a slow WC wind velocity of 900 km s^{-1} and a WC mass loss rate of $5 \times 10^{-6} M_{\odot} \text{ yr}^{-1}$, it has an overall WC wind momentum far lower than the other candidate systems. Because of this, the system has far lower dust production rates, and also exhibits some dust variability (Lau et al., 2020). Due to these factors the system is markedly easier to simulate, and thus provided a good starting point for our work as we refined the model and implemented features into the hydrodynamical system. A comparatively wide orbit reduces the number of cells required to simulate the system, as the WCR is easily resolved from the OB star, simplifying the simulation of the system further. Finally, WR98a has previously been simulated using a multi-fluid dust

2. BACKGROUND

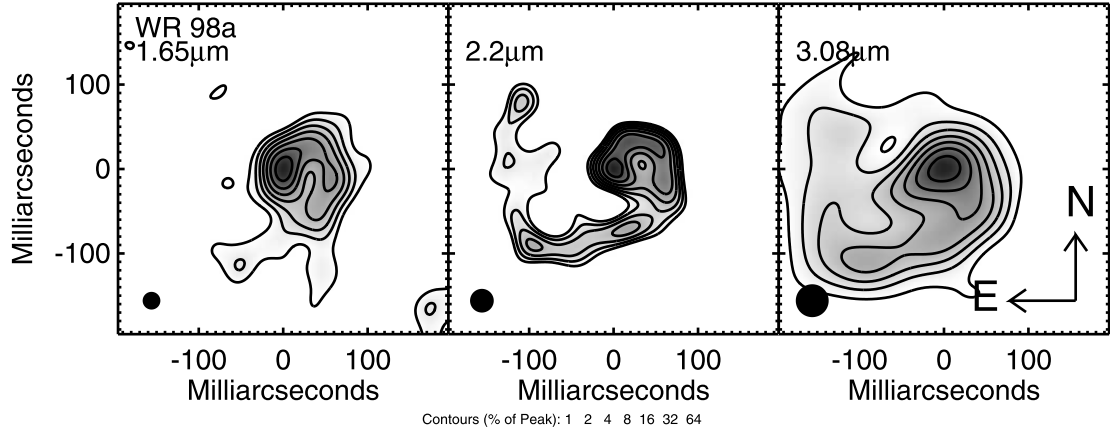


Figure 2.21: Multiwavelength aperture synthesis images of WR98a taken on June 24th 2000, at 1.65, 2.2, and 3.08 μm . Plot sourced from Monnier et al. (2007), the significant IR excess is a clear sign of ongoing dust production. The system also has a pronounced pinwheel structure most prominent at 2.2 μm .

model in Hendrix et al. (2016), this allows us to provide a point of comparison between our work and already published work. This is especially useful as there are only a handful of papers that cover dust models in CWB systems. Because of this relative ease of simulation and relatively slow wind velocity for both stars in the system, WR98a was chosen to be the baseline system for the research conducted in Chapter 4 (Eatson et al., 2022a).

2.3.5.2 WR140

WR140 is significant in that it is the first system observed with episodic WCd properties. Williams et al. (1978) noted a rapid brightening in the infrared, suggesting the formation of a new shell of dust around the system. WR140 has been observed many times over the years, with spectroscopic data dating back to 1972, and is perhaps the most well-observed episodic WCd system. With its eccentricity of $e = 0.8993$, the separation between the stars – and therefore χ – vary by a factor of 17.6 from apastron to periastron. Therefore it is an ideal system to verify that our dust model can naturally handle episodic dust forming systems, as well as to determine which parameters affect an episodic system.

As it is a highly eccentric system with a particularly long period orbit, a number of difficulties present themselves. Firstly, the system has a much longer orbital period than the other systems being considered, as such, a complete orbit would take a long time to simulate as well. Secondly, this requires a corresponding increase in resolution, as the WCR needs to be sufficiently resolved at periastron. Whilst refinement methods such as adaptive mesh refinement (AMR) would alle-

viate these issues somewhat, we found that the current version of the `Athena++` hydrodynamical code lacked stability with passive scalars in AMR. This issue was deeply embedded in `Athena++`, and as such could not be fixed by the end of this PhD. Instead, it was decided to only simulate the system as it undergoes closest approach, from $\phi = 0.95$ to $\phi = 1.10$ (Chapter 5; Eatson et al., 2022b).

2.3.5.3 WR104

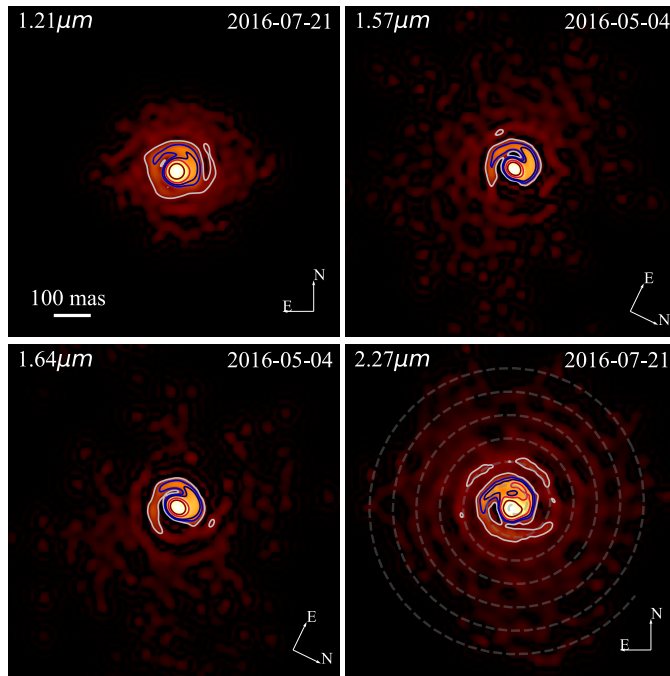


Figure 2.22: Deconvolution of J, H, K, and $2.27\mu\text{m}$ bands of WR104 sourced from Soulain et al. (2018). The spiral pattern and first revolution is visible in all images, in particular at $2.27\mu\text{m}$.

WR104 (Fig. 2.22) is an archetypal example of a continuous WCd system. It is a comparatively tight binary with a semi-major axis of 2.34 AU and a period of ~ 241 days. The system also has a relatively circular orbit, with an eccentricity of $e = 0.06$ (Lamberts et al., 2012). WR104 consists of a WC9 star with a B0.5V partner (Williams & van der Hucht, 2000); this combination of a WC star and a comparatively weak B partner results in a severely imbalanced wind. We estimate a wind momentum ratio of 0.003, an order of magnitude lower than WR98a. This imbalanced wind – combined with the tight orbit – results in an extremely IR bright WCR that is constantly churning out dust. Using radiative transfer models, Harries et al. (2004) calculated a dust production rate of $(8 \pm 1) \times 10^{-7} M_{\odot} \text{ yr}^{-1}$, corresponding to 2% of the total

2. BACKGROUND

mass loss rate of the system. A more advanced model by Lau et al. (2020), which is used to assess the dust formation rates of systems in this thesis, calculated the dust formation rate to be $(4.39^{+1.27}_{-0.97}) \times 10^{-6} M_{\odot} \text{ yr}^{-1}$. This is one of the most prolific dust forming systems found by Lau et al. (2021), and as such is an ideal example of a continuous dust forming system. There are a number of reasons for this prodigious dust formation rate. As the system's orbit is comparatively close and circular with a very dense primary wind, the wind is expected to be highly radiative throughout the entire orbital period, this suggests a cool post-shock WCR, which continuously produces dust.

The system is relatively close, at a distance of 2.5 kpc, and is almost face-on relative to earth, meaning that the pinwheel structure is clearly observed (Soulain et al., 2018; Fig. 2.22). Due to the system parameters, well defined dusty pinwheel structure, and prior observations and simulations of the system, it was found to be an ideal candidate for simulation.

Despite being a very strong candidate for simulation, however, attempting to simulate the system proved to be exceptionally difficult. The very close orbit of the system would mandate a very high simulation resolution, increasing the amount of processing time required to finish the simulation. Only simulating a small region would prevent the pinwheel from being formed and observed, which we would have ideally wanted to include. In addition the strong radiative cooling resulted in a test simulation being very unstable unless the Courant number was exceedingly small. As timestep is governed by the Courant number, this would significantly increase the time needed to simulate the system. With a limited amount of compute resources as well as a limited amount of time, this stretched the feasibility of simulating this system. As the wind from the primary star is significantly stronger than its partners, WR104 has a much lower momentum ratio than the other systems being considered, and the WCR is situated much closer to the secondary star. At closest approach, $r_{\text{OB}} \approx 60 R_{\odot}$, which would require WR104 to be simulated at a much higher resolution, in turn further increasing computational requirements. Physical effects, such as radiative inhibition and sudden braking may also significantly alter the wind velocity and post-shock environment, reducing the pre-shock primary wind velocity (Gayley et al., 1997). The pre-shock secondary wind velocity would also be influenced, due to insufficient acceleration from line driving before the winds collide. As radiative line driving is not simulated these effects cannot be taken into account, and would have resulted in an inaccurate simulation of the system. Sudden braking in highly wind-imbalanced systems is discussed more substantially in section 3.6.1.

With limited time remaining in the project, as well as the above factors, simulation work on WR104 was abandoned in favour of a parameter space search of a system with baseline

properties similar to WR98a, as well as a limited simulation of WR140.

Simulating this system however, is a particularly enticing avenue of future research.

2.3.6 WR+WR systems

Recently, two candidates of a theorised subset of CWB have been discovered: WR+WR systems. These double WR systems have a secondary stellar wind around 3 orders of magnitude denser than a WR+OB system. This would of course results in truly titanic wind collisions. These candidates are the recently discovered WR70-16 (Callynham et al., 2019), and the previously discovered WR48a system (Danks et al., 1983), which exhibits the spectroscopic lines of both a WC and WN system (Williams, 2019). These systems are predicted to be comparatively rare, even among CWB systems. This is due to the unlikelihood that both stars in the system would be in their Wolf-Rayet phase at the same time. Despite these systems having an enormous combined mass-loss rate, initial estimates of the dust production rates of both systems indicate that their dust conversion efficiencies are comparatively low compared to less energetic systems, and overall quite mundane dust production rates in general. Whether this suppressed dust production rate is a common phenomena among WR+WR systems remains to be seen, as more systems would need to be discovered in order to determine this. Extragalactic WR+WR binaries have also been detected in the Magellanic clouds, though all detected systems so far have been found to be WN+WN pairs, which are not known to produce dust (Shenar et al., 2019).

2.3.6.1 WR70-16 (“Apep”) – a recently discovered WR+WR system

A potential avenue of research for this field is the simulation of WR+WR systems such as the recently discovered WR70-16 (Fig. 2.23) system (hereafter referred to as “Apep”). This system was discovered due to the significant difference between the spectroscopically derived wind velocity of $(3,400 \pm 200) \text{ km s}^{-1}$ and the observed expansion speed of $(570 \pm 70) \text{ km s}^{-1}$ (Callynham et al., 2019). This inhibited wind velocity, far below any categorised WR wind velocity, suggests that much of the wind undergoes collision with the wind of a binary partner. The extremely luminous non-thermal and infrared emission, suggested two extremely high mass loss rate stars within the system, as well as evidence for a third, distant partner in a loose triple system (Callynham et al., 2020). Spectroscopic analysis suggested that the central component of the Apep system consists of a nitrogen sequence WN4-6b and a carbon sequence WC8 star, with the more massive and luminous WN4-6b star kinematically dominating the system. This discovery is very significant as it was the first galactic WR+WR system discovered – and is only

2. BACKGROUND

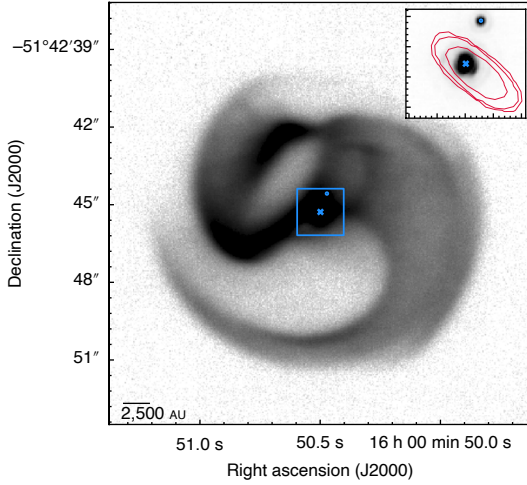


Figure 2.23: A VLT image of Apep (Callingham et al., 2019), a recently discovered WR+WR system with a WN primary and WC secondary star. This class of system presents an interesting avenue of future research; though these systems are extremely rare.

one of two galactic WR+WR systems. Other systems have been identified, but are extragalactic in nature.

Further work by Han et al. (2020) has estimated the orbital parameters of Apep, finding that it is a highly eccentric system with a period of (125 ± 20) yr and an eccentricity of 0.7 ± 0.1 , inclined at $\pm 30^\circ \pm 5^\circ$ towards Earth. An initial estimate of the dust formation rate was made, finding a dust production rate of $\sim 5 \times 10^{-7} M_\odot \text{ yr}^{-1}$, while observation of the surrounding dust shell suggests that it is a periodic dust forming system, which is sensible considering the systems high eccentricity. The opening angle of the WCR was found to be very wide, at $125^\circ \pm 10^\circ$, further suggesting the presence of two very high mass loss rate objects within the system due to a balanced wind momenta. Additional calculations by Marcote et al. (2021) estimated the systems wind momentum ratio to be 0.44 ± 0.08 , again in line with the WR+WR hypothesis. Finally, del Palacio et al. (2022) finds a mass loss rate of $4 \times 10^{-5} M_\odot \text{ yr}^{-1}$ for the WN star and $2.9 \times 10^{-5} M_\odot \text{ yr}^{-1}$ for the WC star, which all but confirms the presence of a WR+WR binary at the heart of the Apep system.

With an estimated combined mass loss rate of $6.9 \times 10^{-5} M_\odot \text{ yr}^{-1}$ we estimate that the system has a dust conversion efficiency of 0.7%. Whilst this system is therefore not a prodigious producer of dust, this is most likely due to the extremely high wind terminal velocity and high separation distance, which would suggest a fairly smooth and adiabatic post-shock region. We can estimate the cooling parameter of the system to be ~ 80 , based on the angular separation from Han et al. (2020), confirming that at present, the winds are adiabatic. It is most likely the

case that the system is highly elliptic, and is currently dormant in a similar manner to WR140 is for most of its orbit. In order to estimate the closest approach of the system, and therefore the minimum cooling parameter an accurate measure of the stellar mass of both objects would need to be made. There is insufficient data for this at the time of writing.

2.3.6.2 WR48a – revisiting a WR+WR candidate

WR48a is a system that was previously considered to be a CWB system with a WR primary star and an unknown secondary star (Zhekov et al., 2014). Recently, however, it has been reclassified to a WR+WR system, with a dust forming WC8 and a WN8 partner (Williams, 2019; Zhekov et al., 2022). This change in classification is contemporaneous with the discovery and classification of Apep, though there is a distinct lack of recent observations of this system compared to the newer, more exciting WR+WR candidate. Lau et al. (2020) calculated a dust formation rate for WR48a of $(8.46^{+3.48}_{-4.38}) \times 10^{-8} M_{\odot} \text{ yr}^{-1}$ with a dust conversion efficiency of 0.12%, markedly less than other systems with much less available material. A future avenue of research would be to simulate these systems to understand why the dust formation rate is comparatively low, despite the readily available stellar material. The main difficulty of simulating these systems is the lack of orbital parameters and accurate mass loss rates. As WR48a has insufficient data and Apep has only been recently discovered, there are currently too many unknown factors in order to build an adequate simulacrum of the systems¹. Another difficulty is the large degree of orbital separation, high eccentricity and long orbital timescales required to simulate these systems. The current limitations of the hydrodynamical code being used in this project render it difficult to simulate entire orbital passes of highly elliptical systems with long periods. If these issues are resolved in later versions of the hydro code however, this would present an interesting avenue of future research.

2.4 Summary

In this chapter, we have discussed the underlying physics of this thesis, from star formation to dust production, before discussing the crux of this project, the colliding wind binary. However, we must discuss the mathematical and computational aspects of our work before discussing our simulations and results. In the following chapter we shall do this, discussing our model and

¹A lack of accurate orbital parameters is a significant issue in devising simulations for more conventional WR+OB systems

2. BACKGROUND

methodology in detail.

CHAPTER 3

Methodology & Numerical Simulation

3. METHODOLOGY & NUMERICAL SIMULATION

Observational astrophysics is a field based on snapshots. The universe can be thought of as a near-infinite number of laboratory experiments that are viewed by astronomers from a fixed perspective. Additionally, most phenomena evolve over incredibly long timescales. It may in some cases take the entire lifetime of a researcher to collect enough information on a single system – in other cases, they may be long dead before their predictions can be validated. Despite this, by observing many systems at once we can overcome this limit, piecing together the properties and formation of phenomena from a thousand disparate snapshots in space and time. This kind of “natural parallelisation” has historically worked extremely well – but has its limitations. And in situations where it doesn’t work numerical simulation can step in.

Numerical simulation is a relatively recent method of research; only within the last two decades has computing hardware been up to the task of simulating 3D environments. Numerical simulation has proven itself vital, however, for gaining insight on regions that are hard to observe. The WCR of a CWB system is extremely difficult to observe, and as such, we can turn to simulation in order to understand these regions better. Unfortunately, many aspects of a CWB system are also comparatively difficult to simulate, as we will discuss.

As mentioned in the introduction to this thesis, theoretical astrophysics straddles two complex fields, astrophysics and computer science. While we have discussed the underlying physics and physical phenomena of this project, we have so far neglected to cover the simulation side of this work. Some astrophysicists reading this thesis may be unfamiliar with the computational side of the work, while computer scientists would be unfamiliar with the astrophysics. As such it is best to describe both in detail. Furthermore, discussing our methodology in its own section consolidates it and makes it easier for the reader to understand and replicate it. In particular: we will discuss numerical simulations and why they are utilised in this thesis, as well as the development and implementation of a CWB model inside the *Athena++* hydrodynamical code. We also detail our attempts to implement radiative cooling, as well as our advected scalar dust model, *BIDMAS*.

3.1 The History & Mathematics of Numerical Simulations

In astrophysical fluid dynamics, the most fundamental of equations are the Euler equations. These are a specific case of the more general Navier-Stokes equations of fluid dynamics, covering the case of an inviscid fluid lacking thermal conductivity. These properties make the equations ideal for application to astrophysical fluids. At vast length scales the aggregate properties of a collection of molecules in near vacuum essentially behave as an inviscid fluid. Because of

3.1 The History & Mathematics of Numerical Simulations

the general lack of physical contact the influence of thermal conduction and convection on the fluid are ruled out. Astrophysical fluids at first appear strange and unintuitive compared to the familiar terrestrial fluid dynamics that we have a more innate understanding of. However, if one zooms out enough and starts thinking in terms of parsecs and astronomical units, some similarities do appear, such as instabilities, turbulence and shocks.

In a one-dimensional adiabatic case, with a fluid of density, ρ , a velocity of u , a fluid pressure, P , and a total energy per unit volume, E , the Euler equations take the form:

$$\frac{\partial \rho}{\partial t} + \frac{\partial}{\partial x}(\rho u) = 0, \quad (3.1a)$$

$$\frac{\partial \rho u}{\partial t} + \frac{\partial}{\partial x}(\rho u^2 + P) = 0, \quad (3.1b)$$

$$\frac{\partial E}{\partial t} + \frac{\partial}{\partial x}[u(E + P)] = 0. \quad (3.1c)$$

As the Euler equations are a non-linear series of partial differential equations, no general analytical solution exists, to make it worse, numerical solutions aren't exactly easy either. The most fundamental method of numerically solving such problems is Godunov's scheme (Godunov, 1959); this scheme is a finite-volume method wherein the simulation domain is split into a series of cells, with a Riemann problem between the interfaces of each cell. The Riemann problem is composed of a series of conserved variables on each side of a discontinuity (see Fig. 3.1). A solution to the Euler equations can then be made by solving all of these Riemann problems in sequence and integrating across a time-step, dt . The problem can be simulated and solved by marching through many time-steps until the required simulation time is achieved. This provides a first-order accurate approximation in a more general form, compared to the otherwise intractable set of PDEs. Whilst this piecewise method of solving many thousands of Riemann problems may provide a more generalised method of solving the Euler equations than the non-linear partial differential form, solving them by hand would invoke a terrible strain on a mathematician's wrists.

Godunov's novel method, however, coincided with the burgeoning field of computer science. Computers are extremely well suited to this type of calculation, and can solve Riemann problems many orders of magnitude faster than any mathematician. Furthermore, solving a higher-dimensional problem is a conceptually trivial extension to the original 1-D problem. In the 2-D case the number of interfaces per cell increases to 4, with each interface being the analogous to each side of a square or rectangle, while in the 3-D case the interfaces can be thought of as the 6 faces of a cuboid. As such, the general formulation of the Euler equations becomes:

3. METHODOLOGY & NUMERICAL SIMULATION

$$\frac{\partial \mathbf{U}}{\partial t} + \nabla \cdot [\mathbf{F}(\mathbf{U})] = 0, \quad (3.2)$$

where \mathbf{U} is a vector of conserved variables and $\mathbf{F}(\mathbf{U})$ is a vector of the corresponding fluxes of the conserved variables:

$$\mathbf{U} = \begin{bmatrix} \rho \\ \rho u \\ E \end{bmatrix}, \quad \mathbf{F}(\mathbf{U}) = \begin{bmatrix} \rho \mathbf{u} \\ \rho u \mathbf{u} + P \\ \mathbf{u}(E + P) \end{bmatrix}. \quad (3.3)$$

Whilst this extension is trivial, in practise solving higher-dimensional problems are significantly more computationally intensive. This is due to the increased number of interfaces and the exponentially increased number of cells required to simulate the problem.

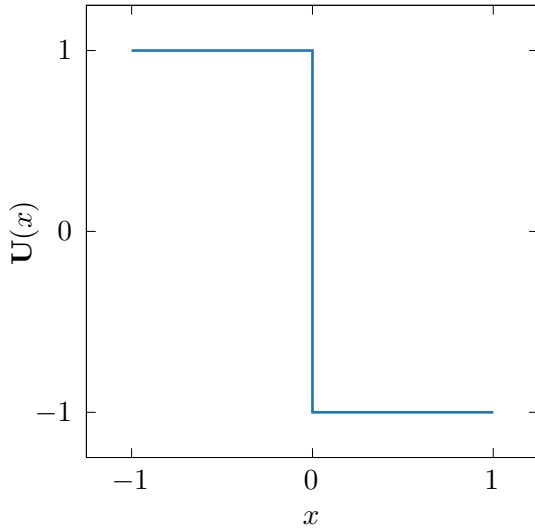


Figure 3.1: The initial conditions of a Riemann problem of $\mathbf{U}_L = 1$ and $\mathbf{U}_R = -1$, where \mathbf{U} is an arbitrary conserved variable. A discontinuity is present between the left and right sides of the problem, at $x = 0$.

Initial methods involved exact solutions to the Riemann problems, however, this is a time consuming method. Instead, approximate methods were developed to improve numerical performance. However, early methods were less exact, and could not preserve the contact surface, these methods were also markedly less stable, limiting their effectiveness. Later models, such as the Harten-Lax-van Leer-Contact (HLLC) solver (Toro et al., 1994) are approximate solvers that offer a similar order of accuracy to the exact solution, while being significantly faster than

3.1 The History & Mathematics of Numerical Simulations

the exact solution and more numerically stable than earlier approximate solvers. As such, this method is commonly used in hydrodynamical codes, and is used throughout this project.

Godunov's method is commonly used as a base for higher-order extensions, which employ methods to interpolate and reconstruct the flow between the interfaces of each Riemann problem. Piecewise linear methods linearly interpolate the fluid state between cells to reconstruct the fluxes at the cell interfaces, this is generally considered to be significantly more versatile than a simple piecewise constant method (van Leer, 1979). The piecewise parabolic method performs a parabolic interpolation step instead across a multitude of cells. This is generally more accurate for a smooth and continuous flow, but most scheme must account for and detect discontinuities – otherwise they might be smoothed out (Colella & Woodward, 1984). Throughout this project we utilise the piecewise linear method, which is the default for `Athena++`.

In order to solve the problem, the fluxes along each cell interface are integrated over a timestep. In the case of this project, two distinct types of Runge-Kutta (RK) method are used. The integration timestep is typically much smaller than the overall simulation time. As such, many timesteps are required. With n spatial dimensions and 1 time dimension, it is clear how computationally intensive hydrodynamical simulations are. This timestep must be carefully calibrated to ensure that the duration of the integration step is less than the time taken for a fluid to advect through to an adjacent cell. If a clump of gas travels across two adjacent cells in a single timestep, for instance, the interaction occurring in the middle cell would be lost, and unphysical behaviour would occur. This is especially a problem in the case of highly supersonic flows, where the fluid is moving extremely fast. This problem is further compounded with multiple dimensions, which must all be accounted for in a similar manner. The Courant-Friedrichs-Lowy (CFL) condition determines that the maximum integration time should not be higher than the time taken for a fluid to advect between adjacent cells in a numerical grid. With this condition we can define the CFL number, C , which is the ratio between the wave propagation speed, u , and the grid speed, $\Delta x/\Delta t$. For multiple dimensions, the CFL number is calculated with the formula

$$C = \Delta t \sum_{i=1}^n \frac{u_{x_i}}{\Delta x_i}, \quad (3.4)$$

where Δt is the timestep, u_{x_i} is the velocity of the fluid along a spatial dimension, i , and Δx_i is the cell spacing for each spatial dimension (Toro, 2013, Ch. 5). Hydrodynamical codes typically allow the user to define C such that the code can calculate the necessary timestep. For instance, in the case of a three-dimensional problem, Δt is found to be

3. METHODOLOGY & NUMERICAL SIMULATION

$$\Delta t = C \left(\frac{u_x}{\Delta x} + \frac{u_y}{\Delta y} + \frac{u_z}{\Delta z} \right)^{-1}. \quad (3.5)$$

For an explicit time-integration problem such as numerical simulation, the value of C is typically ≤ 1 , with the timestep decreasing with additional dimensions for a given value of C . For 3-dimensional problems in this thesis, we typically start at $C = 0.15$, and decrease if necessary. It is important to note that there is also a constraint due to the sound speed of the fluid, c_s . As such, for highly hypersonic flows the timestep should be reduced further.

Numerical simulations - whilst extremely processing intensive - are a class of problems that are considered to be *embarrassingly parallel*. A hydrodynamical problem can be divided into a series of smaller problems and solved independently for a common timestep. These numerical grids must be checked for concurrency at the interfaces between grids, which introduces some overhead to the parallelism, but on the whole is significantly faster than a single-threaded method. This subdivision can be performed through striping along one of the dimensional axes, with stripes distributed to a specific processor (as performed by **MG** and **VH1**¹). Another method for parallelism is reducing the entire problem to a series of blocks that are solved in parallel (performed by **Athena++**). Other enhancements to numerical simulation include mesh refinement, which is covered in more detail in Section 3.5.

3.2 The Purpose of Numerical Simulations

Numerical simulations, thanks to their generalised but calculation-intensive approximation of partial differential equations, have an enormous range of uses – especially in the field of astrophysics. Numerical simulations particularly excel in modelling large timescales and regions that are otherwise difficult to observe.

For instance, the laws of physics have remained consistent over the last 13.8 billion years², and as such simulations have been performed of the early universe. The dynamics and collapse of the universe into filaments and galaxies provides our only continuous look into the long-term evolution of the universe.

Regions that undergo too much extinction from dust or that are too distant to observe can also be simulated, as long as a reasonable estimation of the initial system parameters can be

¹<https://wonka.physics.ncsu.edu/pub/VH-1/>

²With some earlier exceptions, see cosmological inflation.

3.2 The Purpose of Numerical Simulations

made. Numerical simulation, in a sense, fills in the gaps and weaves together the many snapshots of the universe we have made from our vantage point in the cosmos.

I must stress, however, that this is not me screwing my simulationist hat firmly onto my head and claiming that theoretical astrophysics is inherently superior to observational astrophysics. Whilst an immensely versatile and useful weapon in an astrophysicists arsenal, numerical simulations are almost entirely reliant on the understanding of the laws of physics as we know them. The remainder of that reliance rests on the ability of the programmer, and on the assumptions and initial conditions of the simulation. In the case of poor assumptions and parameters, we find that the computer scientist idiom of “garbage input, garbage output” begins to apply.

Colliding wind binaries are a class of astrophysical phenomena that have a particularly strong dependence on numerical modelling in order to study them. The WCR is extremely difficult to observe for a variety of reasons:

- The nearest WCR are typically over 1 kpc away, and the structure is comparatively small, on the order of a few AU.
- The structure can also be obscured by the parent stars, which are typically brighter in the optical and UV spectra.
- In some cases, the WCR is extremely dense, leading to significant reddening and extinction.
- Dense winds from the WR star can also worsen extinction.

Observation of the large-scale dusty structure of the WCR is possible with current telescopes, and the surrounding dust cloud (and pinwheel structure in the case of persistent WCd systems) has been observed in multiple WCd systems (Callingham et al., 2019; Soulain et al., 2018). However, observation of the compact dust forming region is far more difficult. In most cases, a telescope with an angular resolution $< 50 \mu\text{as}$ would be required to resolve the region, ruling out even the highest resolution instrumentation. Thus, numerical simulation is a requirement. Implementation of a dust model in order to analyse how dust growth occurs within the region can also be performed and compared to observational estimates. Radiative transfer models can also be used to model the dust production rate of these systems¹.

CWB systems, however, are difficult to *simulate* as well!

Numerical simulations are vastly simplified by reducing the number of dimensions. Single object systems can be reduced to 1-D spherically symmetric or 2-D cylindrical axisymmetric

¹However, this was not feasible given the difficulties of this project.

3. METHODOLOGY & NUMERICAL SIMULATION

representations. This is the case in earlier simulations of supernovae and jets. Simulations of CWB systems are possible with cylindrical symmetry, but inclusion of orbits will negate the effects due to orbital motion, such as pinwheel formation. The apex of the WCR must be properly resolved from either of the stars, in the case of systems with imbalanced winds this can result in a cell width, Δx , of $< 1/100^{\text{th}}$ of the orbital separation¹. Ideally, to simulate a CWB system, it is preferable to simulate a large domain, typically 100 AU to 1,000 AU. This further increases the number of cells required to simulate the system. Finally, the extreme degree of cooling in the post-shock WCR can render the simulation unstable, requiring robust cooling techniques or very small timesteps to ensure stability. All of these factors enact a significant computational cost, requiring a large number of cores to effectively simulate the systems. Fortunately, mesh refinement techniques can improve this situation by drastically reducing the number of cells that need processing; simplifying our problem from *impossibly* intensive to *extremely* intensive.

3.3 The MG Hydrodynamical Code

Initially this project intended to use the MG hydrodynamical code, as CWB systems had already been simulated, and the resultant code being readily available within the department.

MG also had a number of features that were useful for this project, such as MPI parallelism and adaptive mesh refinement. It was initially estimated that it would take little more than a year to implement the dust and cooling models; with large-scale simulations on the ARC3 and ARC4 computers being commenced mid-way through the second year of research.

How wrong we were!

Unfortunately the advected scalar dust model never adequately worked in MG. When implemented in MG, the dust model either produced dust rates measurable in grams per year, or the simulation rapidly converted all gas into dust. Attempts to implement the dust model through modification of the conserved variables or through a rate-based source function were made, with many different implementation attempts. None of these panned out, resulting in a large amount of work being discarded. Using strict constraints to prevent rigorous dust production resulted in strange looking systems that did not behave as observations suggested. Furthermore, building a model that relied on dozens of constraints based on limited empirical data is rarely a good model, and is analogous to building a clock without a driving mechanism – such that it is at least right twice a day.

¹This value is derived from experimentation, and can vary for certain simulations, such as those of WR104.

3.3 The MG Hydrodynamical Code

In addition to incompatibility with the dust model, numerous technical issues also meant that MG was unsuitable for the work in this thesis. Mapping the wind onto the CWB also proved difficult when combined with AMR, as the provided implementation of wind remapping required a circular region with a radius of 3 coarse cells. In order to get the required separation for systems with close orbits, a very high coarse resolution would be required, massively increasing memory usage and removing the benefits of mesh refinement. Using a source function for wind mapping allowed for more refined cells to be used. This could also produce artefacts at level transitions, however, while also producing wind temperatures of the order 10^7 K.

While being very extensible in terms of being able to implement a problem generator fairly easily, low-level manipulation of the MG source code was found to be extremely difficult due to limited documentation and a complex, linked-list grid structure. Writing workarounds and fixes to the issues described was very time-consuming, slowing progress in the project significantly. Iteration time was also extremely long, requiring multiple hours to run a simulation to determine if the fixes worked. Debugging was rendered difficult by the use of OpenMPI, and the general structure of the code rendered the setting of breakpoints difficult even in the single-threaded case. Finally, the numerical integrator was found to be unstable in the face of extremely radiative cooling environments. Complex multi-step cooling processes were considered and implemented, but even these could not handle such rapid cooling without breakdown if a reasonable Courant number was to be used. The solution to this was to artificially limit cooling to a fraction of the energy in the cell per timestep. This reduced the simulation accuracy, and resulted in much slower cooling within the post-shock WCR¹.

In the end, the decision was made to switch from MG to the then-new **Athena++** hydrodynamical code. This decision was made in mid-2020. By the end of 2020 the problem generators were built, the necessary modifications to the underlying code of **Athena++** were completed and the dust model was fully implemented. What began next was a frenzy of activity in order to assure that there was sufficient data to complete this project in time.

¹I understand, reader, that this section reads like a series of complaints... This is because it is. I recommend that you humour me, as attempting to debug MG ate up more than two years of my life and was the direct cause of many, *many* sleepless nights. Thankfully this is the last time we will ever speak of it, unless you and I share a pint or two at a local pub.

3. METHODOLOGY & NUMERICAL SIMULATION

3.4 The Athena++ hydrodynamical code

The [Athena++¹](#) hydrodynamical code was found to be a much more suitable fit for this project. **Athena++** is a total re-write of the older Athena MHD code in C++ focussing on adding adaptive mesh refinement, source code clarity, modularity, and improved performance (Stone et al., 2020). This clarity and modularity allowed us to port our dust model and CWB problem from MG to **Athena++** in a few months. The hydrodynamical problem is defined at compile time, and as such ensures there is no overlapping code from other problem generator codebases. As such we were able to rapidly iterate and build a new version extremely quickly.

Multiple time-integration and spatial reconstruction methods are implemented into **Athena++**. The time-integration method can vary from a computationally simple 2nd order van Leer (van Leer, 1979) method to strong stability preserving methods (Ruuth & Spiteri, 2005) to super time-stepping Runge-Kutta-Legendre methods (Meyer et al., 2014). Changing of the time-integration method can be implemented without recompilation, and can even be changed upon restart of an in-progress simulation. This was useful in the case of simulations where lowering the CFL number of the simulation did not improve stability. For this project either the 3rd order accurate strong stability preserving Runge-Kutta method (`rk3`) or the 4th order accurate, five-stage, 3 register, SSPRK method (`ssprk5_4`) were utilised – depending on the instability of the simulation. The `rk3` method was found to be more than twice as fast as the `ssprk5_4` method in the case of a CWB system (Table 3.1), though could crash in the case of rapid cooling and dust production. In the case of a simulation crashing multiple times, the simulation would be run from the nearest checkpoint using `ssprk5_4`. While there were some concerns regarding numerical dispersion and diffusion by changing integrators mid-simulation, this was found to not influence the simulation significantly. **Athena++** must be recompiled for the specific spatial reconstruction method, as the number of overlapping “ghost” cells needs to be defined at compile-time. For this project the piecewise linear method was utilised, as this was sufficiently fast and stable. The Riemann solver can also be changed at compile-time, however this was left to the default solver, the Harten-Lax-van Leer-Contact (HLLC) solver (Toro et al., 1994).

Athena++ has exceptional parallel performance, with our tests indicating a parallel fraction of > 98% (see Appendix B.2). Large scale weak-scaling testing by Stone et al. (2020) found an 80% parallel efficiency after overhead and memory bandwidth bottlenecks. Parallelism through block-based division of the numerical problem is utilised, dividing the problem into a regular array of sub-volumes containing a defined number of $X \times Y \times Z$ cells. This is referred to as a “meshblock”,

¹<https://github.com/PrincetonUniversity/athena>

Integrator	Elapsed Time	Relative Time	Simulation Time
<code>rk3</code>	1,444.6 s	100.0%	5.467×10^5 s
<code>ssprk5_4</code>	2,352.4 s	163.1%	5.542×10^5 s

Table 3.1: Benchmarking of the `rk3` and `ssprk5_4` integrators. A simulation of WR140 was conducted for 1,000 timesteps. We find that the `rk3` model is significantly faster. Tests were conducted on an Intel Xeon Gold 6152 workstation and compiled with `GCC 4.8.5` with the `O3` optimisation set.

and are distributed to the processing cores available to the programme in order to be solved in parallel. Meshblocks are encoded in an octree structure, as the relationship between parent and child blocks must be preserved in order for mesh refinement to work correctly. In comparison to MG, the linked-list method is comparatively slow on modern hardware, as the larger caches in newer processors can store arrays contiguously, while linked-lists require fetching elements from RAM. Athena++ uses both OpenMP and OpenMPI for parallelism. These two methods can be leveraged in a hybrid shared/distributed memory parallelism scheme, which scales well to the thousands of processing cores available on ARC4. To prevent numerical errors from occurring between the interfaces between meshblocks, “ghost cells”, or cells from adjacent meshblocks copied into the current meshblock, are used. In this work, the two outermost layers of cells in a meshblock are distributed to the processing nodes solving adjacent meshblocks. Typically, 128 cores were used for each simulation, as this represented a good trade-off in processing throughput and node availability, as ARC4 is a heavily utilised resource.

3.5 Mesh Refinement

A problem previously discussed with modelling CWB systems is that the apex of the WCR is extremely small relative to the system itself. As such we must resolve an area approximately 4-5 orders of magnitude smaller than the overall domain of the simulation. For a 3-D simulation this results in an effective resolution of 10^9 cells or higher. In the case of the more ambitious simulations in this project, a region approximately 1,000 AU was defined, with an effective resolution of approximately 1.07×10^{12} cells. This amount of data is difficult to *store*, let alone *compute*, and was far beyond the capabilities of any computing resources available to the project. As the spacing between cells is reduced, the maximum stable timestep decreases as well, in accordance with the CFL condition, worsening the computational requirements.

Algorithms such as adaptive mesh refinement, first discussed by Berger and Oliger (1984) and expanded upon by Berger and Colella (1989), start with a much lower resolution “coarse” mesh, and refine specific parts of the simulation. At each step each cell is tested against pre-

3. METHODOLOGY & NUMERICAL SIMULATION

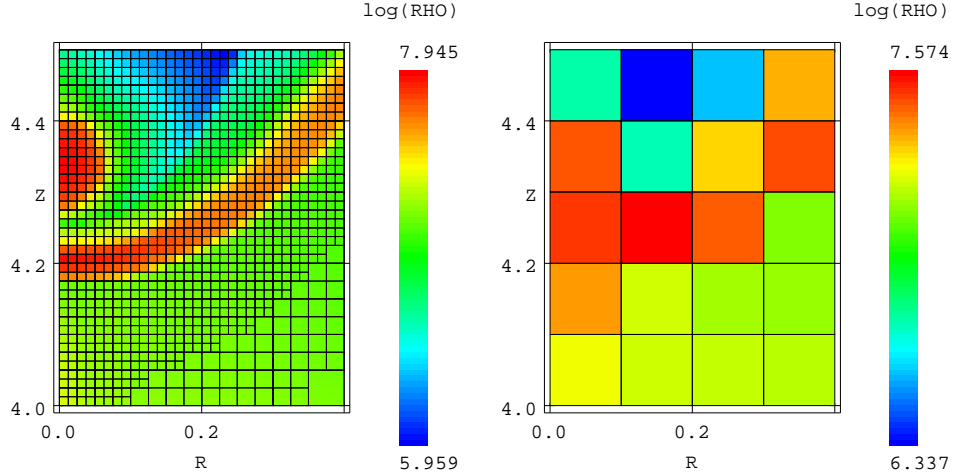


Figure 3.2: An example of adaptive mesh refinement in the MG hydrodynamical code around the OB star in a colliding wind binary problem using cylindrically symmetric co-ordinates. With AMR the WCR is properly resolved, while without the system cannot adequately resolve the WCR.

defined conditions, such as the proximity to an object in the simulation, a conserved parameter or the truncation error between lower and higher level. If the cell passes these tests, it is flagged for refinement. Truncation error in particular, is a useful general purpose refinement criteria, and is used as the refinement mechanism in MG (Fig. 3.2). Refinement occurs at the end of a simulation step, splitting the cell in half along each simulation dimension. The effective dimensional resolution of a simulation with n levels is given by the formula

$$x_{\text{AMR}} = x_{\text{coarse}} \cdot 2^{n-1}, \quad (3.6)$$

where x_{coarse} is the number of cells along the dimensional axis at the lowest level, $n = 0$. In the case of a CWB simulation, this would ensure the region inside the orbit of the star and the WCR would be correctly resolved. Care must be taken not to over-refine the simulation or to rapidly refine and de-refine a region. The former can be mitigated by defining a maximum refinement level, while the latter can be mitigated by defining a minimum number of timesteps required for a cell to be repeatedly flagged for refinement and de-refinement. Another issue with this method is multiple refinements per timestep for a cell, which can cause the simulation to crash.

Athena++ implements mesh refinement by refining and de-refining meshblocks. The refined blocks are stored as children of the coarser, higher level parent meshblock in the meshblock octree. In order to test the efficacy of this implementation, a double Mach reflection simulation

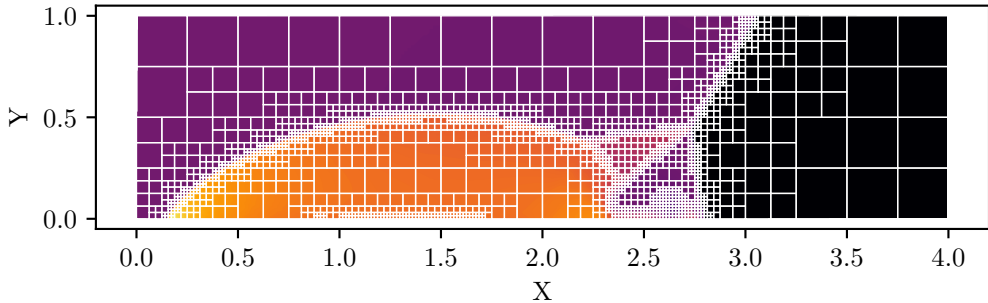


Figure 3.3: An example of AMR usage in `Athena++`. A double Mach reflection test with a meshblock size of 16×16 cells and 5 levels. Meshblock interfaces are represented by grid lines.

was configured with 2-D Cartesian symmetry and a coarse grid resolution of 256×64 cells and 5 refinement levels. This was compared to a grid not undergoing refinement, with a resolution equivalent to the effective simulation of the AMR grid simulation of (4096×1024) cells (See Fig. 3.3). Both simulations were run for 10^4 timesteps, and benchmarked with `hyperfine` to derive an average runtime while accounting for I/O and shell latency. The results are detailed in Table 3.2, where we find a significant speedup and reduction in cell count and memory usage. The resultant numerical results were effectively identical. Whilst there is some overhead from the refinement mechanism and redundant calculation of coarser numerical grids, the method is easily more performant. The performance advantage of AMR scales significantly better with additional dimensions, as a greater amount of the simulation can potentially be refined at a lower resolution.

	Cells	Memory Usage	Cells/s	Wall time	Speedup
No AMR	4,194,304	$\sim 2,502$ MiB	4.42×10^7	(969.00 ± 2.90) s	—
AMR	201,472	~ 330 MiB	3.77×10^7	(82.277 ± 0.400) s	1,178%

Table 3.2: Time taken to simulate 10^4 timesteps of a double mach reflection test when AMR is disabled and enabled. AMR significantly increases performance without a significant amount of overhead. Test was conducted a dual-socket 2.1 GHz Intel Xeon Gold 6152 workstation with 44 cores and compiled with GCC 4.8.5 with the `03` optimisation set. Benchmarking was conducted with `hyperfine`.

Unfortunately, there is a known issue with `Athena++`¹ which prevents the use of AMR with advected scalars enabled. Scalar values are not conserved properly around meshblock interfaces, which can rapidly escalate and result in physical inaccuracy and breakdown of the simulation (Fig 3.4). As there was ultimately no time to address this bug, the decision was made to persist with using static mesh refinement (SMR) for the work in Chapter 5, despite a version of the

¹<https://github.com/PrincetonUniversity/athena/issues/365>

3. METHODOLOGY & NUMERICAL SIMULATION

code already being written with AMR in mind. Refinement for CWB systems was intended to ensure a minimum of 128 cells separating the stars, while also refining regions around the current position of each star, and the predicted wind collision region. Beyond these refined regions steady de-refinement over distance would occur.

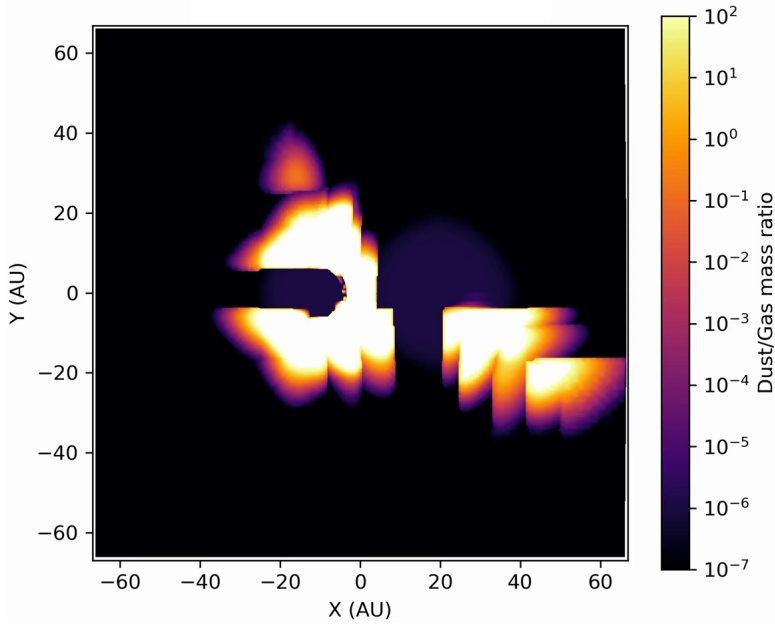


Figure 3.4: An example of scalar conservation breakdown in `Athena++`. Continuity is not preserved for scalars between block interfaces and levels, resulting in incorrect behaviour, such as there being more dust than gas within the simulation.

SMR is a significantly simpler method of refining cells, where a region is defined when initialising the simulation which is refined to a higher level. The code will then progressively de-refine meshblocks beyond this region until the coarsest level is reached. This method is much less flexible, and is less efficient, but is still useful for simulations where a small region requires a higher spatial resolution at all times. In the case of CWB systems this is a reasonably good approximation, as the region around the orbit of the stars can be refined to a higher resolution, while progressively de-refining further out from the barycentre (Fig. 3.5). For the previously mentioned 1,000 AU simulation with 1.07×10^{12} cells, naïvely refining a region around 1.5 times the orbital separation from the barycentre with 7 refinement levels resulted in a reduction to 1.55×10^6 cells, a 6 order of magnitude reduction in cell count and memory usage. As such, SMR was found to be suitable for our simulations, as a fix was not available for AMR from the `Athena++` developers at the time of computation.

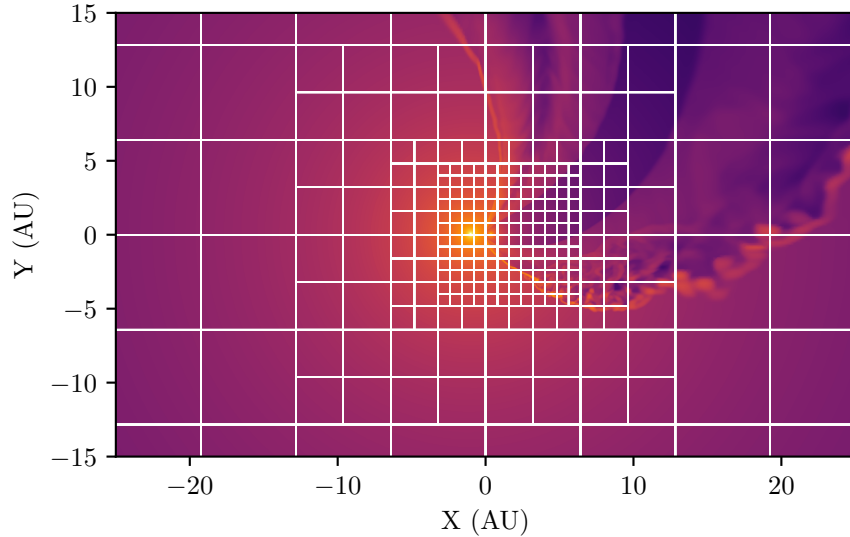


Figure 3.5: An example of SMR usage in **Athena++**. A simulation of WR140 was generated with a bounding box around the orbit of the stars at periastron. Within this bounding box the simulation is refined 4 numerical levels deeper than the coarse resolution, and is de-refined based on distance from the bounding box. The overlaid grid represents individual meshblocks with a resolution of $40 \times 40 \times 10$ cells.

3.6 Simulating CWB systems

As stated in an earlier section, a numerical simulation is only as accurate as its assumptions and input data. Our goals for the simulation of dust producing CWB systems throughout this project are as follows:

- Two stars are produced and orbit each other with eccentricity e and period P based on star masses M_{WR} and M_{OB} .
- The stars should produce a user-defined outflow of wind with mass loss rate \dot{M} and terminal velocity v^∞ .
- The outflowing wind must be of a pre-defined metallicity, and cool through radiative processes such as forbidden lines, recombination and resonance line emission.
- Dust should be able to condense in dense, cool regions.
- The resultant dust grains should be able to grow and shrink in accordance with grain growth and grain destruction mechanisms.

3. METHODOLOGY & NUMERICAL SIMULATION

- The dust should also be able to cool through collisional excitation and subsequent radiative emission.

As well as the following goals and targets for the model itself:

- All radiative processes should be accurate, but not make up a significant fraction of the overall processing time of a cell.
- The dust model should be highly modular, and capable of implementing new growth and destruction mechanisms in the future.
- The model should be reliable and stable if presented with sensible initial conditions.
- Code should be well documented and easy to understand in order to streamline future work from other researchers.

These goals were achieved, and improvements to the current model have been considered for future implementation. Initially a multi-fluid model for dust was considered, but could not be implemented due to time constraints. For future research this would improve accuracy significantly, for a variety of reasons that will be discussed.

In this section we will discuss how the systems are simulated, as well as the assumptions made and specific optimisations made in order to accomplish this task.

3.6.1 Assumptions

There are a number of assumptions imposed for both the stellar winds and dust within the simulation. First, it is assumed that the outflow velocity of the stars is greater than the system escape velocity, v_{esc} . We also assume that the self-interaction dynamical timescale of the winds are significantly larger than the timescale of the fluid leaving the numerical domain. Based on these two assumptions, gravitational self-interaction and interaction between the outflow and the stars is not simulated. This significantly reduces processing time, as gravitationally self-interacting fluids are very computationally complex. Another assumption is that the outflow from each star is rapidly accelerated to the star's wind terminal velocity, v^{∞} . This negates the need for simulating radiative line driving effects on the stellar wind, or calculating the CAK parameters for each wind. However, this can result in over-estimation of the wind collision velocity if the wind momentum is sufficiently imbalanced, or if the apex of the WCR is close

to the secondary star. If the wind velocity is sufficiently reduced this can affect the structure of the wind collision region, as the wind momentum ratio and wind cooling parameter, χ , will be changed. Additional factors such as sudden radiative braking can also affect the primary star, where in the case of an extremely unbalanced wind, the primary stellar wind can become rapidly decelerated as it approaches the secondary star and its radiative flux is more influential than the driving force of the parent star (Gayley et al., 1997). This should be considered when analysing the results of each simulation, and understanding how the secondary wind velocity can affect the cooling and dust production rate of the WCR. It is also assumed that all energy radiated leaves the simulation, with no subsequent re-adsorption. This assumption is valid in the case of mid and far-IR radiation, which is the predominant radiation method in the cool, dense post-shock region. Whilst re-adsorption and subsequent re-emission would significantly increase the complexity of the simulation, as the effects of radiative transfer would have to be calculated.

Finally, a number of assumptions are made for the dust model. We assume that the number density of the dust grains is constant, such that the net amount of grains being shattered and grains being agglomerated is zero. As gas-grain sputtering and coagulation are significantly more common processes and do not change the number density, this is a reasonable assumption considering the dust evolution mechanisms currently implemented and the limitations of an advected scalar model. We assume that grain growth occurs below 14,000 K, which is below the sublimation temperature of carbon dust grains. Conversely, we assume that dust destruction processes are not significant until the gas temperature is above 10^6 K, when a micron sized grain has a lifespan of $\gtrsim 10^7$ yr in a flow with a density of 1 g cm^{-3} and the destruction rate begins to reach its maximum (see Fig. 2.9). We also assume grain growth due to grain-gas accretion is approximately 10% efficient, which is a conservative estimate for grain growth, and could be as high as 100% in the case of uncharged dust grains (Spitzer, 2008, Ch. 9).

3.6.2 Stars, wind propagation & refinement

Stars are implemented as point masses, with their orbital positions and velocities governed by Keplerian dynamics. A solver for the orbital motion was written to calculate the positions of the stars relative to a barycentre at simulation position $(0, 0, 0)$ at the start of every timestep. The orbital method is 2 dimensional, with both stars at $z = 0$ and with no z axis orbital motion. The solver includes a Newton-Raphson approximation method for improved accuracy. As there are only two gravitationally interacting bodies in the system, it was deemed unnecessary to

3. METHODOLOGY & NUMERICAL SIMULATION

implement a more complex n-body gravitational system to model the dynamics of the stars. As the orbital path of the system is already known, this also allowed the use of a “phase offset” to change the starting point of each simulation, such as in the case of the WR140 simulation, which begins at $\Phi = 0.95$.

With the assumption that winds are rapidly accelerated to v^∞ , propagating stellar winds through a simulation has been drastically simplified. In the simulation, the conserved variables inside a small spherical region 6 fine cells in radius are modified in order to inherent the parameters of a stellar outflow, with a mass loss rate of \dot{M} and a wind velocity of v^∞ radially outwards from the star. The modified conserved variables in this “remap zone” correspond to the formulae:

$$\rho_R = \frac{\dot{M}}{4\pi r^2 v^\infty}, \quad (3.7a)$$

$$p_R = \rho_R v^\infty, \quad (3.7b)$$

$$E_R = \frac{P_R}{\gamma - 1} + \frac{1}{2} \rho_R v^\infty{}^2, \quad (3.7c)$$

where ρ_R is the remap density, p_R is the remap momentum, E_R is the remap energy, r is the radial distance from the star, P_R is the cell pressure and γ is the ratio of specific heats (typically 5/3). Whilst this method is very fast and effective, it requires the remap region to remain completely undisturbed, if the WCR impinges upon the remap region this will result in significant physical inaccuracy. In order to mitigate this, it was found that there should be 75 fine cells separating the stars for a system with $\eta \sim 0.01$ ¹. For systems with a WCR closer to the secondary star the number of cells should be higher.

Throughout this thesis SMR is used to increase the effective resolution of simulations. A box around the CWB orbit is refined to the highest level defined in the simulations input file, **Athena++** de-refines the cells gradually around this box until the simulation is at its coarsest resolution.

3.6.3 Cooling in numerical simulations

As discussed in section 2.3.3, there are many cooling processes that need to be considered when simulating a complex system such as a CWB. In particular, this is due to the wide temperature

¹This was determined experimentally.

3.6 Simulating CWB systems

range within the WCR. We have also discussed that sufficient cooling is essential to the dust growth process. Gas temperature in the immediate post-shock region can exceed 10^8 K, far beyond the temperatures required to destroy dust, as any nascent grains would quickly be shattered by thermal processes. There is sufficient evidence to suggest that significant, rapid temperature loss occurs in the post-shock regime, the high metallicity of the WC wind and high number density of atoms and ions makes it the ideal region for rapid cooling due to radiative processes.

Another boundary to dust formation due to an insufficiently radiative post-shock flow is a lack of sufficient downstream density. In the case of strong shocks (where the Mach number, $M \gg 1$) that are adiabatic, constraints are set on the downstream gas parameters of the system such that:

$$u_b = \frac{1}{4}u_a, \quad (3.8a)$$

$$\rho_b = 4\rho_a, \quad (3.8b)$$

$$P_b = \frac{3}{4}\rho_a u_a^2, \quad (3.8c)$$

$$T_b = \frac{3}{16} \frac{\mu m_H}{k_B} u_a^2, \quad (3.8d)$$

in a reference frame co-moving with the shock – where a is the upstream side and b is the downstream, post-shock side. As the gas density can only be a factor of 4 larger than the post-shock flow, the post shock density (even if it were at temperatures suitable for dust formation) is insufficiently dense for sufficient dust production. However, in a radiative shock behaving isothermally (where the temperature change, ΔT throughout the entire lifespan of the fluid is equal to zero), the final density, ρ_f can be approximated with the formula

$$\rho_f \approx \gamma M_a^2 \rho_a, \quad (3.9)$$

where M_a is the pre-shock mach number. For a shock with $M_a = 100$ the final density can exceed the pre-shock density by a factor of 10^4 !

Performing radiative cooling within a numerical simulation is computationally difficult, and trade-offs between accuracy and performance must be considered at every step of designing the simulation, as every single cell must undergo cooling. For this project, the final cooling can be out by a few percent at worst, but is fast enough to run the simulations in a reasonable amount

3. METHODOLOGY & NUMERICAL SIMULATION

of time without excessive memory requirements. In order to simplify the radiation calculations, radiation does not re-interact with the simulation, instead it is completely removed from the simulation. Due to this, scattering, re-adsorption and radiative transfer are not simulated at all¹. Other methods of reducing computational cost and optimising the code are used in this project, and will be described in detail in this section.

3.6.4 Plasma cooling

Cooling due to radiative emission of gas and plasma is a very complex topic, and has to factor in multiple mechanisms of emission, which are heavily dependent on the elemental abundance of a wind. Cooling codes such as MEKAL are used to calculate the emissivity, Λ , of a wind given the current temperature, abundance and density (Mewe et al., 1985; Mewe et al., 1986). However, these codes are somewhat computationally complex and difficult to solve for every cell at every timestep. As such, this step is abstracted away by the use of a lookup table. This lookup table is pre-calculated from MEKAL and SPEX data and loaded into the simulation at runtime. Lookup tables for solar and WC abundances are generated by combining a series of lookup tables generated for pure flows of elements, and combined based on the abundance of the element within the stellar wind. A typical lookup table in this project utilises logarithmically spaced temperature bins from 10^4 K to 10^9 K, with 101 bins in total. If the calculated temperature is between bins a linear interpolation step is used to improve the accuracy of the emissivity solution. In order to calculate the energy loss from the normalised emissivity stored in the lookup table, the following formula is used

$$\mathcal{L}_g = \left(\frac{\rho}{m_H} \right)^2 \Lambda_g(T), \quad (3.10)$$

where $\Lambda_g(T)$ is the normalised emissivity at the cell temperature, T . This solution is orders of magnitude faster than performing an emissivity calculation in every cell, and is essential to performing fast hydrodynamical simulations with plasma radiative cooling.

Other optimisations relied on replacing a naïve linear search with an indexing method that relied on the uniform logarithmic spacing of the temperature bins. Instead of performing a search, we can calculate the index, n , of the closest bin that is cooler than the cell temperature with the formula

¹If these are considered, your programme is now a ray-tracing programme as well as a hydrodynamical code, which is its own, even more complicated field.

$$n = \left\lfloor \frac{\log_{10}(T) - \log_{10}(T)_{\min}}{\delta \log_{10}(T)} \right\rfloor, \quad (3.11)$$

where $\log_{10}(T)$ is the log of the cell temperature, $\log_{10}(T)_{\min}$ is the minimum log temperature in the lookup table and $\delta \log_{10}(T)$ is the log spacing of the temperature bins. The closest hotter temperature bin has an index of $n + 1$, and a linear interpolation step can be used to calculate an approximate value of $\Lambda_g(T)$:

$$\Lambda_g(T) \approx \Lambda_n + (T - T_n) \frac{\Lambda_{n+1} - \Lambda_n}{T_{n+1} - T_n}. \quad (3.12)$$

This speed-up is fairly significant as the average search performance changes from $\mathcal{O}(n)$ to $\mathcal{O}(1)$ time, a marked improvement over even a binary search, which would resolve in an average of $\mathcal{O}(\log n)$ time. In the case of a 101-bin array this is only a minor speed-up, but with the sheer number of calculations being performed, any optimisation to a function used multiple times per cell can significantly improve performance. In the case of larger, or multi-parameter lookup tables this method would only improve in performance, and is a good example of general optimisation in a numerics programme.

In order to integrate the energy loss rate to determine the exact amount of energy lost within a timestep, an integration method needs to be chosen. For this project, a fast, first-order Euler method with multiple sub-steps was chosen. Whilst this method is typically not known to be very accurate compared to higher-order methods, it was found to be fast, and the adaptive sub-step method was found to calculate a reasonably accurate approximation of a cells change in temperature in a very small amount of time. This sub-step method is elaborated on in section 3.6.6.

3.6.4.1 Other calculation methods

Other methods of refining the emissivity value were also considered, such as fitting a local curve to the data or using a spline-based interpolation step instead of a linear step. However these were only marginally more accurate, while significantly increasing calculation time. An exact cooling method was also considered, which was found to be significantly more performant but had a series of limitations that prevented it from being used in the codebase. This exact cooling method, described by Townsend (2009), introduces a temporal evolution function (TEF), $Y(T)$, into the solution, which describes a measure of the total time required to cool from an arbitrary temperature to T . This function, as well as its inverse, need to be calculated prior

3. METHODOLOGY & NUMERICAL SIMULATION

to the start of simulation, but do not have to be calculated for every cell and timestep. While solving the TEF for the cell temperature takes approximately the same amount of time as a single first order Euler method integration, an *exact* calculation of the post-step temperature is found. This scheme is a rare example of a numerical method that is both accurate *and* fast, taking approximately the same time as a second order explicit method overall, whilst also being perfectly accurate even in highly radiative hypersonic flows. Unfortunately this method has a number of limitations that precluded its usage in this project. First, this method would not have been able to accurately model mixed wind situations, hampering its usage in cooling winds with different abundances. Second, and most importantly, dust cooling could not have been modelled with this single parameter TEF method, which would have required using a two stage cooling method. As the gas temperature would not be synchronised between stages, this would have resulted in a highly inaccurate cooling solution, obviating the advantages of the exact cooling method.

3.6.5 Dust cooling

We discussed in Section 2.3.3.5 that photon emission from dust is primarily due to grain heating through collisional excitation, which in turn causes the heated grain to emit radiation in a method approximating a black body. This produces an approximately continuous spectra, dependent primarily on the grain size, grain temperature and number density of particles in the surrounding fluid.

Gas and plasma emissivity for a wind of a specific elemental composition is only dependent on temperature, $\Lambda_g(T)$, with a corresponding energy loss rate of $\mathcal{L}_g(n_H, T) = n_H^2 \Lambda_g(T)$. This is convenient for the sake of calculating gas cooling, as the calculation of the emissivities of thousands of emission lines and multiple radiative mechanisms across a temperature domain from 10^4 K to 10^9 K would be exceedingly computationally demanding. Instead, we can use a lookup table, as described in the previous section. Unfortunately, while the calculation of emission rate of a dust grain is simpler and does not depend on many discrete calculations, it is dependent on more parameters, which can change per cell. We find that the energy loss rate due to dust is calculated by the formula:

$$\mathcal{L}_d = n_d H_T(\rho_w, a, T), \quad (3.13)$$

where H_T is the total grain heating rate due to collisions from electrons, atoms, and ions, while ρ_w is the wind density. Therefore, in order to calculate energy loss due to dust emission, we

must either build a far more complex lookup table, or determine methods of calculating energy loss quickly. In this section we will discuss the pros and cons of both methods, and discuss the final methodology used in this project.

When debating whether or not to include a feature in a numerical simulation, we must weigh up the computational cost versus necessity of inclusion. In the immediate post-shock environment we find that the cooling rate due to dust is significantly higher than the cooling due to gas and plasma ($\mathcal{L}_g < \mathcal{L}_d$) by approximately a factor of five (Fig. 3.6). Dust cooling therefore can play an important role in the initial cooling of the post-shock cooling, resulting in faster cooling to temperatures suitable for grain growth. As such, dust cooling should ideally be included in these simulations.

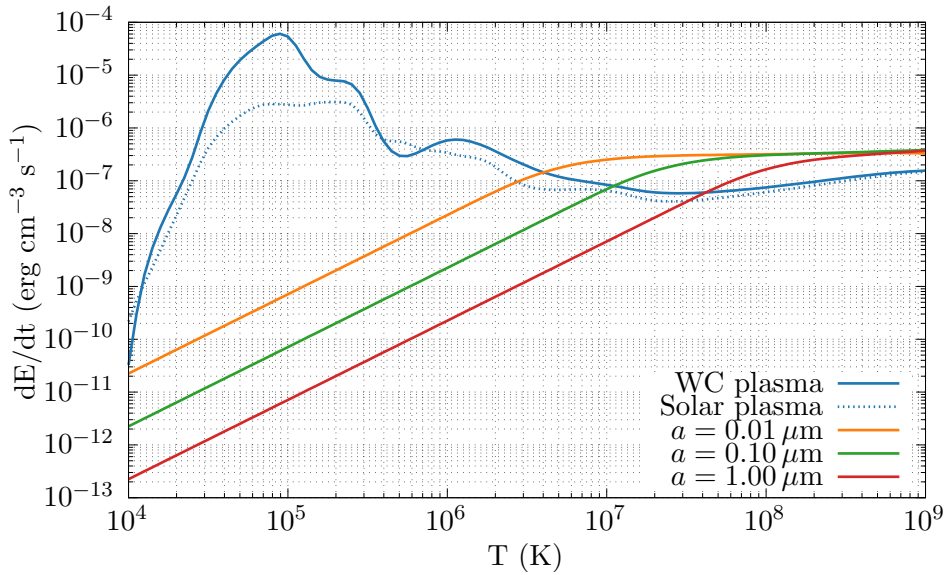


Figure 3.6: Comparison of energy loss due to plasma & dust cooling with varying grain sizes in a typical post-shock flow, where $\rho_g = 10^{-16} \text{ g cm}^{-3}$ and a dust-to-gas mass ratio of 10^{-4} . Whilst less influential at lower temperatures, dust cooling can aid cooling in the immediate post-shock environment.

Throughout this project, we utilise the Dwek and Werner (1981) prescription for dust radiation emission. In the case of a dust grain of radius a flowing through a pure elemental gas with an atomic mass m and a number density n , we find the grain heating rate, H , to be

$$H = \left(\frac{32}{\pi m} \right)^{1/2} n \pi a^2 (k_B T)^{3/2} h(a, T) \\ = 1.26 \times 10^{-19} \frac{n}{A^{1/2}} a^2 (\mu\text{m}) T^{3/2} h(a, T) \text{ erg s}^{-1} \quad (3.14)$$

3. METHODOLOGY & NUMERICAL SIMULATION

where A is the atomic mass of the gas in AMU and $h(a, T)$ is the effective grain heating factor. This last parameter, also referred to as the grain “transparency”, is the fraction of the energy deposited from the field particle onto the grain. We can then calculate H_T using the equation

$$H_T = H_{\text{el}} + H_{\text{coll}}, \quad (3.15)$$

where H_{el} is the grain heating due to electrons and H_{coll} is the grain heating due to atom and ion collisions. Atoms and ions are grouped as the grain is assumed to be uncharged. For solar and WC abundances elements heavier than oxygen are effectively trace – as such we simplify H_{coll} throughout this thesis to be

$$H_{\text{coll}} = H_{\text{H}} + H_{\text{He}} + H_{\text{C}} + H_{\text{N}} + H_{\text{O}}. \quad (3.16)$$

In order to determine $h(a, T)$ we define a critical energy, E^* , which is the amount of energy required by a field particle to penetrate the grain. This critical energy varies depending on the atom and the grain size, and was calculated by Dwek and Werner (1981) in the case of an uncharged grain to be

$$E^* = \begin{cases} 23 a^{2/3} & \text{for electrons,} \\ 133 a & \text{for hydrogen,} \\ 222 a & \text{for helium,} \\ 665 a & \text{for C, N \& O,} \end{cases} \quad (3.17)$$

where a is in microns. The grain transparency can then be calculated using the formula:

$$h(a, T) = \begin{cases} 1 - \left(1 + \frac{E^*}{2k_B T}\right) e^{E^*/k_B T} & \text{for atoms and ions} \\ 1 - \frac{e^{x^*}}{2} \int_0^\infty \mathcal{K}(x^*, z) dz & \text{for electrons,} \end{cases} \quad (3.18)$$

where

$$\mathcal{K}(x^*, z) = (z + x^*) \left[(z + x^*)^{3/2} - x^{*3/2} \right]^{2/3} e^{-z}, \quad (3.19)$$

$x^* = E^*/k_B T$ and z is an arbitrary value.

Performing an indefinite integral inside of a hydrodynamical code is not ideal, and must be either constrained or simplified in such a way that it can be made performant. Additionally, electron-grain heating cannot be discounted, as it typically outweighs atom-grain heating by more than two orders of magnitude (see Section 2.3.3.5 & Fig. 2.18). Another factor in determining the contribution due to free electrons was determining the free electron number density, which can vary significantly with temperature in a highly metallic wind.

We trialled two methods involving solving the integral, before settling on using an approximation described in Dwek and Werner (1981).

3.6.5.1 Integration Method

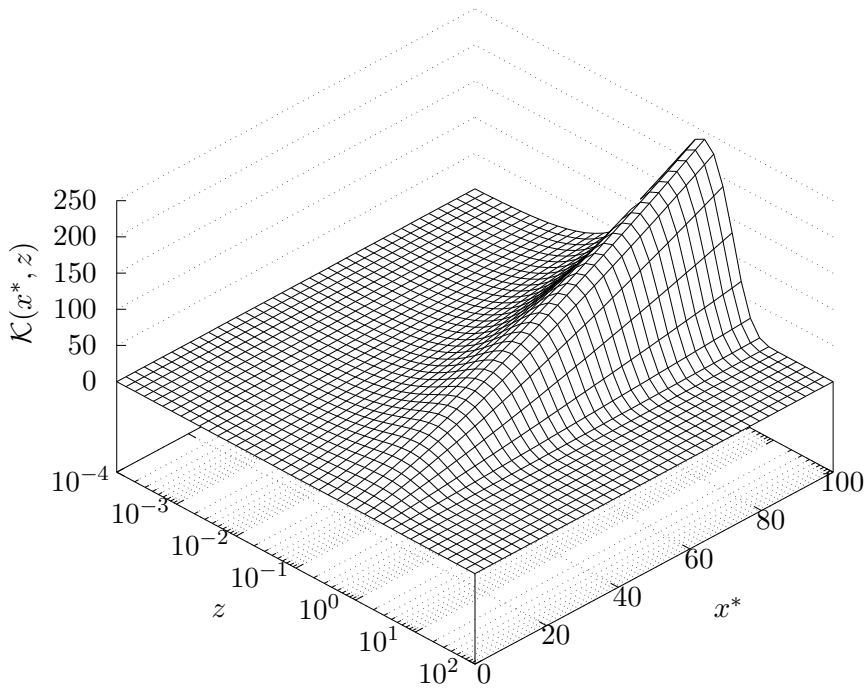


Figure 3.7: Surface plot of $\mathcal{K}(x^*, z)$, for a given x^* we can see that $\mathcal{K} \rightarrow 0$ before $z = 100$, suggesting that the integral can be constrained from $z = 10^{-3}$ to $z = 10^2$.

The first – and most naïve – method of determining h_e considered was by calculating h_e for each cell at each cooling step. This includes performing an integration of the function $\mathcal{K}(x^*, z)$, which can be constrained and calculated using a definite integral estimation method. It was determined that the equation peaks at $z \sim 1$ in all cases, and reduces to 0 before $z = 100$ (Fig.

3. METHODOLOGY & NUMERICAL SIMULATION

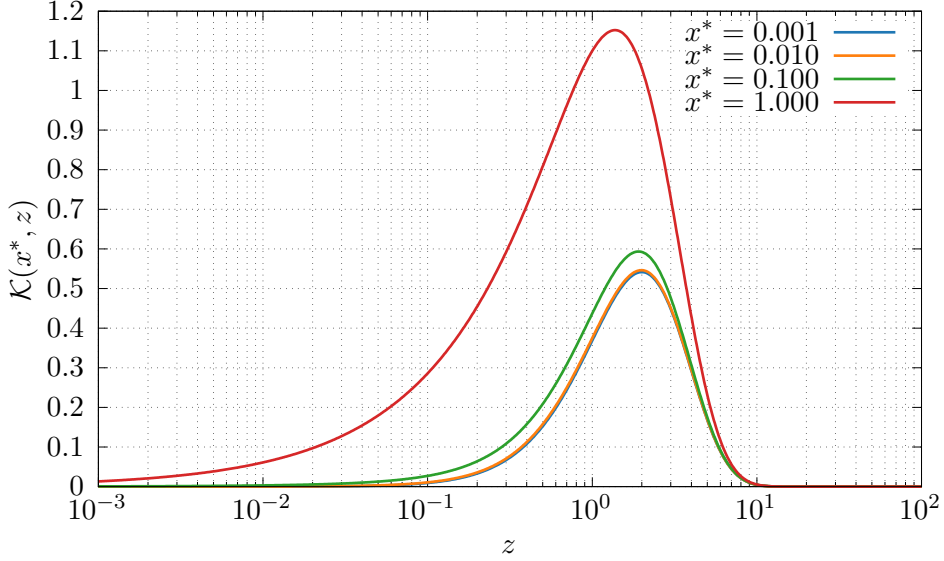


Figure 3.8: Plot of $\mathcal{K}(x^*, z)$ with values of z between 0.001 and 1 . we see that the function is non-zero between $z = 10^{-3}$ and $z = 10^2$. Therefore, the equation can be calculated in the form of a definite integral.

3.7 & 3.8). The integral was constrained such that

$$h_e = 1 - \frac{e^{x^*}}{2} \int_{10^{-2}}^{10^2} \mathcal{K}(x^*, z) dz, \quad (3.20)$$

and solved through the trapezoidal rule with logarithmically spaced integration steps. While this integral can be constrained in such a manner, it was found that a large number of bins was required to solve the equation correctly (Fig. 3.9). Through testing it was found that 400 bins to integrate z was the minimum amount required to reliably calculate h_e , which would result in the integral taking approximately 90% of the overall execution time of a typical cooling cycle. Values below 400 bins would result in negative values for h_e , which would render the simulation completely unphysical. Subtle improvements to performance could be made by forcing $h_e = 1.0$ for temperatures below 10^6 K, but this was found to still be comparatively slow. A more complex integration method would not improve performance at this point, instead, other methods were considered.

3.6.5.2 Lookup table

Another method considered was the use of a multidimensional lookup table, containing values for a normalised dust emissivity, Λ_d , for specific values of ρ_g , T and a . A moderately sized array

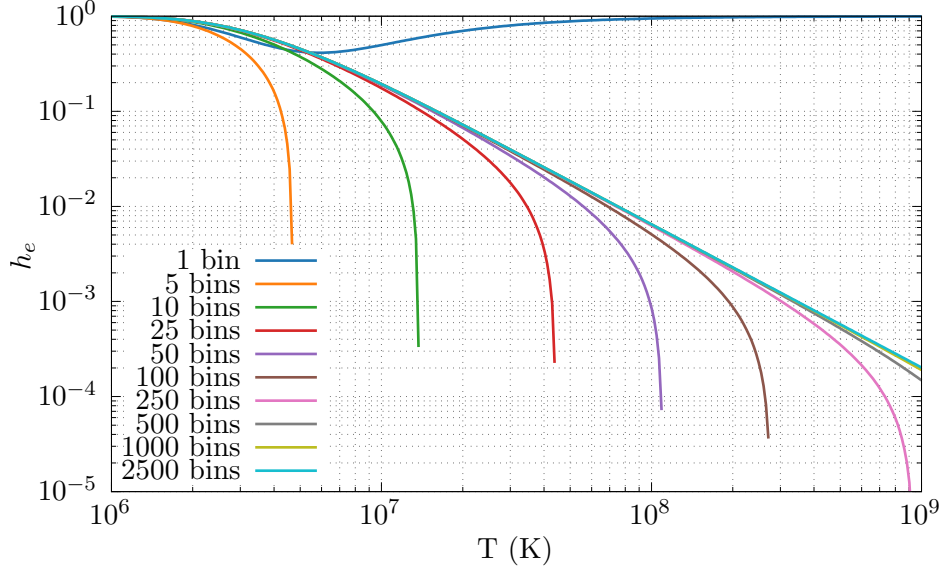


Figure 3.9: Comparison of h_e as a function of temperature for dust grains with a radius of 0.005 μm , h_e is calculated via the trapezium rule with a varying number of bins, bin counts below 400 bins result in wildly inaccurate or in some case negative values for h_e , while beyond 400 bins the result is accurate and converges slowly.

of $101 \times 101 \times 101$ elements was used, with a total of 1,030,301 possible values of Λ_d , spaced logarithmically. The values for Λ_d were generated from the integral method of solving Eq. 3.18 using a 10,000 bin integration with a parameter space described in Table 3.3.

Parameter	Min	Max	Bins
ρ_g	$10^{-25} \text{ g cm}^{-3}$	$10^{-10} \text{ g cm}^{-3}$	101
T	10^4 K	10^9 K	101
a	$10^{-3} \mu\text{m}$	$10^2 \mu\text{m}$	101

Table 3.3: Parameter space of Λ_d 3-parameter lookup table.

Similarly to the 1-D lookup table used for gas cooling, for each parameter, P , we determine the closest value smaller than (P_l) and greater than (P_u) the actual value. This is then used to calculate an offset, P_d :

$$P_d = \frac{P - P_l}{P_u - P_l}, \quad (3.21)$$

these offsets are then used to perform a trilinear interpolation to calculate Λ_d from the lookup table, through the equation:

3. METHODOLOGY & NUMERICAL SIMULATION

$$\begin{aligned}
\Lambda_{ll} &= \Lambda_{lll}(1 - \rho_d) + \Lambda_{ull}\rho_d, \\
\Lambda_{lu} &= \Lambda_{llu}(1 - \rho_d) + \Lambda_{ulu}\rho_d, \\
\Lambda_{ul} &= \Lambda_{lul}(1 - \rho_d) + \Lambda_{uul}\rho_d, \\
\Lambda_{uu} &= \Lambda_{luu}(1 - \rho_d) + \Lambda_{uuu}\rho_d, \\
\Lambda_l &= \Lambda_{ll}(1 - a_d) + \Lambda_{ul}a_d, \\
\Lambda_u &= \Lambda_{lu}(1 - a_d) + \Lambda_{uu}a_d, \\
\Lambda_d &= \Lambda_l(1 - T_d) + \Lambda_u T.
\end{aligned} \tag{3.22}$$

This method is markedly faster, and can be improved if multiple cooling sub-steps are performed. During the cooling process of a particular cell, the offset, “upper” and “lower” values for the quantities ρ_g and a do not change. Therefore, a bilinear interpolation can be made to solve these components, while a linear interpolation can be performed to solve the T components of the interpolation. As such, only Λ_d in Eq. 3.22 must be calculated for each sub-step, while all other components can be calculated at the start of the cooling process. This reduces the number of calculations significantly for a complex cooling step. Further improvements via handwritten loop-unrolling and SIMD optimisations were performed to increase performance by a factor of two. This final bilinear+linear method improves performance from the integral method by approximately 1,800%, and scales well when run in a numerical simulation (Fig. 3.10).

3.6.5.3 The Dwek and Werner (1981) approximation

Dwek and Werner (1981) provide a series of equations to estimate h_e based on the value of x^* :

$$h_e(x^*) = \begin{cases} 1, & \text{if } x^* > 4.5 \\ 0.37x^{*0.62}, & \text{if } x^* > 1.5 \\ 0.27x^{*1.50}, & \text{otherwise.} \end{cases} \tag{3.23}$$

This method is less accurate, especially between cases, but is multiple orders of magnitude faster. We find this estimate is at worst divergent from the integral method by 8%, and closely matches the results from the integral method (Fig. 3.11). After some optimisation, the resultant estimate was found to be approximately 25,000% faster than the integral method, meaning the electron contribution to dust cooling has a negligible impact on the processing time of a single time-step. Table 3.4 shows the results of benchmarking attempts on all of the methods tested.

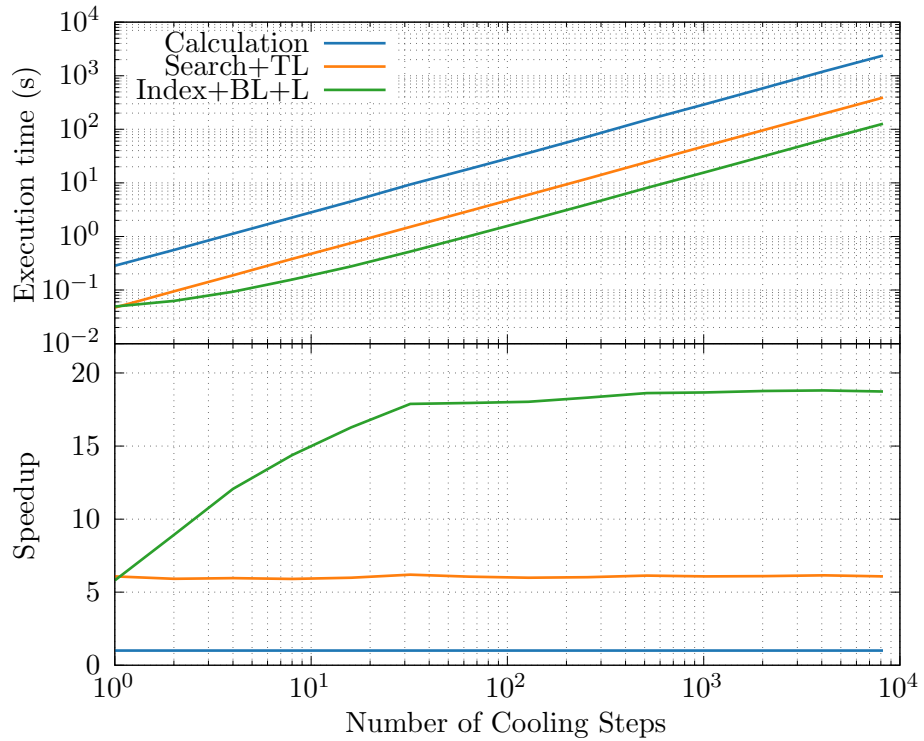


Figure 3.10: Comparison of execution time and speedup for lookup table methods. The bilinear+linear method improves performance significantly up to a point, as the linear step begins to take up a larger fraction of the problem.

As we can see, the approximation method is by far the fastest method, with an acceptable worst-case deviation from the integral method result. Because of this, it was decided that the approximation method would be used.

Method	t(s)	Iter/s	Speedup	Worst result
400-bin integration	36.03	35,526	-	0%
Trilinear	6.016	212,751	599%	0.3%
Bilinear + linear	1.999	640,447	1,803%	0.3%
Approximation	0.147	8,693,171	24,510%	8%

Table 3.4: Comparison of methods explored for estimating $\Lambda_d(\rho, a, T)$ in cooling code, 10^4 initial values were chosen and 128 cooling sub-steps were performed, benchmark code was compiled and run using `GCC 10.3.0` with the `-O3` optimisation set on an Intel i7-7700HQ processor with a maximum clock speed of 3.8 GHz.

3.6.5.4 Calculating n_e

Initially, a solar abundance approximation of the electron number density, n_e , was used, where $n_e = 1.32 n_H$, where n_H is the expected number density in a pure hydrogen flow ($n_H = \rho_g/m_H$).

3. METHODOLOGY & NUMERICAL SIMULATION

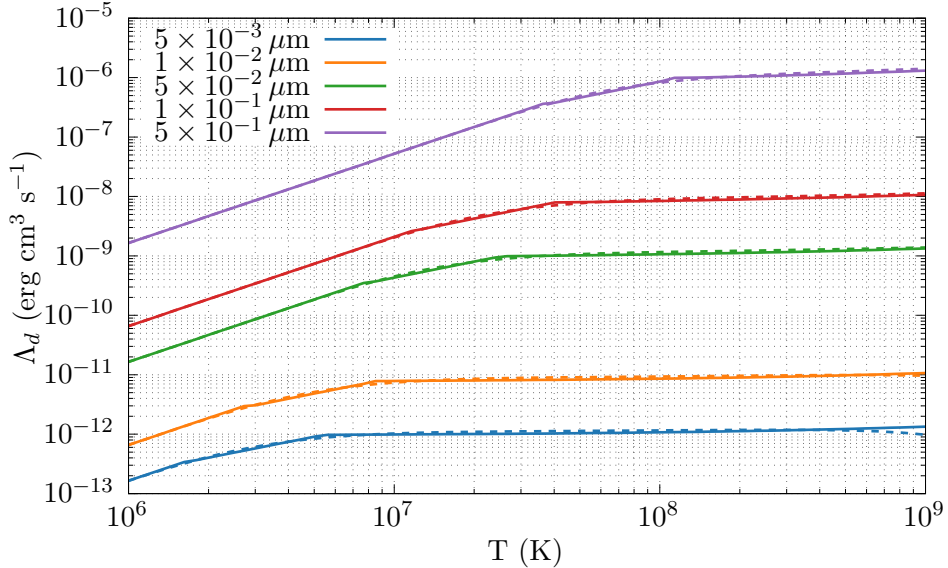


Figure 3.11: Λ_d as a function of temperature for various grain sizes and solar abundances. Solid lines represent calculations from the Dwek and Werner (1981) estimation, dashed lines represent the integral method. The estimation method is extremely close to the integral value aside from at the highest temperatures.

This can vary as much as a factor of three in the case of a WC wind, and vary significantly from 10^4 K to 10^7 K as the wind becomes increasingly ionised. A logarithmically spaced lookup table similar to the plasma cooling curve was used, containing the electron-to-ion ratio between 10^4 and 10^9 Kelvin for both winds (Fig. 3.12). This method was found to be comparatively fast, as the index method and calculation of the ion number density are computational trivial.

3.6.6 Model implementation

In order to simulate energy loss due to radiation in **Athena++**, the conserved variable array is adjusted to remove energy from a specific cell. This is analogous to energy being removed from the system due to radiative processes in an optically thin gas. Radiative processes are part of a source function that is performed for every mesh block. The cooling routine within the source function iterates through all cells within the meshblock, calculating radiative energy loss for each cell. Within the loop, the cell parameters are loaded from the conserved variables array, and additional gas and dust parameters are calculated from these conserved variables. In particular, the mean molecular mass of a cell, μ , is calculated with the formula

$$\mu = C\mu_{WR} + (1 - C)\mu_{OB}, \quad (3.24)$$

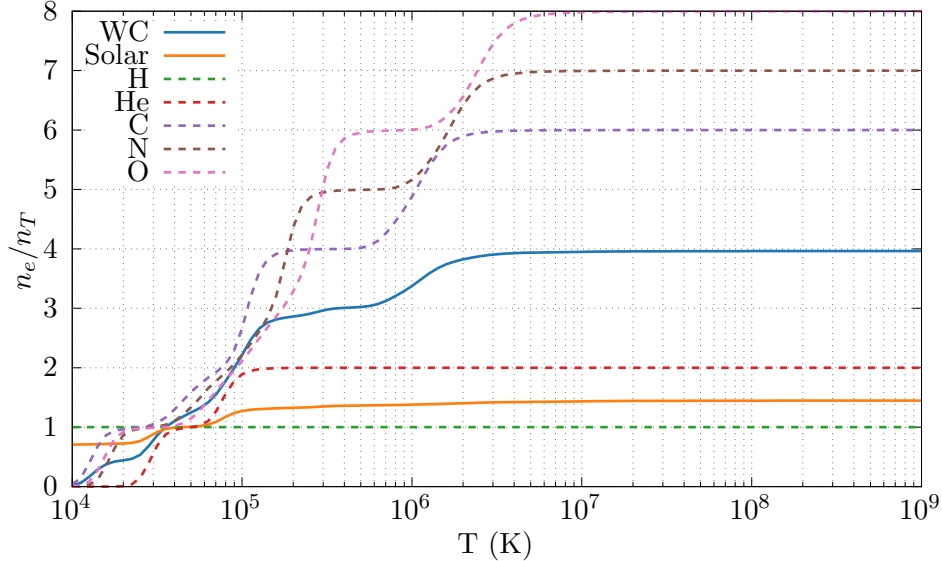


Figure 3.12: A comparison of the electron-ion ratio in both winds as a function of temperature. Also shown are the electron-to-ion ratios for the individual elements.

where μ_{WR} and μ_{OB} are the mean molecular masses of the winds and C is the wind ‘‘colour’’ scalar, the contribution of each wind to the gas density of the cell. The temperature is subsequently calculated using the ideal gas law:

$$T = \frac{P\mu m_H}{\rho k_B}. \quad (3.25)$$

At the current temperature, the cooling parameter, $\Lambda_g(T)$ for each wind is found from the lookup tables, and weighted in a similar manner as Eq. 3.24. The energy loss due to dust grains is then calculated, with the total energy loss rate per unit volume within the cell defined through the formulae:

$$\mathcal{L}_g = \left(\frac{\rho_g}{m_H} \right)^2 \Lambda_g(T), \quad (3.26a)$$

$$\mathcal{L}_d = n_d (H_{\text{coll}} + H_{\text{el}}), \quad (3.26b)$$

$$\mathcal{L}_T = \mathcal{L}_g + \mathcal{L}_d, \quad (3.26c)$$

where ρ_g is the gas density, m_H is the mass of a hydrogen atom, and n_d is the dust number density. As we can see from Eq. 3.25 and Eq. 3.26c, the temperature is proportional to μ ,

3. METHODOLOGY & NUMERICAL SIMULATION

therefore both Λ terms are dependent on μ . This therefore mandates that μ must be calculated accurately.

Performing the exact calculation of \mathcal{L}_g as described in Townsend (2009) would only work for gas cooling, and would require significant modification to work with a combination of gas and dust cooling. Mixed winds are also not supported, and the amount of cooling varies significantly based on the level of metallicity within a system, thus this is significantly less accurate for this use-case. Adaptive sub-stepping is utilised instead to improve accuracy of a fast Euler integration by increasing the temporal resolution as needed in cases of rapid cooling. At the end of each sub-step, after \mathcal{L}_T is calculated, a cooling time is calculated using the formula

$$\tau_{\text{cool}} = \frac{E_i}{\mathcal{L}_T}, \quad (3.27)$$

where E_i is the internal energy of the cell. A fraction of this cooling time is used as a timestep if $\kappa\tau_{\text{cool}} \leq t_{\text{rem}}$, where κ is a user-defined fraction and t_{rem} is the remaining time in the time-step. This process is repeated until the timestep is completed. Throughout this project we adopt a value for κ of 0.1. This method allows for more accurate calculations of cooling in cells with a higher cooling rate, while also being very fast in regions that are not undergoing excessive cooling. Fig. 3.13 shows the adaptive sub-stepping routine in operation. At the initial time, the cooling parameter Λ is maximised, as such the timestep is significantly lower than when the gas has cooled and is less radiative. This compares favourably to a single sub-step example, which would cause the simulation to crash due to negative temperatures. It also compares well to a cooling code with linearly spaced sub-steps, which could be unstable and inaccurate in a similar manner in cases of very strong cooling.

Additional testing with starting temperatures of 10^5 K, 10^6 K and 10^7 K and similar parameters to Fig. 3.13 were used to determine the accuracy of the sub-step method versus the exact integration method proposed in Townsend (2009). κ was also varied, in order to determine a suitable value with a reasonable error of no more than 10% at worst. Table 3.5 shows that $\kappa = 0.1$ produces an error of 6% at worst, while $\kappa = 0.01$ requires an order of magnitude more sub-steps to improve the accuracy to 1%. This is due to the slow convergence time of a first-order integration method such as Euler method, but this error was deemed acceptable. At higher temperatures and less intense cooling we find fewer sub-steps are required to calculate \mathcal{L}_T , with much greater accuracy. A single sub-step took an average of 134 ns using the adaptive sub-step method, while the Townsend (2009) method took 151 ns, when conducted on a 3.2 GHz M1 ARM processor and O3 optimisation. The speed benefit of the estimation method is di-

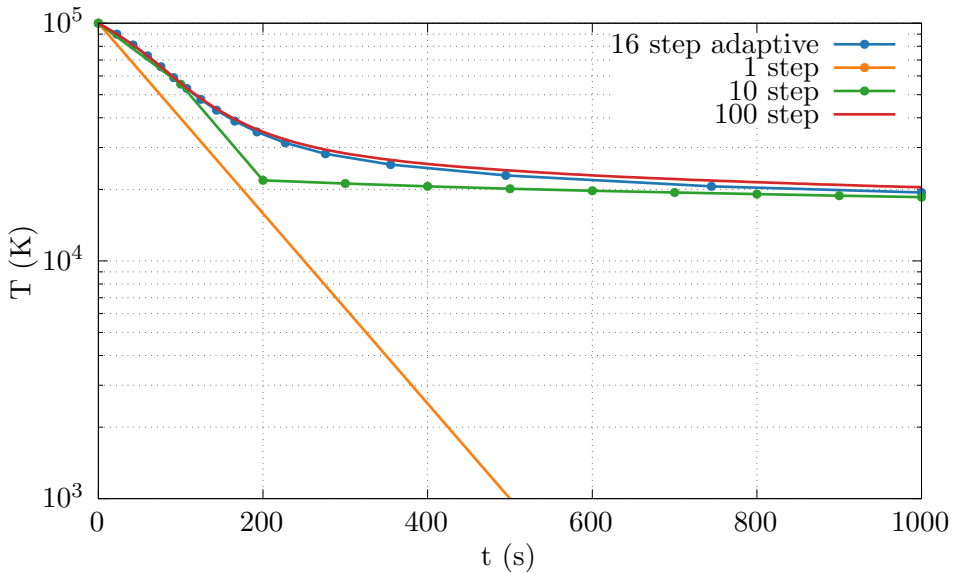


Figure 3.13: Comparison of the adaptive timestep method versus linearly spaced sub-steps for a solar abundance flow with a density of $10^{-16} \text{ g cm}^{-3}$ and an initial temperature of 10^5 K . Cooling was artificially limited to prevent negative temperatures, which would have occurred in the case of the 1 sub-step method.

minished at lower temperatures, but is necessary considering the limitations of the Townsend (2009) method. Whilst this is a fairly simplistic method of performing adaptive sub-stepping, it is fast, effective, and not prone to failure. Improved models in the future could utilise an adaptive RK method, in a similar manner to the numerical integrator in **Athena++**, though the implementation attempted had some numerical stability and execution time issues, and would require significant optimisation.

$\kappa = 0.1$			$\kappa = 0.01$			$\kappa = 0.001$		
T_i	Steps	Error	Steps	Error	Steps	Error	Steps	Error
10^5 K	16	6.025×10^{-2}	159	1.282×10^{-2}	1585	7.637×10^{-3}		
10^6 K	1	8.233×10^{-4}	6	1.012×10^{-4}	58	3.359×10^{-5}		
10^7 K	1	1.577×10^{-7}	1	1.577×10^{-7}	2	1.411×10^{-7}		

Table 3.5: Accuracy of the adpative sub-step Euler method compared with the Townsend, 2009 exact cooling method, with $\kappa = 0.1$ this method is out by 6% at worst in the low-temperature example, while very accurate at higher temperatures with only a single step needed.

3. METHODOLOGY & NUMERICAL SIMULATION

3.7 The BIDMAS Advectected Scalar Dust Model

In order to determine the rate of dust production, as well as the growth “hot spot” areas of a WCR, it was decided to implement a full dust model within a numerical simulation. The dust model would utilise advected scalars as this would be computationally lightweight. Additionally, this model was designed to be extensible; while grain destruction and accretion mechanisms that were the most influential were implemented first, a number of additional mechanisms could be implemented later for improved accuracy. The Binary Interaction Dust Model with Accretion and Sputtering (**BIDMAS**)¹ model is the result of this work. Although only a few dust evolution mechanisms were implemented due to time restrictions, it is a good first step towards modelling dust growth in WCd systems.

3.7.1 BIDMAS features

Currently the **BIDMAS** model supports grain advection, growth and destruction, as well as the dust cooling model discussed in Section 3.6.5. The mechanisms changing the quantity of dust in the system are gas-grain accretion and gas-grain sputtering. The dust also effects the radiative cooling. Furthermore, amorphous carbon is the only species of dust grain considered in this simulation, as it is observed to consist of an overwhelming, if not total, fraction of dust in all observed WCd systems (Crowther, 2003). Gas-grain accretion occurs with low-velocity collisions between carbon atoms and dust grains. Grain-grain collision is not simulated as it was determined to occur with significantly less frequency than gas-grain collisions, whilst also being difficult to implement without a grain size distribution. Dust destruction via gas-grain sputtering occurs when ions with a high thermal velocity collide with the dust grains and a small amount of material is ablated from the surface of the grain. Shattering is not simulated for similar reasons to grain-grain collisions. The decision of which mechanisms to simulate for each cell are based on the cell temperature: growth mechanisms occur at lower temperatures while destruction mechanisms occur at higher temperatures. The **BIDMAS** model assumes that all gas accreted from dust comes from the stellar wind, therefore any accreted material is subtracted from the gas density of the cell. This did present issues when initially developing the model, as on occasion this would result in runaway dust accretion. This was solved by using a lower Courant number, and ensuring a high spatial resolution in the apex of the WCR. Dust cooling is also implemented, utilising the method described in Section 3.6.5.

¹Any good thesis (though this one, again, is of debatable quality) has an incredibly laboured acronym!

Other important considerations for this model were to use as few “magic numbers” as possible, and for the code to be very well documented, in order to assist future PhD researchers. The initial conditions of the model were based on sensible values for the initial size of grain nuclei and dust mass fractions, while using a comparatively conservative value for the grain sticking probability. Whilst much of the work in this thesis was accomplished on a slightly earlier build of this model, a more advanced, cleaned up version of the model has been written¹. This improved model is ready for when the AMR stability issues of `Athena++` have been solved by the software developers.

3.7.2 Implementation

At its most fundamental level, BIDMAS uses advected scalars² to model dust. An advected scalar behaves like a tracer or dye in a physical fluid, and for a particular scalar of species i , evolves through the simulation with the equation:

$$\rho \frac{dC_i}{dt} = \frac{\partial}{\partial t} (\rho C_i) + \nabla \cdot (C_i \rho \mathbf{u}) = -\nabla \cdot \mathbf{Q}_i, \quad (3.28)$$

where \mathbf{Q}_i is the diffusive flux density of the species:

$$\mathbf{Q}_i = -\nu_{AS}\rho \nabla C_i \quad (3.29)$$

and ν_{AS} is the advected scalar diffusion coefficient (Stone et al., 2020). For this work a value of $\nu_{AS} = 0$ was used. As there is no diffusion, all scalars are perfectly co-moving with the gas (Toro, 2013, Ch. 10). Multiple scalars are used to describe the wind and dust parameters within each cell of a simulation:

- `scal_0`: The wind “colour”, C , or mass fraction of each wind in the cell.
- `scal_1`: The dust-to-gas mass ratio, $z = \rho_d/\rho_g$.
- `scal_2`: The average grain radius, \bar{a} , in microns.

This method is markedly simpler to implement and faster to compute, as the dust can be described on a per-cell basis in a series of simple calculations, this allows dust evolution mechanisms

¹<https://github.com/atomsite/athena>

²These can also be referred to as passive scalars, particularly in the `Athena++` documentation. These terms are considered to be interchangeable throughout this thesis.

3. METHODOLOGY & NUMERICAL SIMULATION

to be implemented easily, as long as they can be defined by these parameters either directly or through a derivative, such as the grain number density.

3.7.2.1 Dust injection

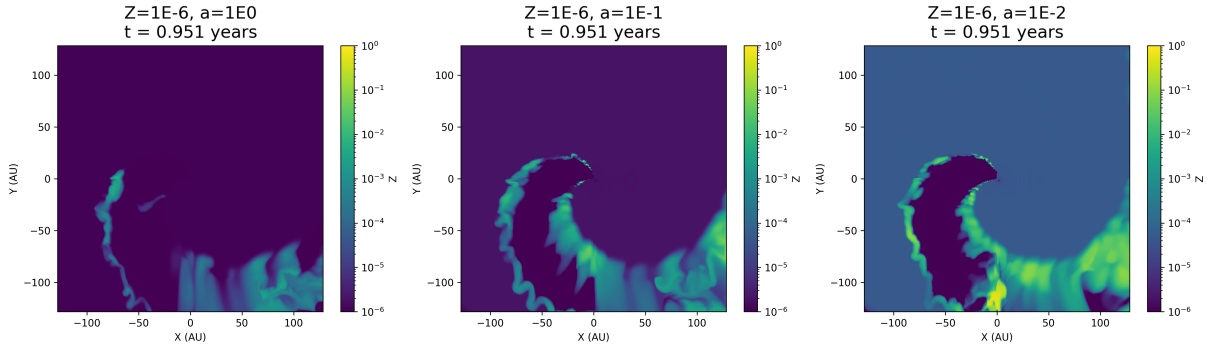


Figure 3.14: A comparison of WCR dust distribution when a_i is varied in a system with WR98a parameters. The dust yield increases significantly if a smaller, realistic initial grain size is chosen.

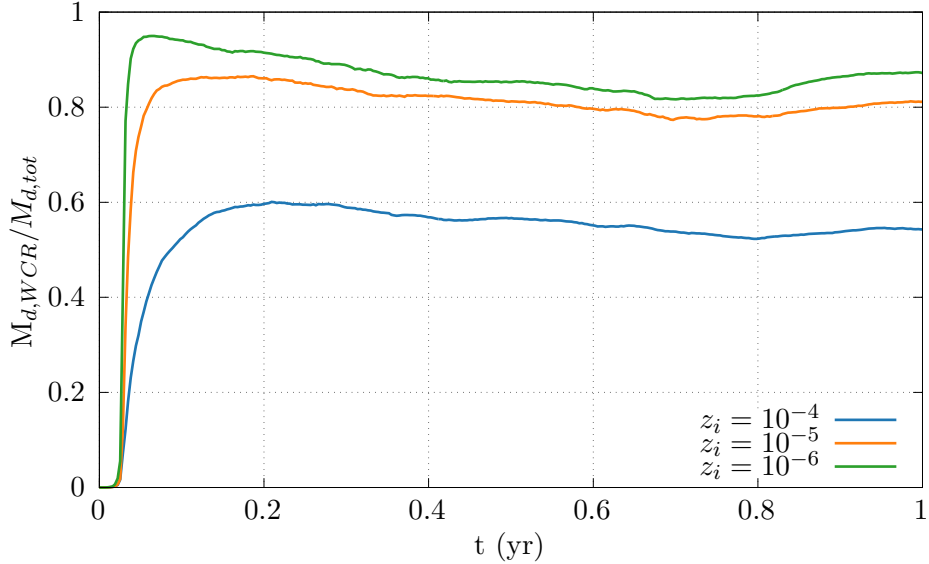


Figure 3.15: A comparison of the WCR dust fraction ($M_{d,WCR}/M_{tot}$) over the course of a simulation with WR98a properties. As z_i decreases the amount of dust produced outside of the WCR decreases significantly. This is consistent across all grain sizes, and does not result in a significantly increased amount of dust.

Dust is injected into the system in small quantities from the wind remap zone of the WC star. If we were to describe this mechanism in physical terms, this would be as if refractory carbon grain cores condensed into the WC wind. Whilst the exact mechanism for initial grain

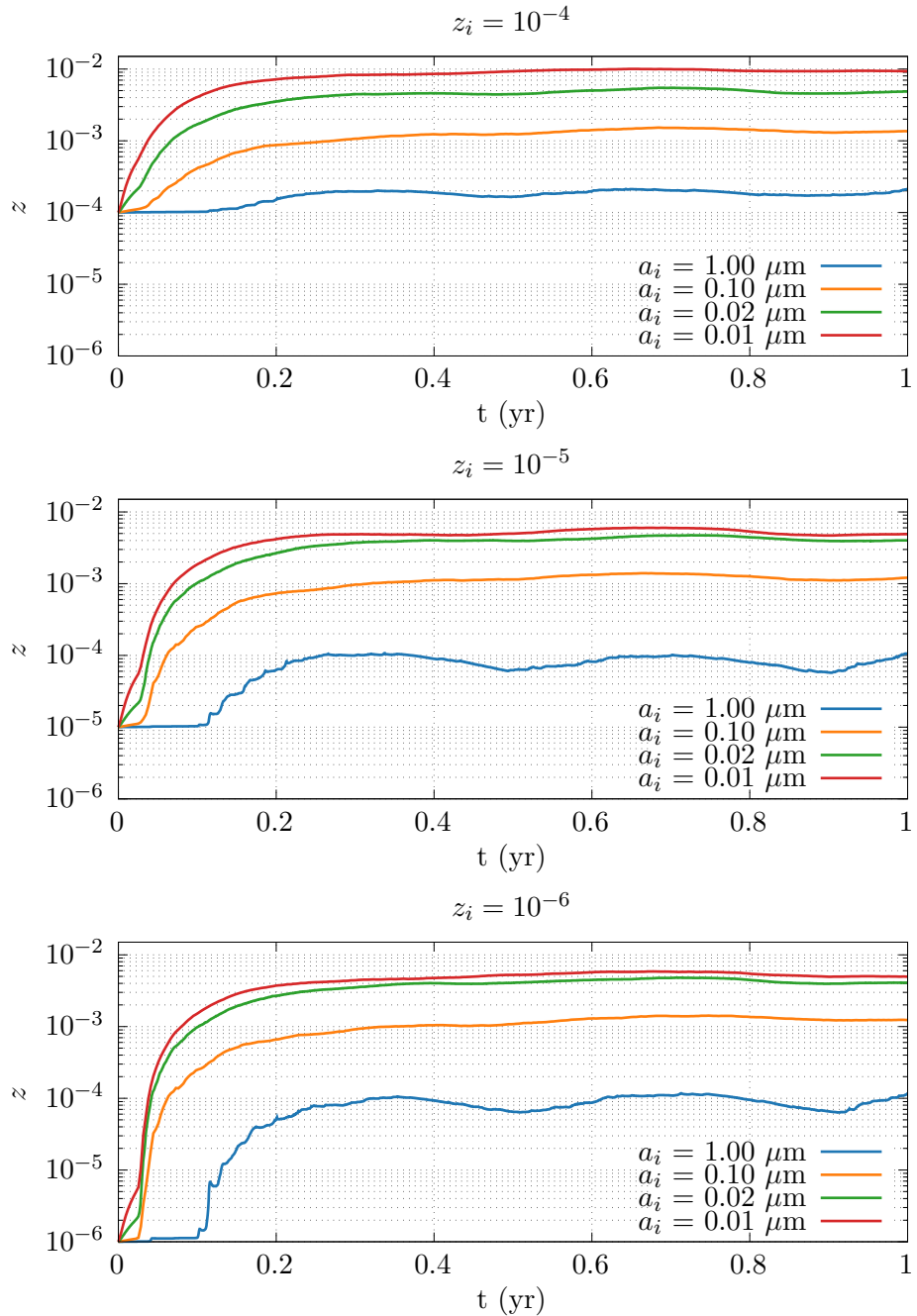


Figure 3.16: A comparison of z over the course of a simulation with WR98a properties. z_i and a_i are varied for each simulation. We find that dust yield increases significantly if a smaller, realistic initial grain size is chosen. Varying z_i does not result in a corresponding change in dust yield.

3. METHODOLOGY & NUMERICAL SIMULATION

nucleation is not known, this is an ideal first step as it assures that dust grains are present in the post-shock WCR wind. Another important consideration of this model was for it to be fairly general purpose, and not require significant degrees of initial parameter “tuning” in order to simulate a new system. Therefore, it was decided that the model would operate on as few initial parameters as possible. Determining the injected scalar values at this remap zone was an important first step, as it was not known how these initial parameters would impact the final dust yield, $M_{d,f}$, or the dust formation rate, \dot{M}_d . In order to determine the ideal initial parameters, and to determine the sensitivity of the model to its initial conditions, a series of simulations were conducted using the orbital and wind parameters of WR98a. The initial grain radius, a_i was varied from $0.01 \mu\text{m}$ to $1 \mu\text{m}$, while the initial dust-to-gas mass ratio, z_i was varied from 10^{-6} to 10^{-4} . These simulations were run over the course of a week on the ARC4 HPC cluster over 128 cores. The total elapsed time within the simulation was one year, with the simulation advecting fully to the simulation extent of $100 \times 100 \times 10 \text{ AU}$ in around 0.1 yr. Whilst the results of Lau et al. (2021) had not been published at this time, a final dust-to-gas mass fraction of $\sim 1\%$ was assumed to be an ideal starting point for a model of WR98a.

As can be seen in Fig. 3.14, we find that decreasing a_i creates a much more defined WCR, at the cost of increasing dust outside of the WCR. Dust formation occurs where expected, on the WC edge of the WCR, with the bulk of dust formation occurring within a short distance from the apex of the WCR shock. Therefore, we must aim for a small grain radius, and not start with large grains. Additionally, Zubko (1998) notes that the initial dust grain nuclei are expected to be extremely small, on the order of 5 \AA , and rapidly grow to 100 \AA through interactions of small, charged grains with impinging carbon ions. This is expanded on in Fig. 3.15, where we find that changing z_i significantly affects the amount of dust produced in the WCR compared to the total dust yield. As we do not observe significant quantities of dust being produced outside of the WCR, we prioritised a small value of z_i , as long as it does not significantly influence dust yields. Finally, Fig. 3.16 shows that changing z_i does not affect the total dust yield significantly, which is far more sensitive to changes in a_i . We can therefore discern from these previous two results that z_i should be kept to a fairly small value.

The parameter z_i was found to not affect the dust production within the WCR significantly. Therefore, we were able to reduce the effective initial parameter space of dust in the wind to a single parameter, a_i , which was found to operate best when set to a realistic value. After this preliminary parameter space exploration, an a_i of 50 \AA and a z_i value of 10^{-8} were utilised. Whilst these initial parameters were based on an extrapolation of our test data, these initial values were found to be more than adequate. Other dust injection mechanisms were considered

for this project, such as injecting dust into the apex of the WCR. These were found to give inconsistent results when initially tested in the MG hydrodynamical code, however.

3.7.2.2 Assumptions & limitations

From this we can determine further assumptions for our dust model. We assume that the number density ratio, n_d/n_g , is constant throughout the simulation, and is calculated based on the initial grain radius and the initial dust-to-gas mass ratio. We therefore assume that the net rate of grain shattering and grain agglomeration is zero, no grains are created or destroyed – they just increase or decrease their radii. We also assume that there is no variation in grain size within each numerical cell. Whilst other models assume that dust grains are coupled through a drag force, it was found that the dust was effectively coupled to the wind as if it was co-moving (Section 3.7.3.1). This may however prevent significant dust mixing in the immediate post-shock region, due to the increased inertia of the dust grains compared to the gas. As a single grain size for each cell is assumed, dynamics between grains of different sizes, such as grain agglomeration cannot be accurately simulated. These issues could be addressed with a multi-scalar or multi-fluid model, which is a potential future feature of this project.

All grains in the simulation are assumed to be circular, with a volume, V_{gr} , of $4/3\pi a^3$ and a mass, $m_{\text{gr}} = V_{\text{gr}}\rho_{\text{gr}}$, where ρ_{gr} is the grain bulk density. As we assume all dust grains in the simulation are composed of amorphous carbon, we assume that $\rho_{\text{gr}} = 3.0 \text{ g cm}^{-3}$, which is on the upper end of densities expected for amorphous carbon (Bhattarai et al., 2018).

3.7.2.3 Dust cooling

Dust cooling is handled within the cooling loop, and functions by removing energy from each cell of the simulation. The gas is assumed to be optically thin to infrared, and the radiative losses are therefore removed from the simulation without re-adsorption. The emissivity of the grains at the current temperature and radius, $\Lambda(a, T)$, is calculated for each cell, and the rate of energy loss per unit volume due to dust emission is calculated with the formula

$$\mathcal{L}_d = n_d (H_{\text{el}} + H_{\text{coll}}), \quad (3.30)$$

where n_d is the dust number density, H_{el} is the grain heating rate due to electrons and H_{coll} is the grain heating rate due to atom/ion collisions. Dust cooling, as well as the optimisations

3. METHODOLOGY & NUMERICAL SIMULATION

needed to run quickly in a numerical simulation, is discussed in significantly more detail in Section 3.6.5.

3.7.2.4 Dust evolution

Once the energy loss due to dust emission has been calculated, the growth rate and destruction rate for dust grains in each cell is calculated. The code loops through every cell in the simulation, first calculating the average particle mass in the cell, μ :

$$\mu = C \left(2X_{\text{WR}} + \frac{3}{4}Y_{\text{WR}} + \frac{1}{2}Z_{\text{WR}} \right)^{-1} + (1 - C) \left(2X_{\text{OB}} + \frac{3}{4}Y_{\text{OB}} + \frac{1}{2}Z_{\text{OB}} \right)^{-1}, \quad (3.31)$$

where C is the wind “colour”, and X, Y, Z are the individual wind hydrogen, helium and metal mass fractions, respectively (Mihalas, 1978). The cell temperature is then calculated using the ideal gas law, which is used to determine which dust evolution mechanism occurs. For temperatures above 10^6 K, dust destruction occurs, while at temperatures below 1.4×10^4 K dust growth occurs instead. As the dust grains are assumed to be spherical, we can model dust growth and destruction in a unified manner, corresponding to a change in grain radius. In the case of dust destruction, ions sputter off atoms from the surface of the dust grain, wearing the grain evenly over time, while in the case of accretion, low velocity collisions cause atoms to stick, growing the grain evenly.

For both processes we find a change in the grain radius of da/dt , which can be extrapolated to find the rate of change in dust density with the formulae:

$$\frac{dV_{\text{gr}}}{dt} = 4\pi a^2 \frac{da}{dt}, \quad (3.32a)$$

$$\frac{dm_{\text{gr}}}{dt} = \rho_{\text{gr}} \frac{dV_{\text{gr}}}{dt}, \quad (3.32b)$$

$$\frac{d\rho_{\text{d}}}{dt} = n_{\text{d}} \frac{dm_{\text{gr}}}{dt}, \quad (3.32c)$$

where dV_{gr}/dt is the rate of change in the dust grain volume and dm_{gr}/dt is the associated change in dust grain mass. To simulate dust growth due to grain-gas accretion we use a method from Spitzer (2008, Ch. 9). Carbon atoms accrete onto a dust grain at a constant rate, resulting in a change in radius such that:

$$\frac{da}{dt} = \frac{\xi \rho_C w_C}{4 \rho_{\text{gr}}}, \quad (3.33)$$

where ξ is the grain sticking factor, ρ_C is the density of carbon in the wind ($\rho_C = \rho_g X(C)$, where $X(C)$ is the carbon mass fraction), and w_C is the RMS velocity of the carbon atoms:

$$w_C = \sqrt{\frac{3k_B T}{12m_H}}. \quad (3.34)$$

Throughout this thesis we use a grain sticking factor of 0.1. From Eq. 3.33 we can derive a corresponding rate of change in the dust density:

$$\frac{d\rho_{\text{d,acc}}}{dt} = \pi \xi \rho_C w_C n_{\text{d}} a^2. \quad (3.35)$$

Dust destruction is carried out through the Draine and Salpeter (1979a) prescription. We estimate an amorphous carbon grain 1 μm to have a lifespan, τ_{gr} , of 3×10^6 yr. As described in Draine and Salpeter (1979a), with additional work by Tielens et al. (1994) and Dwek et al. (1996), this grain lifespan is dependent on the gas density, n_g , as well as the grain radius, taking the form

$$\tau_{\text{gr}} = \frac{a}{da/dt}. \quad (3.36)$$

In the case of temperatures beyond 10^6 Kelvin this is approximately constant, and in the case of a carbon grain with radius 1 μm moving through a gas with number density 1 cm^{-3} we approximate a lifespan of 3×10^6 yr. As such we find a lifespan for a grain of radius a and gas number density n_g such that:

$$\tau_{\text{gr}} \approx 3 \times 10^6 \text{ yr} \cdot \frac{a(\mu\text{m})}{n_g} \equiv 9.467 \times 10^{17} \cdot \frac{a}{n_g}. \quad (3.37)$$

This can be further simplified to find a value for da/dt dependent on the gas number density:

$$\frac{da}{dt} = 1.056 \times 10^{-18} \cdot n_g. \quad (3.38)$$

Finally, we can calculate an associated rate of change in the dust density of:

3. METHODOLOGY & NUMERICAL SIMULATION

$$\frac{d\rho_{d,sp}}{dt} = -4\pi n_d \rho_{gr} a^2 \frac{da}{dt} = -1.33 \times 10^{-17} \cdot n_d n_g \rho_{gr} a^2, \quad (3.39)$$

In order to find the total change in the dust density, $\Delta\rho_g$, and the grain radius, Δa , we perform an Euler integration over the simulation timestep, Δt :

$$\Delta x = \int_t^{t+\Delta t} \frac{dx}{dt} dt \approx \frac{dx}{dt} \Delta t, \quad \text{where } \Delta t \ll t_{\text{sim}}, \quad (3.40)$$

where x is the quantity being integrated and t_{sim} is the total simulation time. Whilst a Euler method integration is less accurate than a sub-stepping method or higher-order integration method, this was found to be adequate, as the growth rate of the dust grain was found to be small over a single time step. After the total change for ρ_d and a are calculated, the post-step grain radius, a_{new} , is calculated:

$$a_{\text{new}} = a_{\text{old}} + \Delta a. \quad (3.41)$$

Then the post-step dust and gas densities are calculated, with the mass of the new dust being subtracted from the fluid:

$$\rho_{d,\text{new}} = \rho_{d,\text{old}} + \Delta\rho_d, \quad (3.42a)$$

$$\rho_{g,\text{new}} = \rho_{g,\text{old}} - \Delta\rho_d. \quad (3.42b)$$

Finally, the new dust-to-gas mass ratio can be calculated from the new dust and gas densities:

$$z_{\text{new}} = \frac{\rho_{d,\text{new}}}{\rho_{g,\text{new}}}. \quad (3.43)$$

These new scalar values then overwrite the previous scalar values. Passive scalars in **Athena++** are stored in the following arrays for a scalar species N in a meshblock with indices i, j, k :

- `pmb->pscalar->r(N,i,j,k)`: Primitive variables between 0.0 and 1.0.
- `pmb->pscalar->s(N,i,j,k)`: Conserved variables between 0.0 and `rho`, the conserved cell density.

These values have to be updated simultaneously at the end of each iteration of the main processing loop such that:

```

1 // Update primitive scalars
2 pmb->pscalars->r(1,k,j,i) = z_new; // Update z primitive
3 pmb->pscalars->r(2,k,j,i) = a_new; // Update a primitive
4 // Update conserved scalars
5 pmb->pscalars->s(0,k,j,i) = col * rho_new; // Update colour conserved
6 pmb->pscalars->s(1,k,j,i) = z_new * rho_new; // Update z conserved
7 pmb->pscalars->s(2,k,j,i) = a_new * rho_new; // Update a conserved

```

`Athena++` automatically re-scales scalar values lower than 0.0 or greater than 1.0 or `rho` (depending on the variable type) at the end of each time-step¹.

3.7.3 Contemporary dust models

At the time of writing, there has been no research conducted that has accomplished all three of the following criteria:

1. Model a CWB system using a numerical simulation.
2. Implement a dust model inside this numerical simulation.
3. Simulate multiple dust evolution mechanisms such as accretion, sputtering and radiative cooling.

There are two dust models in particular, however, that should be discussed, as they fulfil some of these conditions. These are the Harries et al. (2004) and Hendrix et al. (2016) dust models. Research conducted by Harries et al. (2004) involved the simulation of dust emission through a ballistic particle model, with the CWB simulated as a conical region. Dust of a uniform size of 0.01 μm was used, with the cone being simulated with a radiative transfer model, in order to constrain the dust production rate of the WR104 system through comparison to observations.

3.7.3.1 The Hendrix dust model

Perhaps the most similar contemporary dust model is the model described in Hendrix et al. (2016) - as this model is concerned with simulating the dynamics of dust within a CWB. This is not to say that these models are identical, of course, as the Hendrix model explores how dust

¹This method also limits the grain size to a maximum radius of 1 μm , as the primitive value for a scalar is limited to 1, but growth of this level outside of testing - where the grain radius was stored in centimetres - was never observed.

3. METHODOLOGY & NUMERICAL SIMULATION

spreads throughout the WCR of WR 98a, in order to compare with observational data using a radiative transfer code.

The main differentiating factors between this model and our model are the driving mechanism and dust evolution. In the Hendrix model dust is modelled as a separate fluid, with an Epstein drag function between the wind and dust fluids; this method allows for dust kinematics that aren't implicitly co-moving. This is a more accurate method of modelling dust, however it requires significantly more processing time and is much more difficult to implement, requiring a numerical code that supports multiple fluids. At the start of this PhD this was considered but eventually rejected due to time constraints.

However, the Hendrix model has limitations that this model does not have. This is because the purpose of the Hendrix model is to analyse the distribution of dust within a CWB system, rather than to model the evolution of the dust itself. Because of this, the Hendrix model does not calculate dust growth or destruction, and only uses a single small grain size, with the dust-to-gas mass ratio calculated based on observations of the target system, WR98a.

3.7.4 Future dust models

Due to time constraints and limitations in the code in use, only a limited set of mechanisms for dust evolution were included in this project's simulations. While the **BIDMAS** model represents an interesting start for the modelling of dust grains in colliding wind binaries, future models could implement more complex models which incorporate additional destruction and growth mechanisms, as well as multiple dust grain sizes.

A multiple grain size scalar model could be used to more accurately measure the growth of dust grains, rather than a single average grain size. This would be more difficult to implement than a single model but would be able to accurately simulate grain-grain collision, and better calculate dust growth and destruction rates. **Athena++** and MG both have issues with a large number of scalars, as such both numerical codes may require significant modification to cope with this. A multi-fluid model with dust being physically simulated rather than assumed to be co-moving would be an ideal next step. Multiple grain size distributions could also be modelled in a similar way to the proposed multi-scalar model, but with the kinematics of the dust grains being simulated separately. The increased inertia of more massive dust grains could result in the kinematics of the dust flow diverging from the co-moving assumption. To that end, a successor dust model would adopt a multi-fluid and drag function method. This multi-fluid model would also allow for more physically accurate simulation of grain-gas and grain-grain interactions, as

the collision velocities would be exactly calculated rather than estimated through bulk motion properties. High speed collision of gas on dust grains in the immediate post-shock environment could also shatter grains, though this (as well as grain spalling) would be complex to simulate.

Furthermore, non-collisional mechanisms for dust destruction such as photodissociation and sublimation could also be implemented. The implementation of these could be used to determine the effectiveness of the WCR in protecting nascent grain cores.

The initial grain nucleation model could also be improved, injection of extremely small grains into the simulation through the stellar remap zones was chosen as the underlying chemical process for formulation of these dust grains is poorly understood at the time of writing. The small grain nucleation model was also found to be only dependent on the initial grain radius, a_i , whilst changing the initial amount of grain nuclei in the WR wind does not change the amount of dust produced (Fig. 3.16). Due to this, the simulations are currently bound by a single input parameter, which can be constrained based on what is currently understood about dust grain accretion. A more complex model may require additional parameters, and as such could be highly dependent on these initial parameters. As such, another round of initial parameter hunting would be required.

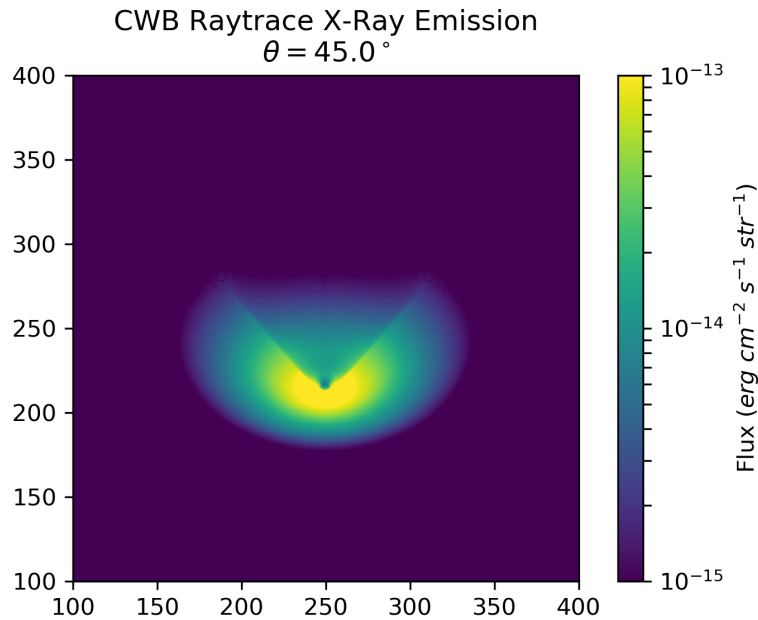


Figure 3.17: An x-ray radiative transfer image from 0.1 keV to 10.0 keV of a test CWB system with a momentum ratio of $\eta = 0.01$ inclined at $\phi = 45^\circ$ from the observer at a distance of 1 kpc. Radiative transfer was performed on an in-house code, which was to be modified to support dust emission.

3. METHODOLOGY & NUMERICAL SIMULATION

Another avenue of future research would be performing a radiative transfer calculation upon a fully advected system, in order to compare with observational results. Some initial tests were performed with an in-house x-ray emission code that was to be modified to support dust emission (Fig. 3.17). Using other radiative transfer codes such as HYPERION were also considered (Robitaille, 2011), but this was abandoned due to time constraints from changing hydrodynamical codes from MG to *Athena++*. Radiative transfer modelling was performed by Hendrix et al. (2016), with the resultant images emulating the sensitivity and angular resolution characteristics of UKIRT, Keck and ALMA (figure 3.18).

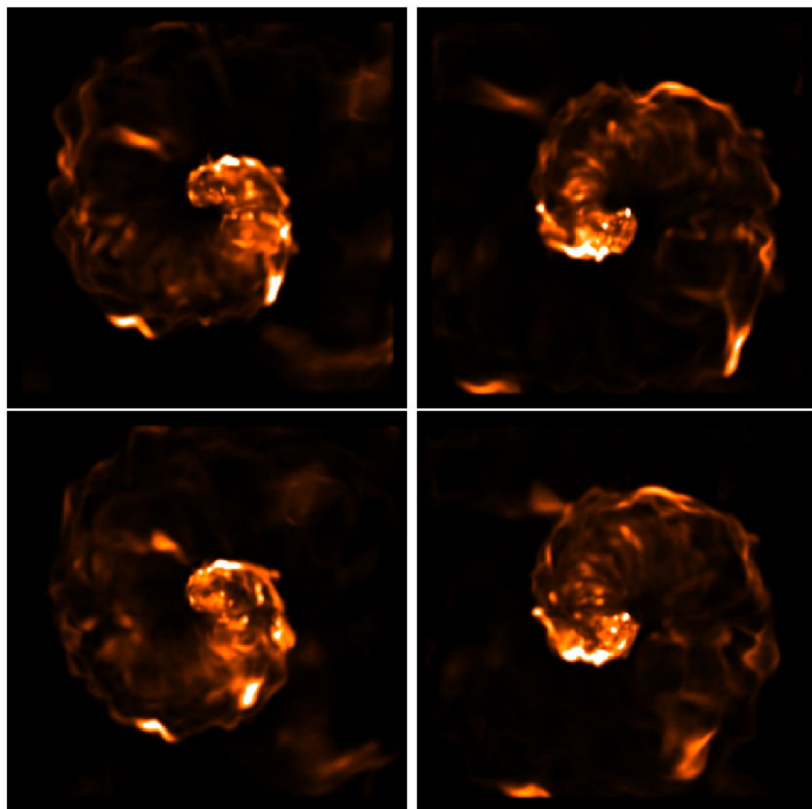


Figure 3.18: Synthetic images of WR 98a emulating the capabilities of ALMA using a radiative transfer model, reproduced from Hendrix et al. (2016).

3.8 Summary

In this chapter, we have discussed the details, trials and tribulations of modelling CWB systems numerically. Whilst there are some limitations to our model, it is suitable for qualitative analysis

3.8 Summary

of dust production in WCR systems. Future models will include more dust evolution mechanisms, more accurate cooling, and a coupled dust fluid to analyse how dust advects through the turbulent post-shock environment. Regardless, this represents the first numerical model that calculates the growth of dust in WCd systems. In the following chapters, we will apply this model to two types of systems:

- Persistent WCd systems in the form of a parameter space study with a system representative of WR98a as a baseline (Chapter 4; Eatson et al., 2022a).
- The episodic WCd system WR140 at periastron passage (Chapter 5; Eatson et al., 2022b).

Whilst this work was elucidating, we are eager to continue this work with more detailed simulations and more advanced models.

3. METHODOLOGY & NUMERICAL SIMULATION

CHAPTER 4

An Exploration of Dust Growth Within WCd Systems
Using An Advectored Scalar Dust Model (Eatson et al.,
[2022a](#))

4. AN EXPLORATION OF DUST GROWTH WITHIN WCD SYSTEMS

Abstract

Dust production is one of the more curious phenomena observed in massive binary systems with interacting winds. The high temperatures, UV photon flux and violent shocks should destroy any dust grains that condense. However, in some extreme cases dust production yields of approximately 30% of the total mass loss rate of the stellar winds have been observed. In order to better understand this phenomenon a parameter space exploration was performed using a series of numerical models of dust producing carbon phase Wolf-Rayet (WCd) systems. These models incorporated a passive scalar dust model simulating dust growth, destruction and radiative cooling. We find that reasonable dust yields were produced by these simulations. Significant changes in the dust yield were caused by changing the mass loss rates of the stars, with a greater mass loss rate contributing to increased dust yields. Similarly, a close orbit between the stars also resulted in higher dust yields. Finally, a high velocity wind shear, which induces Kelvin-Helmholtz (KH) instabilities and wind mixing, drastically increases the dust yields.

4.1 Introduction

Binary systems with colliding stellar winds are a fascinating type of system, capable of producing a variety of peculiar phenomena. The shocks produced from this wind interaction creates some of the most luminous persistent stellar-mass x-ray sources in the night sky (Rosslowe & Crowther, 2015). Within the wind collision region the available mechanical energy can exceed $10^4 L_\odot$, producing shocks with post-shock temperatures up to 10^8 K.

In particularly energetic colliding wind binary (CWB) systems with a Wolf-Rayet (WR) star and OB-type partner, dust in the form of amorphous carbon grains has been observed to form (Allen et al., 1972). This is particularly curious, as the high temperatures, strong shocks and UV luminosities of these systems should result in dust grains being rapidly destroyed through sublimation processes. These dust forming CWB systems have only been observed to occur if a carbon phase WR star (WC star) is partnered with either another WR star or an OB main sequence star (a WR+OB system). While the exact methods of dust formation and evolution in these systems are poorly understood, dust formation rates have been observed to be extremely high, up to $10^{-6} M_\odot \text{ yr}^{-1}$. This is approximately 36% of the total wind by mass in the case of WR104 (Lau et al., 2020).

4.1 Introduction

Within different colliding wind binary systems, dust may form either continuously or periodically. The first such observed dust forming system was the episodic dust forming system WR140, first reported by Williams, van der Hucht, Pollock et al. (1990) who observed a significant and highly variable infrared excess, consistent with emission from dust grains. The dust production rate was later found to vary by a factor of 40 over the orbital period of 7.9 yr (Thomas et al., 2021; van der Hucht et al., 1999). Persistent dust forming systems were subsequently discovered, such as WR104 (Tuthill et al., 1999) and WR98a (Monnier et al., 1999). Whilst the exact mechanism for dust formation is not currently known, there is a strong correlation between periodicity and eccentricity, with less eccentric systems forming dust continuously, while highly eccentric systems exhibit episodic dust formation (Crowther, 2003). Due to this orbital dependency, it is likely that there is an optimal dust forming separation, where dust can form in large quantities. This could be due to factors such as strong post shock cooling, which is highly dependent on the wind speed and orbital separation. Additionally, dust may be protected from the bulk of the stellar radiation due to the extremely large degree of extinction that may occur in the dense post-shock environment of radiative shocks (Cherchneff, 2015).

Direct observation of dust forming CWBs and in particular the wind collision region (WCR) is exceptionally difficult for a number of reasons:

- WR+OB CWB systems are extremely rare. Of the 667 catalogued WR stars at the time of writing, 106 have been confirmed to be in a binary system (Rosslowe & Crowther, 2015; Williams, 2019).
- A WC star is required for dust formation. No nitrogen sub-type Wolf-Rayet (WN) stars have been observed to form dust.
- Not all WC+OB systems are dust producing, limiting the sample size further.
- 56 dust forming systems with a known spectral type have been observed overall. Despite producing an extremely large quantity of dust in their local region, they are outnumbered by AGB stars by ~ 3 orders of magnitude (Ishihara et al., 2011).
- Galactic CWB systems are comparatively distant from earth. For instance, WR 104, a well-studied system, is ~ 2.5 kpc distant (Soulain et al., 2018) and no WCd systems have been detected at a distance of < 1 kpc (Rosslowe & Crowther, 2015). This prevents observations of these systems at a high spatial resolution.
- Grain growth from small nucleation grains is predicted to be very rapid in CWB systems

4. AN EXPLORATION OF DUST GROWTH WITHIN WCD SYSTEMS

(Zubko, 1998). Therefore studying the initial grain evolution would require observations of extremely high angular resolution.

For these reasons, numerical simulations are useful for modelling the growth of dust grains within this unresolved region. In order to better understand what influences dust production in a CWB system, a parameter space exploration of the wind and orbital parameters was performed. In particular the orbital separation, mass-loss rate and wind velocity were modified for both stars in order to vary the wind momentum ratio, η , and the cooling parameter, χ . The wind momentum ratio is defined as:

$$\eta = \frac{\dot{M}_{\text{OB}} v_{\text{OB}}^{\infty}}{\dot{M}_{\text{WR}} v_{\text{WR}}^{\infty}}, \quad (4.1)$$

where \dot{M} is the mass loss rate of a star and v^{∞} is the terminal velocity of a star's outflow. A low value for η indicates that the winds are extremely imbalanced, with the WR typically dominating the wind dynamics of the system. The wind momentum ratio determines for a given orbital separation, d_{sep} , the distance from each star to the apex of the wind collision. We define the terms r_{WR} and r_{OB} , representing the distance from the WR and OB stars to the stagnation point of the WCR:

$$r_{\text{WR}} = \frac{1}{1 + \eta^{1/2}} d_{\text{sep}}, \quad (4.2a)$$

$$r_{\text{OB}} = \frac{\eta^{1/2}}{1 + \eta^{1/2}} d_{\text{sep}}. \quad (4.2b)$$

This assumes the winds both accelerate to terminal speed and that there is no radiative inhibition (Stevens & Pollock, 1994) or braking (Gayley et al., 1997). In some systems the winds may be so imbalanced that the stronger wind collides directly with the companion star. The half-opening angle of the WCR can be estimated by the formula

$$\theta_c \simeq 2.1 \left(1 - \frac{\eta^{2/5}}{4}\right) \eta^{-1/3} \quad \text{for } 10^{-4} \leq \eta \leq 1, \quad (4.3)$$

to a relatively high degree of accuracy (Eichler & Usov, 1993; Pittard & Dawson, 2018).

The cooling parameter, χ , compares the cooling time to the escape time from the shocked region for a parcel of gas in the immediate post-shock environment. An approximation can be made using the known parameters of a system using the equation:

$$\chi = \frac{t_{\text{cool}}}{t_{\text{esc}}} \approx \frac{v_8^4 d_{12}}{\dot{M}_{-7}}, \quad (4.4)$$

where v_8 is the wind terminal velocity in units of 10^8 cm s^{-1} , d_{12} is the distance to the WCR apex in units of 10^{12} cm , and \dot{M}_{-7} is the mass loss rate in units of $10^{-7} M_\odot \text{ yr}^{-1}$ (Stevens et al., 1992). $\chi \leq 1$ indicates that radiative cooling is very important, while $\chi \gg 1$ indicates that the system is adiabatic. Strong cooling is aided with slow, dense winds and a high metallicity. As such in many systems the post-shock WR flow will rapidly cool from the immediate post-shock temperature of $\sim 10^{7-8} \text{ K}$ to temperatures in the dust formation range, $T \lesssim 10^4 \text{ K}$. A strongly radiating WCR can also be significantly compressed far more as it loses energy. In comparison, an adiabatic WCR is limited to a maximum density increase of a factor of 4 above the pre-shock wind density for a ratio of specific heats, $\gamma = 5/3$. The density increase and cool temperatures result in rapid dust growth and protection from the stellar UV radiation in some systems. Note also that Eq. 4.4 takes account of gas and plasma cooling only, but other cooling, such as dust cooling, may also be important.

In this paper, we aim to explore how dust growth is affected by the orbital and wind parameters of persistent dust forming WR+OB systems. This is performed by running a series of hydrodynamical simulations with an advected scalar dust model. In Section 4.2 we outline the methodology of our simulations, and how our dust model is implemented. We discuss our model series parameters, and why these parameters were chosen in Section 4.3. Finally we discuss our results and conclude in Sections 4.4 and 4.5.

4.2 Methodology

Numerical simulations within this paper utilise the Athena++ hydrodynamical code, a highly modular fluid dynamics code (Stone et al., 2020). Simulations are generated in 3D and the Euler hydrodynamical equations are solved in the form:

$$\frac{\partial \rho}{\partial t} + \nabla \cdot (\rho \mathbf{u}) = 0, \quad (4.5a)$$

$$\frac{\partial \rho \mathbf{u}}{\partial t} + \nabla \cdot (\rho \mathbf{u} \mathbf{u} + P) = 0, \quad (4.5b)$$

$$\frac{\partial \rho \varepsilon}{\partial t} + \nabla \cdot [\mathbf{u} (\rho \varepsilon + P)] = \mathcal{L}_T, \quad (4.5c)$$

4. AN EXPLORATION OF DUST GROWTH WITHIN WCD SYSTEMS

where ε is the total specific energy ($\varepsilon = \mathbf{u}^2/2 + e/\rho$), ρ is the gas density, e is the internal energy density, P is the gas pressure, \mathbf{u} is the gas velocity and \mathcal{L}_T is the energy loss rate per unit volume from the fluid due to gas and dust cooling.

Athena++ has been configured to run using a piecewise linear reconstruction method with a 4th order Strong Stability Preserving Runge-Kutta time-integration method (Spiteri & Ruuth, 2002). Athena++ was forked from the original repository and additional routines were written for a colliding wind binary scenario. Routines were created to produce a steady outflow from a small spherical region around a set of cartesian co-ordinates as well as a function to move these co-ordinates with each time-step; these were used to simulate stellar wind outflow and orbital motion, respectively. Additionally, Athena++ was further modified to include an advected scalar dust model for simulating dust growth and destruction as well as a photon emission cooling model to approximate cooling for gas and dust particles within the fluid.

Athena++ utilises OpenMPI for parallelism, breaking the simulation into blocks, which are distributed between processors. The block size is variable, but for these simulations a block size of $32 \times 32 \times 8$ was found to be optimal. This meshblock system is also utilised in mesh refinement for increasing the effective resolution. As the CWB systems are being simulated in their entirety, a very large volume needs to be simulated, while at the same time the region between the stars must be resolved with a resolution of at least 100 cells in order to adequately resolve the WCR. This difference in length scales necessitates the use of static mesh refinement (SMR) to improve the effective resolution of the simulation. A base coarse resolution of $320 \times 320 \times 40$ cells in XYZ is defined for the simulations, while a region close to the stars operates at a higher refinement level. This rectangular region encompasses the entire orbital path of the stars and is refined to the maximum level. This results in a resolution increase of a factor of 2^{n-1} greater than the coarse resolution, where n is the refinement level (see Fig. 4.1). In the case of 7 levels (inclusive of the base, “coarsest” level) as used in most of the simulations in this paper, this results in an effective resolution of $20480 \times 20480 \times 2560$ cells. SMR is utilised instead of adaptive mesh refinement, a more flexible conditional method, as it has proven to be more reliable for our simulations. As much of the grain evolution occurs a small distance from the WCR stagnation point, much of the simulation volume can be run at a lower resolution without affecting the simulation results.

The wind outflow from each star is simulated by replacing the conserved variables (density, momentum and energy) within a small region around the expected position of the stars; this region is typically on the order of 6 maximally refined cells in radius. This rewrite corresponds to a change in density, ρ_R , pressure, P_R , and total energy, E_R , imparted by an outflowing wind,

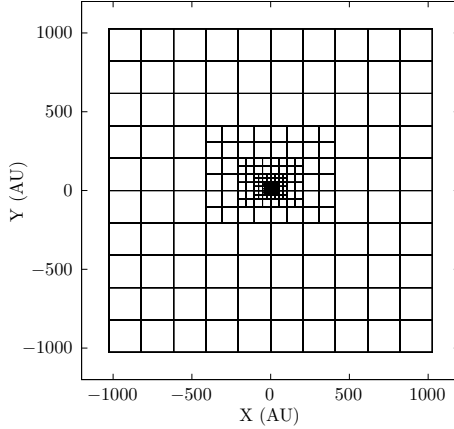


Figure 4.1: A plot of the blocks used in a 7 level simulation with a block size of $32 \times 32 \times 8$ cells. The block density increases dramatically closer to the barycentre. The coarse simulation resolution is $(320 \times 320 \times 40)$ cells with a block size of $(32 \times 32 \times 8)$ cells. The diagram is sliced about the z axis at $z = 0$.

such that:

$$\rho_R = \frac{\dot{M}}{(4\pi r^2 v_\infty)}, \quad (4.6a)$$

$$P_R = \rho_R k_B T_w / \mu m_H, \quad (4.6b)$$

$$E_R = \frac{P_R}{\gamma - 1} + \frac{1}{2} \rho_R v_\infty^2, \quad (4.6c)$$

where v_∞ is the wind velocity as it flows radially from the center of the “remap zone”, T_w is the wind temperature and r is the radial distance from the current cell to the centre of the remap zone. Orbits are calculated by moving the remap zones in a manner consistent with Keplerian dynamics, which are repositioned at the start of every timestep. This orbital speed is also added to the remap wind speed.

4.2.1 Gas and dust cooling

Cooling due to photon emission from atoms, ions and free electrons, as well as dust particles, is simulated by removing energy from the cells at each timestep. The total energy loss is calculated by integrating the energy loss rates due to gas, plasma and dust cooling using the Euler method; in regions with very rapid cooling sub-stepping is used to improve accuracy, with the number of sub-steps being determined by comparing the timestep to the cooling timescale

4. AN EXPLORATION OF DUST GROWTH WITHIN WCD SYSTEMS

	X(E)	
	Solar	WC9
H	0.705	0.0
He	0.275	0.546
C	3.07×10^{-3}	0.4
N	1.11×10^{-3}	0.0
O	9.60×10^{-3}	0.05

Table 4.1: Abundances by mass used for the OB and WR stars being simulated. Other elements are assumed trace when calculating dust emission (Williams et al., 2015).

of the cell. Gas cooling is simulated using a lookup table method. A data file containing the gas temperature and associated normalised emissivity, $\Lambda_w(T)$, of the wind at that temperature is read into the simulation. In a typical cooling step, the temperature is calculated and compared with the lookup table to find the closest temperature bins that are lower and higher than the cell temperature. A linear interpolation is then performed to find an appropriate value for $\Lambda_w(T)$. As the two winds have significantly different abundances and can be thoroughly mixed in the WCR, we calculate an emissivity value for gas in a particular cell with the equation

$$\Lambda_g(T) = C\Lambda_{w,WR}(T) + (1 - C)\Lambda_{w,OB}(T), \quad (4.7)$$

where C is the wind “colour”, or mixing fraction, where 1 is a pure WR wind and 0 is a pure OB wind. The rate of change in energy per unit volume due to plasma and gas cooling, \mathcal{L}_g , is then calculated through the equation:

$$\mathcal{L}_g = \left(\frac{\rho_g}{m_H} \right)^2 \Lambda_g(T), \quad (4.8)$$

where ρ_g is the gas density and m_H is the mass of a hydrogen atom. The lookup table was generated by mixing a series of cooling curves generated by MEKAL simulations of elemental gasses. These simulations were combined based on the elemental abundances of each wind, with the WC star having typical WC9 abundances and the OB star having a solar abundance (see Table 4.1). Figure 4.2 shows the resulting cooling curves used for each star. The most significant abundances used are noted in Table 4.1. The cooling regime of the simulations ranges between temperatures of 10^4 to 10^9 K. A floor temperature of 10^4 K is implemented. Temperatures between $10^4 \text{ K} < T \leq 1.1 \times 10^4 \text{ K}$ are set to 10^4 K as they are assumed to be either rapidly cooling or a part of the stellar wind.

A model for cooling due to emission from dust grains is also included as dust cooling is

4.2 Methodology

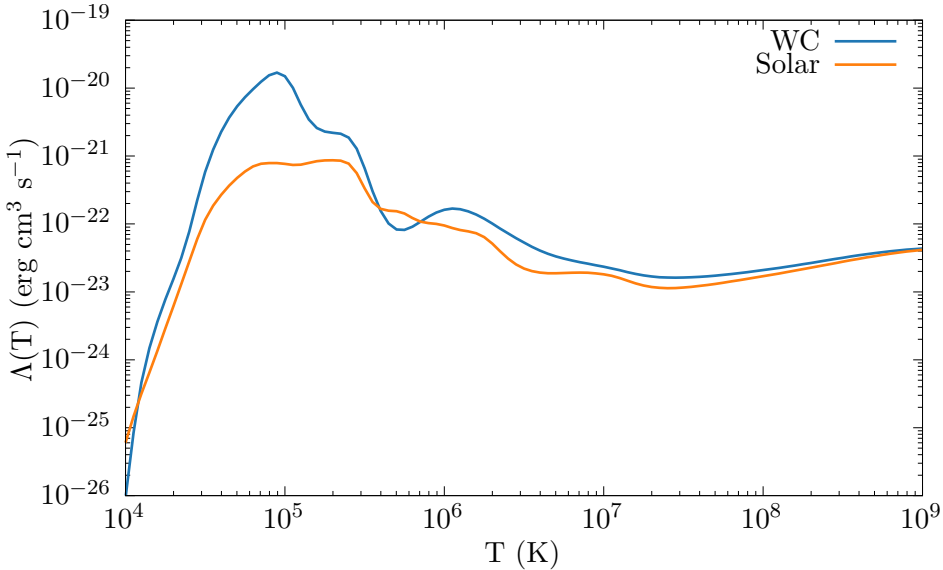


Figure 4.2: Comparison of WC and solar cooling curves for calculating the energy loss due to gas cooling.

expected to play a significant role in each system. The rate of cooling is calculated using the uncharged grain case of the Dwek and Werner (1981) prescription. Grains are heated due to collisions with ions and electrons, causing them to radiate, with energy being removed from the simulation. This assumes that the region being simulated is optically thin to far infrared photons. The grain heating rate (in erg s^{-1}) is calculated with the following formula

$$H = 1.26 \times 10^{-19} \frac{n}{A^{1/2}} a^2(\mu\text{m}) T^{3/2} h(a, T), \quad (4.9)$$

where H is the heating rate due to atom and ion collisions, n is the particle number density, A is the mass of the incident particle in AMU, $a(\mu\text{m})$ is the grain radius in microns, T is the temperature of the ambient gas, and $h(a, T)$ is the effective grain “heating factor”, also referred to as the grain transparency.

To obtain the collisional heating due to incident atoms, H_{coll} , the heating rates are summed for hydrogen, helium, carbon, nitrogen and oxygen atom collisions:

$$H_{\text{coll}} = H_{\text{H}} + H_{\text{He}} + H_{\text{C}} + H_{\text{N}} + H_{\text{O}}. \quad (4.10)$$

Other elements are not considered as they are present in trivial proportions in both winds. As dust grains are assumed to be uncharged, the grain transparency for each species is calculated

4. AN EXPLORATION OF DUST GROWTH WITHIN WCD SYSTEMS

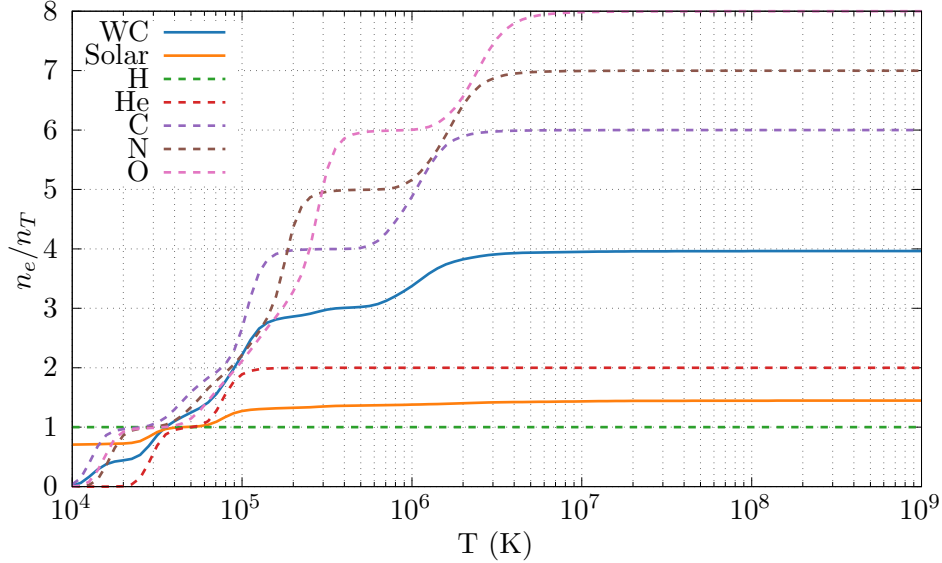


Figure 4.3: A comparison of the electron-ion ratio in both winds as a function of temperature. Also shown are the electron-to-ion ratios for the individual elements.

with the formula

$$h(a, T) = 1 - \left(1 + \frac{E_0}{2k_B T}\right) e^{-E_0/k_B T}, \quad (4.11)$$

where E_0 is the initial energy required to overcome the grain's potential and k_B is the Boltzmann constant.

Electron-grain collisional heating, H_{el} , is modelled using the same calculation for H_{coll} , albeit with some differences. For accurately calculating the energy loss due to electron collisions, the electron number density, n_e , needs to be known. This is achieved with a second series of lookup tables that contain the electron-to-ion ratio of each wind across a temperature range of 10^4 to 10^9 K (Fig. 4.3). The electron number density is

$$n_e = \beta n_i, \quad (4.12)$$

where β is the electron-to-ion ratio and n_i is the ion number density. Another difference between calculating electron-grain and gas-grain cooling is calculating electron-grain transparency, which is a significantly more complex problem than calculating ion-grain transparency. An assumed full opacity proves to be extremely inaccurate at temperatures $> 10^6$ K. Electron-grain transparency is therefore calculated via an approximation described in Dwek and Werner (1981):

$$\begin{aligned}
 h(x^*) &= 1, & x^* > 4.5, \\
 &= 0.37x^{*0.62}, & x^* > 1.5, \\
 &= 0.27x^{*1.50}, & \text{otherwise,}
 \end{aligned} \tag{4.13}$$

where $x^* = 2.71 \times 10^8 a^{2/3} (\mu\text{m})/T$. This approximation is approximately 4 orders of magnitude faster than using an integration method, while differing by less than 8%. Grain-grain collisions are not modelled, as this would be difficult to calculate due to the single-fluid model in use. Further simulations utilising a multi-fluid model could allow for this to be simulated. Finally, in order to calculate the change in energy due to dust cooling, the rate of energy change, \mathcal{L}_d , is calculated using the formulae:

$$H_T = H_{\text{coll}} + H_{\text{el}}, \tag{4.14a}$$

$$\mathcal{L}_d = n_d H_T, \tag{4.14b}$$

where H_T is the total grain heating rate and n_d is the dust number density. The total energy loss rate per unit volume due to gas and dust cooling is given by:

$$\mathcal{L}_T = \mathcal{L}_g + \mathcal{L}_d. \tag{4.15}$$

4.2.2 Numerical modelling of dust through advected scalars

The most important modification to Athena++ was the addition of a dust growth and destruction model to simulate the production of dust within the WCR. A series of passive scalars were used where the dust parameters described by the scalars can evolve and advect through the simulation, analogous to a co-moving fluid, which previous work has noted is an accurate dynamical model for dust within the WCR (Hendrix et al., 2016). In these simulations, information about the dust is stored in the form of two variables, the average grain radius, a , and the dust-to-gas mass ratio, z . From these constants the dust growth rate, number density, and total dust mass can be derived. A co-moving model allows for a simplified model of dust formation. In such a model, the mean relative velocity between the dust and gas is given by:

$$\langle u \rangle = \sqrt{\frac{8kT}{\pi m_r}}, \tag{4.16}$$

4. AN EXPLORATION OF DUST GROWTH WITHIN WCD SYSTEMS

where m_r is the familiar reduced mass between a test particle of mass m_t and a field particle of mass m_f , such that $m_r = m_f m_t / (m_f + m_t)$.

As the dust grain is significantly more massive, the reduced mass is approximately equal to the grain mass, simplifying the dynamics of the simulation in a co-moving case.

In this model, growth and destruction occur in distinct temperature regimes. Dust growth occurs when $T \leq 1.4 \times 10^4$ K whilst dust destruction occurs at temperatures of $T \geq 10^6$ K.

Dust growth is modelled through approximating growth due to grain-gas accretion where grains co-moving with a gas perform relatively low-velocity collisions with the surrounding gas, causing it to accrete onto the surface of the dust grain (Spitzer, 2008). Assuming a single average grain size the rate of change in the average grain radius is given by:

$$\frac{da}{dt} = \frac{\xi \rho_C w_C}{4 \rho_{gr}}, \quad (4.17)$$

where w_C is the Maxwell-Boltzmann distribution RMS velocity for carbon ($w_C = \sqrt{3k_B T / 12m_H}$), ξ is the grain sticking efficiency, ρ_C is the carbon density in the gas ($\rho_C = X(C)\rho_g$, where $X(C)$ is the wind carbon abundance), and ρ_{gr} is the grain bulk density. The associated rate of dust density change, $d\rho_d/dt$ is calculated with the formulae:

$$\frac{dm_{gr}}{dt} = 4\pi \rho_{gr} \frac{da}{dt} a^2 = \pi \xi \rho_C w_C a^2, \quad (4.18a)$$

$$\frac{d\rho_d}{dt} = \frac{dm_{gr}}{dt} n_d, \quad (4.18b)$$

where n_d is the grain number density and dm_{gr}/dt is the rate of change of the grain mass. In this paper we take $\xi = 0.1$ as a conservative value, though this value can rise to as high as 1 (Spitzer, 2008). A bulk density analogous to amorphous carbon grains ($\rho_{gr} = 3.0 \text{ g cm}^{-3}$) is used.

Dust destruction gas-grain sputtering is calculated using the Draine and Salpeter (1979b) prescription. A dust grain has a lifetime which is dependent on the number density of the gas the grain is moving through, n_g . In the case of amorphous carbon grains, the dust lifetime is:

$$\tau_{gr} = \frac{a}{da/dt} \approx 3 \times 10^6 \text{ yr} \cdot \frac{a(\mu\text{m})}{n_g} \equiv 9.467 \times 10^{17} \cdot \frac{a}{n_g}. \quad (4.19)$$

This value is based on an average lifetime of carbon grains in interstellar shocks at shock temperatures between 10^6 and 3×10^8 K (Dwek et al., 1996; Tielens et al., 1994). The rate of change

4.2 Methodology

in grain radius can be calculated with the formula

$$\frac{da}{dt} = \frac{a}{\tau_{\text{gr}}} = 1.056 \times 10^{-18} \cdot n_g, \quad (4.20)$$

The rate of change in grain mass and dust density can then be calculated with the formulae:

$$\frac{dm_{\text{gr}}}{dt} = -4\pi\rho_{\text{gr}}a^2 \frac{da}{dt} = -1.33 \times 10^{-17} \cdot n_g \rho_{\text{gr}} a^2, \quad (4.21a)$$

$$\frac{d\rho_d}{dt} = \frac{dm_{\text{gr}}}{dt} n_d. \quad (4.21b)$$

Application of the dust growth and destruction routines in the code is determined by the gas temperature of a cell.

In order to propagate dust through each simulation, a small initial value for the advected scalars is set in each cell in the remap zones. An initial grain radius of $a_i = 50 \text{ \AA}$ and initial dust-to-gas mass ratio of $z_i = 10^{-6}$ is imposed. Changing z_i does not significantly impact the final dust-to-gas mass ratio of the system as z rapidly increases within the WCR and dust growth in the WCR dominates the total production. Dust also grows to some extent in the unshocked winds but at a much lower rate than within the WCR. A small initial grain radius is sensible, as small dust grains are believed to rapidly nucleate from impinging carbon ions (Harries et al., 2004; Zubko, 1998).

In order to determine if our dust model is producing reasonable dust yields, we calculate the maximum expected dust production rate in each system, $\dot{M}_{\text{d,max}}$. This rate would occur if 100% of the carbon in the WR wind being shocked by the WCR was converted into dust. The fraction of the WR wind that passes through the WCR is given by

$$f_{\text{WR}} = \frac{1 - \cos(\theta_{\text{WR}})}{2}, \quad (4.22)$$

where θ_{WR} is the opening angle of the WR shock front, approximated as $\theta_{\text{WR}} \approx 2 \tan^{-1}(\eta^{1/3}) + \pi/9$ (Pittard & Dawson, 2018). The theoretical maximum dust production rate is then

$$\dot{M}_{\text{d,max}} = \dot{M}_{\text{WR}} X_{\text{C,WR}} f_{\text{WR}}, \quad (4.23)$$

where X_{C} is the carbon mass fraction in the WR star.

4. AN EXPLORATION OF DUST GROWTH WITHIN WCD SYSTEMS

Parameter	WR	OB
\dot{M}	$5.0 \times 10^{-6} M_{\odot} \text{ yr}^{-1}$	$5.0 \times 10^{-8} M_{\odot} \text{ yr}^{-1}$
v_{∞}	$1.0 \times 10^8 \text{ cm s}^{-1}$	$2.0 \times 10^8 \text{ cm s}^{-1}$
T_w	$1.0 \times 10^4 \text{ K}$	$1.0 \times 10^4 \text{ K}$

Table 4.2: Wind properties of the baseline system.

Parameter	Value
$M_{\text{WR/OB}}$	$10.0 M_{\odot}$
d_{sep}	4.0 AU
P	1.80 yr

Table 4.3: Baseline system orbital properties.

4.3 Model Parameters

In this paper we do not attempt to model particular systems. Rather we aim to gain a deeper understanding of the primary influences of dust formation in a CWB system. A series of simulations were therefore run in order to determine how dust formation varies due to changes in orbital separation and wind momentum ratio. A baseline simulation with properties similar to WR98a with a circular orbit and identical stellar masses was created. This baseline simulation has a momentum ratio of 0.02. Other simulations were then run with different orbital separations and/or wind momentum ratios. Another set of simulations were run where the cooling mechanisms were selectively disabled, in order to understand how radiative cooling affects the dust production rate. Tables 4.2 and 4.3 detail the wind and orbital parameters of the baseline simulation. The orbital separation is modified by changing the orbital period of the simulation, while the wind momentum ratio is modified by adjusting the mass loss rate and wind terminal velocity for each star. Two simulation sub-sets for this were performed: simulations where the wind terminal velocities were adjusted for each star and simulations where the mass loss rates for each star were adjusted.

4.3.1 Cooling mechanisms

For this set of simulations, the influence of cooling was changed by varying which cooling routines are operating. All simulations in this set keep the same orbital and wind parameters, which are that of the baseline system described in Tables 4.2 & 4.3. One simulation has both plasma and dust cooling in operation (the `fullcool` simulation), while the other two simulations have plasma cooling only and no cooling, respectively (`plasmacool` and `nocool`, Table 4.4). The final, no radiative cooling simulation instead relies on adiabatic expansion for temperature change in

Name	Plasma cooling?	Dust cooling?
<code>fullcool</code>	Yes	Yes
<code>plasmacool</code>	Yes	No
<code>nocool</code>	No	No

Table 4.4: Cooling series simulation parameters.

the WCR; as such, this simulation behaves as if it has a χ value for both winds that is arbitrarily high. The post-shock flow in the `nocool` model will also be unable to compress as much due to the lack of energy loss via radiative cooling. The role of these simulations is to discern whether cooling alone, or other system parameters can affect dust production.

4.3.2 Wind momentum ratio

Another set of simulations was devised in order to assess the influence of the wind parameters on the formation of dust within a CWB. As the wind momentum ratio is dependent on both the mass loss rate and wind velocity of each star, each of these properties is modified over a set of different simulations. η is varied from 0.01 to 0.04 by adjusting the wind parameters for each star. This is further subdivided by which property is modified, either the mass loss rate or wind terminal velocity (Table 4.5). As the cooling parameter, χ , has a much stronger dependency on v^∞ than \dot{M} , the modification of either parameter while maintaining a similar value for η allows us to determine whether χ is the primary parameter determining the formation of dust within WCd systems. This can be seen when comparing simulations `mdot-1` and `vinf-1`, which have similar wind momentum ratios but the cooling parameters for the WC star differ by a factor of 32. These simulations are compared to the baseline simulation, which has a radiative post-shock WCR. All simulations were run for a minimum of 1 orbit. As these orbits are circular, there should be no major variance of the winds after the start-up transients are fully advected, save for some fluctuations.

4.3.3 Separation distance

A final series of simulations was performed with the wind parameters equivalent to the baseline model, but with differing orbital separations. The separation was altered by modifying the orbital period. The separation distance was varied from the baseline model of 4 AU up to 64 AU (Table 4.6), which has the effect of modifying the cooling parameter, χ , of each simulation without changing the wind momentum ratio; allowing us to further discern which is the dominant parameter influencing dust formation. For instance, simulation `dsep-64AU` has a cooling

4. AN EXPLORATION OF DUST GROWTH WITHIN WCD SYSTEMS

Name	\dot{M}_{WR}	\dot{M}_{OB}	v_{WR}^{∞}	v_{OB}^{∞}	η	χ_{WR}	χ_{OB}
baseline	$5.0 \times 10^{-6} M_{\odot} \text{ yr}^{-1}$	$5.0 \times 10^{-8} M_{\odot} \text{ yr}^{-1}$	10^8 cm s^{-1}	$2 \times 10^8 \text{ cm s}^{-1}$	0.02	1.20	1915
mdot-1	$1.0 \times 10^{-5} M_{\odot} \text{ yr}^{-1}$	$5.0 \times 10^{-8} M_{\odot} \text{ yr}^{-1}$	10^8 cm s^{-1}	$2 \times 10^8 \text{ cm s}^{-1}$	0.01	0.60	1915
mdot-2	$2.5 \times 10^{-6} M_{\odot} \text{ yr}^{-1}$	$5.0 \times 10^{-8} M_{\odot} \text{ yr}^{-1}$	10^8 cm s^{-1}	$2 \times 10^8 \text{ cm s}^{-1}$	0.04	2.39	1915
mdot-3	$5.0 \times 10^{-6} M_{\odot} \text{ yr}^{-1}$	$1.0 \times 10^{-7} M_{\odot} \text{ yr}^{-1}$	10^8 cm s^{-1}	$2 \times 10^8 \text{ cm s}^{-1}$	0.04	1.20	957
mdot-4	$5.0 \times 10^{-6} M_{\odot} \text{ yr}^{-1}$	$2.5 \times 10^{-8} M_{\odot} \text{ yr}^{-1}$	10^8 cm s^{-1}	$2 \times 10^8 \text{ cm s}^{-1}$	0.01	1.20	3830
vinf-1	$5.0 \times 10^{-6} M_{\odot} \text{ yr}^{-1}$	$5.0 \times 10^{-8} M_{\odot} \text{ yr}^{-1}$	$2 \times 10^8 \text{ cm s}^{-1}$	$2 \times 10^8 \text{ cm s}^{-1}$	0.01	19.1	1915
vinf-2	$5.0 \times 10^{-6} M_{\odot} \text{ yr}^{-1}$	$5.0 \times 10^{-8} M_{\odot} \text{ yr}^{-1}$	$5 \times 10^7 \text{ cm s}^{-1}$	$2 \times 10^8 \text{ cm s}^{-1}$	0.04	0.07	1915
vinf-3	$5.0 \times 10^{-6} M_{\odot} \text{ yr}^{-1}$	$5.0 \times 10^{-8} M_{\odot} \text{ yr}^{-1}$	10^8 cm s^{-1}	$4 \times 10^8 \text{ cm s}^{-1}$	0.04	1.20	30638
vinf-4	$5.0 \times 10^{-6} M_{\odot} \text{ yr}^{-1}$	$5.0 \times 10^{-8} M_{\odot} \text{ yr}^{-1}$	10^8 cm s^{-1}	10^8 cm s^{-1}	0.01	1.20	120

Table 4.5: Wind parameters for simulations varying the wind mass loss rate, \dot{M} , and terminal velocity, v^{∞} . η is the wind momentum ratio (Eq. 4.1), and χ is the cooling parameter (Eq. 4.4). Note that the value of χ does not take into account cooling due to dust.

Name	P	d_{sep}	χ_{WR}	χ_{OB}	Levels	Effective Resolution
dsep-4AU	1.80 yr	4 AU	1.20	1915	7	$(20480 \times 20480 \times 2560)$ cells
dsep-8AU	5.06 yr	8 AU	2.39	3830	6	$(10240 \times 10240 \times 1280)$ cells
dsep-16AU	14.3 yr	16 AU	4.79	7659	5	$(5120 \times 5120 \times 640)$ cells
dsep-32AU	40.5 yr	32 AU	9.57	15319	4	$(2560 \times 2560 \times 320)$ cells
dsep-64AU	115 yr	64 AU	19.1	30638	3	$(1280 \times 1280 \times 160)$ cells

Table 4.6: Parameters of simulations varying the separation distance, d_{sep} , between the stars.

parameter value approaching the fast WR wind model **vinf-1**, despite having a wind momentum ratio of 0.02.

Each simulation has a coarse resolution of $320 \times 320 \times 40$ cells, with a varying number of levels. As the separation distance is doubled, the static mesh refinement box around the stars is doubled in size and the number of levels is decremented. This manipulation of levels ensures that the number of cells between the stars is kept consistent and reduces memory usage. The extent for all simulations in this series were doubled over the other series in this paper to approximately $2000 \times 2000 \times 250$ AU. Similarly to the previous set of simulations, a minimum of 1 orbit was needed for each simulation, however, as the orbital period of each simulation varies, certain simulations were able to run for a significantly longer length of time, with data for multiple orbits being obtained.

4.3.4 Data collection

HDF5 files were generated at regular time intervals containing the primitive variables of the simulation: gas density, ρ , gas pressure, P , and wind velocity components, v_x , v_y and v_z . These variables were then used to derive other variables such as temperature and energy. The scalars

containing the dust-to-gas mass ratio, z , is also included. The wind “colour”, the proportion of gas from each star, was also tracked. A value of 1.0 indicates a pure WR wind while 0.0 indicates a pure OB wind.

The volume-weighted totals of all parameters of interest were also collected, such as the total gas and dust mass of the system and average grain radius. Average values, such as \bar{z} and \bar{a} , are mass-weighted. To calculate dust formation within the WCR, a method of determining if a cell was part of the wind collision region was devised - the cell density would be compared to the predicted density of a single smooth wind with the wind parameters of the WC star in the system:

$$\rho_{WC} = \frac{\dot{M}_{WC}}{4\pi r^2 v_{WC}^\infty}, \quad (4.24)$$

where r is the distance from the barycentre. This threshold value was set to $1.25\rho_{SW}$. Higher threshold values were found to be inaccurate at large distances from the barycentre. Other methods of detecting the WCR, such as determining wind mixing levels, were not successful in general.

4.4 Results

The first set of simulations were performed in order to assess whether the implemented cooling model would influence dust formation within the WCR. This was found to be the case. Figure 4.4 shows that with no cooling only a very small amount of dust formation occurs. Dust production in the radiative simulations is significantly higher, with the `fullcool` simulation having consistently higher dust formation rates than the `plasmacool` simulation. Figure 4.5 shows that at the temperatures present within the WCR, dust grains that are present can enhance the cooling, allowing the shocked gas to reach temperatures low enough for dust formation faster than if only plasma cooling was simulated.

In the case of the `fullcool` simulation, a peak dust formation rate of $7 \times 10^{-9} M_\odot \text{ yr}^{-1}$ was calculated. This fluctuation appears to be due to dust forming mostly in high density clumps (see Fig. 4.6). The average dust formation rate from these simulations is noted in Table 4.7. The observed rates are less than 0.1% of the theoretical maximum given by Eq. 4.23, which indicates that the average dust-to-gas ratio, z , in the WCR, does not exceed 10^{-3} .

As cooling is significant in the post-shock WR wind ($\chi_{WR} = 1.2$), further compression

4. AN EXPLORATION OF DUST GROWTH WITHIN WCD SYSTEMS

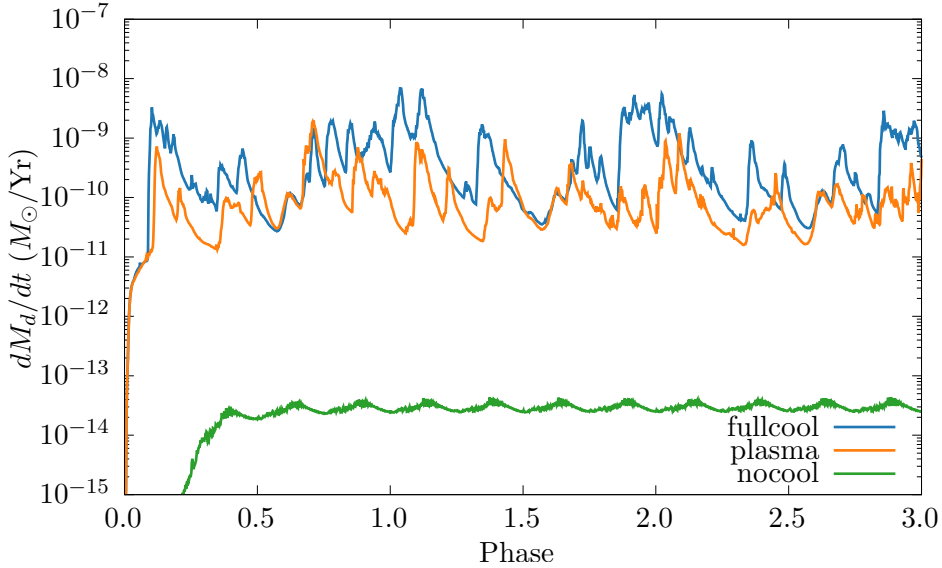


Figure 4.4: A comparison of the dust formation rates as the cooling mechanisms in the simulation are changed. Without adequate cooling barely any dust is formed. While dust formation increases with all cooling mechanisms enabled, plasma cooling is still the dominant cooling process between 10^4 and 10^9 K for dust production.

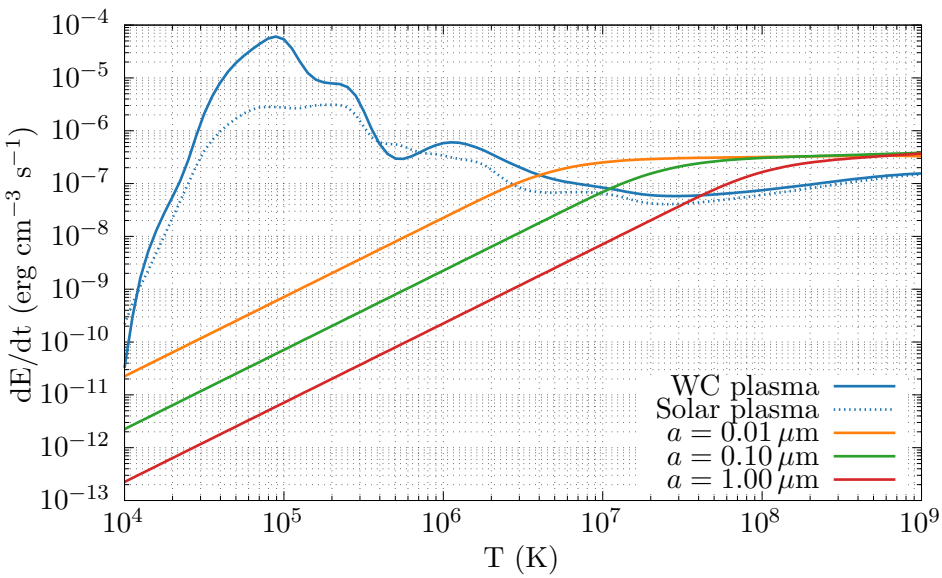


Figure 4.5: Comparison of the energy loss rate due to plasma and dust cooling with varying grain sizes, where $\rho_g = 10^{-16} \text{ g cm}^{-3}$ (typical of the density in the WCR) and a dust-to-gas mass ratio of 10^{-4} is assumed. Whilst less influential at lower temperatures, dust cooling can aid the overall cooling in the immediate high temperature post-shock environment.

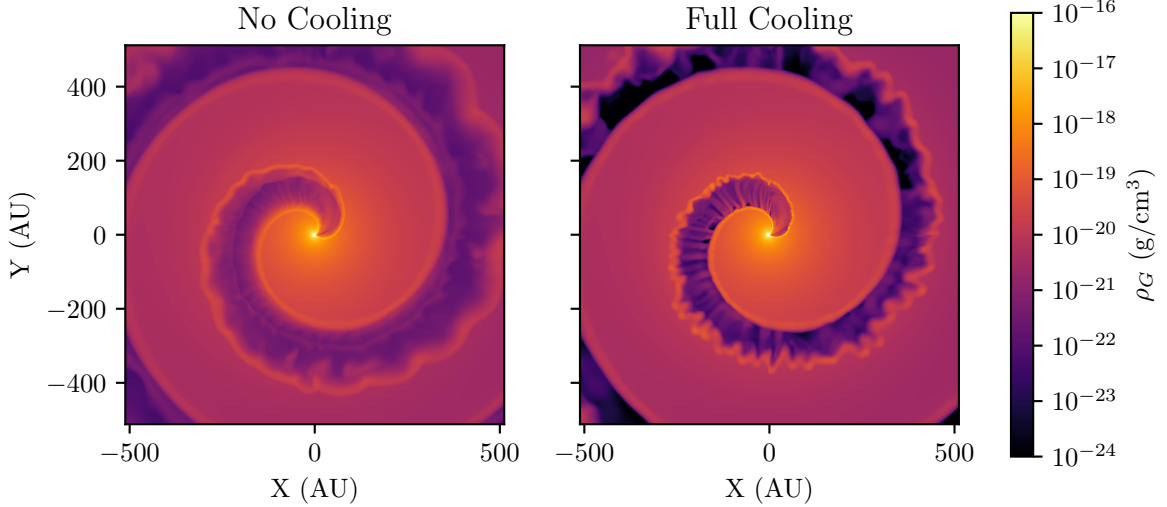


Figure 4.6: Density comparison in the orbital plane for the `nocool` and `fullcool` models. With cooling enabled instabilities are far more prevalent, with pockets of very high density material within the WCR.

occurs, resulting in much higher post-shock densities (Fig. 4.7). This rapid cooling results in ideal conditions for dust formation, especially within high density instabilities. A similar effect for the OB wind is not observed, as radiative energy losses are not influential on the dynamics of the flow, due to the faster, significantly less dense stellar wind ($\chi_{\text{OB}} = 1915$). Fig. 4.8 shows that the `fullcool` simulation has a similar immediate-post shock temperature to an adiabatic model, but the shocked WR wind cools to the floor temperature within an extremely short timescale, allowing the nascent dust grains to grow. We also observe that simulations with cooling have a markedly more mixed wind, due to instabilities in the post-shock environment (Fig. 4.9). Fig. 4.10 shows that dust clumps form shortly after the initial wind collision. These clumps rapidly convert post-shock gas to dust. However, rapid dust production tapers off as the post-shock flow becomes more diffuse. This behaviour is similar to the dust simulations described in Harries et al. (2004) and Hendrix et al. (2016), which indicate that the bulk of dust formation occurs only a short distance from the parent stars. The post-shock temperature is significantly lower in the leading edge of the WCR relative to the orbital motion, leading to a larger portion of dust forming in this region. The lower temperature is due to the more rapid cooling caused by the higher density on this side of the WCR (see below).

Pittard (2009) notes that in the case of colliding winds with $\eta = 1$ the trailing edge of the WCR takes part in oblique shocks with the stellar winds, while the leading edge is shadowed by the upstream WCR from the colliding material. This results in a trailing edge with strong

4. AN EXPLORATION OF DUST GROWTH WITHIN WCD SYSTEMS

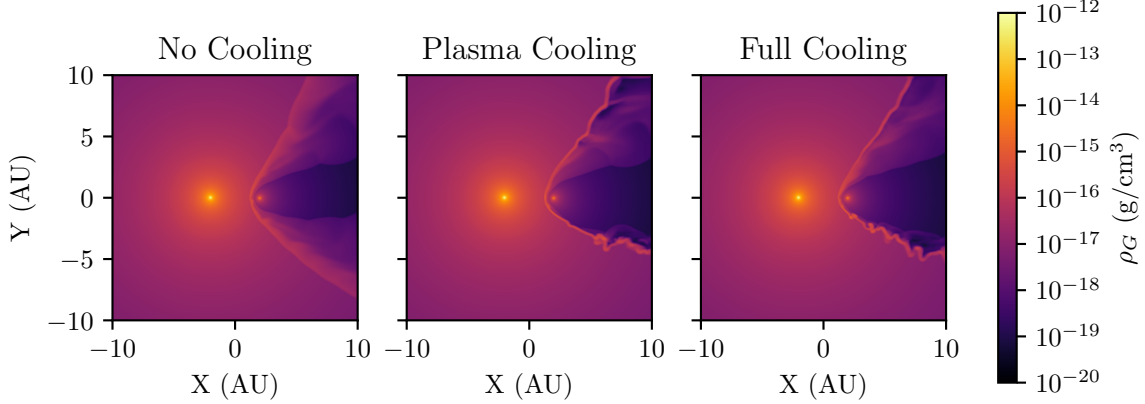


Figure 4.7: Density comparison in the orbital plane of simulations with differing radiative processes.

Model	η	χ_{WR}	χ_{OB}	$\dot{M}_{\text{d},\text{avg}}$ $M_{\odot} \text{ yr}^{-1}$	$\dot{M}_{\text{d},\text{max}}$ $M_{\odot} \text{ yr}^{-1}$
<code>fullcool</code>	0.02	1.20	1915	5.38×10^{-10}	9.06×10^{-7}
<code>plasmacool</code>	0.02	1.20	1915	1.29×10^{-10}	9.06×10^{-7}
<code>nocool</code>	0.02	1.20	1915	2.71×10^{-14}	9.06×10^{-7}

Table 4.7: Average rate of dust production for the set of different radiative simulations. $\dot{M}_{\text{d},\text{max}}$ is the maximum expected dust formation rate (Eq. 4.23).

instabilities and cool, high density clumps of post-shock wind, while the leading edge has a low density flow that is not dominated by instabilities. This does not appear to occur in these low- η systems, as oblique shocks occur at a much greater distance, where the stellar wind is significantly less dense. Instead, the leading edge of the WCR appears to be much thinner and denser than the trailing edge. This is believed to be due to the leading edge interacting more strongly with the outflowing material due to the orbital motion of the stars, sweeping up material and obliquely shocking with the downstream WCR. Most of the dust formation then occurs in the downstream post-shock region of the leading edge of the WCR, as soon as it has sufficiently cooled (Fig. 4.10). Furthermore, dust formation slows significantly as the post-shock wind begins to diffuse, limiting the dust formation to a region around 100 AU from the WCR apex. This is in agreement with Williams, van der Hucht, Thé and Bouchet (1990) and Hendrix et al. (2016), who found that there is a limited region suitable for dust formation.

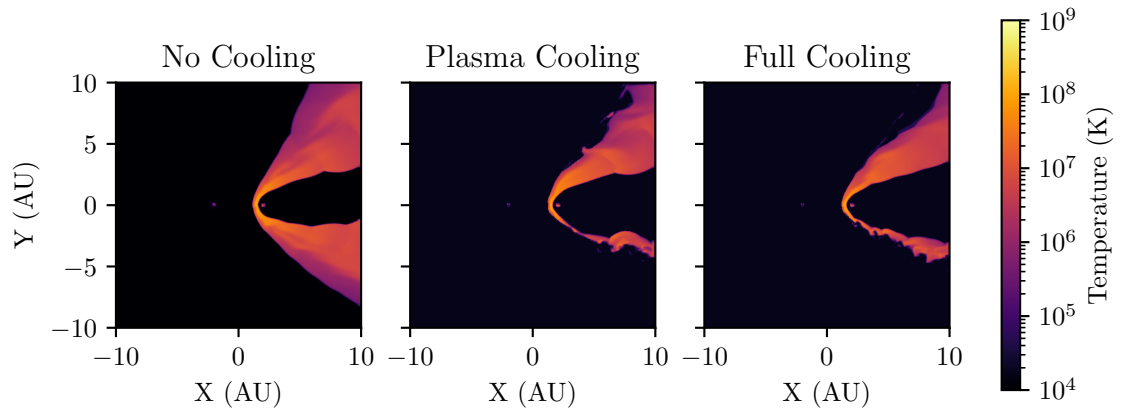


Figure 4.8: Temperature comparison in the orbital plane of simulations with differing radiative processes.

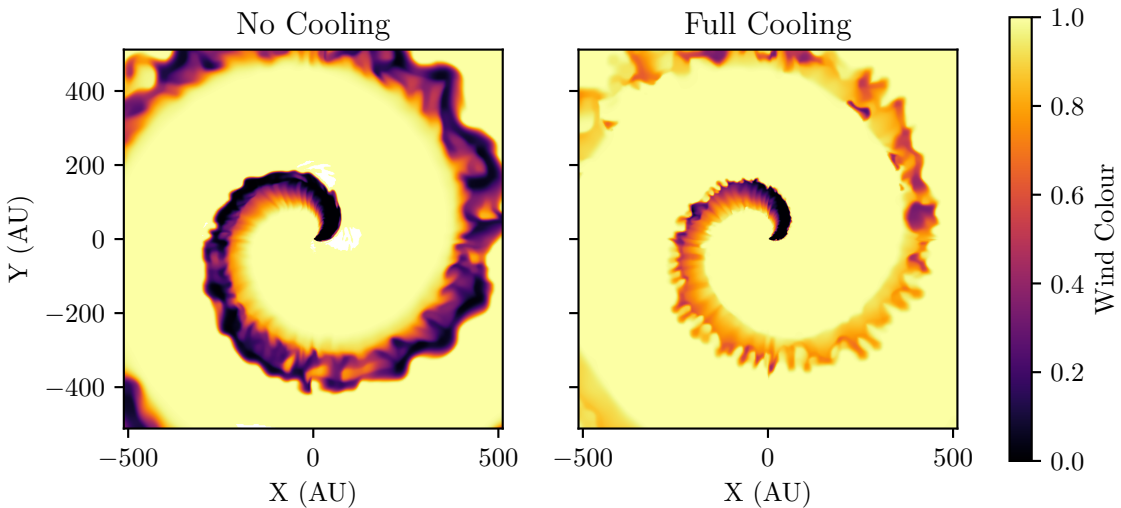


Figure 4.9: Wind “colour” for `nocool` and `fullcool` models. The WCR is more thoroughly mixed if the simulation is allowed to cool.

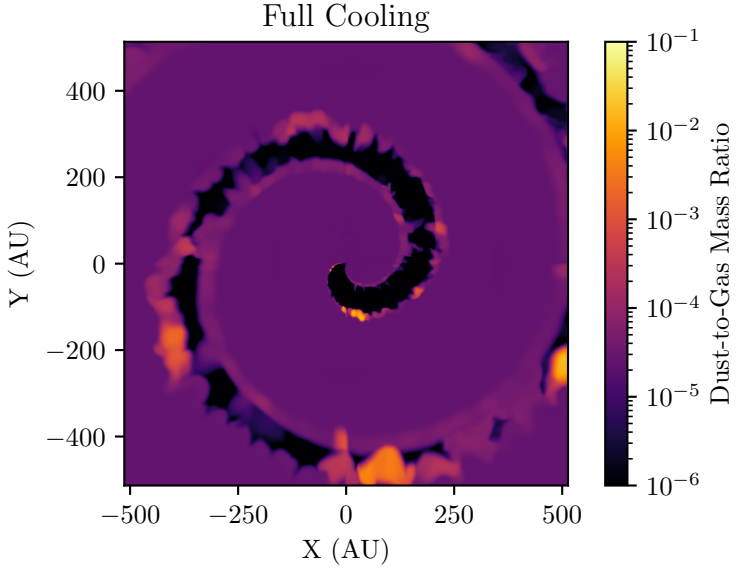


Figure 4.10: The full extent of the `baseline` simulation, showing the dust-to-gas mass ratio in the orbital plane. Dust typically forms in clumps within instabilities, leading to a variation of the dust formation rate as the simulation progresses. Most of the dust forms in the leading arm of the WCR.

4.4.1 Mass loss rate variation

The dust formation rate in the mass loss rate variation simulations was found to be dependent on the strength of the WC or OB winds. As can be seen in Fig. 4.11 and Table 4.8, the rates are separated into similar dust production rates for simulations with increases or decreases in mass loss rates; simulations with either wind being stronger than the `baseline` simulation produced most dust, while simulations with weaker winds produced approximately 3 orders of magnitude less dust than the most productive simulations. This result appears to be proportional to the wind momentum ratio. For instance, `mdot-1` and `mdot-3` produce on average two orders of magnitude more dust than the `baseline` simulation. These simulations have an identical value for η , but differ in total mass loss rate by a factor of 2. This suggests that a stronger shock can increase the dust production rate, due to higher post-shock densities and more cooling. Some of this value can be attributed to the changing number density of grains, particularly in simulations `mdot-1` and `mdot-2`, where the relative grain number density increases and decreases by a factor of 2 respectively. In the case of `mdot-1` this doubles the number density of grains, increasing the amount of dust cooling, and increases the number of grain nucleation sites for dust formation.

4.4 Results

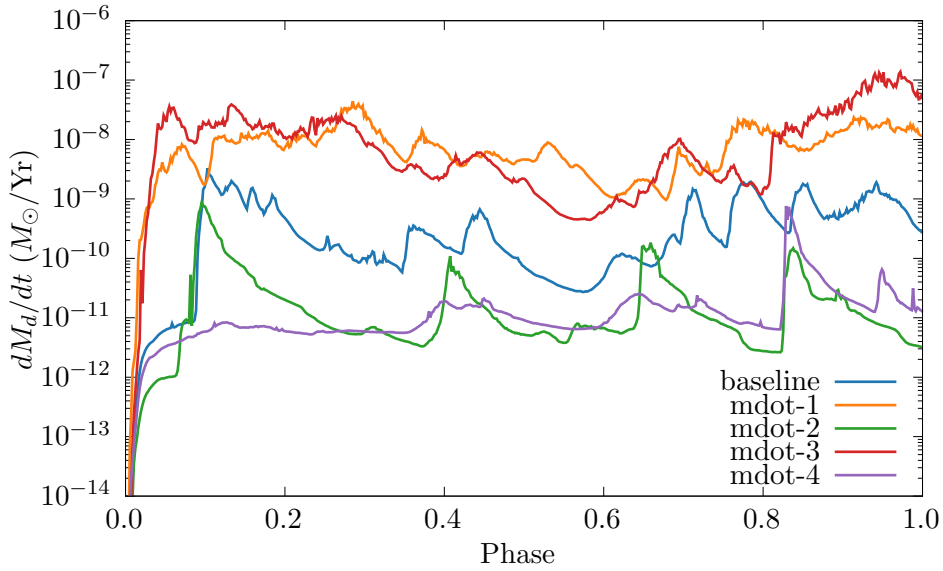


Figure 4.11: A comparison of the dust production rates for simulations that vary the mass loss rate, \dot{M} . Simulations with either a strong primary or secondary wind produce similar levels of dust, whilst if either wind is weaker, the dust production rate is reduced.

Model	η	χ_{WR}	χ_{OB}	$\dot{M}_{\text{d,avg}}$ $M_{\odot} \text{ yr}^{-1}$	$\dot{M}_{\text{d,max}}$ $M_{\odot} \text{ yr}^{-1}$
baseline	0.02	1.20	1915	5.38×10^{-10}	9.06×10^{-7}
mdot-1	0.01	0.60	1915	8.79×10^{-9}	1.42×10^{-6}
mdot-2	0.04	2.39	1915	2.53×10^{-11}	5.83×10^{-7}
mdot-3	0.04	1.20	957	2.34×10^{-8}	1.17×10^{-6}
mdot-4	0.01	1.20	3830	3.81×10^{-11}	7.11×10^{-7}

Table 4.8: Average rate of dust production for the mass loss rate simulation set.

4. AN EXPLORATION OF DUST GROWTH WITHIN WCD SYSTEMS

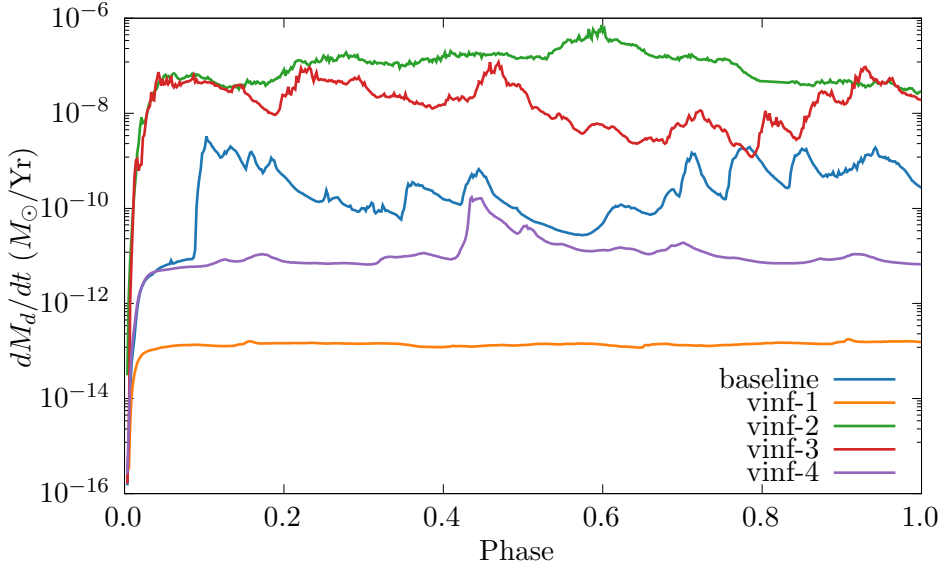


Figure 4.12: Comparison of the dust production rate for simulations varying the wind terminal velocity, v^∞ . Simulations with a strong wind velocity imbalance produce significantly more dust than their counterparts.

4.4.2 Terminal velocity variation

Varying the wind terminal velocity also has an extremely strong effect on the dust formation (see Fig. 4.12 and Table 4.9). The dust production rate is exceptionally high in the case of vinf-2, which has an extremely slow wind velocity of 500 km s^{-1} , closer to that of a typical LBV star than that of a WC (Table 4.9). This very slow, dense wind experiences very strong radiative cooling in the post-shock environment ($\chi_{\text{WR}} = 0.07$), leading to high density pockets of cooled gas. This can be seen in Fig. 4.13, where vinf-2 produces large quantities of dust near the apex of the WCR on the WR side, which is then mixed throughout the WCR. The factor of 4 difference in the wind velocity between the WR and OB winds creates a very strong velocity shear, leading to the formation of Kelvin-Helmholtz instabilities.

It should be noted that the dust production in general increased *outside* of the WCR in the case of vinf-2 (i.e. in the unshocked WR wind). This is largely due to the significantly higher wind density within the WC wind, and the increase in the time available for grain growth before the wind collision. Despite this, the dust production outside of the WCR does not dominate the total dust production, most of which occurs in the WCR still. In the numerical analysis (Fig. 4.12 and Table 4.9) of dust production we do not include dust produced outside of the wind collision region. In the case of a fast WC wind (vinf-1) with a largely adiabatic WCR, dust production effectively ceases, with an average dust production rate of $9 \times 10^{-14} M_\odot \text{ yr}^{-1}$,

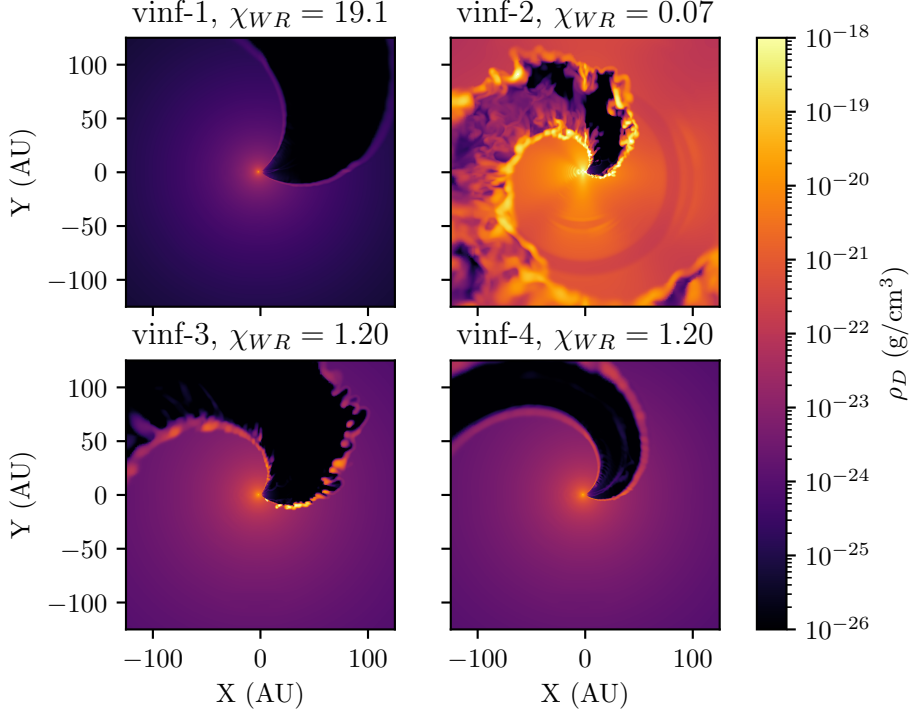


Figure 4.13: Comparison of the dust density in the simulations that vary v^∞ . Simulations with either a high OB wind velocity or low WC wind velocity produce large quantities of dust. Simulation **vinf-1**, which has a high velocity WC wind with $\chi_{WR} = 19.1$, does not produce any appreciable dust within the WCR. **vinf-1** and **vinf-4** have a smoother WCR with less instabilities as both winds have identical terminal speeds, resulting in no velocity shear.

two orders of magnitude less than **vinf-4**, despite the latter having a similar wind momentum ratio.

Simulations **vinf-3** and **vinf-4** show that when the secondary wind velocity is altered, drastic changes to the dust formation rate again occur, which is partially due to the prevalence and strength of instabilities. A greater velocity shear along the discontinuity results in strong Kelvin-Helmholtz instabilities in **vinf-3**, whereas these are missing in **vinf-4** which has equal wind speeds. Both **vinf-2** and **vinf-3** exhibit very strong KH instabilities, and both have a terminal velocity ratio, $v_{\text{OB}}^\infty/v_{\text{WR}}^\infty = 4$. This augments the already present thermal instabilities due to radiative cooling, leading to a less ordered, clumpy post-shock environment. In Fig. 4.14 where **vinf-3** and **vinf-4** are directly compared, the presence of a much faster secondary wind results in a velocity shear that produces a much broader WCR, with high density pockets formed within instabilities, which appear to produce the bulk of the dust, despite both simulations having an adiabatic second wind. This suggests that prolific dust formation occurs in a post-shock

4. AN EXPLORATION OF DUST GROWTH WITHIN WCD SYSTEMS

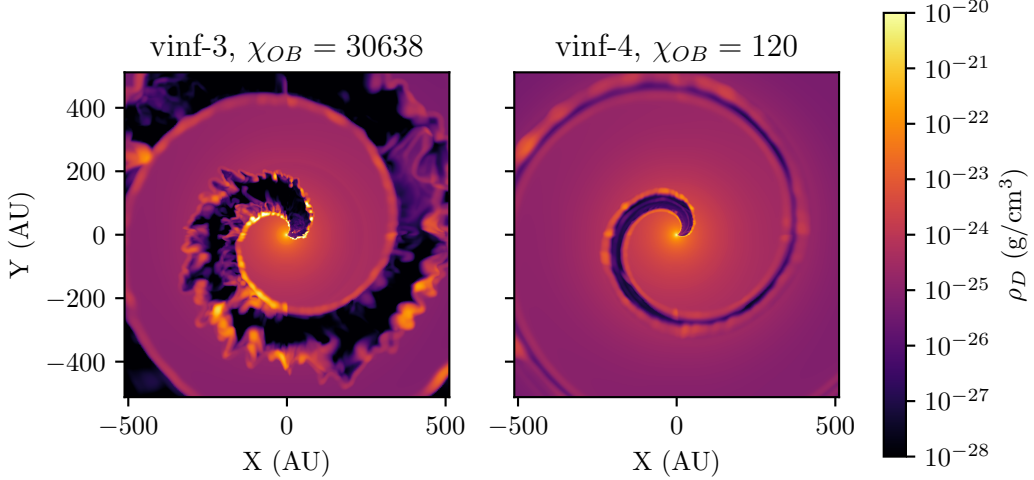


Figure 4.14: Comparison of the dust density in simulations with modified OB wind terminal velocities. The simulations are fully advected with 3 orbits calculated. Dust formation and instabilities are far more pronounced in `vinf-3`, which has an OB wind velocity a factor of 4 larger than `vinf-4`.

Model	η	χ_{WR}	χ_{OB}	$\dot{M}_{\text{d},\text{avg}}$ $M_{\odot} \text{ yr}^{-1}$	$\dot{M}_{\text{d},\text{max}}$ $M_{\odot} \text{ yr}^{-1}$
<code>baseline</code>	0.02	1.20	1915	5.38×10^{-10}	9.06×10^{-7}
<code>vinf-1</code>	0.01	19.1	1915	8.88×10^{-13}	7.11×10^{-7}
<code>vinf-2</code>	0.04	0.07	1915	1.17×10^{-7}	1.17×10^{-6}
<code>vinf-3</code>	0.04	1.20	30638	6.30×10^{-11}	1.17×10^{-6}
<code>vinf-4</code>	0.01	1.20	120	1.94×10^{-8}	7.11×10^{-7}

Table 4.9: Average rates of dust production for the terminal velocity simulation set.

primary wind shaped by instabilities, produced either from strong radiative cooling, or through a strong velocity shear, leading to K-H instabilities. We note also that the dust formation rates appear to be stratified somewhat in terms of η . Simulations where $\eta = 0.04$ produce significantly more dust than simulations with more imbalanced winds (Fig. 4.12).

By directly comparing two prolific dust producing models with $\eta = 0.04$, models `vinf-3` and `mdot-3`, we can see that both WCRs are dominated by instabilities. However, of the two, `vinf-3` is more thoroughly mixed (Fig. 4.15). In particular, it has a much larger trailing edge that produces large quantities of dust (Fig. 4.16). These simulations produce approximately the same amount of dust, with `vinf-3` also consistently producing dust in the trailing edge of the WCR. From these results it is clear that the dust production rate is increased if there is a highly imbalanced wind velocity (with a slow WC and fast OB wind), as this leads to a post-shock environment governed by thin-shell and Kelvin-Helmholtz instabilities.

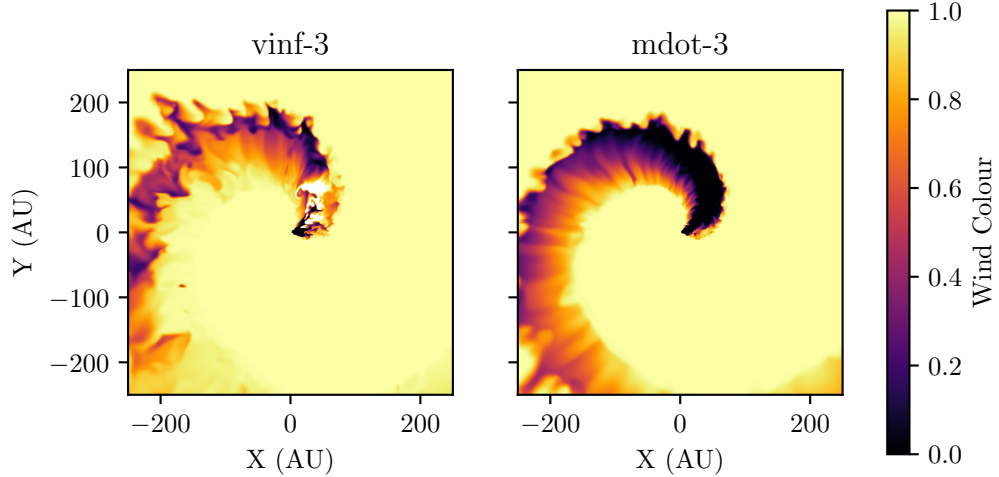


Figure 4.15: Comparison of the wind colour in simulations `vinf-3` and `mdot-3`. The WR wind has a colour of 1.0 while the OB wind has a colour of 0.0. Wind mixing is significantly more pronounced in `vinf-3` than in `mdot-3`. In `vinf-3` the post-shock WR wind is strongly influenced by Kelvin-Helmholtz instabilities, due to the increased wind velocity imbalance and lower degree of cooling.

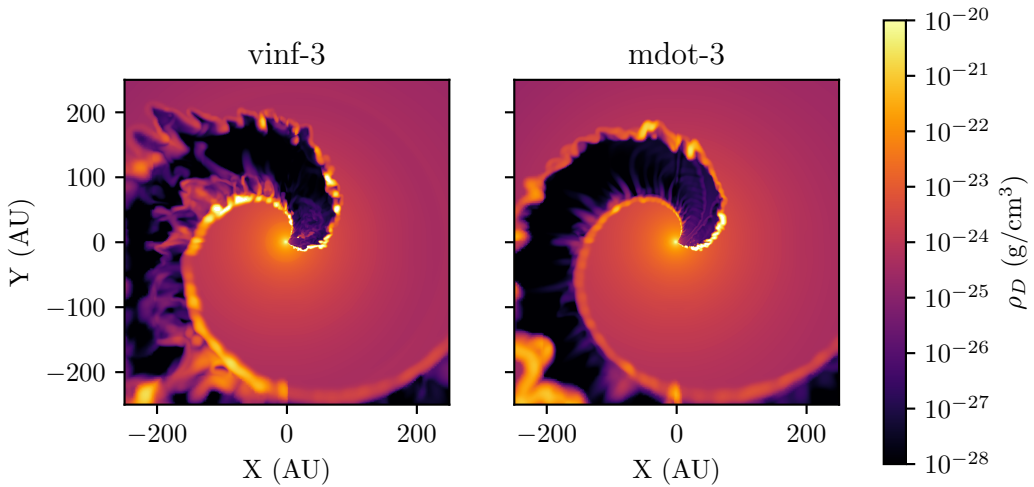


Figure 4.16: Comparison of the dust density in simulations with a strong secondary wind, models `vinf-3` and `mdot-3`. Dust in `vinf-3` is produced to a much higher degree in the trailing edge of the WCR wind, rather than on the leading edge as in `mdot-3`. The increased mixing of the winds in `vinf-3` due to Kelvin-Helmholtz instabilities has led to dust forming throughout the WCR, rather than being concentrated near the apex of the WCR.

4. AN EXPLORATION OF DUST GROWTH WITHIN WCD SYSTEMS

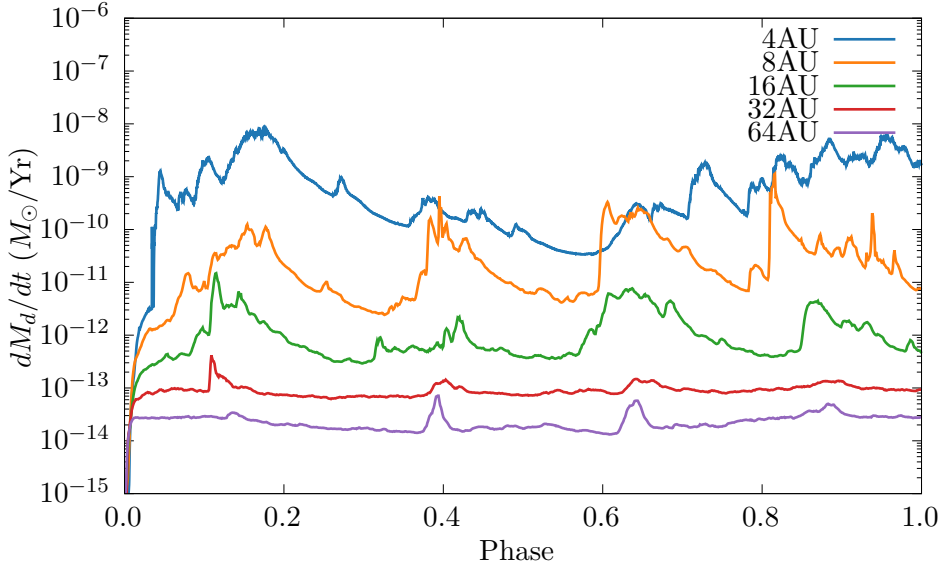


Figure 4.17: A comparison of dust formation rates versus orbital phase for a set of simulations that vary the separation of the stars, d_{sep} . A clear inverse relationship between separation distance and dust production rate exists, due to the WCR behaving more adiabatically when the stars have a greater separation.

4.4.3 Separation variation

There is a clear correlation between the separation distance of the stars and the dust formation rate, with dust production drastically increasing as the orbital separation is decreased (Fig. 4.17 and Table 4.10). This influence on the dust formation rate is non-linear, with a doubling of the separation distance decreasing the dust production rate by approximately one order of magnitude. At very large separations, very little dust is produced. Clearly, dust formation is strongly influenced by the wind density at collision and the strength of the post-shock cooling. The variability of the dust production rate also appears to increase as the separation distance is reduced, leading to instances where a simulation may temporarily produce more dust than a simulation with a tighter orbit, such as the case with $d_{\text{sep}}=4\text{AU}$ and $d_{\text{sep}}=8\text{AU}$ at an orbital phase of $0.6 < \Phi < 0.65$. As we have previously discussed, instabilities drive slightly intermittent, but highly efficient dust formation, which cause these fluctuations (Fig. 4.18). Our results are consistent with observations of episodic dust forming systems, where infrared emission due to dust is maximised at or shortly after periastron passage.

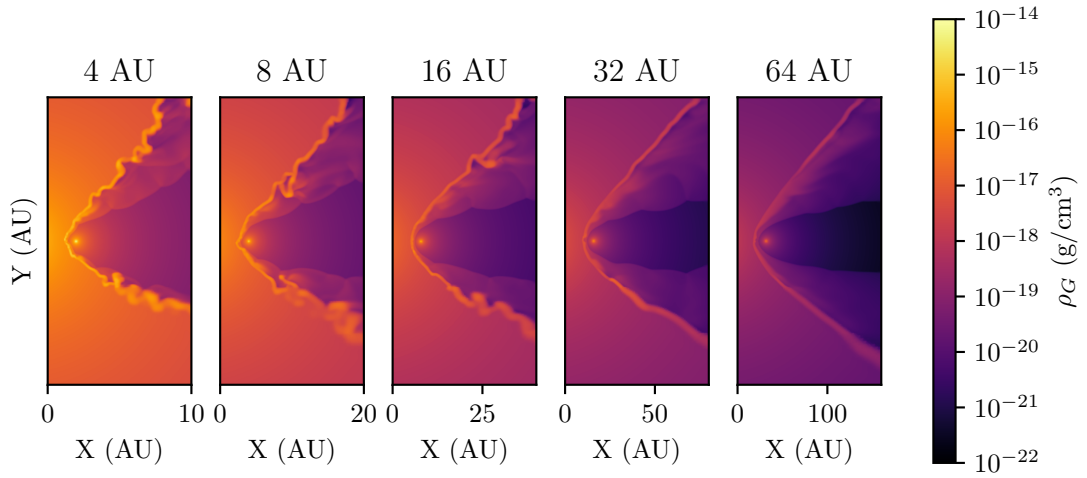


Figure 4.18: A comparison of the structures of simulations varying d_{sep} . The scale of each plot has been changed to allow for a similar feature size. Simulations with a closer stellar separation have collision regions whose structure is more strongly influenced by instabilities – in particular by thin-shell instabilities brought on by the radiative behaviour in the WCR.

Model	χ_{WR}	χ_{OB}	$\dot{M}_{\text{d,avg}}$ $M_{\odot} \text{ yr}^{-1}$	$\dot{M}_{\text{d,max}}$ $M_{\odot} \text{ yr}^{-1}$
<code>baseline</code>	1.20	1915	5.38×10^{-10}	9.06×10^{-7}
<code>dsep-8AU</code>	2.39	3830	4.39×10^{-11}	9.06×10^{-7}
<code>dsep-16AU</code>	4.79	7659	1.77×10^{-12}	9.06×10^{-7}
<code>dsep-32AU</code>	9.57	15319	8.83×10^{-14}	9.06×10^{-7}
<code>dsep-64AU</code>	19.1	30638	2.41×10^{-14}	9.06×10^{-7}

Table 4.10: Average rates of dust production for the separation distance simulation set. The stellar parameters are the same as in the `baseline` model, which has a $d_{\text{sep}} = 4.0 \text{ AU}$.

4. AN EXPLORATION OF DUST GROWTH WITHIN WCD SYSTEMS

4.5 Summary & Conclusion

Through these simulations we have how the dust yield changes for systems with differing wind and orbital parameters. The simulations in this paper were conducted over a fairly limited parameter space of mass loss rates and wind terminal velocities. Despite this, the dust production rate varied by up to 6 orders of magnitude. Dust formation was found to be extremely sensitive to the wind properties of both stars, which imposes a limited range of wind parameters for dust to form efficiently. As the stellar mass loss rates change, we find that dust production increases if either star has a greater mass loss rate; additionally systems with higher mass loss rates undergo stronger cooling. This change could also be attributed to the increased number density of dust grains in the WC wind in the case of simulation `mdot-1`. However, we find that a similar effect occurs when increasing the mass loss rate of the OB star, which does not inject dust into the simulation. If the wind *velocities* are more imbalanced we find that the dust production rate increases significantly as well. This is most likely due to the presence of KH instabilities from an increased wind shear. Dust production is also affected by the orbital properties. As the stellar separation increases, we find a corresponding drop in the dust production rate, due to the reduction in instabilities that generate high-density clumps, as well as the reduced shock intensity as the winds become more diffuse with distance.

Our simulations explain why dust forming systems are comparatively rare, compared to the total number of systems with massive binary stars and interacting winds, and also why periodic dust forming systems have eccentric orbits. The baseline system, which is representative of WR98a, has a significantly lower stellar mass loss rate than other well-characterised WCd systems, such as WR140 and WR104. Future simulations will focus on these other systems to explore how closely they match observations. The production of dust in high density clumped regions could also explain the formation of dust in single WC stars, which can form dust in significantly lower quantities.

Furthermore, we note that the dust production rate from our `baseline` simulation is somewhat lower than the predicted dust production rate of WR98a. A predicted value of approximately $6 \times 10^{-7} M_{\odot} \text{ yr}^{-1}$ was calculated for WR98a (Lau et al., 2020). This discrepancy is due to a variety of factors:

- Slightly different mass loss rates and wind terminal velocities of the system and the simulation. The estimated value of v_{WR}^{∞} in WR98a is 90% of the simulation value, and as such would correspond to a significant increase in production rate based on our results.

- Incompleteness of the grain growth model and a lack of other growth mechanisms, such as initial growth due to impinging carbon ions.
- An incorrect value for the grain sticking factor, which was extremely conservative and could underestimate dust growth by a significant amount.

These factors should not affect the qualitative analysis of this work, however. A more in-depth analysis of WCd systems using an improved version of this model will allow us to make quantitative comparisons of the dust formation rate in future work.

4.5.1 Wind mixing within the WCR

While the interaction between hydrogen and dust grains is not simulated by our dust model, elements such as hydrogen are crucial for forming complex organic molecules. As the WC wind is extremely hydrogen-poor, significant wind mixing would need to occur (Herbst & van Dishoeck, 2009). Figure 4.9 shows that the wind is far more effectively mixed by instabilities if it is sufficiently radiative. An improved dust model which can calculate grain yields from chemical reactions could be used to investigate this further. Conveniently, implementation of a chemical model into Athena++ through passive scalars is a future feature in the projects roadmap. Additionally, a multi-fluid model could be used to model the dynamics of grains, as larger grains may not necessarily be co-moving in a turbulent wind environment.

4.5.2 Summary

Our parameter space exploration of colliding wind binary systems undergoing dust formation yields new insights into how dust forms within the WCR. Dust production within these systems is poorly understood, and with direct observations of the WCR rendered difficult by the extreme conditions of these systems, it falls on numerical simulation to elucidate the nature of dust production in CWBs. Our simulations reveal how sensitive to changing wind conditions this dust production is. This parameter space exploration, whilst quite conservative, resulted in a change in dust formation rates of up to 6 orders of magnitude. In all simulations, the bulk of dust formation was found to occur within high-density pockets formed through thin-shell or Kelvin-Helmholtz instabilities, suggesting that strong cooling and a fast secondary wind are both important factors for dust production. For high levels of dust formation, an ideal system should have a slow, dense primary wind and a fast, dense secondary wind, with a close orbit.

4. AN EXPLORATION OF DUST GROWTH WITHIN WCD SYSTEMS

This combination of properties ensures the formation of dense pockets of cool post-shock gas in which dust formation proceeds.

There is significant potential for additional research in this field. Parameter mixing was not performed, due to the simulation time required for producing many more simulations, but performing examples on more extreme systems, such as those with a LBV primary star or a WR+WR system is a potential avenue of research. Future work could introduce additional dust formation and destruction mechanisms, such as grain-grain collision or photodissociation. Modelling effects such as radiative line driving or use of a multi-fluid model could also prove fruitful. Another interesting avenue of research is the simulation of eccentric, periodic dust forming systems; simulating either an entire or a partial orbit of a system such as WR140 would be a logical next step for this work.

CHAPTER 5

Exploring Dust Growth in the Episodic WCd System
WR140 (Eatson et al., [2022b](#))

5. EXPLORING DUST GROWTH IN WR140

Abstract

The wind collision region (WCR) in a colliding wind binary (CWB) is a particularly violent place, as such, it is surprising that it is also a region where significant quantities of interstellar dust can form. In extreme cases, approximately 30% of the total mass loss rate of a system can be converted into dust. These regions are poorly understood, as observation and simulation of these systems are difficult. In our previous paper we simulated dust growth in CWB systems using an advected scalar model and found our model to be suitable for qualitative study. For this paper we simulated the periodic dust forming CWB (WCd) system WR140 with our dust model, to determine how dust growth changes over the systems periastron passage. We found that dust production increases significantly at periastron passage, which is consistent with IR emission of the surrounding dusty shell. We also find that the dust production rate of the system decreases rapidly as the stars recede from each other, though the rate of decrease is significantly lower than the rate of increase during periastron passage. This was found to be due to strong cooling and its associated thermal instabilities, resulting in cool, high-density pockets of gas in the WCR where dust forms. The WCR also shows a degree of hysteresis, resulting in a radiative post-shock flow even when the stars are separated enough for the region to behave adiabatically.

5.1 Introduction

Dust formation in massive star binary systems is a particularly fascinating subject. Considering the immense photon fluxes and strong shocks involved, these systems should not form dust at all, and yet in some systems all evidence points to the contrary. Colliding wind binary (CWB) systems were first hypothesised to explain highly luminous and variable x-ray emission in systems such as V444 Cyg and γ^2 Vel (Prilutskii & Usov, 1976). These extremely bright emissions were found to be due to stellar wind collision with shock velocities of the order 10^3 km s^{-1} . The variability in x-ray emission can be explained if the phenomena occurs due to the orbit of a binary system, such as the Wind Collision Region (WCR) being occluded by the outflowing stellar winds and being occluded by the stars themselves. The system can also have an eccentric orbit, changing the shock strength as the orbital separation, d_{sep} , varies. Despite this dust-

hostile environment, CWB systems containing a Wolf-Rayet carbon phase star (WC) have been observed producing copious quantities of dust (so-called WCd systems). These systems typically convert around 1% of the stellar wind into dust a short time after wind collision; in more prolific systems such as WR104 up to 36% of the Wolf-Rayet (WR) outflow is converted into dust (Lau et al., 2020). This corresponds to dust production rates on the order of $10^{-6} M_{\odot} \text{ yr}^{-1}$, rivalling other profuse dust producing phenomena such as AGB stars.

WCd systems can be sub-categorised further, into persistent, variable and episodic dust forming systems. Persistent systems, such as WR104 (Tuthill et al., 1999), produce dust at a constant rate, and as such produce extreme quantities of dust, as well as well-defined pinwheel patterns if the system is viewed face-on. Episodic systems, meanwhile, only produce dust for a limited period before entering a period of dormancy; this pattern is cyclical, and is predictably periodic. A good example of such an episodic system is WR140 (Williams, van der Hucht, Pollock et al., 1990), the subject of this paper. Variable systems have some characteristics of these two sub-types, having a distinct variability without a period of dust producing dormancy, such as WR98a (Monnier et al., 1999).

Whether a system is persistent, variable or episodic is based on the system's orbital eccentricity. Highly eccentric systems appear to form episodic systems, with the “active” dust production period occurring immediately after periastron passage, and a relatively short time thereafter. Meanwhile, persistent and variable systems have been observed to have more circular orbits, suggesting that the effect of a change in system separation distance, d_{sep} , has a role in dust formation. The initial mechanism behind dust formation is not well understood. Whilst nascent amorphous carbon dust grain cores can condense within the photosphere of WC7-9 stars, these grain cores would be vaporised by the UV flux of both stars. However, within the WCR these grains appear to flourish. Observations of these systems show that infrared excess in wavelengths associated with amorphous grains is detected almost exclusively within the post-shock WCR (Soulain et al., 2018). Observations also indicate that dust formation occurs rapidly and close to the system, this requires strong radiative cooling for the immediate-post shock temperature to reduce from $\sim 10^7 \text{ K}$ to $\sim 10^4 \text{ K}$ (Williams, van der Hucht, Pollock et al., 1990; Williams et al., 1987).

As such, dust formation appears to be encouraged in the WCR through a multitude of factors:

- Strong radiative cooling produces clumps of cool, high density gas where dust can rapidly grow.

5. EXPLORING DUST GROWTH IN WR140

	Persistent		Variable		Episodic	
	Total	Example	Total	Example	Total	Example
WC4	1	WR19	0	—	0	—
WC5	0	—	0	—	1	WR47C
WC6	1	WR124-10	0	—	0	—
WC7	3	WR102-22	0	—	4	WR140
WC8	6	WR13	1	WR48a	3	WR122-14
WC9	45	WR104	6	WR98a	1	WR75-11
Total	56		7		9	

Table 5.1: WCd systems with a known spectral type and dust formation type from the Galactic Wolf Rayet Catalogue (Rosslowe & Crowther, 2015). Systems with uncertain spectral types are not included, while systems labelled “d” are included within the “persistent” category for their associated spectral type.

- The high density of the post-shock WCR results in a high collision rate between carbon atoms and dust grains.
- The high density also shields nascent dust grains from the bulk of the UV emission from the stars.
- The rapid cooling in the immediate post-shock environment reduces gas-grain sputtering.

The dust formation can also be influenced by orbital separation, velocity shear and momentum ratio imbalance between the winds, producing variability on the timescale of a single orbit, or $t_{\text{dyn}} \ll P$.

WCd systems are comparatively rare. Out of 106 confirmed WR binaries, only 9 are categorised as episodic WCd systems (Table 5.1). As these systems have a typical distance on the order of 1 – 10 kpc, observation of WCds is difficult. Whilst these systems can be observed and the dusty WCR can be resolved, observation of the innermost, immediate post-shock dust forming region is not possible at this distance. As such, numerical simulation is necessary to determine dust formation in WCd systems. A contemporary example of such simulations is Hendrix et al. (2016), though the evolution of dust grains through cooling, growth and sputtering was not performed. In this paper we present a numerical simulation of the archetypical episodic WCd system WR140 with a co-moving dust model simulating grain growth and sputtering through gas-grain collisions. This simulation covers a temporal slice of the orbit of WR140 from phase $\Phi = 0.95$ to $\Phi = 1.10$, or the period immediately prior to and after periastron passage. We will discuss our methodology in Section 5.2, with a particular emphasis on our dust model in Subsection 5.2.2. Afterwards we will discuss the simulation and WR140 system parameters, as well as our data collection techniques in Section 5.3. Finally, we will discuss our results and conclude in Sections 5.4 and 5.5.

5.2 Methodology

The periodic dust forming system WR140 was simulated using a fork of the Athena++ hydrodynamical code (Stone et al., 2020). A series of modifications were implemented to simulate binary system orbits, stellar wind outflows and dust evolution. These simulations were conducted in 3D in a Cartesian co-ordinate system. The code solves a Riemann problem at each cell interface to determine the time-averaged values at the zone interfaces, and then solves the equations of hydrodynamics:

$$\frac{\partial \rho}{\partial t} + \nabla \cdot (\rho \mathbf{u}) = 0, \quad (5.1a)$$

$$\frac{\partial \rho \mathbf{u}}{\partial t} + \nabla \cdot (\rho \mathbf{u} \mathbf{u} + P) = 0, \quad (5.1b)$$

$$\frac{\partial \rho \varepsilon}{\partial t} + \nabla \cdot [\mathbf{u} (\rho \varepsilon + P)] = \mathcal{L}_T, \quad (5.1c)$$

where ε is the total specific energy ($\varepsilon = \mathbf{u}^2/2 + e/\rho$), ρ is the gas density, e is the internal energy density, P is the gas pressure and \mathbf{u} is the gas velocity. In order to simulate radiative losses, the parameter \mathcal{L}_T is included, which is the energy loss rate per unit volume from the fluid due to gas and dust cooling.

Spatial reconstruction using a piecewise linear method was performed, while the simulation was run with one of two numerical integrators, depending on the system stability. The integrators used were a 3rd order accurate Runge-Kutta integrator (**rk3**), as well as a 4th order accurate, 5-stage, 3 storage register strong stability preserving Runge-Kutta integrator (**ssprk5_4**; Ruuth and Spiteri (2005)). The **ssprk5_4** integrator was found to be approximately 60% slower, but significantly more stable.

Several passive scalars are utilised to model wind mixing and dust evolution, which are transported by the fluid. For a given scalar, i , the scalar is advected through the following equation:

$$\frac{\partial}{\partial t} (\rho C_i) + \nabla \cdot (C_i \rho \mathbf{u}) = 0, \quad (5.2)$$

where C_i is the scalar quantity.

Stellar winds are simulated by modifying the density, ρ_R , momentum, p_R , and energy, E_R in a small region around both stars. Winds flow from this “remap” region at the stars wind terminal velocity, v^∞ . Remap zone parameters are calculated with the formulae

5. EXPLORING DUST GROWTH IN WR140

$$\rho_R = \frac{\dot{M}}{4\pi r^2 v_\infty}, \quad (5.3a)$$

$$p_R = \rho_R v_R, \quad (5.3b)$$

$$E_R = \frac{P_R}{\gamma - 1} + \frac{1}{2} \rho_R v_\infty^2, \quad (5.3c)$$

where P_R is the cell pressure ($P_R = \rho_R k_B T_w / \mu m_H$), T_w is the wind temperature, μ is the mean molecular mass, m_H is the mass of a hydrogen atom, v_R is the wind velocity as it flows radially from the center of the “remap zone” and r is the distance from the current cell to the centre of the remap zone. This method produces radially out-flowing winds from the star with an expected density and velocity.

Line driving and wind acceleration effects are not simulated; instead, winds are instantaneously accelerated to their terminal velocity. Gravitational forces are not calculated as the winds are assumed to be travelling in excess of the system escape velocity.

Athena++ utilises Message Passing Interface (MPI) parallelism. The numerical problem is broken into blocks, which are distributed between processing nodes on a High Performance Compute (HPC) cluster. The block size is variable, but for this simulation a block size of $40 \times 40 \times 10$ cells in XYZ was found to be optimal. Static mesh refinement is used to increase the effective resolution of the simulation. A region around the orbital path of the stars in the simulation is refined to a higher resolution, with gradual de-refinement as a function of distance from this refinement region. This refinement is covered in more detail in Section 5.3.2.

5.2.1 Radiative cooling

Cooling is simulated via the removal of thermal energy from a cell at each time-step. A cooling rate for radiative emission from the stellar winds, \mathcal{L}_g , is calculated and integrated using a sub-stepping Euler method. The number of sub-steps is determined by the estimated cooling timescale of the cell. Cooling is calculated via individual lookup tables from each wind. These lookup tables contain the normalised emissivity, $\Lambda_w(T)$ at a logarithmically spaced series of temperatures from 10^4 K to 10^9 K. The cooling rate is determined for a cell by calculating the cell temperature and estimating $\Lambda_w(T)$ using linear interpolation between the nearest emissivity values in the lookup table. As the two winds have significantly different abundances and can be thoroughly mixed in the WCR, we calculate an emissivity value for gas in a particular cell with the equation

$$\Lambda_g(T) = C\Lambda_{w,WR}(T) + (1 - C)\Lambda_{w,OB}(T), \quad (5.4)$$

where C is the wind “colour”, or mixing fraction, where 1 is a pure WR wind and 0 is a pure OB wind. \mathcal{L}_g , is then calculated through the equation

$$\mathcal{L}_g = \left(\frac{\rho_g}{m_H} \right)^2 \Lambda_g(T), \quad (5.5)$$

where ρ_g is the gas density and m_H is the mass of hydrogen. The lookup table was generated by mixing a series of cooling curves from MEKAL calculation of elemental gasses. These curves were combined based on the elemental abundances in the WC and OB winds. To save calculation time, temperatures between $10^4 \text{ K} < T \leq 1.1 \times 10^4 \text{ K}$ are set to 10^4 K as they are assumed to be either rapidly cooling or a part of the stellar wind outside of the WCR. A minimum temperature of 10^4 K is defined by the simulation, as it is assumed that a radiating post-shock wind will tend to the temperature of the pre-shock wind, $T_{\text{final}} \rightarrow T_{\text{pre-shock}}$.

5.2.2 Dust model

In order to simulate dust evolution in WR140 a passive scalar dust model that simulates dust growth and destruction is included in the simulation. The dust model operates on passive scalars, and as such simulates dust that is co-moving with the stellar wind. Two scalars are used to describe dust in a cell, a , the grain radius in microns, and z , the grain dust-to-gas mass ratio

$$z = \frac{\rho_d}{\rho_g}, \quad (5.6)$$

where ρ_d is the dust density in the cell. A number of assumptions are made in this dust model; for instance, the dust grains in the model are spherical, with a uniform density. Dust grains are assumed to have a single size each grid cell. The number density of grains varies in the simulation volume, however the ratio of grain number density is fixed and constant throughout the simulation. As such, this model does not simulate grain fracturing. Additional mechanisms for dust formation and destruction could also be implemented such as grain-grain agglomeration and photoevaporation. A multi-fluid model with drag force coupling could also be implemented, however this is beyond the scope of this paper.

Dust grows through grain accretion using formulae described by Spitzer (2008) where dust grains grow via low-velocity collisions with surrounding carbon atoms, causing them to accrete

5. EXPLORING DUST GROWTH IN WR140

onto the surface of the dust grain. Carbon is removed from the gas, reducing the cell gas density, while the corresponding dust density increases. This ensures that mass is preserved in the simulation. Assuming a single average grain size the rate of change in the grain radius in a cell due to accretion, da_{acc}/dt , is given by the equation:

$$\frac{da_{\text{acc}}}{dt} = \frac{\xi \rho_C w_C}{4\rho_{\text{gr}}}, \quad (5.7)$$

where ξ is the grain sticking factor, ρ_C is the carbon density ($\rho_C = X_C \rho_g$), w_C is the Maxwell-Boltzmann RMS velocity for carbon ($w_C = \sqrt{3k_B T / 12m_H}$), k_B is the Boltzmann constant and ρ_{gr} is the grain bulk density. The rate of change in the mass of a single grain due to accretion, $dm_{\text{gr,acc}}/dt$, is calculated with the formula:

$$\frac{dm_{\text{gr,acc}}}{dt} = 4\pi \rho_{\text{gr}} a^2 \frac{da_{\text{acc}}}{dt} = \pi \xi \rho_C w_C a^2, \quad (5.8)$$

A bulk density approximating that of amorphous carbon grains ($\rho_{\text{gr}} = 3.0 \text{ g cm}^{-3}$) is used for this simulation.

Dust destruction through gas-grain sputtering is calculated using the Draine and Salpeter (1979b) prescription. Within a flow of gas number density n_g a dust grain of radius a has a grain lifespan, τ_{gr} of:

$$\tau_{\text{gr}} = \frac{a}{da/dt} \approx 3 \times 10^6 \text{ yr} \cdot \frac{a(\mu\text{m})}{n_g} \equiv 9.467 \times 10^{17} \cdot \frac{a}{n_g}. \quad (5.9)$$

This value is based on an average lifetime of carbon grains in an interstellar shock with a temperature of $10^6 \text{ K} \leq T \leq 3 \times 10^8 \text{ K}$ (Dwek et al., 1996; Tielens et al., 1994). From this we find a rate of change in the grain radius due to sputtering of

$$\frac{da_{\text{sp}}}{dt} = 1.056 \times 10^{-18} \cdot n_g. \quad (5.10)$$

The rate of change in the mass of a single dust grain due to sputtering, $dm_{\text{gr,sp}}/dt$, can then be calculated with a similar formula to the rate of change in grain mass due to accretion:

$$\frac{dm_{\text{gr,sp}}}{dt} = -4\pi \rho_{\text{gr}} a^2 \frac{da_{\text{sp}}}{dt} = -1.33 \times 10^{-17} \cdot n_g \rho_{\text{gr}} a^2, \quad (5.11)$$

The change in dust density is then calculated through the equation

$$\frac{d\rho_d}{dt} = \begin{cases} n_d (dm_{\text{gr,acc}}/dt) & \text{if } T \leq 1.4 \times 10^4 \\ n_d (dm_{\text{gr,sp}}/dt) & \text{if } T \geq 1.0 \times 10^6, \end{cases} \quad (5.12)$$

where n_d is the dust grain number density.

Cooling via emission of photons from dust grains is also included in this model. The rate of cooling is calculated using the uncharged grain case of the prescription described in Dwek and Werner (1981). Grains are collisionally excited by collisions with ions and electrons, causing them to radiate. Similarly to the gas/plasma emission model used, the emitted photons are not re-adsorbed by the WCR medium, causing energy to be removed from the simulation. This therefore makes the assumption that the WCR is optically thin to far-infrared photons, which is observationally correct (Callingham et al., 2019; Monnier et al., 2007; Soulain et al., 2018). The grain heating rate, H_{coll} , in erg s^{-1} for a dust grain is calculated with the formula:

$$H = 1.26 \times 10^{-19} \frac{n_g}{A^{1/2}} a^2 (\mu\text{m}) T^{3/2} h(a, T), \quad (5.13)$$

where n_g is the gas number density, A is the mass of the incident particle in AMU, $a(\mu\text{m})$ is the grain radius in microns, T is the temperature of the ambient gas, and $h(a, T)$ is the effective grain heating factor. Individual heating rates for hydrogen, helium, carbon, nitrogen and oxygen are calculated, in order to calculate the total ion collisional heating, H_{coll} :

$$H_{\text{coll}} = H_{\text{H}} + H_{\text{He}} + H_{\text{C}} + H_{\text{N}} + H_{\text{O}}. \quad (5.14)$$

The effective grain heating factor for each element is calculated via the equation:

$$h(a, T) = 1 - \left(1 + \frac{E^*}{2k_B T}\right) e^{-E^*/k_B T}, \quad (5.15)$$

where E^* is the critical energy required for the particle to penetrate the dust grain (Table 5.2). The rate of heating due to electron-grain collisions, H_{el} , is similar to Eq. 5.13. The grain heating factor for electron collisions, h_e , is calculated via an approximation rather than the exact calculation in the case of baryonic matter. h_e is estimated through the following conditions:

$$\begin{aligned} h_e(x^*) &= 1, & x^* > 4.5, \\ &= 0.37x^{*0.62}, & x^* > 1.5, \\ &= 0.27x^{*1.50}, & \text{otherwise,} \end{aligned} \quad (5.16)$$

5. EXPLORING DUST GROWTH IN WR140

Particle	E^*
e^-	$23 a^{2/3}(\mu\text{m})$
H	$133 a(\mu\text{m})$
He	$222 a(\mu\text{m})$
C	$665 a(\mu\text{m})$
N	$665 a(\mu\text{m})$
O	$665 a(\mu\text{m})$

Table 5.2: Grain critical energy, E^* , for a dust grain of a in μm for electrons, e^- , as well as the elements considered for grain cooling. The values for carbon, oxygen and nitrogen are identical.

where $x^* = 2.71 \times 10^8 a^{2/3}(\mu\text{m})/T$. This approximation differs from the integration method by less than 8% while being 3 orders of magnitude faster. Excitation due to grain-grain collisions were not modelled, due to the limitations of the passive scalar model. In order to calculate the change in energy due to dust cooling, we find the radiative emissivity for dust, $\Lambda_d(T, a)$, to be

$$\mathcal{L}_d = n_d(H_{\text{coll}} + H_{\text{el}}), \quad (5.17)$$

and added to the gas/plasma energy loss rate, such that the total energy loss rate is:

$$\mathcal{L}_T = \mathcal{L}_g + \mathcal{L}_d. \quad (5.18)$$

5.3 System parameters

We have previously simulated WCd systems in the form of a parameter space exploration, in order to discern which wind and orbital parameters are influential on the dust growth rates (Eatson et al., 2022a). It was determined that the primary factors of dust growth in a WCd system were the mass loss rates, \dot{M} , and wind terminal velocities, v^∞ , for each star, as well as the orbital separation, d_{sep} . In particular, it was found that imbalances between the wind velocity produced Kelvin-Helmholtz (KH) instabilities due to a shear in the winds. Slower winds were found to be more radiative in the post-shock WCR flow, cooling to temperatures suitable for dust formation. This was found to influence the dust growth rate by as much as six orders of magnitude through a factor of four variation of the WR wind terminal velocity. We also found that increasing d_{sep} significantly reduced the dust production rate, due to less radiative cooling and less shock compression as the out-flowing winds became less dense with distance. In the case of WCd systems with eccentric orbits, the separation distance can vary significantly. In the case of WR140, d_{sep} varies by a factor of 18 from apastron to periastron. This is hypothesised

5.3 System parameters

to be the primary cause of dust production variability within episodic systems. The pre-shock velocity can also vary somewhat due to radiative inhibition and orbital motion.

In order to understand the structure and dynamics of the CWB system we must define some important parameters, such as the wind momentum ratio, η , which is defined as:

$$\eta = \frac{\dot{M}_{\text{OB}} v_{\text{OB}}^{\infty}}{\dot{M}_{\text{WR}} v_{\text{WR}}^{\infty}}. \quad (5.19)$$

As η decreases we find that the wind becomes more imbalanced. In the case of WR+OB CWB systems we find that the WR stars wind typically dominates the WCR. Assuming that there is no radiative inhibition (Stevens & Pollock, 1994) or radiative braking (Gayley et al., 1997), we can approximate the WCR to a conical region with an opening angle about the contact discontinuity:

$$\theta_c \simeq 2.1 \left(1 - \frac{\eta^{2/5}}{4} \right) \eta^{-1/3} \quad \text{for } 10^{-4} \leq \eta \leq 1, \quad (5.20)$$

to a relatively high degree of accuracy (Eichler & Usov, 1993). Another important value for determining the nature of the WCR is the cooling parameter, χ , which is the ratio of the time taken for the shocked wind to completely cool to the time taken for the wind to escape the shocked region:

$$\chi = \frac{t_{\text{cool}}}{t_{\text{esc}}} \approx \frac{v_8^4 d_{12}}{\dot{M}_{-7}}, \quad (5.21)$$

where v_8 is the wind terminal velocity in units of 10^8 cm s^{-1} , d_{12} is the separation distance in units of 10^{12} cm and \dot{M}_{-7} is the wind mass loss rate in units of $10^{-7} M_{\odot} \text{ yr}^{-1}$ (Stevens et al., 1992). As χ decreases, the structure of the WCR becomes more influenced by cooling. If $\chi < 1$, the WCR is completely dominated by radiative cooling, while if $\chi \gg 1$, the WCR behaves adiabatically. If the WCR is highly radiative the total compression can be significantly greater than the adiabatic limit of 4 for a $\gamma = 5/3$ gas, which facilitates dust production. Finally, we define a maximum dust production rate of the system, $\dot{M}_{\text{d,max}}$, assuming a 100% conversion rate of WR wind in the WCR into dust. The fraction of the WR wind that is passed through the WCR is given by the equation:

$$f_{\text{WR}} = \frac{1 - \cos(\theta_{\text{WR}})}{2}, \quad (5.22)$$

5. EXPLORING DUST GROWTH IN WR140

Parameter	Value	Citation
M_{WR}	$10.31 M_{\odot}$	Thomas et al. (2021)
M_{OB}	$29.27 M_{\odot}$	Thomas et al. (2021)
P	7.926 yr	Thomas et al. (2021)
e	0.8993	Thomas et al. (2021)
\dot{M}_{WR}	$5.6 \times 10^{-5} M_{\odot} \text{ yr}^{-1}$	Williams, van der Hucht, Pollock et al. (1990)
\dot{M}_{OB}	$1.6 \times 10^{-6} M_{\odot} \text{ yr}^{-1}$	Williams, van der Hucht, Pollock et al. (1990)
v_{WR}^{∞}	$2.86 \times 10^3 \text{ km s}^{-1}$	Williams, van der Hucht, Pollock et al. (1990)
v_{OB}^{∞}	$3.20 \times 10^3 \text{ km s}^{-1}$	Williams, van der Hucht, Pollock et al. (1990)
η	0.031	Calculated
$X_{\text{WR},\text{min}}$	2.12	Calculated

Table 5.3: The system parameters for the WR140 system as used in this paper. References for each parameter are provided.

where θ_{WR} is the opening angle of the WR shock front ($\theta_{\text{WR}} \approx 2 \tan^{-1}(\eta^{1/3}) + \pi/9$, see Pittard and Dawson, 2018). $\dot{M}_{\text{d,max}}$ is then calculated with the formula

$$\dot{M}_{\text{d,max}} = \dot{M}_{\text{WR}} X_{\text{C,WR}} f_{\text{WR}}, \quad (5.23)$$

where $X_{\text{C,WR}}$ is the carbon mass fraction in the WR star.

5.3.1 WR140 parameters

WR140 was simulated in this paper as it is an archetypical example of an episodic WCd system. The system has an extremely eccentric orbit, which significantly affects the cooling parameter as the orbit progresses, and is also observed in detail. Both stellar winds are expected to be accelerated to close to their terminal wind velocities before they collide (Lamers & Cassinelli, 1999).

Recent improved estimations of the orbital parameters of WR140 by Thomas et al. (2021) were used to calculate the orbit for these simulations, while the mass loss rate, and the wind terminal velocity were taken from Williams, van der Hucht, Pollock et al. (1990) (see Table 5.3). A typical wind composition for WC stars was assumed for the Wolf-Rayet star, while a solar abundance was assumed for the OB star (Table 5.4).

5.3.2 Simulation parameters

A domain of $128 \times 128 \times 16$ AU was used for this simulation, with a coarse (0^{th} level) grid resolution of $400 \times 400 \times 50$ cells in the XYZ domain. The simulation has 4 refinement levels,

Element	Solar	WC
X_{H}	0.705	0.000
X_{He}	0.275	0.546
X_{C}	0.003	0.400
X_{N}	0.001	0.000
X_{O}	0.010	0.050

Table 5.4: Abundances used for the OB and WR stars being simulated. Other elements are assumed to be trace when calculating dust emission (Williams et al., 2015).

corresponding to an effective resolution of $6400 \times 6400 \times 800$ cells and a cell size of 0.02^3 AU^3 . At periastron passage this results in ~ 80 cells between the stars, which was found to be enough to adequately resolve the WCR. This simulation has an XYZ aspect ratio of 8:8:1 in order to reduce processing time, as the bulk of dust formation was expected to occur a short distance from the WCR. A section of the systems orbit, corresponding to an orbital phase of $0.95 \leq \Phi \leq 1.10$ was simulated. This represents 1.2 year section of the systems orbit, and is the orbital period where much of the dust forms - prior to and shortly after periastron passage (Crowther, 2003). Fig. 5.1 shows the orbit overlaid onto the statically refined numerical grid. The area of maximum refinement is around the orbital paths of the stars from $0.94 \leq \Phi \leq 1.11$, in order to ensure that the stars and the apex of the WCR are maximally refined. Prior to periastron passage the `rk3` integrator was used for its speed, but increasing numerical instability as the stars grew closer resulted in this proving untenable, and it was switched to `ssprk5_4` for the remainder of the simulation.

During periastron passage the average time-step was found to reduce by an order of magnitude, resulting in a corresponding increase to simulation time. At the most numerically complex portion of the simulation, a Courant number of $C = 0.04$ had to be used instead of the initial value of $C = 0.15$, in order to preserve numerical stability.

5.3.3 Data collection

Simulation data was exported as HDF5 files at regular time intervals. 3D meshes were collected every increment of $\delta\Phi = 1.5 \times 10^{-3}$, while 2D slices in the XY plane were collected every increment of $\delta\Phi = 1.5 \times 10^{-4}$. These HDF5 files contain the primitive variables of the simulation: gas density, ρ , gas pressure, P , and wind velocity components, v_x , v_y and v_z . The scalars governing the dust properties were also stored for each cell, in particular the dust-to-gas mass ratio, z . The volume-weighted totals of all parameters of interest were also collected, such as the average values for the dust production rate within the WCR, \dot{M}_d .

5. EXPLORING DUST GROWTH IN WR140

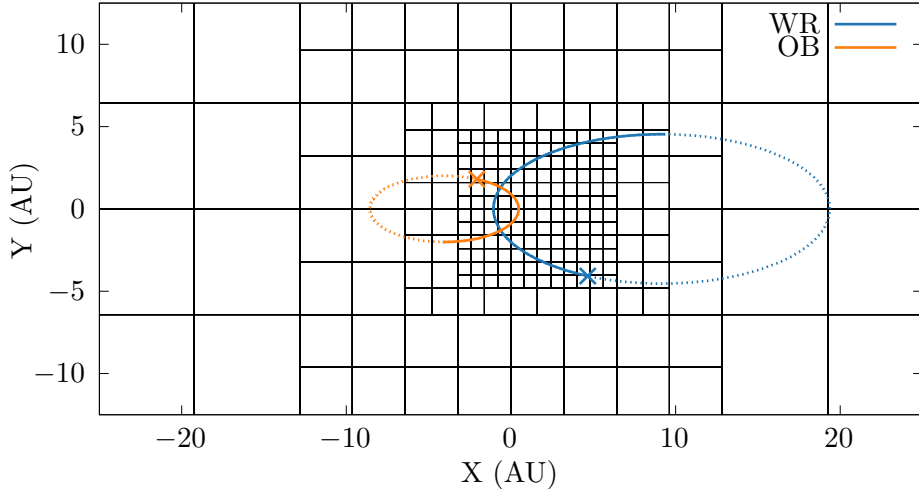


Figure 5.1: Numerical grid of the WR140 system simulation at $z = 0$ near the maximally refined region. Static mesh refinement was used to increase the resolution around the orbital path from $0.95 \leq \Phi \leq 1.10$. The orbital path of both stars are overlaid onto this numerical grid. The stars are typically in the 3rd or 4th level.

Parameter	Mean	Maximum
$\dot{M}_d (M_\odot \text{ yr}^{-1})$	7.68×10^{-8}	1.24×10^{-6}
$\bar{a} (\mu\text{m})$	1.32×10^{-2}	1.44×10^{-2}
\bar{z}	3.98×10^{-4}	3.32×10^{-3}

Table 5.5: Advected scalar yields from the WR140 simulation.

5.4 Results

We observe that as the system approaches periastron passage, the WCR temperature decreases and the WCR on the whole becomes radiatively dominated. Instability appears on the leading shock prior to and during periastron passage. Similarly to what was observed in our previous paper, the leading shock typically has more instability, as it sweeps through the WR stellar wind. After the periastron passage, both the leading and trailing shock display instabilities. We observe that these instabilities persist for some time after periastron passage, even when the value of χ suggests that the wind interaction region should be behaving adiabatically. This is curious, and is further discussed in more detail in Section 5.4.1.

Dust growth was found to be consistent with previous uses of this particular dust model, and well below the theoretical maximum dust formation rate, $\dot{M}_{d,\max} \approx 4.8 \times 10^{-6} M_\odot \text{ yr}^{-1}$. After an initial adjustment phase lasting until $\Phi \approx 0.96$, the dust production rate rapidly increased

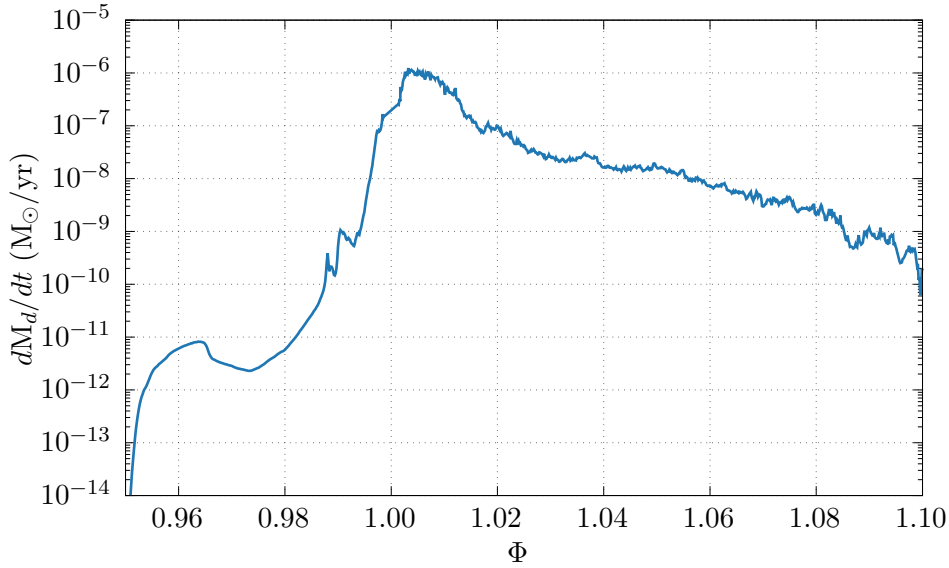


Figure 5.2: A graph of the dust production rate in the WCR over the orbital phase $0.95 \leq \Phi \leq 1.10$. The dust production rate sharply increases as the stars pass their closest approach. Afterwards, the dust production rate begins to falter and slow, due to weaker wind collision effects via the separation distance and radial velocity.

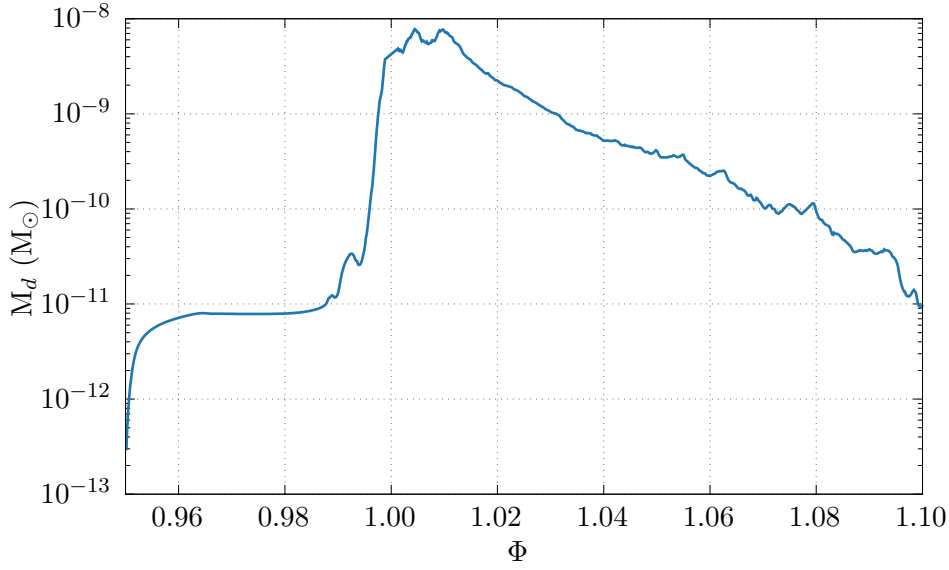


Figure 5.3: A graph of the overall dust mass in the simulation of WR140 over the orbital phase $0.95 \leq \Phi \leq 1.10$. The amount of dust quickly reduces after periastron due to a decreased dust growth rate (Fig. 5.2), as well as dust advecting off the numerical grid.

5. EXPLORING DUST GROWTH IN WR140

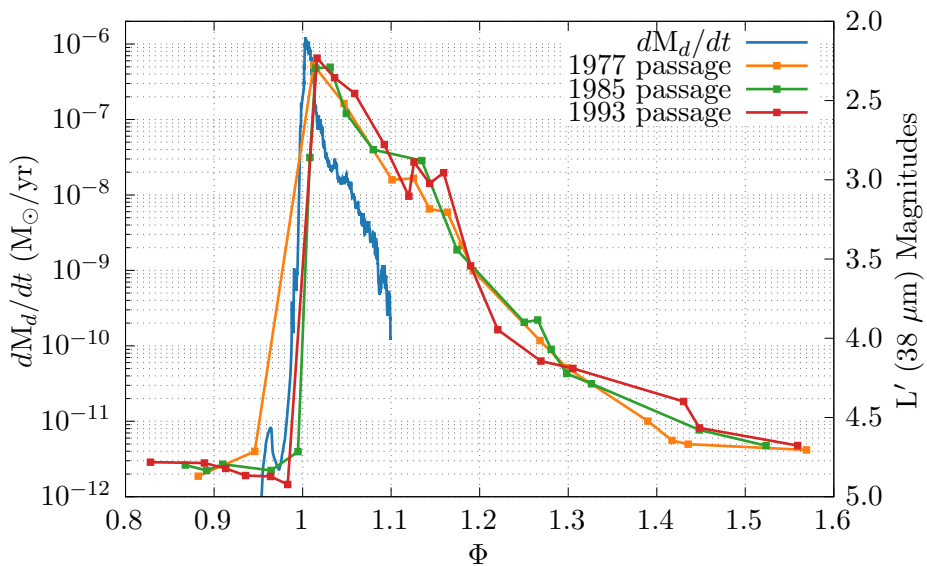


Figure 5.4: A comparison of the dust production rate in our simulation of WR140 and L' photometry of the WR140 system at three periastron passages in 1977, 1985 and 1993 (Crowther, 2003). Radiance from dust emission peaks shortly after $\Phi = 1.00$ in all cases, and reduces to regular levels by $\Phi \sim 1.50$. The dust production rate peaks at the same time and reduces in a similar manner. Whilst dust production is expected to reach pre-periastron levels sooner than $\Phi \sim 1.50$, this is not a direct comparison as dust can radiate long after leaving the dust production region. Conversion from observation date to orbital phase is performed with orbital parameters defined in Fahed et al. (2011).

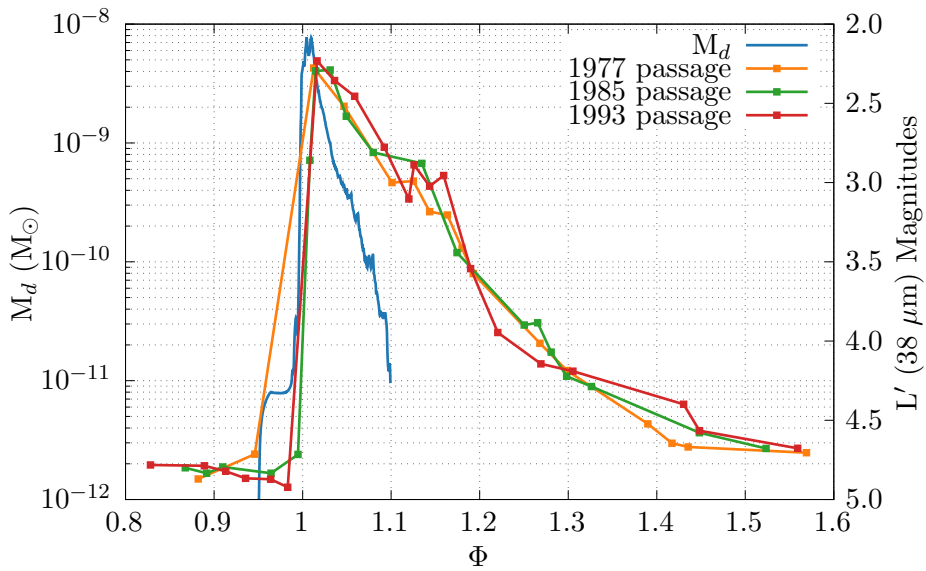


Figure 5.5: A comparison of the simulation dust mass and L' photometry of the WR140 system at three periastron passages in 1977, 1985 and 1993 (Crowther, 2003). Radiance from dust emission peaks shortly after $\Phi = 1.00$ in all cases, and reduces to regular levels by $\Phi \sim 1.50$. Dust mass in the simulation reaches a maxima at the same time as dust luminosity peaks, with dust mass steadily reducing in a similar manner. The dust mass reduces to pre-periastron levels faster than the dust production rate in Fig. 5.4 as the dust quickly advects off of the numerical grid.

5. EXPLORING DUST GROWTH IN WR140

as the stars approached periastron passage, peaking at $\Phi \sim 1.01$ (Fig. 5.2). This maximum dust production rate of $1.24 \times 10^{-6} M_{\odot} \text{ yr}^{-1}$ is sensible, but incredibly prodigious. We find peak conversion efficiency of gas into dust of $\sim 26\%$ in the WCR compared to the theoretical maximum dust production rate described in Eq. 5.23, as well as a total conversion efficiency of $\sim 2.2\%$ throughout the entire system (assuming a total mass loss rate of $5.76 \times 10^{-5} M_{\odot} \text{ yr}^{-1}$). The majority of dust ($\gtrsim 90\%$) is produced within the WCR, with only a very small amount being produced outside the WCR. Most, if not all of this dust is produced near to the apex of the WCR shock, with dust growth being less prevalent further away from this apex. The dust produced outside of the WCR is likely an artefact of the initial injection of dust into the simulation. After reaching this maximum value, the dust production rate steadily decreases as the stars recede from each other. Assuming this decrease in dust production rate is steady, dust production reaches a pre-periastron level of $\sim 10^{-11} M_{\odot} \text{ yr}^{-1}$ by $\Phi \lesssim 1.15$, giving us an active dust production period of $\lesssim 1.2 \text{ yr}$. This is consistent with L' photometry of WR140 (see Crowther, 2003; Fig. 2) – which sharply decreases over the first year – and suggests our model can qualitatively assess dust production rates of episodic WCd systems. This is reflected in the overall dust mass of the simulation (Fig. 5.3), as well as in infrared observations of WR140, where the infrared emission due to dust rapidly reaches a maximum value after periastron passage, and slowly relaxes to a minimum value. Fig. 5.4 compares the dust production rate in the simulation and available L' photometry of WR140, we observe that the dust production rate of the simulation drops in a similar manner to the drop in dust emission in the system after periastron passage. Whilst the rate of decay of dust production rate is much faster than the rate of decay of L' luminance, this is not a direct comparison – dust is still capable of radiating after leaving the region of the WCR where dust growth occurs most intensely. Fig. 5.5 shows a similar result, though the dust mass reduces significantly faster as the dust rapidly traverses through the simulation and off and out of the numerical domain. This asymmetry in the time-dependent change in infrared luminosity implies the existence of several factors for suppression and encouragement of dust formation than just the change in orbital separation distance. It should be noted that due to the small size of the simulation, the dust mass in the system will reduce quickly, as dust advects off the numerical grid.

The evolution of dust in this system would result in the formation of an expanding cloud of dust every time the system passes periastron, with no contiguous spiral pattern forming, due to the lengthy “dormant” period occurring shortly after periastron passage. This is consistent with observations of WR140, where these disconnected clouds are observed (Williams et al., 2009). We find an average dust production rate of $\dot{M}_d = 7.68 \times 10^{-8} M_{\odot} \text{ yr}^{-1}$ over the entire simulation, and

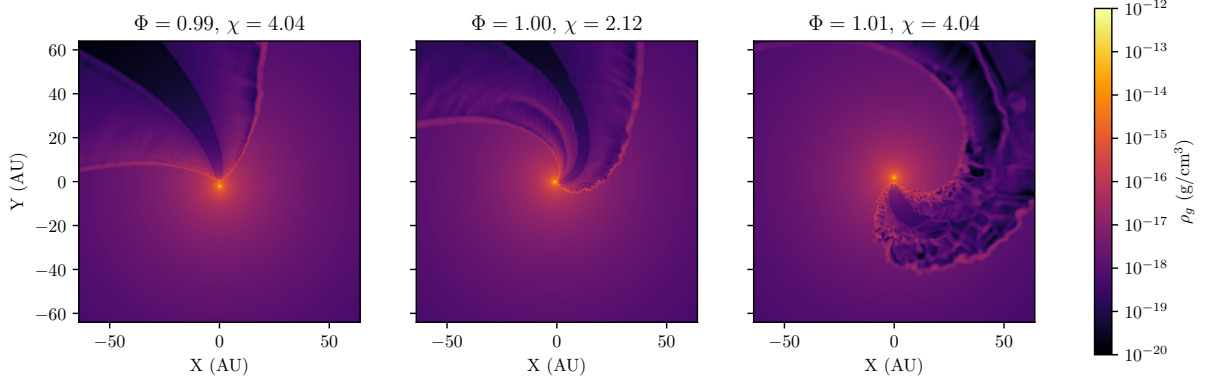


Figure 5.6: Gas density in a simulation of the WR140 system shortly before, during, and after periastron. The value of χ_{WR} is calculated using Eq. 5.21 and the WR wind parameter is noted in each panel. The simulation becomes dominated by instabilities after periastron. These instabilities persist despite the system behaving adiabatically at $\Phi = 0.99$, when the orbital separation distance is identical. This suggests that the radiative behaviour of the post-shock WCR is due to other factors, in addition to d_{sep} .

a change in the dust production rate by approximately five orders of magnitude over the course of the simulation. This fits our understanding of an episodic dust forming WCd system, with an extremely clear “active” period followed by a slow tapering off of dust production as the system approaches the “dormant” period. Our value for the dust-to-gas mass ratio within the system appears to be sensible, while our average dust production rate is significantly higher. This is due to the limited temporal sample of the simulation. We would find a significantly lower average dust production rate over the course of a full orbit due to more sampling of the system over the “dormant” period. We can compare our results to the estimated dust yields from Lau et al. (2020), which found an average dust production rate of $\dot{M}_d = 8.11 \times 10^{-10} M_\odot \text{ yr}^{-1}$ throughout an entire orbit of WR140. Extrapolating our results with a dust production period of 1.2 yr we find an average dust production rate of $\sim 10^{-8} M_\odot \text{ yr}^{-1}$ over the total orbit. This is within an order of magnitude of the estimated dust production rate from Lau et al. (2020), though indicates that the model requires additional work in order to perform quantitative analysis of these systems – which is in line with our conclusions in our previous paper.

5.4.1 Instabilities

As can be seen in Fig. 5.6, after periastron passage the post-shock WCR region transitions from a smooth adiabatic wind to a highly radiative wind dominated by radiative, thin-shell instabilities. As the WCR becomes increasingly radiative, dust growth drastically increases, with the bulk of dust production occurring within the high density regions produced by these

5. EXPLORING DUST GROWTH IN WR140

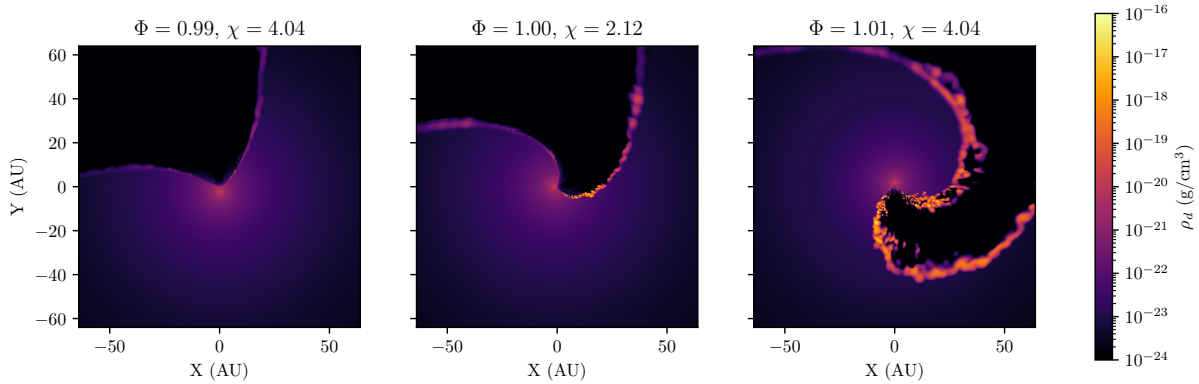


Figure 5.7: Dust density in a simulation of the WR140 system shortly before, during, and after periastron. Dust growth occurs as a direct result of the formation of cold, dense gas in the post-shock WCR.

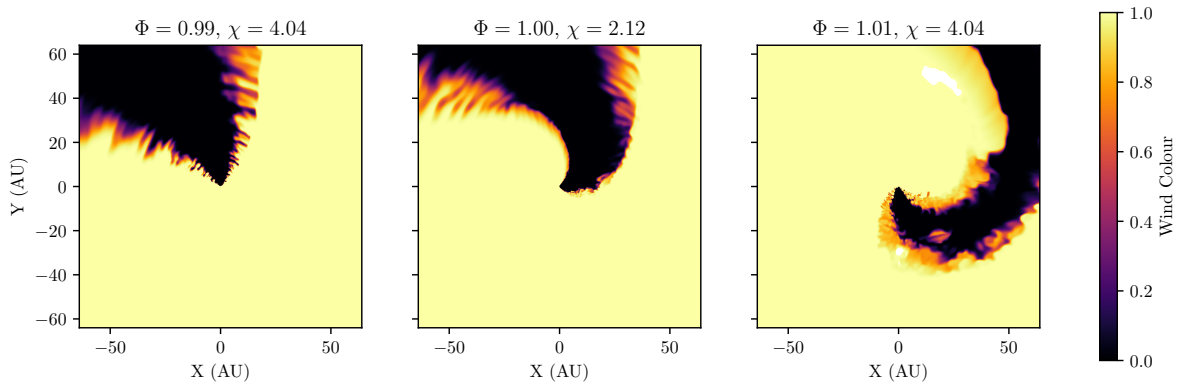


Figure 5.8: Wind ‘colour’ in a simulation of the WR140 system shortly before, during, and after periastron. A colour of 1 represents a pure WR wind and a colour of 0 represents a pure OB wind. We find that the wind undergoes more mixing during and after periastron.

instabilities. However these clumpy pockets of gas do not exhibit significant dust growth beyond ~ 20 AU from the simulation barycentre, with concentrations of dust remaining approximately constant (Fig. 5.7). KH instabilities can also be present, and have been observed to result in significantly increased dust formation (Eatson et al., 2022a), the ratio of wind terminal velocities for WR140 is comparatively low. Therefore, radiative instabilities are the primary motivator driving dust formation in WR140. By the end of the simulation at $\Phi = 1.10$, the WCR is still somewhat dominated by instabilities, with an elevated dust production rate even though the cooling parameter has increased significantly to $\chi = 19.7$, which would normally imply adiabatic behaviour. Whilst the dust production rate has reduced significantly, there is still a significantly greater growth rate than at the start of the simulation (after advection). Clearly the transition from radiative back to adiabatic behaviour has a degree of latency, with instabilities still driving the structure of the WCR long after an adiabatic flow should have re-established. Such behaviour was first reported by Pittard (2009) and leads to hysteresis in the x-ray emission (Pittard & Parkin, 2010). This is the key physics responsible for the asymmetric dust growth rate about periastron. It seems that once instabilities form in the WCR, they are somewhat difficult to stop - and cause oblique shocks, with lower post-shock temperature and ultimately stronger cooling than expected. The amount of wind being mixed in the WCR also significantly increases after periastron passage, which would be conducive to the formation of complex organic molecules on the surface of the dust grains (Fig. 5.8). Whilst this is beyond the scope of the current work, evolution of dust grains from WCd systems on longer time and length scales would be an enlightening avenue of research.

5.4.2 Influence of varying wind velocity on dust production

As we have previously discussed, varying the wind terminal velocity for both stars in a simulation can result in significant changes in the dust production rate. This is theorised to be due to the increased cooling in the WCR caused by slower winds, as well as through KH instabilities driven by a wind velocity shear (if the wind terminal velocities are significantly different, see Stevens et al., 1992). Previous work on this subject considered systems with circular orbits (Eatson et al., 2022a), where the pre-shock velocities are constant over the orbit of the system. However, in the case of a system with an eccentric orbit (such as WR140), the outflow velocity for each wind, as well as their ratio, can markedly vary over the systems orbit. As the stars approach periastron, the radial velocity, v_r , for each star rapidly changes from a maximum value to a minimum, as the stars approach and then swing past one another (Fig. 5.9). This causes a rapid change in the pre-shock velocity for both winds. This then influences the amount of radiative cooling in

5. EXPLORING DUST GROWTH IN WR140

the post-shock wind, suppressing radiative cooling pre-periastron and inciting it post-periastron; leading to changes in the dust production rate. While the change in wind velocity is relatively small (with the wind velocity varying by as much as 6% over the course of an orbit) it still impacts the cooling of the system, and can vary χ by as much as a factor of 1.26 in the case of WR140.

The rate of dust production is also affected by the presence of a large wind velocity ratio, Υ , where:

$$\Upsilon = v_{\text{OB}}/v_{\text{WR}}. \quad (5.24)$$

As the mass of each star is different, the change in radial velocity differs for each star, causing a variability in the velocity ratio and therefore velocity shear. Previous research with dust models suggests that a strong velocity shear drives an increased dust production rate. We find that the maximum velocity shear occurs at $\Phi = 1.01$ (Fig. 5.9), around the same time where the dust growth rate is at a maximum; this is consistent with our previous work. This change in velocity shear may therefore be another factor behind the increased dust growth of WR140 post-periastron.

We also note that in reality there could be significant change in the pre-shock velocity of the O wind due to the WCR encroaching into the acceleration region during periastron (Sugawara et al., 2015).

5.5 Summary

Despite only simulating a limited section of the orbit of WR140, we have made a number of insights into the behaviour of the system. We find a significant degree of change in the dust production rate as a direct consequence of the changing orbital separation of the system. This is related to the change in the behaviour of the post-shock WCR wind, which goes from a smooth adiabatic wind to a clumpy, high density wind dominated by instabilities ideal for dust growth. It is particularly interesting to note that the system does not revert to behaving adiabatically as quickly as expected. This suggests that the post-shock WCR condition of the system is dependent on additional factors, instead of being solely due to d_{sep} . One of the factors on this delayed return to the adiabatic state is potentially due to the orbital motion of the stars themselves. As the stars approach each other at periastron, the radial velocity of the stars adds velocity to the wind beyond the outflow velocity, resulting in higher wind collision velocities,

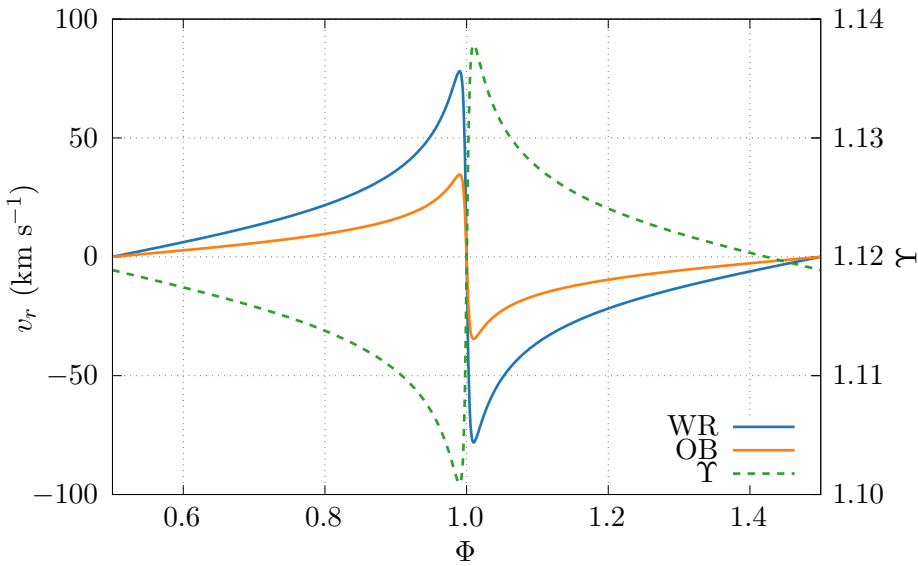


Figure 5.9: Radial velocity as a function of the orbital phase for the WR and OB stars in the WR140 system relative to the barycentre. As periastron passage occurs, the sudden inversion from approaching to receding can alter pre-shock the wind velocity of the WR star by as much as 160 km s^{-1} . Whilst this is $\sim 6\%$ of the WR wind velocity, it can significantly increase dust production when the stars recede from each other. The velocity shear, $\Gamma = v_{\text{OB}}/v_{\text{WR}}$, also sharply increases during periastron passage, peaking at the point of maximum dust production.

5. EXPLORING DUST GROWTH IN WR140

which encourages adiabatic behaviour in the post-shock flow. The inverse is true as the stars recede from one another: the effective wind velocity for both stars is reduced, which encourages cooling and the formation of instabilities in the WCR. Furthermore, an increased wind velocity ratio occurs after periastron due to the orbital dynamics which can drive KH instabilities.

CHAPTER 6

Final Notes and Conclusions

6. FINAL NOTES AND CONCLUSIONS

In this chapter we will discuss the general conclusions of our work, as well as some observations that were made over the course of this project. Whilst there were significant setbacks of our work – namely two years of debugging and well as a total refactoring of our work for a different hydrodynamical code – the main goals of the project were completed. During this project we have developed a flexible and fast dust evolution code which can be used to simulate the growth of grains in numerical simulations of a WCd system. Our dust model has been found to produce realistic yields of dust within both persistent and episodic dust forming CWB systems. This is despite dust production not being artificially limited with orbital separation in the case of episodic WCd systems, while producing a similar degree of variability compared to observational studies of these systems. Hysteresis of dust production is observed, which is also in-line with what is observed in episodic WCd systems.

Despite these successes, there is still much to add to this model. More complex future models could incorporate additional dust growth and destruction mechanisms, and be more kinematically accurate. WCd systems are still quite poorly known, and comparatively rare in the stellar catalogues. However, more detailed studies of new and previously observed systems will be possible with the next generation of telescopes.

Whilst our dust production rates were typically on the order of what is expected for a WCd system, the production rate was out by an order of magnitude certain cases, in particular in the parameter space search. This is most likely due to three factors:

- Missing grain growth mechanisms, such as grain-grain collision.
- An incomplete grain nucleation model, which was out of the scope of this project.
- Conservative choices in model parameters, such as the grain sticking factor, ξ .

As such, the bulk of this thesis was centred around qualitative research of the dust production of WCd systems. Quantitative work would be preferable when undergoing future research with more advanced models.

6.1 Conclusions

In this section we will discuss the key conclusions of the papers published from this project, *An Exploration of Dust Growth Within WCd Systems Using An Advected Scalar Dust Model* (Eatson et al., 2022a) and *Exploring Dust Growth in the Episodic WCd System WR140* (Eatson et al.,

2022b). In particular, we will discuss the changes in the production of dust in these systems as well as how these matched with our predictions and observational findings.

6.1.1 Causes of dust growth in WCd systems

In our first paper, *An Exploration of Dust Growth Within WCd Systems Using An Adveded Scalar Dust Model* (Eatson et al., 2022a), we explore the system parameters thought to affect dust growth and dust production rates within WCd systems. The system parameters that were studied were:

- The mass loss rate, \dot{M} .
- The wind terminal velocity, v^∞ .
- The orbital separation distance between the stars, d_{sep} .

We conclude that while all of these parameters influenced the dust production rates of the system, two of the parameters had an outsized influence on production. Modifying the wind terminal velocity of either star resulted in a significant increase or decrease in the dust production rate. We observed a change in the dust production rate by as much as six orders of magnitude between the most and least prolific dust forming systems. Slow dense winds have more radiative, cooler WCRs, which are more conducive to dust production. However, we also observed that systems with a fast secondary wind can also drive significant dust production in the primary wind. This suggests that in addition to cooling, the ratio of the wind velocities plays an important role in dust production, as an increased shear drives KH instabilities. We also find that the change in orbital separation, d_{sep} also significantly changes the dust production rate. Closer orbits result in a significantly increased dust production rate. This is due to a higher wind density upon collision, resulting in stronger post-shock cooling.

One of the key underlying factors of dust production – in addition to cooling – appears to be due to the formation of instabilities of either the KH or radiative thin-shell types. As the wind parameter, χ , decreases, we begin to observe rapid cooling in the WCR, as well as the presence of instabilities. We also observe the aforementioned KH instabilities from velocity shear. These instabilities result in the formation of high density clumps of cool, post-shock wind. These clumps then form significant quantities of dust, which were observed when comparing the density to the dust-to-gas mass ratios of the simulations.

6. FINAL NOTES AND CONCLUSIONS

Whilst varying the stellar mass loss rates can contribute to a change in dust production rate, this is for the most part due to an increased initial grain number density. However, an increased mass loss rate for either star can result in both more gas that can be converted to dust, as well as stronger shocks, leading to more cooling.

6.1.2 The role of eccentricity in dust formation

In our second paper, *Exploring Dust Growth in the Episodic WCd System WR140* (Eatson et al., 2022b), we confirmed that the dust production is significantly influenced by a continuously changing orbital separation. This is in line with observations of WR140 at periastron, as well as our predictions from our previously published paper. Part of the orbit around periastron was simulated, as dust production was anticipated to be greatest there. Dust yields were found to be sensible, albeit higher than the average dust production rates predicted by Lau et al. (2020).

Dust production also shows a degree of hysteresis. The maximum dust production rate of the system occurs shortly after periastron passage. This is partially due to the travel time between the stars to the WCR, which is on the order of a few days. The maxima is reached extremely rapidly, and as the stars recede from each other, we find that the dust production rate tapers off slowly. This is expected based on observations of characteristic carbon dust emission lines, where we see a similar tapering of the L' emission of WR140 (Crowther, 2003). It was also observed that the time taken for the system to cease producing dust was similar to the time taken for the observed L' flux to diminish to regular levels. Finally, we observe that even after the simulation should be behaving adiabatically, there is significant post-shock WCR cooling and instabilities, which encourage the production of dust.

Some part of this hysteresis is due to the radial velocity of the system. As we have found in our previous paper, WCd systems dust production rates are extremely dependent on the wind pre-shock velocity. An increase in radial velocity as the stars approach periastron will increase the perceived wind velocity relative to the WCR. As such, there is a corresponding decrease in the dust formation rate; the inverse is true as the stars recede from one another. This velocity variability was found to be on the order of 160 km s^{-1} , suggesting it is not the primary reason for the asymmetry in the rate of dust production – though it could be an influencing factor.

6.1.2.1 Radiative driving

Radiative line driving was not modelled in any simulations in this thesis. Whilst this may not significantly change the results of the research in Chapter 4, it could be the case that the wind velocity of the secondary star is lower than anticipated. Analysing the single wind outflow of each star in the system we find that the wind velocity is reduced to 84% of the expected amount. Whilst this would somewhat lower the dust production at periastron by reducing χ and reducing the wind velocity shear (though the latter is most likely a secondary effect). This discrepancy is most likely smaller than the influence due to the conservative value for the grain sticking factor, ξ . However, this would be a useful consideration in future models, especially when simulating systems which extremely close periastron passages.

6.2 Future Study

As we have frequently discussed throughout this thesis, there are still many things to cover in this field. Some potential future avenues of research will be discussed, categorised into theoretical or observational research, as well as whether they are a short-term or long-term project.

6.2.1 More complex models

Our dust model, BIDMAS, is designed to be comparatively flexible and extensible. Additional dust growth and destruction mechanisms could be included; such as grain-grain collision and photoevaporation (Section 3.7.4). Long-term goals would be significant rewriting of the dust model in order to incorporate a multi-fluid dust grain model that is coupled to the gas through drag forces. This would behave similarly to Hendrix et al. (2016), though with grain growth, destruction and cooling. This would be useful as the velocities between gas and dust grains could be better calculated, allowing for more accurate growth and destruction rates. This extended model could also be used to simulate dust mixing within the post-shock WCR. As dust has significantly more inertia than the medium it is travelling through, it could be the case that dust grains could enter the secondary, hydrogen rich OB flow, which could affect grain growth, and allow for complex chemical models.

A dust grain nucleation model could also be implemented, in order to better determine the initial conditions of the system – and therefore make more quantitative evaluations of these systems. Finally, a chemical model could also be included, though this would take significant

6. FINAL NOTES AND CONCLUSIONS

work...

6.2.2 Further simulations of observed systems

A deeper parameter search of the effect of modifying wind terminal velocity for each star was considered, but there was insufficient time to complete the simulations and analyse the data before the end of the PhD. Deriving a fuller relation between dust production and v^∞ for both systems would be a useful near-term project. A similar study for orbital separation using a wider range of orbits, or system eccentricities could also be performed. Simulation of other systems that were considered for this project such as WR104 would also be an additional significant near-term goal. Qualitative studies of these systems would be easier to implement, compared to broader parameter space studies. However, AMR would be required in order to simulate these systems, due to their close-in or distant orbits, which do not favour the refinement conditions of SMR. The main limiting factor to simulating systems is having well known wind parameters and orbital parameters. As large telescopes are built and more detailed surveys of WCd systems are performed, more of these systems will become amenable to simulation in the future.

6.2.3 Radiative transfer

Another future project could be the use of an IR radiative transfer code such as HYPERION (Robitaille, 2011) to generate synthetic observations of the systems being simulated. Whilst this was an initial goal of the project, there was little time to modify the in-house radiative transfer code to calculate IR emissivities instead of x-ray and radio. There was also insufficient time to study these systems using open source codes. This is similar to research conducted by Hendrix et al. (2016), and would allow the gap to be bridged between our numerical studies and observational studies of these systems. This research could also be performed in conjunction with research into these systems from newer telescope arrays that have not been used to observe these systems, such as ALMA.

6.2.4 WR+WR systems

Another topic of extreme interest is WR+WR systems like Apep (Section 2.3.6.1) and WR48a (Section 2.3.6.2). So far, only two such systems have been confirmed. They are predicted to be quite rare due to the improbability of both stars being in their short lived WR phases at the same time. These systems, while having tremendous total mass loss rates, do not produce

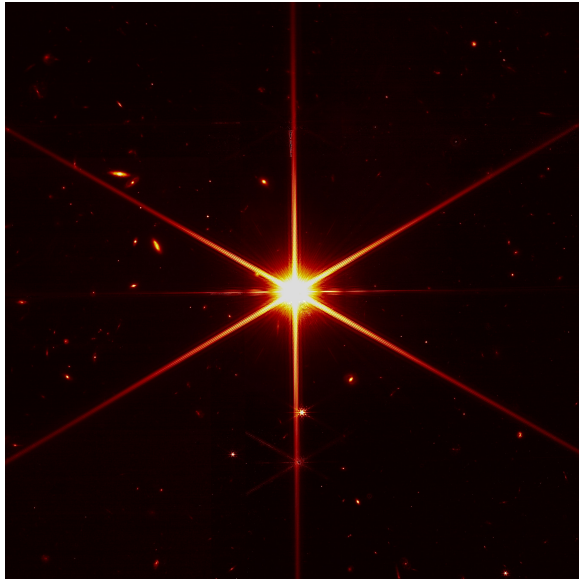


Figure 6.1: First telescope alignment evaluation image from the JWST. Despite the initial alignment performing better than expected, we are still months away from scientific observations, and perhaps years away from observing WCd systems.

significant quantities of dust. This is quite curious, though it may be potentially due to their comparatively similar wind velocities and wide overall separation (though the orbital elements are still quite uncertain, see Han et al., 2020), if we are to extrapolate from our current results. The presence of another hydrogen depleted wind, such as that of an WN sequence WR star would result in interesting conditions for the systems, such as both winds being highly radiative. Both systems are found to be quite eccentric, with the orbital period of Apel being (125 ± 20) yr (Han et al., 2020). This also may explain their comparatively low dust production rates. More data is needed to properly assess these systems, however. Extra-galactic systems could also be potentially simulated, with best-guess values for their orbital and wind parameters. Comparison of these systems with galactic systems could also present an interesting avenue of research.

6.2.5 Telescopes: The Next Generation

The James Webb Space Telescope (JWST; Fig. 6.1) represents the pinnacle of the observational sciences. From a nail biting launch to month-long deployment, I'm sure it is safe to say that many astrophysicists were more than a little bit nervous throughout the month of December. But now, the mirrors are aligned and cooling, and scientific observation is due to commence within the next few months – we can all breathe a sigh of relief. JWST is uniquely well-suited to observing

6. FINAL NOTES AND CONCLUSIONS

these systems, due to its incredible sensitivity, high angular resolution and near/mid-IR spectral range. Additionally, extremely high sensitivity spectrographic observation from JWST would help determine orbits and wind compositions to a greater degree of accuracy. Ground based arrays such as ALMA could also perform this, especially as instrumentation such as ALMA band 2 come online. Other future space-based telescopes, like the spiritual successor to the Hubble, the Luvoir telescope, could overcome the difficulties of observing WCd systems. Though this would not be for a number of decades. Astronomy is – as many of us know – occasionally a waiting game...

6.3 Other Observations

This short section covers other, more personal observations made throughout this PhD.

6.3.1 *Doctorate Strangelove or: How I Learned to Stop Worrying and Love Numerics*

Numerical simulation is an extremely complex topic, and when things go wrong, it can be enormously time consuming and sanity testing to fix. Sometimes code that works fine on one platform being used for testing will not run correctly, or refuse to compile at all. On occasion it felt like the software paradigm of WOCA¹ simply did not apply when writing in allegedly portable languages, such as C. The code is also difficult to debug and fix, due to the performance impact, and being essentially unable to set breakpoints unless the simulation crashes within the first timestep.

Simulation work is difficult, and often frustrating, but is extremely satisfying when things begin to go right. On top of that, being able to run dozens of simulations on parallel on HPC resources meant that an entire parameter space search could be performed simultaneously, something that isn't possible in observational work. As such, once the model was finished, running simulations took approximately 4 months in total, not including analysis. Based on experiences other researchers I have talked to who undertook simulation-based work, this is a fairly common experience.

¹Write Once, Compile Anywhere.

6.3.2 Become a researcher, see the world!

Between the issues in our earlier attempts to get our model to work correctly in the MG hydrodynamical code, to a personal injury to the current global pandemic (see Section 6.3.4), to the simple unavailability of relevant conferences, no conferences were attended throughout this project. I'm sure (especially considering the pandemic) that many other researchers are or have been in the same boat, though it is a considerable shame.

I look forward to any future conference that I may visit in my academic career.

6.3.3 Paul Erdős was probably onto something

The second half of my PhD represented for the first time in my life that I was consistently treating my ADHD with medication. Whilst this made me nervous initially, I found myself for the first time being able to think *clearly*. To those who don't know, there are few things quite as frustrating as finding yourself completely, utterly unable to work because you simply can't think clearly or keep on topic. In fact, I'm not confident I would have been able to finish this PhD without a small amount of (prescribed) chemical assistance.

The sheer difference in the amount and consistency of my work after I began medicating constantly reminded me of a quote from the mathematician Paul Erdős. After successfully quitting cold turkey from amphetamines for a month after a bet with his colleague Ronald Graham, he said this to Graham as he collected his \$500:

“You've showed me I'm not an addict. But I didn't get any work done. I'd get up in the morning and stare at a blank piece of paper. I'd have no ideas, just like an ordinary person. You've set mathematics back a month.”

In closing: if you, the reader, empathise with this... It might be a good idea to get yourself checked.

6.3.4 Carinae Strain: PhD research in a time of pandemic

Whilst the world outside was terrifying, and everything seemed like it was only going to get worse during the pandemic lockdowns, it is hard to stay motivated about anything. But there truly is nothing more helpful and calming than enjoying a show or a game with your friends and loved ones, even if it is over the internet rather than in person.

6. FINAL NOTES AND CONCLUSIONS

Thank you, everyone, for helping me through this.

6.4 The Last Word

This thesis demonstrates the effectiveness of an advected scalar dust model to estimate the yields of dust produced in a WCd system. We also use this model to quantitatively evaluate how various system parameters and behaviours change the growth rate of dust in the system. We find two system parameters in particular to be particularly important to the production of dust, v^∞ and d_{sep} . Subsequently, we conclude that the episodic nature of some WCd systems is due to their eccentric orbits. Continued development of the model and further observational work is essential to better understanding WCd systems. Due to many difficulties throughout the project, there was limited time to include a fully comprehensive dust model composed of a separate, coupled fluid. Other avenues of research include synthetic imaging through radiative transfer, as well as improved observations and surveys using next-generation telescopes. WCd systems represent a tremendous scientific curiosity still, in particular how the initial nascent grains form and survive in these systems.

As my supervisor wrote when ending his thesis:

“There remains much work to be done...”

APPENDIX A

Breakdown of Computational Models

A. BREAKDOWN OF COMPUTATIONAL MODELS

This section contains a simplified breakdown of the cooling and dust models for the sake of clarity.

A.1 Initialisation

Operation occurs at the start of the simulation.

1. Read in data from model file.
2. Check to see if cooling is enabled, if so, read in the cooling curve.
3. Check to see if dust model is enabled.
4. Check to see if dust cooling is enabled, if so, read in ionisation curve.
5. Check to see if required numbers of scalars are available.
 - At least 1 in general.
 - At least 3 if dust model is enabled.
 - Exit with error if there is any issue.
6. Check to see if AMR is enabled, if so, enroll refinement condition.
7. Enroll source functions.
8. Calculate orbit for Φ defined in model as `phase_offset`, use as orbital starting position.
9. Finish initialisation, print model details.

A.2 Cooling Model

Operation occurs for every cell in numerical grid.

1. Read in conserved gas variables and simulation timestep, Δt .
2. Calculate gas velocity from momentum.
3. Calculate gas kinetic energy.

4. Calculate cell pressure and cell internal energy.
5. Calculate cell temperature, T , using ideal gas equation.
6. If temperature is $< 1.1 \times 10^4$ K and wind is purely WR or OB, set cell temperature as 10^4 K and finish for this cell. This is performed to prevent time-wasting calculations when cooling the wind.
7. If dust cooling is enabled:
 - (a) Read in z and a for cell.
 - (b) Calculate V_{gr} , m_{gr} , ρ_d and n_d from z and a .
8. Set substep time, $\delta t = 0$.
9. Iterate until $\delta t = \Delta t$:
 - (a) Calculate emissivity each wind for T using Eq. 3.11 & Eq. 3.12.
 - (b) Calculate \mathcal{L}_g for each wind.
 - (c) Calculate total \mathcal{L}_g based on C .
 - (d) If dust cooling is enabled:
 - i. Calculate H_T from Eq. 3.15.
 - ii. Calculate \mathcal{L}_d from Eq. 3.13 and add to \mathcal{L}_g .
 - (e) Calculate substep interval, dt using Eq. 3.27, compare with remaining time in Δt .
 - (f) Integrate using Euler method to find total change in energy.
 - (g) Calculate change in temperature from ideal gas law, update temperature.
 - (h) Check to see if temperature has reached lower bound, if so, break out of loop and set temperature to 10^4 K.
 - (i) March forward, such that $\delta t_{\text{new}} = \delta t_{\text{old}} + dt$ and iterate if needed.
10. Calculate new pressure from final temperature, recalculate total energy, update cell conserved parameters.

A.3 Dust Model

Operation occurs for every cell in numerical grid and only if dust model is enabled.

A. BREAKDOWN OF COMPUTATIONAL MODELS

1. Read in conserved gas variables and simulation timestep.
2. Read in dust and wind “colour” scalars.
3. Calculate temperature.
4. Calculate V_{gr} , m_{gr} , ρ_{d} and n_{d} from z and a .
5. If temperature is $\leq 1.4 \times 10^4$ K, dust growth occurs:
 - (a) Calculate grain RMS velocity of carbon using Eq. 3.34.
 - (b) Calculate da/dt using Eq. 3.33.
 - (c) Calculate $d\rho_{\text{d}}/dt$ using Eq. 3.35.
6. If temperature is greater than 10^6 K, dust destruction occurs:
 - (a) Calculate τ_{gr} using Eq. 3.36.
 - (b) Calculate da/dt using Eq. 3.38.
 - (c) Calculate $d\rho_{\text{d}}/dt$ using Eq. 3.39.
7. If $d\rho_{\text{d}}/dt \neq 0$:
 - (a) Calculate new grain radius using Eq. 3.41.
 - (b) Calculate new dust density after cell timestep Δt using Eq. 3.42a.
 - (c) Calculate new gas density using Eq. 3.42b.
 - (d) Calculate new z using Eq. 3.43.
 - (e) Ensure that a is not negative or unrealistically large.
 - (f) Ensure that z is not negative or > 1 .
 - (g) Update cell conserved parameters.
 - (h) Update dust scalars and wind “colour”.

APPENDIX B

Software Carpentry

B. SOFTWARE CARPENTRY

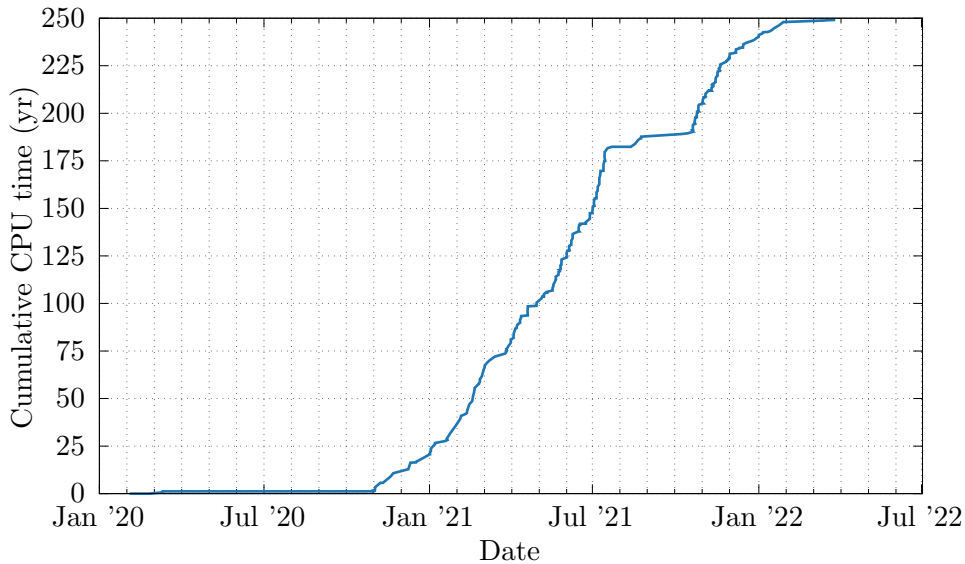


Figure B.1: Cumulative CPU time in core-years for ARC4 from 2020 to 2022. Most of, if not all of the data produced in this project was generated over this period. One shudders to think how much electricity was used.

B.1 Software & Resource Acknowledgements

This project relied on a number of resources available from the University of Leeds, as well as many open source projects scattered around the globe. Not to opine on the importance of open source projects for too long; but we as researchers should be aware of the time, effort and labour of programmers who develop open source projects. Learning that perhaps the bulk of the infrastructure we use rests almost entirely on a series of freely-developed projects came as a shock to me many years ago, and in lieu of payment, this section will acknowledge these projects.

This simulations in this thesis were performed on the ARC3 and ARC4 computers, part of the High Performance Computing facilities at the University of Leeds, UK. According to the SGE log file I had used approximately 8×10^9 s of cumulative CPU time on ARC3 and ARC4 (Fig. B.1) over the course of this PhD, which is over 250 core-years! Much of the earlier development and testing work was undertaken on workstations provided by the department. In particular was the 44 core workstation my supervisor used¹, whose computing brunt was used frequently throughout the project.

A good deal of the data reduction of this thesis was conducted using the Python 3 programming language (Van Rossum & Drake, 2009), in particular, the following open source modules

¹Which I always referred to as `jumpcannon`, after Annie Jump Cannon, though the name didn't catch on.

B.1 Software & Resource Acknowledgements

were used extensively:

- [NumPy¹](#) (Harris et al., 2020).
- [Astropy²](#) (Astropy Collaboration et al., 2018; Astropy Collaboration et al., 2013).
- [Matplotlib³](#) (Hunter, 2007).

[Athena++](#) (Stone et al., 2021) was also used extensively throughout the work in this thesis. Whilst there are some aspects of this that need further development - in particular, passive scalars in AMR problems - it was found to be extremely robust, and easy to develop for. Some diagrams in this thesis, specifically Fig. 2.14 and Fig. 2.15 use the [Quiver⁴](#) communicative diagram editor. GNU Parallel (Tange, 2021) was used to speed up the batch processing of data within this project. If parallelism is difficult to implement for a problem, sometimes the best option is to run many, *many* serial programmes at once. The [Hyperfine⁵](#) command line benchmarking tool was used to benchmark [Athena++](#) throughout the project, in order to find ideal configuration parameters such as numerical integrators, core counts and meshblock sizes. Most of the line plots in this project were produced by the [Gnuplot](#) graphing tool, whilst the [turbo⁶](#) palette was used to generate readable and accessible colour schemes for our plots. A modified version of the `turbo.pal` palette file from the [gnuplotting.org GitHub repo⁷](#) was used to import the colour scheme into [gnuplot](#).

Finally, this thesis was typeset with [LATEX](#), using the [TeXlive](#) distribution and [latexmk](#) for compilation. It is abundantly clear that scientists the world over owe an enormous debt of gratitude to Donald Knuth and Leslie Lamport for their work on the [TeX](#) and [LATEX](#) projects. The thesis template is a modified version of the [Leeds Condensed Matter Physics Group LATEX template⁸](#), which suited the needs of this thesis extremely well.

¹<https://numpy.org/>

²<https://www.astropy.org/>

³<https://matplotlib.org/>

⁴<https://q.uiver.app/>

⁵<https://github.com/sharkdp/hyperfine>

⁶<https://ai.googleblog.com/2019/08/turbo-improved-rainbow-colormap-for.html>

⁷<https://github.com/Gnuplotting/gnuplot-palettes/blob/master/turbo.pal>

⁸<https://github.com/stonerlab/Thesis-template>

B.2 Parallelism & Amdahl's Law

One of the more prominent mistaken expectations of computing in the last few decades was the idea of extreme scaling of processors. Early in the lifecycle of the NetBurst architecture, Intel predicted the Pentium 4 and the subsequent generations of their flagship processors would scale up to 10 GHz – or even beyond! This of course, never panned out, only a handful of processors can reliably scale to 5 GHz – albeit with an enormous thermal penalty – with contemporary high-end desktop processors drawing as much as twice the power of the hottest running NetBurst designs. Instead, processors, while significantly faster in single threaded applications due to improvements to branch prediction, and cache speed, now have more than one processing core. In most cases in scientific computing, single-threaded performance has been entirely supplanted by multi-threaded performance and parallel programming. If a large problem can be divided into a series of smaller problems, with little to or no dependence between the smaller problems, it is ripe for parallelisation. A good example of this would be performing the dot product of two matrices together, each element of the resultant matrix can be calculated individually. For extremely large matrices, this speedup would eclipse any gains of using a more efficient single-threaded method. This doesn't apply to all problems, of course, many problems are inherently serial in nature, such as iterative calculations, and compiling a thesis using L^AT_EX. Additionally, with smaller problems communication and synchronisation costs would offset parallel gains in a lot of cases.

Two forms of parallelism are typically used in scientific computing applications, *shared memory* parallelism and *distributed memory* parallelism. Shared memory parallelism defines a single block of memory which can be accessed by all processing cores. This is generally easier to implement, but does not scale beyond a single computer, and can result in memory unsafe conditions if the same data is manipulated by multiple cores. Race conditions can also occur if processes are conducted out of sequence, though this can occur with other paradigms, and typically require thread synchronisation, such as with the `OpenMP barrier` construct. In the case of distributed memory parallelism sections of memory are siloed off for each processing core, in order to gather or distribute information between cores messages are passed requesting copies of or alteration to data. This scales significantly better, but can introduce inefficiencies due to redundant memory and communication bottlenecks. This can also be referred to as a Message Passing Interface (MPI) paradigm. The primary standards for parallel processing in C++ are `OpenMP` for shared memory parallelism and `OpenMPI` for distributed memory parallelism.

Numerical simulation is one of these problems that is typically described as “embarrassingly

parallel”, one where very little effort is required to parallelise the problem, with each element of the problem being completely independent of another. Other problems like this include Monte Carlo analysis and per-pixel image rendering. In the case of `Athena++`, this parallelism is accomplished by dividing the problem into a series of blocks, that can be distributed to processing cores. This also ensures minimal bandwidth overhead, as communication between cores only needs to occur between each time-step. Only a small amount of duplicate work and communication is required between the interfaces of these blocks at each timestep, in order to ensure that gas can traverse between cells stored in memory designated to different processing cores.

High-performance computing has two common rules for parallel scalability:

- *Strong* scaling, how the solution scales for a number of cores for a fixed problem size.
- *Weak* scaling, where the solution time varies with cores for a fixed per-processor problem size.

Strong scaling is governed by Amdahl's law, which shows that for a given problem where a fraction of the problem can be efficiently parallelised, the resultant speedup for a given number of cores takes the form

$$S_s(N) = \frac{1}{(1 - p) + \frac{p}{N}}, \quad (\text{B.1})$$

where S is the speedup of the task, p is the fraction of the code that can be effectively parallelised, and N is the number of processing cores (Amdahl, 1967). This imposes a limit on the theoretical maximum speedup given an arbitrary number of cores, calculated with the formula

$$\lim_{N \rightarrow \infty} S_s = \frac{1}{1 - p}. \quad (\text{B.2})$$

This is demonstrated in Fig. B.2, where the speedup rises asymptotically to meet a maximum value, equivalent to $(1 - p)^{-1}$. This suggests that throwing cores at a problem will not solve it faster beyond a certain point, especially if the problem is not well parallelised (Trobek et al., 2018, Ch. 2).

In order to test the parallel performance of `Athena++`, hydrodynamical problems in this thesis were run for a specific number of simulation steps. In the case of a single processor with

B. SOFTWARE CARPENTRY

22 cores in Fig. B.3, we find a parallelisation fraction of $p = 0.987$. This is extremely large, but could be even higher, due to overhead issues and the size of the problem.

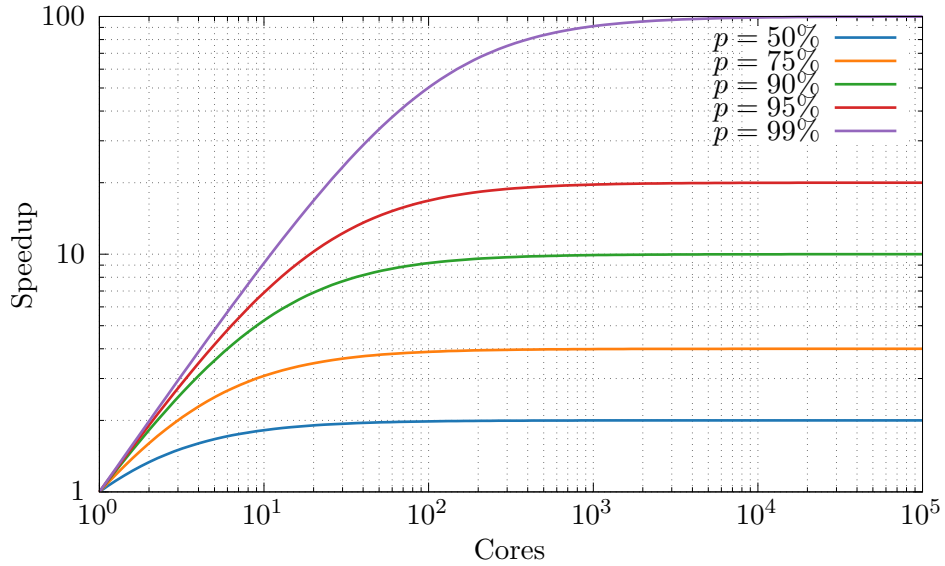


Figure B.2: A demonstration of Amdahl’s law, showing that as parallel fraction increases, there are significant gains in performance for a modest number of processing cores. Beyond a certain point, however, we find that speedup slows, and is asymptotic to a point where $S = 1/(1 - p)$.

Weak scaling is determined through Gustafson’s law, which shows that as a problem increases in size to scale with the number of cores available, the theoretical speedup is linear, such that:

$$S_w(N) = (1 - p) + pN. \quad (\text{B.3})$$

As $\lim_{N \rightarrow \infty} S_w = \infty$, there is no limit to the amount of scaling for an increasing problem size (Gustafson, 1988). As such we find that more powerful computers with many thousands of cores still benefit from parallelisation if the problem scales accordingly (Pacheco & Malensek, 2022, Ch. 2).

Beyond these theoretical laws, there are practical limitations to parallel processing. The first of which is die size and cost: a single large, multi-core processor would be extremely expensive to manufacture, while also reducing yield significantly due to manufacturing defects. This was the basis of supercomputing, such as the vector processors manufactured by Cray, prior to the advent of Beowulf-based HPC clusters. Intel attempted to solve this problem with KNL, implementing dozens of simple, slow cores and fast matrix math throughput, but these were impractical for a variety of reasons. GPUs could also be considered an alternative implementation of this concept,

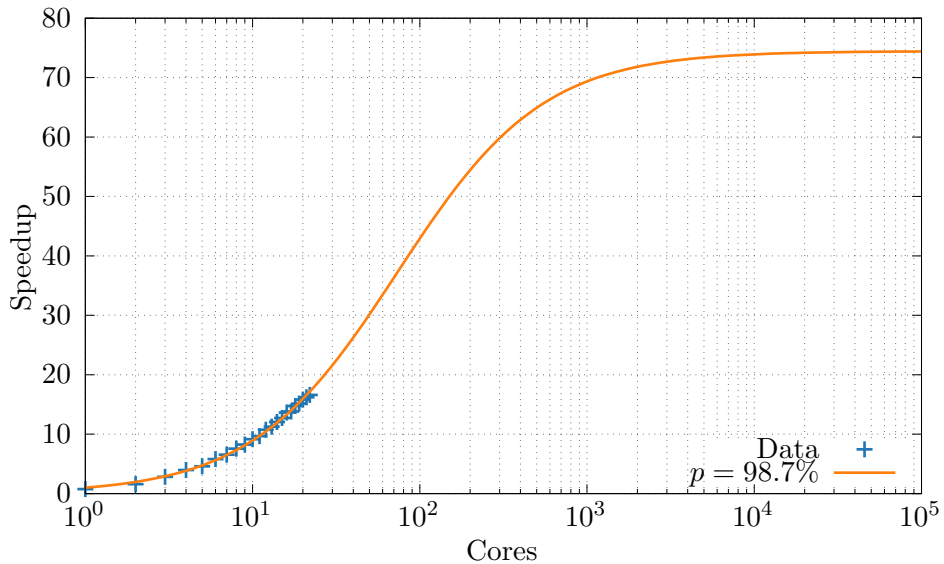


Figure B.3: Strong scaling test of **Athena++** running the simulation of WR140 as defined in Chapter 5 for 100 timesteps. The parallel fraction of **Athena++** running this problem is found to be 98.7%. The test was conducted over 22 cores of a dual-processor 2.1 GHz Intel Xeon Gold 6152 workstation using `hyperfine`. The second processor was not used as this introduced a penalty to performance due to inter-processor bandwidth bottlenecks. Due to the scale of the problem being relatively small, the parallel fraction may be underestimated.

and have seen much more success, chiplet-based designs such as AMDs Infinity Fabric or the Apple M1 Ultra. Another issue is memory and communication bandwidth, as the problem scales to dozens of cores a single processing node would see reduced throughput due to memory bandwidth issues. Furthermore as the problem scales beyond a single processor, we see a reduced level of performance as the programme has to leverage motherboard processor interconnects, or the much slower interconnects between nodes in an HPC cluster.

In testing **Athena++** we found that the communication overhead became significant above 200 cores, with the current network topology and node availability of **ARC4**. There was also an observed increase in communication overhead with **MG** as well, as the programme handles parallelism by slicing the problem along the y axis, resulting in a very large number of “ghost” cells that require communication.

B.3 Datatypes & Visualisation

Output data from **Athena++** was exported at regular time-elapsed intervals in the form of 3-D HDF5 files (The HDF Group, 1997–2022) and 2-D slices at $z = 0$ HDF5 files. A separate, comma-

B. SOFTWARE CARPENTRY

delimited “history” filetype was written to regularly to store summated values of conserved variables and advected scalars. This was used primarily to determine simulation-wide dust production rates and average grain sizes as the simulation evolved. Checkpoint files were also written at regular intervals to ensure a restart in the event of a simulation crash or process kill by the ARC4 job-sharing queue system. For most simulations 3-D data and checkpoints were saved every 1/100th of an orbital period, while 2-D data and “history” data was written every 1/1000th of an orbital period.

Data was plotted using a series of custom programmes designed to parse data as quickly as possible, the **Python** plotting library provided in the **Athena++** repository was modified to incorporate Delaunay triangulation, instead of interpolating static meshes to the finest level in order to operate correctly with **Matplotlib** `imshow` routine (Hunter, 2007), data-points are triangulated with each other. This is a markedly more memory and processing efficient method, as data is not duplicated or smoothed at the interpolation step, and was found to be approximately 2000% faster. Whilst this can result in artefacts at low resolutions, the resolution of the simulation was sufficient such that these artefacts were not observed. The GNU Parallel library was used to batch-process 2D exports (Tange, 2021), as **Python** is for the most part single threaded and interpreted it was found to be more effective use Parallel to run multiple python instances at once, each processing a single data file using the command:

```
1 seq 0 <max> | parallel -j44 "athena_plot.py plot-config.yaml -n {}"
```

where `<max>` is the number of simulation files. The **Numba** library (Lam et al., 2015) was also used to improve performance by just-in-time (JIT) compiling, parallelising and vectorising certain steps that were not performant in either **Python** or **Numpy** (Harris et al., 2020). In this case, **Numba** was used to restructure numerical array data into a linear series of arrays, performing derived parameter such as dust density and temperature calculations, and matrix co-ordinate transforms. While this is less straightforward to implement, as many of **Python's** data-types cannot be used, this offered a 2 order of magnitude processing speed increase in the case of an 8-core workstation.

For 3D visualisation the **VisIt** application is used (Childs et al., 2012). However for print 2D slices generated using **Matplotlib** were used. The **Gnuplot** utility (Williams et al., 2020) was used for generating line and scatter plots throughout this thesis, in particular history outputs from **Athena++**. Occasionally, rendering video of the batch processes 2D exports was performed in order to better understand how the systems propagated over time, in order to do this **ffmpeg** library (Tomar, 2006) was used to render the videos. For this, the following command was used:

```
1 cat *.png | ffmpeg -f image2pipe -framerate 30 -i - -c:v libx264 -vf format=yuv420p output.mp4
```

B.4 Version Control

This is going to be a very short section, as it is more of a plea to other doctoral students who read this - especially those starting out. Use version control in your projects, the number of times I lost work or code because I did not use version control software like `Git` in my first year is frankly far too high. It'll save you a lot of time in the long run, trust me.

Keep your thesis on there too!

B. SOFTWARE CARPENTRY

BIBLIOGRAPHY

Book Citations

- Apai, D. & Lauretta, D. S. (Eds.). (2010). *Protoplanetary Dust: Astrophysical and Cosmochemical Perspectives*. Cambridge University Press.
DOI: [10.1017/CBO9780511674662](https://doi.org/10.1017/CBO9780511674662). (Cited on page 30)
- Bodenheimer, P. H. (2011, January 1). *Principles of Star Formation*.
DOI: [10.1007/978-3-642-15063-0](https://doi.org/10.1007/978-3-642-15063-0). (Cited on pages 9, 10)
- Carroll, B. W. & Ostlie, D. A. (2014). *An Introduction to Modern Astrophysics* (Second international). Pearson. (Cited on page 9).
- Cherchneff, I. (2015, January 1). *Dust formation in carbon-rich Wolf-Rayet colliding winds*. (Cited on page 107).
- Conti, P. S., Crowther, P. A. & Leitherer, C. (2012, October 1). *From Luminous Hot Stars to Starburst Galaxies*. (Cited on page 21).
- Draine, B. T. (2011, January 1). *Physics of the Interstellar and Intergalactic Medium*. (Cited on pages 27, 38).
- Dyson, J. E. (2021). *The physics of the interstellar medium* (Third edition.). CRC Press. (Cited on pages 36, 37, 39).
- Kippenhahn, R., Weigert, A. & Weiss, A. (2012, January 1). *Stellar Structure and Evolution*.
DOI: [10.1007/978-3-642-30304-3](https://doi.org/10.1007/978-3-642-30304-3). (Cited on page 20)
- Lamers, H. J. & Cassinelli, J. P. (1999). *Introduction to stellar winds*. Cambridge University Press. (Cited on pages 13, 15, 148).
- Longair, M. S. (2011). *High Energy Astrophysics* (3rd ed). Cambridge University Press. (Cited on pages 25, 40).
- Maciel, W. J. (2014). *Hydrodynamics and Stellar Winds: An Introduction*. Springer International Publishing. (Cited on pages 16, 36).

BIBLIOGRAPHY

- Mihalas, D. (1978, January 1). *Stellar atmospheres*. (Cited on page 96).
- Oswalt, T. D. & Barstow, M. A. (Eds.). (2013). *Planets, Stars and Stellar Systems*. Springer Netherlands.
- DOI: [10.1007/978-94-007-5615-1](https://doi.org/10.1007/978-94-007-5615-1). (Cited on page 23)
- Pacheco, P. S. & Malensek, M. (2022, January 1). *An Introduction to Parallel Programming (Second Edition)* (P. S. Pacheco & M. Malensek, Eds.). Morgan Kaufmann.
- DOI: [10.1016/B978-0-12-804605-0.00009-9](https://doi.org/10.1016/B978-0-12-804605-0.00009-9). (Cited on page 180)
- Ryan, S. G. & Norton, A. J. (2010). *Stellar evolution and nucleosynthesis*. Cambridge University Press. (Cited on page 24).
- Salaris, M. & Cassisi, S. (2005). *Evolution of Stars and Stellar Populations*. (Cited on pages 12, 18, 19).
- Spitzer, L. (2008, November 20). *Physical Processes in the Interstellar Medium*. John Wiley & Sons.
- DOI: [10.1002/9783527617722](https://doi.org/10.1002/9783527617722). (Cited on pages 26, 28, 73, 96, 116, 143)
- Toro, E. F. (2013). *Riemann solvers and numerical methods for fluid dynamics: A practical introduction*. Springer Science & Business Media. (Cited on pages 61, 91).
- Trobec, R., Slivnik, B., Bulić, P. & Robić, B. (2018). *Introduction to Parallel Computing: From Algorithms to Programming on State-of-the-Art Platforms* (R. Trobec, B. Slivnik, P. Bulić & B. Robić, Eds.). Springer International Publishing.
- DOI: [10.1007/978-3-319-98833-7_2](https://doi.org/10.1007/978-3-319-98833-7_2). (Cited on page 179)
- Vink, J. S. (Ed.). (2015). *Very Massive Stars in the Local Universe* (Vol. 412). Springer International Publishing.
- DOI: [10.1007/978-3-319-09596-7](https://doi.org/10.1007/978-3-319-09596-7). (Cited on page 21)
- Ward-Thompson, D. & Whitworth, A. P. (2011). *An Introduction to Star Formation*. Cambridge University Press.
- DOI: [10.1017/CBO9780511974021](https://doi.org/10.1017/CBO9780511974021). (Cited on pages 9, 10, 30)
- Whittet, D. C. B. (2002, October 21). *Dust in the Galactic Environment*. CRC Press.
- DOI: [10.1201/9781482268645](https://doi.org/10.1201/9781482268645). (Cited on pages 26, 43)
- Williams, D. A. & Cecchi-Pestellini, C. (2015, November 18). *The Chemistry of Cosmic Dust*.
- DOI: [10.1039/9781782623694](https://doi.org/10.1039/9781782623694). (Cited on page 30)
- Wong, S. S. M. (1998, August 1). *Introductory Nuclear Physics, 2nd Edition*.
- DOI: [10.1002/9783527617906](https://doi.org/10.1002/9783527617906). (Cited on page 12)

Journal Citations

- Abbott, D. C. (1982). The theory of radiatively driven stellar winds. II. The line acceleration. *The Astrophysical Journal*, 259, 282–301.
DOI: [10.1086/160166](https://doi.org/10.1086/160166) (Cited on page 17)
- Allen, D. A., Swings, J. P. & Harvey, P. M. (1972). Infrared photometry of northern Wolf-Rayet stars. *Astronomy and Astrophysics*, 20, 333–336 (Cited on page 106).
- Amdahl, G. M. (1967). Validity of the single processor approach to achieving large scale computing capabilities. *Proceedings of the April 18-20, 1967, Spring Joint Computer Conference*, 483–485.
DOI: [10.1145/1465482.1465560](https://doi.org/10.1145/1465482.1465560) (Cited on page 179)
- Beals, C. S. (1929). On the nature of Wolf-Rayet emission. *Monthly Notices of the Royal Astronomical Society*, 90, 202–212.
DOI: [10.1093/mnras/90.2.202](https://doi.org/10.1093/mnras/90.2.202) (Cited on page 13)
- Beech, M. (1988). The Schoenberg-Chandrasekhar limit: A polytropic approximation. *Astrophys Space Sci*, 147(2), 219–227.
DOI: [10.1007/BF00645666](https://doi.org/10.1007/BF00645666) (Cited on page 19)
- Berger, M. J. & Colella, P. (1989). Local adaptive mesh refinement for shock hydrodynamics. *Journal of Computational Physics*, 82(1), 64–84.
DOI: [10.1016/0021-9991\(89\)90035-1](https://doi.org/10.1016/0021-9991(89)90035-1) (Cited on page 67)
- Berger, M. J. & Oliger, J. (1984). Adaptive mesh refinement for hyperbolic partial differential equations. *Journal of Computational Physics*, 53(3), 484–512.
DOI: [10.1016/0021-9991\(84\)90073-1](https://doi.org/10.1016/0021-9991(84)90073-1) (Cited on page 67)
- Bethe, H. A. (1939). Energy Production in Stars. *Phys. Rev.*, 55(5), 434–456.
DOI: [10.1103/PhysRev.55.434](https://doi.org/10.1103/PhysRev.55.434) (Cited on pages 11, 12, 20)
- Bhattarai, B., Pandey, A. & Drabold, D. A. (2018). Evolution of amorphous carbon across densities: An inferential study. *Carbon*, 131, 168–174.
DOI: [10.1016/j.carbon.2018.01.103](https://doi.org/10.1016/j.carbon.2018.01.103) (Cited on page 95)
- Birnstiel, T., Fang, M. & Johansen, A. (2016). Dust Evolution and the Formation of Planetesimals. *Space Sci Rev*, 205(1), 41–75.
DOI: [10.1007/s11214-016-0256-1](https://doi.org/10.1007/s11214-016-0256-1) (Cited on page 30)
- Callingham, J. R., Crowther, P. A., Williams, P. M., Tuthill, P. G., Han, Y., Pope, B. J. S. & Marcote, B. (2020). Two Wolf-Rayet stars at the heart of colliding-wind binary Apep. *Mon Not R Astron Soc*, 495(3), 3323–3331.
DOI: [10.1093/mnras/staa1244](https://doi.org/10.1093/mnras/staa1244) (Cited on page 53)

BIBLIOGRAPHY

- Callingham, J. R., Tuthill, P. G., Pope, B. J. S., Williams, P. M., Crowther, P. A., Edwards, M., Norris, B. & Kedziora-Chudczer, L. (2019). Anisotropic winds in a Wolf-Rayet binary identify a potential gamma-ray burst progenitor. *Nature Astronomy*, 3(1), 82–87.
DOI: [10.1038/s41550-018-0617-7](https://doi.org/10.1038/s41550-018-0617-7) (Cited on pages 53, 54, 63, 145)
- Cassinelli, J. P. (1979). Stellar Winds. *Annual Review of Astronomy and Astrophysics*, 17(1), 275–308.
DOI: [10.1146/annurev.aa.17.090179.001423](https://doi.org/10.1146/annurev.aa.17.090179.001423) (Cited on page 15)
- Castor, J. I., Abbott, D. C. & Klein, R. I. (1975). Radiation-driven winds in Of stars. *The Astrophysical Journal*, 195, 157.
DOI: [10.1086/153315](https://doi.org/10.1086/153315) (Cited on pages xvii, 17)
- Cherepashchuk, A. M. (1976). Detectability of Wolf-Rayet binaries from X-rays. *Soviet Astronomy Letters*, 2, 138 (Cited on page 31).
- Chini, R., Hoffmeister, V. H., Nasser, A., Stahl, O. & Zinnecker, H. (2012). A spectroscopic survey on the multiplicity of high-mass stars. *Monthly Notices of the Royal Astronomical Society*, 424, 1925–1929.
DOI: [10.1111/j.1365-2966.2012.21317.x](https://doi.org/10.1111/j.1365-2966.2012.21317.x) (Cited on page 10)
- Choi, J., Dotter, A., Conroy, C., Cantiello, M., Paxton, B. & Johnson, B. D. (2016). Mesa Isochrones and Stellar Tracks (MIST). I. Solar-scaled Models. *The Astrophysical Journal*, 823, 102.
DOI: [10.3847/0004-637X/823/2/102](https://doi.org/10.3847/0004-637X/823/2/102) (Cited on pages 19, 22, 24)
- Chokshi, A., Tielens, A. G. G. M. & Hollenbach, D. (1993). Dust Coagulation. *The Astrophysical Journal*, 407, 806.
DOI: [10.1086/172562](https://doi.org/10.1086/172562) (Cited on page 26)
- Colella, P. & Woodward, P. R. (1984). The piecewise parabolic method (PPM) for gas-dynamical simulations. *Journal of computational physics*, 54(1), 174–201 (Cited on page 61).
- Conti, P. S. (1975). On the relationship between Of and WR stars. *Memoires of the Societe Royale des Sciences de Liege*, 9, 193–212 (Cited on page 22).
- Crowther, P. A., De Marco, O. & Barlow, M. J. (1998). Quantitative classification of WC and WO stars. *Monthly Notices of the Royal Astronomical Society*, 296, 367–378.
DOI: [10.1046/j.1365-8711.1998.01360.x](https://doi.org/10.1046/j.1365-8711.1998.01360.x) (Cited on page 22)
- Crowther, P. A. (2003). Dust Formation around Wolf-Rayet Stars. *Astrophysics and Space Science*, 285(3), 677–685.
DOI: [10.1023/A:1026157126395](https://doi.org/10.1023/A:1026157126395) (Cited on pages 48, 49, 90, 107, 149, 152–154, 164)

JOURNAL CITATIONS

- Crowther, P. A. (2007). Physical Properties of Wolf-Rayet Stars. *Annual Review of Astronomy and Astrophysics*, 45(1), 177–219.
DOI: [10.1146/annurev.astro.45.051806.110615](https://doi.org/10.1146/annurev.astro.45.051806.110615) (Cited on pages 20, 21, 23)
- Danks, A. C., Dennefeld, M., Wamsteker, W. & Shaver, P. A. (1983). Near infrared spectroscopy and infrared photometry of a new WC9 star. *Astronomy and Astrophysics*, 118, 301–305 (Cited on page 53).
- del Palacio, S., Benaglia, P., De Becker, M., Bosch-Ramon, V. & Romero, G. E. (2022). The non-thermal emission from the colliding-wind binary Apep. *Publications of the Astronomical Society of Australia*, 39, e004.
DOI: [10.1017/pasa.2021.60](https://doi.org/10.1017/pasa.2021.60) (Cited on page 54)
- Dotter, A. (2016). MESA Isochrones and Stellar Tracks (MIST) 0: Methods for the Construction of Stellar Isochrones. *The Astrophysical Journal Supplement Series*, 222, 8.
DOI: [10.3847/0067-0049/222/1/8](https://doi.org/10.3847/0067-0049/222/1/8) (Cited on pages 19, 22, 24)
- Draine, B. T. (2003). Interstellar Dust Grains. *Annual Review of Astronomy and Astrophysics*, 41(1), 241–289.
DOI: [10.1146/annurev.astro.41.011802.094840](https://doi.org/10.1146/annurev.astro.41.011802.094840) (Cited on pages 29, 43)
- Draine, B. T. & Salpeter, E. E. (1979a). Destruction mechanisms for interstellar dust. *The Astrophysical Journal*, 231, 438–455.
DOI: [10.1086/157206](https://doi.org/10.1086/157206) (Cited on pages 29, 46, 97)
- Draine, B. T. & Salpeter, E. E. (1979b). On the physics of dust grains in hot gas. *The Astrophysical Journal*, 231, 77–94.
DOI: [10.1086/157165](https://doi.org/10.1086/157165) (Cited on pages 27, 116, 144)
- Dwek, E. & Werner, M. W. (1981). The Infrared Emission From Supernova Condensates. *The Astrophysical Journal*, 248, 138.
DOI: [10.1086/159138](https://doi.org/10.1086/159138) (Cited on pages 44, 79–81, 84, 86, 113, 114, 145)
- Dwek, E., Foster, S. M. & Vancura, O. (1996). Cooling, Sputtering, and Infrared Emission from Dust Grains in Fast Nonradiative Shocks. *The Astrophysical Journal*, 457, 244.
DOI: [10.1086/176725](https://doi.org/10.1086/176725) (Cited on pages 27, 42, 97, 116, 144)
- Eddington, A. S. (1920). The Internal Constitution of the Stars. *The Scientific Monthly*, 11(4), 297–303 (Cited on page 11).
- Eichler, D. & Usov, V. (1993). Particle acceleration and nonthermal radio emission in binaries of early-type stars. *The Astrophysical Journal*, 402, 271–279.
DOI: [10.1086/172130](https://doi.org/10.1086/172130) (Cited on pages 32–35, 108, 147)
- Fahed, R., Moffat, A. F. J., Zorec, J., Eversberg, T., Chené, A. N., Alves, F., Arnold, W., Bergmann, T., Corcoran, M. F., Correia Viegas, N. G., Dougherty, S. M., Fernando,

BIBLIOGRAPHY

- A., Frémat, Y., Gouveia Carreira, L. F., Hunger, T., Knapen, J. H., Leadbeater, R., Marques Dias, F., Martayan, C., ... Williams, P. M. (2011). Spectroscopy of the archetype colliding-wind binary WR 140 during the 2009 January periastron passage. *Monthly Notices of the Royal Astronomical Society*, *418*, 2–13.
DOI: [10.1111/j.1365-2966.2011.19035.x](https://doi.org/10.1111/j.1365-2966.2011.19035.x) (Cited on page 152)
- Friend, D. B. & Abbott, D. C. (1986). The theory of radiatively driven stellar winds. III - Wind models with finite disk correction and rotation. *The Astrophysical Journal*, *311*, 701.
DOI: [10.1086/164809](https://doi.org/10.1086/164809) (Cited on page 18)
- Gamow, G. (1943). On WC and WN Stars. *The Astrophysical Journal*, *98*, 500.
DOI: [10.1086/144581](https://doi.org/10.1086/144581) (Cited on page 20)
- Gayley, K. G., Owocki, S. P. & Cranmer, S. R. (1997). Sudden Radiative Braking in Colliding Hot-Star Winds. *ApJ*, *475*(2), 786.
DOI: [10.1086/303573](https://doi.org/10.1086/303573) (Cited on pages 52, 73, 108, 147)
- Godunov, S. K. (1959). A difference scheme for numerical solution of discontinuous solution of hydrodynamic equations. *Math. Sbornik*, *47*, 271–306 (Cited on page 59).
- Gosset, E., Nazé, Y., Claeskens, J.-F., Rauw, G., Vreux, J.-M. & Sana, H. (2005). An XMM-Newton look at the Wolf-Rayet star WR 40. The star itself, its nebula and its neighbours. *Astronomy and Astrophysics*, *429*, 685–704.
DOI: [10.1051/0004-6361:20040286](https://doi.org/10.1051/0004-6361:20040286) (Cited on page 31)
- Grimaldo, E., Reimer, A., Kissmann, R., Niederwanger, F. & Reitberger, K. (2019). Proton Acceleration in Colliding Stellar Wind Binaries. *The Astrophysical Journal*, *871*, 55.
DOI: [10.3847/1538-4357/aaf6ee](https://doi.org/10.3847/1538-4357/aaf6ee) (Cited on page 33)
- Gustafson, J. L. (1988). Reevaluating Amdahl's law. *Commun. ACM*, *31*(5), 532–533.
DOI: [10.1145/42411.42415](https://doi.org/10.1145/42411.42415) (Cited on page 180)
- Hamaguchi, K., Corcoran, M. F., Pittard, J. M., Sharma, N., Takahashi, H., Russell, C. M. P., Grefenstette, B. W., Wik, D. R., Gull, T. R., Richardson, N. D., Madura, T. I. & Moffat, A. F. J. (2018). Non-thermal X-rays from colliding wind shock acceleration in the massive binary Eta Carinae. *Nat Astron*, *2*(9), 731–736.
DOI: [10.1038/s41550-018-0505-1](https://doi.org/10.1038/s41550-018-0505-1) (Cited on page 3)
- Han, Y., Tuthill, P. G., Lau, R. M., Soulain, A., Callingham, J. R., Williams, P. M., Crowther, P. A., Pope, B. J. S. & Marcote, B. (2020). The extreme colliding-wind system Apep: Resolved imagery of the central binary and dust plume in the infrared. *Monthly Notices of the Royal Astronomical Society*, *498*(4), 5604–5619.
DOI: [10.1093/mnras/staa2349](https://doi.org/10.1093/mnras/staa2349) (Cited on pages 54, 167)

JOURNAL CITATIONS

- Harries, T. J., Monnier, J. D., Symington, N. H. & Kurosawa, R. (2004). Three-dimensional dust radiative-transfer models: The Pinwheel Nebula of WR 104. *Monthly Notices of the Royal Astronomical Society*, *350*(2), 565–574.
DOI: [10.1111/j.1365-2966.2004.07668.x](https://doi.org/10.1111/j.1365-2966.2004.07668.x) (Cited on pages 51, 99, 117, 123)
- Harris, M. J., Fowler, W. A., Caughlan, G. R. & Zimmerman, B. A. (1983). Thermonuclear Reaction Rates, III. *Annual Review of Astronomy and Astrophysics*, *21*(1), 165–176.
DOI: [10.1146/annurev.aa.21.090183.001121](https://doi.org/10.1146/annurev.aa.21.090183.001121) (Cited on page 12)
- Hendrix, T., Keppens, R., van Marle, A. J., Camps, P., Baes, M. & Meliani, Z. (2016). Pinwheels in the sky, with dust: 3D modelling of the Wolf-Rayet 98a environment. *Monthly Notices of the Royal Astronomical Society*, *460*(4), 3975–3991.
DOI: [10.1093/mnras/stw1289](https://doi.org/10.1093/mnras/stw1289) (Cited on pages 50, 99, 102, 115, 123, 124, 140, 165, 166)
- Herbst, E. & van Dishoeck, E. F. (2009). Complex Organic Interstellar Molecules. *Annual Review of Astronomy and Astrophysics*, *47*(1), 427–480.
DOI: [10.1146/annurev-astro-082708-101654](https://doi.org/10.1146/annurev-astro-082708-101654) (Cited on pages 29, 30, 135)
- Ishihara, D., Kaneda, H., Onaka, T., Ita, Y., Matsuura, M. & Matsunaga, N. (2011). Galactic distributions of carbon- and oxygen-rich AGB stars revealed by the AKARI mid-infrared all-sky survey. *A&A*, *534*, A79.
DOI: [10.1051/0004-6361/201117626](https://doi.org/10.1051/0004-6361/201117626) (Cited on pages 46, 107)
- Jones, A. P. (2004). Dust Destruction Processes. *309*, 347 (Cited on pages 26, 29).
- Jones, A. P., Tielens, A. G. G. M. & Hollenbach, D. J. (1996). Grain Shattering in Shocks: The Interstellar Grain Size Distribution. *The Astrophysical Journal*, *469*, 740.
DOI: [10.1086/177823](https://doi.org/10.1086/177823) (Cited on page 26)
- Kaastra, J. S., Raassen, A. J. J., de Plaa, J. & Gu, L. (2013). SPEX: High-resolution cosmic X-ray spectra analysis. *Astrophysics Source Code Library*, ascl:1308.014 (Cited on page 40).
- Kapteyn, J. C. (1909). On the Absorption of Light in Space. *The Astrophysical Journal*, *29*, 46.
DOI: [10.1086/141618](https://doi.org/10.1086/141618) (Cited on page 25)
- Lamberts, A., Dubus, G., Fromang, S. & Lesur, G. (2012). Colliding wind binaries and γ -ray binaries: Relativistic version of the RAMSES code, 406–409.
DOI: [10.1063/1.4772283](https://doi.org/10.1063/1.4772283) (Cited on page 51)
- Lau, R. M., Eldridge, J. J., Hankins, M. J., Lamberts, A., Sakon, I. & Williams, P. M. (2020). Revisiting the Impact of Dust Production from Carbon-rich Wolf-Rayet Binaries. *ApJ*, *898*(1), 74.
DOI: [10.3847/1538-4357/ab9cb5](https://doi.org/10.3847/1538-4357/ab9cb5) (Cited on pages 45, 49, 52, 55, 106, 134, 139, 155, 164)
- Lau, R. M., Hankins, M. J., Kasliwal, M. M., Bond, H. E., De, K., Jencson, J. E., Moffat, A. F. J., Smith, N. & Williams, P. M. (2021). Revealing Efficient Dust Formation at

BIBLIOGRAPHY

- Low Metallicity in Extragalactic Carbon-rich Wolf-Rayet Binaries. *ApJ*, 909(2), 113.
DOI: [10.3847/1538-4357/abd8cd](https://doi.org/10.3847/1538-4357/abd8cd) (Cited on pages 52, 94)
- Lucy, L. B. & Solomon, P. M. (1970). Mass Loss by Hot Stars. *The Astrophysical Journal*, 159, 879.
DOI: [10.1086/150365](https://doi.org/10.1086/150365) (Cited on pages 16, 17)
- Marchenko, S. V., Moffat, A. F. J. & Crowther, P. A. (2010). Population I Wolf-Rayet Runaway Stars: The Case of WR124 and its Expanding Nebula M1-67. *The Astrophysical Journal*, 724, L90–L94.
DOI: [10.1088/2041-8205/724/1/L90](https://doi.org/10.1088/2041-8205/724/1/L90) (Cited on page 21)
- Marcote, B., Callingham, J. R., De Becker, M., Edwards, P. G., Han, Y., Schulz, R., Stevens, J. & Tuthill, P. G. (2021). AU-scale radio imaging of the wind collision region in the brightest and most luminous non-thermal colliding wind binary Apep. *Monthly Notices of the Royal Astronomical Society*, 501(2), 2478–2486.
DOI: [10.1093/mnras/staa3863](https://doi.org/10.1093/mnras/staa3863) (Cited on page 54)
- Medina, E. M., Richardson, N. & Chené, A. (2021). Are all WCd stars binaries? An IGRINS search for companion stars. 53, 215.07 (Cited on pages 23, 45).
- Mewe, R., Gronenschild, E. H. B. M. & van den Oord, G. H. J. (1985). Calculated X-radiation from optically thin plasmas. V. *Astronomy and Astrophysics Supplement Series*, 62, 197–254 (Cited on pages 40, 76).
- Mewe, R., Lemen, J. R. & van den Oord, G. H. J. (1986). Calculated X-radiation from optically thin plasmas. VI - Improved calculations for continuum emission and approximation formulae for nonrelativistic average Gaunt actors. *Astronomy and Astrophysics Supplement Series*, 65, 511–536 (Cited on page 76).
- Meyer, C. D., Balsara, D. S. & Aslam, T. D. (2014). A stabilized Runge-Kutta-Legendre method for explicit super-time-stepping of parabolic and mixed equations. *Journal of Computational Physics*, 257, 594–626.
DOI: [10.1016/j.jcp.2013.08.021](https://doi.org/10.1016/j.jcp.2013.08.021) (Cited on page 66)
- Milne, E. A. (1926). On the possibility of the emission of high-speed atoms from the sun and stars. *Monthly Notices of the Royal Astronomical Society*, 86, 459–473.
DOI: [10.1093/mnras/86.7.459](https://doi.org/10.1093/mnras/86.7.459) (Cited on page 17)
- Monnier, J. D., Tuthill, P. G. & Danchi, W. C. (1999). Pinwheel Nebula around WR 98a. *ApJ*, 525(2), L97.
DOI: [10.1086/312352](https://doi.org/10.1086/312352) (Cited on pages 49, 107, 139)
- Monnier, J. D., Tuthill, P. G., Danchi, W. C., Murphy, N. & Harries, T. J. (2007). The Keck Aperture-masking Experiment: Near-Infrared Sizes of Dusty Wolf-Rayet Stars. *ApJ*,

JOURNAL CITATIONS

- 655(2), 1033.
DOI: [10.1086/509873](https://doi.org/10.1086/509873) (Cited on pages 50, 145)
- Nazé, Y., Gosset, E. & Marechal, Q. (2021). New X-ray detections of known Wolf-Rayet stars. *Monthly Notices of the Royal Astronomical Society*, 501, 4214–4225.
DOI: [10.1093/mnras/staa3801](https://doi.org/10.1093/mnras/staa3801) (Cited on page 31)
- Neufeld, D. A. & Kaufman, M. J. (1993). Radiative Cooling of Warm Molecular Gas. *The Astrophysical Journal*, 418, 263.
DOI: [10.1086/173388](https://doi.org/10.1086/173388) (Cited on page 37)
- Neufeld, D. A., Lepp, S. & Melnick, G. J. (1995). Thermal Balance in Dense Molecular Clouds: Radiative Cooling Rates and Emission-Line Luminosities. *The Astrophysical Journal Supplement Series*, 100, 132.
DOI: [10.1086/192211](https://doi.org/10.1086/192211) (Cited on page 37)
- Neugent, K. & Massey, P. (2019). The Wolf-Rayet Content of the Galaxies of the Local Group and Beyond. *Galaxies*, 7(3), 74.
DOI: [10.3390/galaxies7030074](https://doi.org/10.3390/galaxies7030074) (Cited on page 23)
- Niedzielski, A. & Skorzynski, W. (2002). Kinematical Structure of Wolf-Rayet Winds. I. Terminal Wind Velocity. *Acta Astronomica*, 52, 81–104 (Cited on page 47).
- Oskinova, L. M. (2015). X-ray emission from single WR stars. *Wolf-Rayet Stars : Proceedings of an International Workshop held in Potsdam, Germany, 1.–5. June 2015*, 295–300 (Cited on page 31).
- Pauldrach, A., Puls, J. & Kudritzki, R. P. (1986). Radiation-driven winds of hot luminous stars. Improvements of the theory and first results. *Astronomy and Astrophysics*, Vol. 164, p. 86-100 (1986), 164, 86 (Cited on page 18).
- Paxton, B., Bildsten, L., Dotter, A., Herwig, F., Lesaffre, P. & Timmes, F. (2011). Modules for Experiments in Stellar Astrophysics (MESA). *The Astrophysical Journal Supplement Series*, 192, 3.
DOI: [10.1088/0067-0049/192/1/3](https://doi.org/10.1088/0067-0049/192/1/3) (Cited on pages 19, 22, 24)
- Pittard, J. M. (2009). 3D models of radiatively driven colliding winds in massive O+O star binaries - I. Hydrodynamics. *Monthly Notices of the Royal Astronomical Society*, 396(3), 1743–1763.
DOI: [10.1111/j.1365-2966.2009.14857.x](https://doi.org/10.1111/j.1365-2966.2009.14857.x) (Cited on pages 123, 157)
- Pittard, J. M. & Dawson, B. (2018). Colliding stellar winds structure and X-ray emission. *Mon Not R Astron Soc*, 477(4), 5640–5645.
DOI: [10.1093/mnras/sty1025](https://doi.org/10.1093/mnras/sty1025) (Cited on pages 34, 108, 117, 148)

BIBLIOGRAPHY

- Pittard, J. M. & Parkin, E. R. (2010). 3D models of radiatively driven colliding winds in massive O + O star binaries - III. Thermal X-ray emission. *Monthly Notices of the Royal Astronomical Society*, *403*(4), 1657–1683.
DOI: [10.1111/j.1365-2966.2010.15776.x](https://doi.org/10.1111/j.1365-2966.2010.15776.x) (Cited on page 157)
- Prilutskii, O. F. & Usov, V. V. (1976). X rays from Wolf-Rayet binaries. *Soviet Astronomy*, *20*, 2 (Cited on pages 31, 32, 138).
- Robitaille, T. P. (2011). HYPERION: An open-source parallelized three-dimensional dust continuum radiative transfer code. *A&A*, *536*, A79.
DOI: [10.1051/0004-6361/201117150](https://doi.org/10.1051/0004-6361/201117150) (Cited on pages 102, 166)
- Rosslowe, C. K. & Crowther, P. A. (2015). Spatial distribution of Galactic Wolf-Rayet stars and implications for the global population. *Monthly Notices of the Royal Astronomical Society*, *447*(3), 2322–2347.
DOI: [10.1093/mnras/stu2525](https://doi.org/10.1093/mnras/stu2525) (Cited on pages 46, 106, 107, 140)
- Ruuth, S. J. & Spiteri, R. J. (2005). High-Order Strong-Stability-Preserving Runge-Kutta Methods with Downwind-Biased Spatial Discretizations. *SIAM Journal on Numerical Analysis*, *42*(3), 974–996 (Cited on pages 66, 141).
- Saha, M. N. (1919). On Radiation-Pressure and the Quantum Theory. *The Astrophysical Journal*, *50*, 220.
DOI: [10.1086/142497](https://doi.org/10.1086/142497) (Cited on page 17)
- Salpeter, E. E. (1977). Formation and Destruction of Dust Grains. *Annual Review of Astronomy and Astrophysics*, *15*(1), 267–293 (Cited on page 46).
- Schönberg, M. & Chandrasekhar, S. (1942). On the Evolution of the Main-Sequence Stars. *The Astrophysical Journal*, *96*, 161.
DOI: [10.1086/144444](https://doi.org/10.1086/144444) (Cited on page 19)
- Seward, F. D., Forman, W. R., Giacconi, R., Griffiths, R. E., Harnden, F. R., Jr., Jones, C. & Pye, J. P. (1979). X-rays from Eta Carinae and the surrounding nebula. *The Astrophysical Journal*, *234*, L55–L58.
DOI: [10.1086/183108](https://doi.org/10.1086/183108) (Cited on page 31)
- Shenar, T., Sablowski, D. P., Hainich, R., Todt, H., Moffat, A. F. J., Oskinova, L. M., Ramachandran, V., Sana, H., Sander, A. A. C., Schnurr, O., St-Louis, N., Vanbeveren, D., Götberg, Y. & Hamann, W.-R. (2019). The Wolf-Rayet binaries of the nitrogen sequence in the Large Magellanic Cloud: Spectroscopy, orbital analysis, formation, and evolution. *A&A*, *627*, A151.
DOI: [10.1051/0004-6361/201935684](https://doi.org/10.1051/0004-6361/201935684) (Cited on page 53)

JOURNAL CITATIONS

- Soulain, A., Millour, F., Lopez, B., Matter, A., Lagadec, E., Carbillet, M., Camera, A. L., Lamberts, A., Langlois, M., Milli, J., Avenhaus, H., Magnard, Y., Roux, A., Moulin, T., Carle, M., Sevin, A., Martinez, P., Abe, L. & Ramos, J. (2018). SPHERE view of Wolf-Rayet 104 - Direct detection of the Pinwheel and the link with the nearby star. *A&A*, *618*, A108.
DOI: [10.1051/0004-6361/201832817](https://doi.org/10.1051/0004-6361/201832817) (Cited on pages 51, 52, 63, 107, 139, 145)
- Spiteri, R. J. & Ruuth, S. J. (2002). A New Class of Optimal High-Order Strong-Stability-Preserving Time Discretization Methods. *SIAM J. Numer. Anal.*, *40*(2), 469–491.
DOI: [10.1137/S0036142901389025](https://doi.org/10.1137/S0036142901389025) (Cited on page 110)
- Stevens, I. R. & Pollock, A. M. T. (1994). Stagnation-point flow in colliding-wind binary systems. *Mon Not R Astron Soc*, *269*(2), 226–234.
DOI: [10.1093/mnras/269.2.226](https://doi.org/10.1093/mnras/269.2.226) (Cited on pages 108, 147)
- Stevens, I. R., Blondin, J. M. & Pollock, A. M. T. (1992). Colliding winds from early-type stars in binary systems. *The Astrophysical Journal*, *386*, 265–287.
DOI: [10.1086/171013](https://doi.org/10.1086/171013) (Cited on pages 33, 40, 41, 109, 147, 157)
- Stone, J. M., Tomida, K., White, C. J. & Felker, K. G. (2020). The Athena++ Adaptive Mesh Refinement Framework: Design and Magnetohydrodynamic Solvers. *ApJS*, *249*(1), 4.
DOI: [10.3847/1538-4365/ab929b](https://doi.org/10.3847/1538-4365/ab929b) (Cited on pages 66, 91, 109, 141)
- Sugawara, Y., Maeda, Y., Tsuboi, Y., Hamaguchi, K., Corcoran, M., Pollock, A. M. T., Moffat, A. F. J., Williams, P. M., Dougherty, S. & Pittard, J. (2015). Suzaku monitoring of the Wolf-Rayet binary WR 140 around periastron passage: An approach for quantifying the wind parameters. *Publications of the Astronomical Society of Japan*, *67*(6), 121.
DOI: [10.1093/pasj/pss099](https://doi.org/10.1093/pasj/pss099) (Cited on page 158)
- Thomas, J. D., Richardson, N. D., Eldridge, J. J., Schaefer, G. H., Monnier, J. D., Sana, H., Moffat, A. F. J., Williams, P., Corcoran, M. F., Stevens, I. R., Weigelt, G., Zainol, F. D., Anugu, N., Le Bouquin, J.-B., ten Brummelaar, T., Campos, F., Couperus, A., Davies, C. L., Ennis, J., ... Zurmühl, U. (2021). The orbit and stellar masses of the archetype colliding-wind binary WR 140. *Monthly Notices of the Royal Astronomical Society*, *504*(4), 5221–5230.
DOI: [10.1093/mnras/stab1181](https://doi.org/10.1093/mnras/stab1181) (Cited on pages 107, 148)
- Tielens, A. G. G. M., McKee, C. F., Seab, C. G. & Hollenbach, D. J. (1994). The physics of grain-grain collisions and gas-grain sputtering in interstellar shocks. *The Astrophysical Journal*, *431*, 321.
DOI: [10.1086/174488](https://doi.org/10.1086/174488) (Cited on pages 27, 28, 97, 116, 144)

BIBLIOGRAPHY

- Toro, E. F., Spruce, M. & Speares, W. (1994). Restoration of the contact surface in the HLL-Riemann solver. *Shock Waves*, 4(1), 25–34.
DOI: [10.1007/BF01414629](https://doi.org/10.1007/BF01414629) (Cited on pages 60, 66)
- Townsend, R. H. D. (2009). An Exact Integration Scheme for Radiative Cooling in Hydrodynamical Simulations. *ApJS*, 181(2), 391–397.
DOI: [10.1088/0067-0049/181/2/391](https://doi.org/10.1088/0067-0049/181/2/391) (Cited on pages 77, 88, 89)
- Tuthill, P. G., Monnier, J. D. & Danchi, W. C. (1999). A dusty pinwheel nebula around the massive star WR 104. *Nature*, 398(6727), 487–489.
DOI: [10.1038/19033](https://doi.org/10.1038/19033) (Cited on pages 107, 139)
- Usov, V. V. (1991). Stellar wind collision and dust formation in long-period, heavily interacting Wolf-Rayet binaries. *Monthly Notices of the Royal Astronomical Society*, 252(1), 49–52.
DOI: [10.1093/mnras/252.1.49](https://doi.org/10.1093/mnras/252.1.49) (Cited on page 33)
- van der Hucht, K. A., Koenigsberger, G. & Eenens, P. R. (1999). Wolf-rayet phenomena in massive stars and starburst galaxies. *Wolf-Rayet Phenomena in Massive Stars and Starburst Galaxies*, 193 (Cited on page 107).
- van Leer, B. (1979). Towards the ultimate conservative difference scheme. V. A second-order sequel to Godunov's method. *Journal of Computational Physics*, 32(1), 101–136.
DOI: [10.1016/0021-9991\(79\)90145-1](https://doi.org/10.1016/0021-9991(79)90145-1) (Cited on pages 61, 66)
- Watson, W. D. & Salpeter, E. E. (1972). On the Abundances of Interstellar Molecules. *The Astrophysical Journal*, 175, 659.
DOI: [10.1086/151587](https://doi.org/10.1086/151587) (Cited on page 28)
- Wiener, J., Zweibel, E. G. & Oh, S. P. (2013). Cosmic Ray Heating of the Warm Ionized Medium. *The Astrophysical Journal*, 767, 87.
DOI: [10.1088/0004-637X/767/1/87](https://doi.org/10.1088/0004-637X/767/1/87) (Cited on page 40)
- Williams, P. M. (2019). Variable dust emission by WC type Wolf-Rayet stars observed in the NEOWISE-R survey. *Monthly Notices of the Royal Astronomical Society*, 488(1), 1282–1300.
DOI: [10.1093/mnras/stz1784](https://doi.org/10.1093/mnras/stz1784) (Cited on pages 48, 53, 55, 107)
- Williams, P. M., Beattie, D. H., Lee, T. J., Stewart, J. M. & Antonopoulou, E. (1978). Condensation of a shell around HD 193793. *Monthly Notices of the Royal Astronomical Society*, 185, 467–472.
DOI: [10.1093/mnras/185.3.467](https://doi.org/10.1093/mnras/185.3.467) (Cited on page 50)
- Williams, P. M., Crowther, P. A. & van der Hucht, K. A. (2015). The spectra of WC9 stars: Evolution and dust formation. *Monthly Notices of the Royal Astronomical Society*, 449(2),

JOURNAL CITATIONS

1834–1844.

DOI: [10.1093/mnras/stv409](https://doi.org/10.1093/mnras/stv409) (Cited on pages 112, 149)

Williams, P. M., Marchenko, S. V., Marston, A. P., Moffat, A. F. J., Varricatt, W. P., Dougherty, S. M., Kidger, M. R., Morbidelli, L. & Tapia, M. (2009). Orbitally modulated dust formation by the WC7+O5 colliding-wind binary WR 140. *Monthly Notices of the Royal Astronomical Society*, 395(3), 1749–1767.

DOI: [10.1111/j.1365-2966.2009.14664.x](https://doi.org/10.1111/j.1365-2966.2009.14664.x) (Cited on page 154)

Williams, P. M. & van der Hucht, K. A. (2000). Spectroscopy of WC9 Wolf-Rayet stars: A search for companions. *Monthly Notices of the Royal Astronomical Society*, 314(1), 23–32.

DOI: [10.1046/j.1365-8711.2000.03332.x](https://doi.org/10.1046/j.1365-8711.2000.03332.x) (Cited on page 51)

Williams, P. M., van der Hucht, K. A., Pollock, A. M. T., Florkowski, D. R., van der Woerd, H. & Wamsteker, W. M. (1990). Multi-frequency variations of the Wolf-rayet system HD 193793 - I. Infrared, X-ray and radio observations. *Monthly Notices of the Royal Astronomical Society*, 243, 662–684 (Cited on pages 107, 139, 148).

Williams, P. M., van der Hucht, K. A. & Thé, P. S. (1987). Infrared photometry of late-type Wolf-Rayet stars. *Astronomy and Astrophysics*, 182, 91–106 (Cited on pages 32, 139).

Williams, P. M., van der Hucht, K. A., Thé, P. S. & Bouchet, P. (1990). A Dust Shell around the Early Type Wolf-Rayet Star WR:19. *Monthly Notices of the Royal Astronomical Society*, 247, 18P (Cited on page 124).

Wolfire, M. G., Hollenbach, D., McKee, C. F., Tielens, A. G. G. M. & Bakes, E. L. O. (1995). The Neutral Atomic Phases of the Interstellar Medium. *The Astrophysical Journal*, 443, 152.

DOI: [10.1086/175510](https://doi.org/10.1086/175510) (Cited on page 43)

Zhekov, S. A., Gagné, M. & Skinner, S. L. (2022). Chandra revisits WR 48a: Testing colliding wind models in massive binaries. *Monthly Notices of the Royal Astronomical Society*, 510(1), 1278–1288.

DOI: [10.1093/mnras/stab3469](https://doi.org/10.1093/mnras/stab3469) (Cited on page 55)

Zhekov, S. A., Tomov, T., Gawronski, M. P., Georgiev, L. N., Borissova, J., Kurtev, R., Gagné, M. & Hajduk, M. (2014). A multiwavelength view on the dusty Wolf-Rayet star WR 48a. *Monthly Notices of the Royal Astronomical Society*, 445(2), 1663–1678.

DOI: [10.1093/mnras/stu1880](https://doi.org/10.1093/mnras/stu1880) (Cited on page 55)

Zubko, V. G. (1998). On the physical model of dust around Wolf-Rayet stars. *Monthly Notices of the Royal Astronomical Society*, 295(1), 109–118.

DOI: [10.1046/j.1365-8711.1998.29511348.x](https://doi.org/10.1046/j.1365-8711.1998.29511348.x) (Cited on pages 26, 45, 94, 108, 117)

BIBLIOGRAPHY

Software Citations

Astropy Collaboration, Price-Whelan, A. M., Sipőcz, B. M., Günther, H. M., Lim, P. L., Crawford, S. M., Conseil, S., Shupe, D. L., Craig, M. W., Dencheva, N., Ginsburg, A., VanderPlas, J. T., Bradley, L. D., Pérez-Suárez, D., de Val-Borro, M., Aldcroft, T. L., Cruz, K. L., Robitaille, T. P., Tollerud, E. J., ... Astropy Contributors. (2018, September). *The astropy project: Building an open-science project and status of the v2.0 core package* (No. 3).

DOI: [10.3847/1538-3881/aabc4f](https://doi.org/10.3847/1538-3881/aabc4f). (Cited on page 177)

Astropy Collaboration, Robitaille, T. P., Tollerud, E. J., Greenfield, P., Droettboom, M., Bray, E., Aldcroft, T., Davis, M., Ginsburg, A., Price-Whelan, A. M., Kerzendorf, W. E., Conley, A., Crighton, N., Barbary, K., Muna, D., Ferguson, H., Grollier, F., Parikh, M. M., Nair, P. H., ... Streicher, O. (2013, October). *Astropy: A community Python package for astronomy*.

DOI: [10.1051/0004-6361/201322068](https://doi.org/10.1051/0004-6361/201322068). (Cited on page 177)

Childs, H., Brugger, E., Whitlock, B., Meredith, J., Ahern, S., Pugmire, D., Biagas, K., Miller, M., Harrison, C., Weber, G. H., Krishnan, H., Fogal, T., Sanderson, A., Garth, C., Bethel, E. W., Camp, D., Rübel, O., Durant, M., Favre, J. M. & Navrátil, P. (2012, October). VisIt: An end-user tool for visualizing and analyzing very large data. *High performance Visualization—Enabling extreme-scale scientific insight* (pp. 357–372). (Cited on page 182).

Harris, C. R., Millman, K. J., van der Walt, S. J., Gommers, R., Virtanen, P., Cournapeau, D., Wieser, E., Taylor, J., Berg, S., Smith, N. J., Kern, R., Picus, M., Hoyer, S., van Kerkwijk, M. H., Brett, M., Haldane, A., del Río, J. F., Wiebe, M., Peterson, P., ... Oliphant, T. E. (2020). Array programming with NumPy. *Nature*, 585(7825), 357–362.

DOI: [10.1038/s41586-020-2649-2](https://doi.org/10.1038/s41586-020-2649-2) (Cited on pages 177, 182)

Hunter, J. D. (2007). Matplotlib: A 2D graphics environment. *Computing in Science & Engineering*, 9(3), 90–95.

DOI: [10.1109/MCSE.2007.55](https://doi.org/10.1109/MCSE.2007.55) (Cited on pages 177, 182)

Lam, S. K., Pitrou, A. & Seibert, S. (2015). Numba: A llvm-based python jit compiler. *Proceedings of the Second Workshop on the LLVM Compiler Infrastructure in HPC*, 1–6 (Cited on page 182).

Stone, J. M., Tomida, K., White, C. J. & Felker, K. G. (2021, January). *Princeton University/athena-public-version: Athena++ v21.0* (Version 21.0).

DOI: [10.5281/zenodo.4455880](https://doi.org/10.5281/zenodo.4455880). (Cited on page 177)

OTHER CITATIONS

Tange, O. (2021, September). *GNU parallel 20210922 ('vindelev')*.

DOI: [10.5281/zenodo.5523272](https://doi.org/10.5281/zenodo.5523272). (Cited on pages 177, 182)

The HDF Group. (1997–2022). *Hierarchical data format, version 5*. (Cited on page 181).

Tomar, S. (2006). Converting video formats with FFmpeg. *Linux Journal*, 2006(146), 10 (Cited on page 182).

Van Rossum, G. & Drake, F. L. (2009). *Python 3 reference manual*. CreateSpace. (Cited on page 176).

Williams, T., Kelley, C. & many others. (2020, July). Gnuplot 5.4: An interactive plotting program. (Cited on page 182).

Other Citations

Eatson, J. W., Pittard, J. M. & Van Loo, S. (2022a, April 15). *An exploration of dust grain growth within WCd systems using an advected scalar dust model*. (Cited on pages 6, 50, 103, 105, 146, 157, 162, 163).

Eatson, J. W., Pittard, J. M. & Van Loo, S. (2022b, April 26). *Exploring dust growth in the episodic WCd system WR140*. (Cited on pages 6, 51, 103, 137, 162, 164).

Pittard, J. M. (1999). *X-ray emission from colliding stellar winds: Theoretical modelling and observations*. (Doctoral dissertation). University of Birmingham. (Cited on page 31).

Rauw, G. (2022, March 31). *X-ray emission of massive stars and their winds*. (Cited on page 31).